LA-8323-PR

Progress Report

1

dc Superconducting Power Transmission Line Project at LASL

US DOE Division of Electric Energy Systems

November 1, 1972—September 30, 1979

Final Report

Progress Report No. 24

LOS ALAMOS SCIENTIFIC LABORATORY
Post Office Box 1663 Los Alamos, New Mexico 87545

The four most recent reports in this series, unclassified, are LA-6215-PR, LA-6699-PR, LA-7116-PR, and LA-7707-PR.

This work was supported by the US Department of Energy, Division of Electric Energy Systems.

LA-8323-PR
Progress Report
UC-34
Issued: April 1980

dc Superconducting Power Transmission Line Project at LASL

US DOE Division of Electric Energy Systems

November 1, 1972—September 30, 1979

Final Report

Progress Report No. 24

Compiled by
F. J. Edeskuty

Contributors

R. J. Bartlett
T. R. Bement
R. J. Candler
R. V. Carlson
P. Chowdhuri
J. W. Dean
J. Dickinson
F. J. Edeskuty
K. L. Elsner
C. N. Espinoza
J. H. Fretwell
M. D. Henke
J. K. Hoffer
W. E. Keller
E. C. Kerr
K. Khalafalla
H. L. Laquer
M. McClannahan
M. W. Mahaffy
M. P. Maley
K. Mestas
A. Migliori
L. R. Newkirk
W. C. Overton
C. G. Sanchez
Z. Sandler
P. Smith
W. F. Stewart
R. D. Taylor
J. D. Thompson
R. D. Turner
G. Weeks
S. L. Wipf

CONTENTS

dc SUPERCONDUCTING POWER TRANSMISSION LINE PROJECT AT LASL
US DOE Division of Electric Energy Systems
November 1, 1972 - September 30, 1979
Final Report
(Progress Report No. 24)

Compiled by

F. J. Edeskuty

ABSTRACT

Plans for a large-scale dc SPTL test have been indefinitely postponed because of budgetary restrictions. This report is a final report on the Los Alamos Scientific Laboratory (LASL) dc Superconducting Power Transmission Line (SPTL) Development Project and covers activities in electrical engineering, cryogenic engineering, and superconductor design for the period of November 1, 1972 through September 30, 1979.

---

1. EXECUTIVE SUMMARY

Since November 1972, the Los Alamos Scientific Laboratory (LASL) has been developing a high-capacity, underground dc superconducting power transmission line (dc SPTL) that would use Nb_3Sn superconducting wires cooled to 12 K by gaseous helium. This development was deemed important because accompanying the ever increasing demand for electric power is the expectation for the need of systems that can provide high power transmission densities in certain locations and often over large distances.

The dc SPTL offers a number of potential advantages which justify its development. The dc SPTL would have no system stability or load-flow constraints, would have lower short-circuit current levels than any other transmission system, would not need reactive compensation, would exhibit no

dielectric losses, and would have negligible conductor losses. The dc SPTL cable, of all cables, would have the highest efficiency and the highest current density capability; for example, a single 30-cm-diameter cable could carry up to 10 GW with power losses of less than 0.1% per 100 km.

The requirement for such high power transmission capability is still perhaps several decades in the future, and the SPTL technology must be considered a high risk undertaking. Therefore it is appropriate that this type of investigation be undertaken at a National Laboratory, such as LASL. This work was funded initially by the US Atomic Energy Commission, continued by the US Energy Research and Development Administration, and, subsequently, by the Division of Electric Energy Systems of the US Department of Energy (USDOE).

The goals of the dc SPTL program have included the investigation of those basic principles necessary for the design and fabrication of a dc SPTL and for predicting its operating capabilities. A specific goal of the program has been the construction and operation of a prototype capable of demonstrating high-current (25 kA) and high voltage (100 kV) capability. Until mid-FY 1979 funding was at a level consistent with carrying out these demonstration tests in FY 1982 and FY 1983. However, during FY 1979 funding restrictions rather than technical reasons required a scaling down of the dc SPTL Program. Consequently, the prototype demonstration has been postponed indefinitely, although smaller but more basic research investigations will be continued into FY 1980.

The work to date has produced many valuable results. A conceptual design of a complete cable system has been developed, and many of the problems encountered in its fabrication and use have been solved. Many of the results are generally applicable to any SPTL (and, in some cases, to noncryogenic systems), and even where the work is specific to our design, the methods developed are valid for studying other systems.

Because of the scarcity of data on electrical breakdown strength of dielectric materials at cryogenic temperatures and under dc stress, extensive screening tests were performed on sheets of 11 dielectric materials at four temperatures (12 K, 18 K, 83 K and 298 K) and two helium pressures (0.69 MPa and 1.38 MPa) in order to select the most promising candidates for dc SPTL operation. The data from these tests provided the information necessary to continue with impulse-strength tests of three selected dielectric materials in tape form (wound as in a cable), at 1.38 MPa and at the same three temperatures

as above. The test results show that a dielectric stress rating of 30 mV/m is readily obtainable, a value 50% greater than was expected.

Electrical system analysis has never been performed on other dc SPTL models investigated elsewhere in the world. We have performed analyses of ripple currents in a dc system and have determined their effects on the performance of the dc SPTL. We have also analyzed the characteristics of fault currents in a dc SPTL system and have evaluated the performance of the dc SPTL under fault conditions. Because the dc SPTL is an electrically complex system, particular attention was given to analyzing the wave propagation characteristics along the cable length. The results showed that special overvoltage protection would be needed for the system. This analysis can be extended to other multiconductor systems.

The combined refrigeration and dc SPTL cable systems have been studied, and an 18-m low-voltage and high-current model was constructed to investigate the heat transfer and fluid flow problems as well as the response of the entire system to cool-down (to operating temperature) procedures and to thermal upsets. Current leads were constructed for the model sized for 7 kA, the limit of available refrigeration. Cryogenic refrigerator operation has been studied analytically and experimentally on the model.

New types of superconducting wires have been developed. Two new LASL designs of multifilamentary (mf) Nb_3Sn wire were commercially produced, resulting in conductors capable of carrying over 10^6 A/cm^2 in the superconductor and over 10^4 A/cm^2 in the stabilized wire. We have studied the mechanical and electrical properties of the brittle Nb_3Sn in the composite wire and have established such practical parameters as the minimum bending radius of the wire and optimum heat-treat conditions for forming the Nb_3Sn compound in the final drawn conductor. We have measured the current carrying capability of single wires and cable clusters, both in self-field and under the influence of the magnetic field from the current in neighboring wires, and compared the results with model computation. These results have been incorporated into the design of a complete cable system, including the specification of the cable fabrication process.

System studies have been made including operating characteristics and economics; and designs have been submitted to power companies such as Philadelphia Electric Co. and Commonwealth Edison for inclusion in comparative studies of transmission systems.

The above work has been reported in detail in previous progress reports; in addition, over 50 papers on dc SPTL development have been submitted to scientific journals, and approximately 500 presentations on the subject have been made both at LASL as well as at national and international meetings and conferences. Interest in the dc SPTL program has been shown by several power companies, such as Arizona Public Service, Public Service Company of New Mexico, Consolidated Edison Co., and Commonwealth Edison Co. Visitors from France, West Germany, Japan, England, and the Soviet Union have come to LASL to discuss the program, and we have participated in the US-USSR scientific exchange program on superconducting transmission lines.

The work completed so far has provided a solid basis for constructing a dc SPTL: we believe that all of the major technical problems to be encountered in such construction have been addressed and resolved satisfactorily. The continuation of research on advanced cable systems, especially the dc SPTL, should prove to be of value to the nation. As the requirement for high capacity transmission systems becomes imminent, it will be possible to reinstate the large-scale tests originally planned and to produce a more nearly optimized dc SPTL system.

2. INTRODUCTION

Increasing demand for electric power, increased cost of and restrictions on rights-of-way of transmission lines, lower i^2r-loss requirements, and electrical-system stability criteria are some of the major reasons for building extra-high-voltage (EHV) power transmission lines.

EHV overhead power lines may be objectionable for several reasons:

(1) lack of reliability because of flashover of polluted insulators, breakage of line or towers during storms and hurricanes;

(2) radio-frequency interference;

(3) possible effects of electric fields on man, flora, and fauna;

(4) visual pollution.

Moreover, it may be impossible to build overhead lines in an urban area because of unavailability of rights-of-way and prohibition by statutory regulations. Thus pressing needs appear to exist for underground transmission.

There are three major types of application of underground cables:

(1) transmission of power between generating station (power park) and load center;

(2) transmission link within a power pool;

(3) transmission link between two power pools.

It is generally good design practice to connect one cable to one generator. Therefore, for the first type of application, the required cable rating may be expected to increase from 1.2 GW in 1970 to 1.5 GW in 1980 to 2 GW in 1990. For power-pool connections, it is expected that the desirable cable ratings will be 2 GW in 1980, 4 GW in 1990 and 8 GW in 2000.[1]

The major problems of a conventional high-power, high-voltage underground cable are thermal dissipation of i^2r losses and thermal aging of the dielectric material. Although a forced-cooled SF_6 insulated cable has much promise, a superconducting power transmission line (SPTL) seems to be more suitable for transmission of high power loads. Its dielectric aging should be minimal because of the low operating temperature.

2.1 Principal Advantages of a dc SPTL

A dc SPTL is ideal for transmitting large blocks of electric power, because (1) it has no system constraints, such as stability, load flow, short-circuit current level and reactive compensation; (2) it has negligible conductor losses and no dielectric losses - therefore it is very efficient; and (3) its current density capability is very high so that one coaxial dc SPTL can be equivalent to the three cables of a corresponding three-phase ac system.[1]

2.2 Program History

The Los Alamos Scientific Laboratory (LASL) has been developing an underground dc SPTL for transmitting large power loads with high efficiency. Such lines show considerable promise for providing very high single-circuit power capacity and the dc SPTL program goal is to ensure that transmission lines of this type will be ready when needed and will be able to meet future increased demands of the US power grid in a reliable, economical, and environmentally acceptable manner.

The LASL dc SPTL Program received its initial funding in November 1972 from the Division of Applied Technology, US Atomic Energy Commission. Support has been continued since early 1975 under the auspices of the Energy Research and Development Administration, Division of Electric Energy Systems, and continues under the same division of the US Department of Energy (USDOE). This is the only dc SPTL program in the US.

Because the objectives of the program include the development and application of a novel concept employing both materials and operating procedures not presently encountered in the electric power industry, the undertaking is considered to involve higher risk and longer term benefits than private industrial entities usually assume. It is therefore appropriate that this work be carried out in a National Laboratory such as LASL. On the other hand, the success of the program does not require any scientific breakthroughs but does depend upon careful engineering involving well-established low-temperature principles and techniques. Careful optimization is also required to make the dc-SPTL system economically competitive. The LASL Cryogenics Group has a history of successful completion of this type of project over the past 25 years.

The original LASL program plan called for a demonstration of a working dc SPTL by 1982-3. This was to have been a 300-m-long test section capable of carrying currents up to 25 kA at voltages up to 100 kV. This test would have required a larger cryogenic refrigerator than now available for this project at LASL. A large, cryogenic refrigerator which had become available to the USDOE was to have been sent to LASL for installation and use in the dc SPTL Program. This refrigerator had a capacity of 700 W at 4 K. However, before the planned installation in FY 1979, it become known that a cut in funding to the sponsoring USDOE division would require a substantial reduction in the funding level of the dc SPTL program. This reduction, in turn led to a cancelling of the large refrigerator installation and of the plans for the larger

demonstration tests. A more modest, although still important, program continues and is aimed at the carrying out of several research tasks, most of which are already in progress. These include the cryogenic engineering investigation of fluid flow and heat transfer problems. The first test of this type is the performance of a modest current test of several subcables in a configuration as close as possible to that of a dc SPTL, using only existing equipment and superconducting wire already available. This test has been completed and is reported in Sec. 4.

Other tasks to be continued are the development of processes to optimize the large-scale production of Nb_3Ge superconductor, the investigation of the dielectric strength of electric insulating materials, the development of an acoustical method of examining the integrity of electrical insulators, and the participation in an economic study of the use of the dc SPTL in a long-line (300 km) application. The Nb_3Ge development and the acoustic study will be reported separately for FY 1979 while the insulation and economic studies are discussed in Secs. 3 and 6, respectively. Since the above mentioned program changes represent a major change in effort, this report will represent a summary of work to date and thus contains highlights of work reported in previous progress reports.

2.3 Designs Considered

During the course of the dc SPTL Program two types of design have been considered. The greater effort has gone into the development of a conceptual design of a high-capacity, compact, coaxial cable.

The LASL coaxial cable concept for a 5-GW (50-kA and 100-kV) line, as shown in Fig. 2-1, is a hollow-core, flexible, coaxial cable. The inner bore, formed by a spiral tape or support member, carries the primary helium coolant stream. The high-potential conductor is wound on this support structure and consists of subcables made of mf Nb_3Sn superconductor wires in a copper matrix. The dielectric layer is composed of wrapped paper or plastic tape. The outer, neutral conductor is similar to the inner conductor. An outer flexible armor completes the cable.

The cryogenic enclosure is rigid and consists of a helium container and a vacuum jacket with multilayer thermal insulation within the evacuated annulus. The enclosure will be built in sections roughly 30 m long to be joined in the field and laid in trenches. Lengths of flexible cable up to 900 m long will then be drawn into the enclosure.

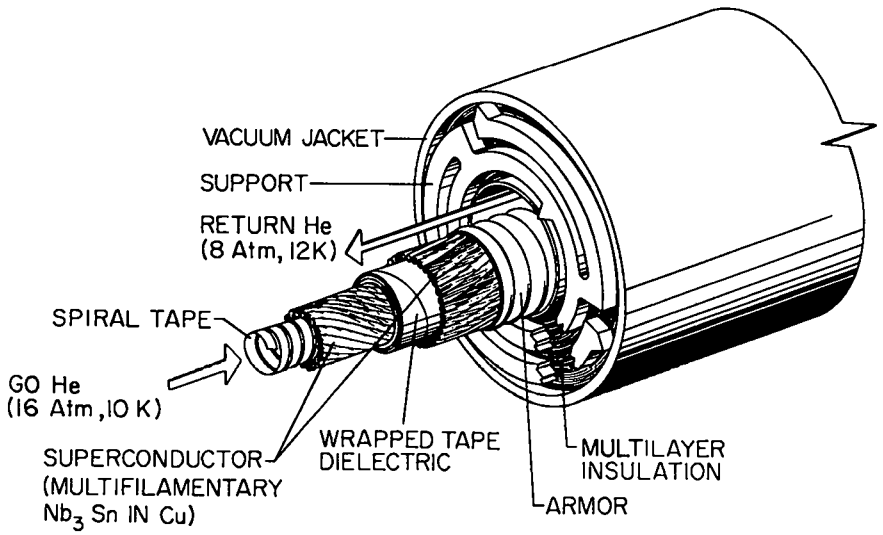

Fig. 2-1
Model of 100-kV, 50-kA (5-GVA) dc SPTL.

The cable plus enclosure thus provide a complete electrical circuit and also a complete refrigeration circuit, with the go and return helium coolant flow paths separated by the cable armor.

The refrigeration system will utilize a series of helium refrigerators along the line with the final expansion engine at the far end of each line section (approximately halfway between adjacent refrigerators). Thus, the cable itself becomes the final heat exchanger of the refrigerator. At the line terminal, current-lead refrigerators will have loads somewhat more like a liquefier than like the straight refrigeration load of the line and will be of a different design. Spacing between the refrigerators along the line could vary from 5 to 30 km, depending on the actual installation situation.

We believe that the above cable concept gives the greatest power density capability within a single-cable system and does so at the lowest cost of refrigeration and cryogenic enclosure systems.

The large power capabilities of the coaxial cable are not always advantageous, even when the total power delivery requirements are large. For example, a recent study by the Philadelphia Electric Company (PECO)[2] specified underground transmission of 10 GW for about 100 km. The contingency requirements established by PECO led us to propose three 7.5-GW coaxial lines, for a total installed capacity of 22.5 GW. Much of this excess capacity could have been avoided, and quite probably at a significantly reduced system cost, had

we proposed a greater number of smaller capacity lines. Therefore, we felt it advisable to make a more detailed examination of a design we had considered earlier, consisting of two monopoles operating at up to 600 kV with electrical insulation at ambient temperature. This design shown in Fig. 2-2, is discussed in Sec. 6 and referred to as the "small line design."

2.4 Program Organization

Through FY 1979 the LASL dc SPTL program has been carried out with work being divided into three major divisions, those of electrical engineering, cryogenic engineering, and cable development. In this report we will discuss these aspects of the work.

2.5 Electrical Engineering

To investigate the prospective electrical problems associated with the dc SPTL, the electrical engineering program has been divided into four sections: (1) electrical system studies, (2) dielectric studies, (3) bushing development, (4) electrical stress analysis, and (5) equipment and instrumentation. Progress has been made in all of these tasks and the work is reported in Sec. 3.

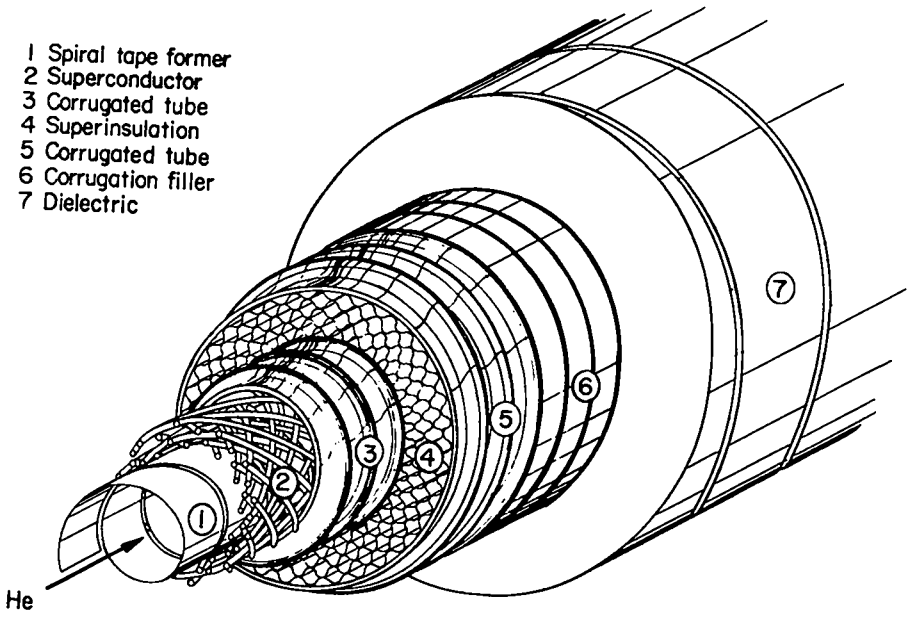

Fig. 2-2.
Small line design.

2.5.1 Electrical Characteristics. A dc SPTL must operate satisfactorily under normal and abnormal system conditions. The areas of concern are: ripple current produced by the converters, overcurrents produced by faults, and overvoltages produced by lightning and switching. The ripple current will cause steady-state power losses in the conductor, requiring the refrigeration system to supply cooling power to compensate for these losses. A transient overcurrent will cause transient power losses in the conductor, which could drive the superconductor "normal," leading, under the worst condition, to power interruption to the load. As shown in Fig. 2-1, the LASL coaxial cable design of the dc SPTL contains four electrically conducting cylinders: the inner and outer current carrying conductors, and the inner and outer cylinders of the cryogenic enclosure. Therefore, the usual analysis of surge propagation performed for a two-conductor coaxial cable system will not apply. For the LASL dc SPTL, multivelocity surges will appear on all four conductors and will need special analysis. Studies on the over voltage and the effects of ripple current and fault currents on the dc SPTL have been completed.

2.5.2 Dielectric Development. Apart from being adequate under electrical stress, the dielectric should also be mechanically and thermally suitable for handling at room temperature and operation at a cryogenic temperature.

It should be borne in mind that the electrical requirements of a dielectric under dc stress are different from those under ac stress. For ac operation, the corona inception voltage and the dielectric losses will be the limiting constraints. For dc applications, the polarity-reversal stress will be the limiting factor. For long-term stress applications, dielectric behavior depends upon two entirely independent phenomena: the statistical nature of breakdown and aging. It is expected that the aging mechanism of a dc SPTL will be slower than that of an ac SPTL because of the absence of dielectric losses under dc stresses. The breakdown process may also be different under flowing and stationary cryogen.

Mechanically, the cable should be able to withstand bending and unbending at room temperature without the dielectric layers buckling. During cooling to operating temperature, the dielectric should be able to withstand the mechanical stress created by the contraction. It will also have to maintain integrity under continuous cryogenic operating temperatures as well as under thermal cycling.

Many data are available on cryogenic dielectrics under ac stress, but very few under dc stress or under polarity reversal. Oil-impregnated cellulose paper will be ideal from the manufacturing standpoint because it is the standard dielectric for high-voltage cables. It has also been found that the strengths of the oil-impregnated paper at liquid nitrogen temperature with dc, impulse, and polarity reversal are significantly higher than those at room temperature. However, no data are available at supercritical helium temperatures, i.e. greater than 5.2 K. There is also the likelihood that the oil vapor might contaminate the helium during the cooldown process.

It should be evident that the selection of a suitable dielectric material for the dc SPTL is a painstaking process which requires careful long-range planning.

2.6 Cryogenic Engineering

The primary objective of the cryogenic engineering program for the dc SPTL is to provide a highly reliable and continuous low-temperature environment for the power cable at the lowest possible cost. To achieve this objective it is necessary to develop several cryogenic system components. First, a low heat-leak thermal enclosure is required to minimize the energy input into the flowing helium coolant. Because the enclosure must be constructed in the field, we plan to use rigid, shop-fabricated sections of simple design. The reflective, multilayer thermal insulation will be wrapped in the evacuated annulus between two concentric pipes. Second, the helium for cooling the line is to be provided by a cryogenic refrigerator that supplies helium gas at about 10 K and 1.5 MPa (15 atm). Additional cryogenic refrigeration systems are required at each end of the line to provide cooling of the current leads.

Cryogenic engineering studies must also be concerned with pressure drop and heat transfer in the cable system. Another priority is refrigerator performance in both steady-state and transient conditions that occur during system cooling or during a thermal upset to the system.

The cryogenic engineering section is responsible for designing and fabricating all cryogenic equipment used in the program as well as for completing the conceptual design of cable systems. Progress made in all of these areas is reported in Sec. 4.

2.7 Cable Development

The design of a conductor for a dc SPTL must meet many criteria in order to insure that the manufacturing techniques are economically feasible, that

the electrical requirements of the system can be met, that the mechanical stresses of cable fabrication, installation, and operation can be tolerated without detrimental effects, and that the conductor is stable under all operating conditions.

To determine these criteria an iterative design process is used; the inputs for this process are the requirements of the power system, properties of commercially available superconductors, knowledge of conductor manufacturing techniques, and system reliability constraints. From the results of experimental and theoretical tests, the design is modified and improved until a working model has evolved.

In Sec. 5 we discuss the work done to develop the wire and cable that will meet the above criteria.

2.8 References

1. P. Chowdhuri and F. J. Edeskuty, "Bulk Power Transmission by Superconducting DC Cable," Electric Power Systems Research 1, 41-49 (1977/78).

2. "Evaluation of the Economical and Technological Viability of Various Underground Transmission Systems for Long Feeds to Urban Load Areas," prepared by Philadelphia Electric Co. for USDOE Division of Electrical Energy Systems, HCP/T-2055/1 (December 1977).

3. ELECTRICAL ENGINEERING

To investigate the prospective electrical problems associated with the dc SPTL, the electrical engineering program has been divided into five sections:

1. Electrical system studies,
2. Dielectric studies,
3. Bushing development,
4. Electrical stress analysis, and
5. Equipment and instrumentation.

3.1. Electrical System Studies.

The electrical system of a dc SPTL must be designed so that it will operate reliably under normal and abnormal system conditions. The areas of concern are:

1. Harmonic currents produced by the converters,
2. Overcurrents produced by faults in the system, and
3. Overvoltages produced by lightning and switching.

The harmonic currents will cause steady-state power losses in the conductor, requiring the refrigeration system to supply additional cooling power to compensate for these losses.

A transient overcurrent will cause transient power losses in the conductor. This may drive the superconductor normal, requiring, under the worst condition, power interruption to the load.

Treatment of overvoltages for the dc SPTL require special considerations. As shown in Fig. 2-1, the LASL design of the dc SPTL contains four electrically conducting cylinders: the inner and outer current-carrying conductors, and the inner and outer cylinders of the cryogenic enclosure. Therefore, the usual analysis of surge propagation performed for a two-conductor coaxial cable system will not apply in this case. When a transient voltage appears on the innermost conductor, multi-velocity voltage waves will propagate along the four conductors, and would create voltage differences across each pair of conductors, caused by the disparity in the wave velocities that did not exist initially.

3.1.1. Study on Harmonic Currents.[1] The dc-side current harmonics on a conventional dc overhead line are of importance with respect to electromagnetic interference to nearby communications and signal lines. The interference

problem can be more severe with a non-coaxial cable (as compared with the LASL coaxial design) because the communications and signal lines may be buried in the same trench as the power cable. The LASL coaxial design of the dc SPTL would not create any electromagnetic interference problems. However, the dc-side current harmonics may impose some restrictions on a dc SPTL because of their effects on the hysteresis losses in the superconductor and on the ac resistive losses in the stabilizing normal metal matrix of the conductor.

The harmonics on the dc side are given by

$$m = pq, \tag{3-1}$$

where m = harmonic number, p = pulse number of the converter, q = an integer (1, 2, 3, . . .). These are the normal harmonics. However, measurements on the existing dc lines have shown that abnormal harmonics exist. The causes of such abnormal (uncharacteristic) harmonics are:

- Perturbation or "jitter" of the converter valve firing pulses,
- Distortion of ac system voltages,
- Imbalance of ac system voltages,
- Imbalance in the leakage reactance of a converter transformer, and
- Mismatch in the operation of the bridges in a 12-pulse converter.

Harmonic currents on the dc SPTL produced both by normal and abnormal harmonic voltage sources have been computed for a 100-km long dc SPTL under various operating conditions. The computations of the normal harmonics are based on the standing-wave theory of long transmission lines. The computations of the abnormal current harmonics were performed by representing the dc SPTL as an equivalent π-network because the line length at these frequencies is less than the quarter-wavelength. It was assumed during the entire analysis that the dc SPTL is terminated at both ends by smoothing reactors. No other filter network is connected to the dc SPTL.

3.1.1.1. Long DC SPTL. The source of harmonics is obviously the converter. It is considered to be a voltage source for the dc-side harmonics. The equivalent circuit of the dc SPTL with the converter stations at both end is shown in Fig. 3-1. The voltages V_1 and V_2 are the harmonic voltage sources and L_T is the inductance of the dc smoothing reactor.

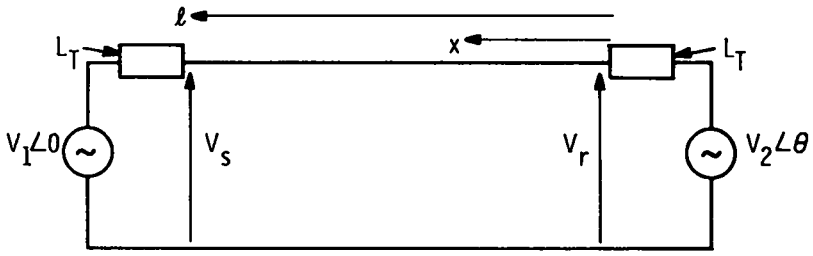

Fig. 3-1.
Schematic representation of a long transmission line.

The harmonic voltages generated at either end will be attenuated by the dc smoothing reactors and will travel along the dc SPTL in opposite directions with almost no attenuation but changing phase. They will be reflected by the reactors repeatedly as they travel back and forth along the dc SPTL. The magnitude of a harmonic at any point along the dc SPTL will be the algebraic sum of these two components. As a result, the harmonic voltage or current level will exhibit standing wave patterns with successive maxima and minima. The maxima occur when these two components are in phase, minima when they are out of phase by π radians.

The analysis is made by a step-by-step process.[2] During the first step, the current distribution $I_1(x)$ caused by one voltage source (V_1) is obtained, assuming the other voltage source (V_2) short-circuited. During the second step, the current distribution $I_2(x)$ caused by the other voltage source (V_2) is obtained, assuming the first voltage source (V_1) short-circuited. During the final step, the two current distributions are superimposed to obtain the resultant current distribution.

The magnitudes and phase angles of the generated harmonic voltages, V_1 and V_2, will generally be different. As the ac systems on both sides of the dc SPTL are asynchronously connected, the phase angles will vary randomly. The maxima of the harmonic current are given for the special cases when the two generated harmonic voltages V_1 and V_2 are equal in magnitude, i.e., V_n, but differ in phase angle θ by 0, $\pi/2$ and π: for $V_1 = V_2 = V_n$ and $\theta = 0$,

$$I_{max} = V_n / [2\pi f_n L_T \sin(\beta\ell/2)], \tag{3-2}$$

for $V_1 = V_2 = V_n$ and $\theta = \pi/2$,

$$I_{max} = V_n / [\, 2\sqrt{2}\pi f_n L_T \sin(\beta\ell/2)\,] \text{ , and} \qquad (3\text{-}3)$$

for $V_1 = V_2 = V_n$ and $\theta = \pi$

$$I_{max} = V_n / [\, 2\pi f_n L_T \cos(\beta\ell/2)\,] \text{ ,} \qquad (3\text{-}4)$$

where V_n = generated harmonic voltage (V), f_n = harmonic frequency (Hz), L_T = inductance of smoothing reactor (H), $\beta = 2\pi f_n \sqrt{LC}$ (rad/m), L = inductance of dc SPTL (H/m), C = capacitance of dc SPTL (F/m), and ℓ = length of dc SPTL (m).

3.1.1.2. Short DC SPTL. For short transmission lines ($\ell < \lambda/4$), the line can be represented by its lumped constants, either as a π- or as a T-network. A π-network was selected for this analysis (Fig. 3-2).

With this method, the current (I_3) through Z_ℓ can be assumed to be the harmonic current in the dc SPTL. Filter capacitances can be incorporated into the admittances ($Y_\ell/2$), if necessary. The current through the dc SPTL is given by

$$I_3 = (V_1 - V_2) / [\, 4\pi f_n L_T \cos^2(\beta\ell/2) + Z_c \sin \beta\ell\,] \text{ ,} \qquad (3\text{-}5)$$

where V_1, V_2 = generated harmonic voltages at the ends of the dc SPTL (V) and Z_c = surge impedance of SPTL (Ω).

It should be noticed from Eq. (3-5) that if $V_1 = V_2$, no harmonic current will exist in the dc SPTL. Computations were made with the assumption that $V_1 = -V_2$.

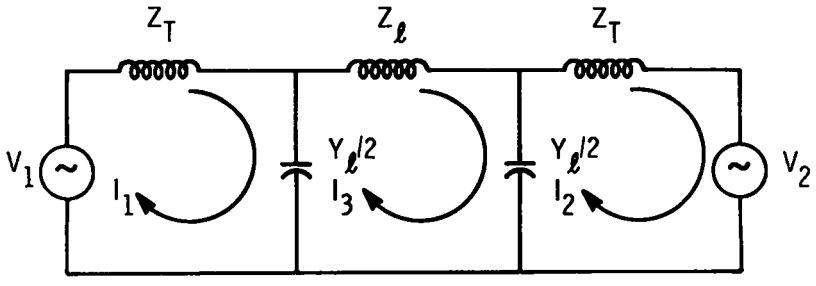

Fig. 3-2.
Schematic representation of a short transmission line.

3.1.1.3. Computation of Harmonic Currents and Losses. The dc SPTL characteristics (L_T,L,C) and the converter characteristics (V_n,f_n) are required to compute the harmonic currents along the dc SPTL.

The harmonic characteristics of the dc SPTL for one application are shown in Table 3-I. Three values for the dc smoothing reactor (L_T) were chosen - 1, 2, and 4 p.u.

A 12-pulse converter was assumed. It means that the normal dc-side harmonics will be the 12th and its multiples. However, abnormal harmonics do exist in actual systems because of imbalances and mismatch in the ac systems and in the converter bridges. The normal harmonic voltages generated on the dc side were obtained from Refs. 3 and 4, the abnormal harmonic voltages from Ref. 5. Computations for the abnormal harmonic currents showed that the resulting heating of the conductor is insignificant.

The ripple current produces two types of losses in the conductor - hysteresis losses in the superconductor and ac resistive losses in the copper matrix.

The hysteresis losses P_s (W/m^2) caused by the ripple current superimposed on dc are given by the Bean-London Equation:[6,7]

$$P_s = 2\mu_o f_n \sigma_p^3 / 3J_c, \qquad (3\text{-}6)$$

TABLE 3-I

HARMONIC CURRENT MAXIMA AND CONDUCTOR LOSSES[a]

Smoothing Reactor p.u.	Frequency Hz	Max. Harmonic Current A(rms)	Conductor Losses W/km
1.0	720.	248.	49.
	1440.	14.	0.2
2.0	720.	124.	12.
	1440.	7.	0.05
4.0	720.	62.	3.
	1440.	3.5	0.01

[a] Twelve-Pulse Operation; 100-kV, 2.5-GW dc SPTL
Line Length = 100 km
Firing Angle = 15^o
Overlap Angle = 22.6^o

where $\mu_o = 4\pi \times 10^{-7}$ (H/m), f_n = harmonic frequency (Hz), σ_p = peak induced current (A/m), and J_c = critical current density of superconductor (A/m^2).

In order to use the loss equation, we made the following assumptions:

1. J_c(4 K) and at zero dc field = 2.0×10^{10} A/m^2 (a pessimistic figure for Nb_3Sn multifilamentary wire),
2. $J_c(T) = J_c(4\ K)\ [1 - (T/T_c)^2]$,
3. T_c = 16.0 K, and
4. The effect of dc bias will be seen primarily as a decrease in J_c.

We chose H_{DC} = 5 kOe on the assumption that a dc current density of about 4×10^5 A/m is carried by the conductor. The field dependence of J_c at 14.0 K is not well known; we estimate a reduction by a factor of 5. This gives J_c (14 K, 5 kOe) = $1 \times 10^9 A/m^2$. These assumptions lead to

$$P_L = 6.032 \times 10^{-7}\ \sigma_p^3\ \mu W/m^2 \text{ at } f = 720 \text{ Hz}. \qquad (3\text{-}7)$$

The ac resistive losses (i^2R_{ac} losses) in the copper cryostabilizer are calculated first by determining the ac resistance (R_{ac}) of the conductor from the equation[8]

$$R_{ac}/R_{dc} \approx 1 + (r_o/\delta)^4\ /48\ , \qquad (3\text{-}8)$$

where R_{ac} = ac resistance of the conductor (Ω), R_{dc} = dc resistance of the conductor (Ω), r_o = radius of the conductor (m), and δ = skin depth (m). Assuming ρ (for copper at 14 K) = 10^{-10} Ω-m, f = 720 Hz, and r_o = 0.5 mm, we get, R_{ac}/R_{dc} = 2.04.

3.1.1.4. Discussion of Ripple Losses. The harmonic currents were computed assuming no dc-side harmonic filters in the system. The hysteresis losses in the superconductor were negligible, most of the losses being incurred in the copper cryostabilizer. As shown in Table 3-I, the conductor losses are well within the design goal of 50 W/km, except at 720 Hz and L_T = 1 p.u. The losses in the cryostabilizer can be further reduced either by installing a 12th harmonic filter, or by increasing L_T, or by redesigning the conductor with more copper. It appears at present that a higher L_T would be the best solution. This would also improve the performance of the dc SPTL under faults.

3.1.2. Overcurrent Study.[1] During an overcurrent condition caused by a fault, the total current may divide between the superconductor and the copper cryostabilizer or it may transfer entirely into the cryostabilizer. This would produce resistive losses in the copper and, hence, cause the temperature to rise. As long as the critical temperature conditions of the conductor are not exceeded, power can continue to be transmitted as soon as the fault is removed. However, if the critical temperature were exceeded, power would have to be interrupted until the conductor is recooled. Therefore, it is essential to know the fault-current capability of the dc SPTL.

The most severe fault current through the dc SPTL would occur if the line-end bushing of the inverter-side smoothing reactor flashes over (Fig. 3-3). The fault current will consist of two components. The first component will be a traveling wave caused by the discharge of the cable. The second component will be driven by the voltage source on the ac side of the rectifier.

The magnitude and duration of the cable discharge current cannot be controlled by any external means, such as valve control of the converter or a dc circuit breaker. The second component of fault current can be controlled by these external means, and the fault current profile will be dependent upon the means of interruption.

3.1.2.1. DC SPTL Discharge Current. The analysis for the first fault current component, the cable discharge current, was made with the following conditions[9]:

1. apply cancellation voltage at the point of flashover,
2. short circuit all other voltage sources, and
3. open circuit all current sources.

Traveling waves (V_f,I_f) will be created at the instant of short circuit; these are given by the relationship

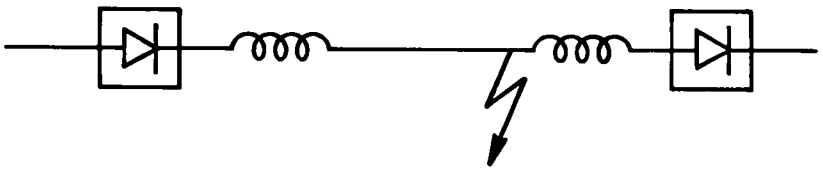

Fig. 3-3.
Flashover of line-end bushing of inverter-side smoothing reactor.

$$I_f = V_f/Z_c \tag{3-8}$$

where V_f = cancellation voltage = system voltage, V_{dc}, Z_c = surge impedance of cable. These waves will travel along the dc SPTL, will be reflected (V_r,I_r) by the smoothing reactor near the rectifier, and will partially penetrate into the reactor ($V_t I_t$). The reflected and the transmitted current waves are given by

$$I_r = (V_f/Z_c)\,[2\exp(-Z_c t/L_T) - 1] \tag{3-9}$$

and $$I_t = (2V_f/Z_c)\,[1 - \exp(-Z_c t/L_T)]\,. \tag{3-10}$$

If L_T/Z_c is large compared with the travel time along the dc SPTL, then Eqs. (3-9) and (3-10) can be simplified to the following:

$$I_r = -V_f/Z_c = -V_{dc}/Z_c \tag{3-11}$$

and $$I_t = 0. \tag{3-12}$$

Physically, a rectangular current wave ($I_f = V_{dc}/Z_c$) will be generated at the flashover point at the instant of flashover. This wave will travel along the dc SPTL and be reflected at the rectifier-end smoothing reactor. A reflected current wave ($I_r = -I_f$) will travel back, canceling the forward current wave (I_f). The duration τ of the discharge current at the point of flashover is given by

$$\tau = 2\ell/v, \tag{3-13}$$

where ℓ = length of dc SPTL and v = velocity of propagation in dc SPTL = $1/\sqrt{LC}$. The duration of the discharge current diminishes monotonically along the dc SPTL and is zero at the rectifier end.

Table 3-II shows the magnitude of the discharge currents for three designs of dc SPTL, the design parameters of which are shown in Table 3-III. Operating voltages and currents for each cable were selected from an economic analysis of the required transmitted power.

TABLE 3-II

DC SPTL DISCHARGE CURRENT AT FAULT
Line Length = 100 km

DC SPTL Design	I kA	τ ms	Conductor Temperature Rise K
A	4.43	1.05	0.24
B	6.65	1.05	0.28
C	8.87	1.05	0.32

3.1.2.2. DC SPTL Fault Current With Valve Control. The second component of the fault current will be maintained by the voltage sources on the ac side of the rectifier. Therefore, the ac-side reactances, the smoothing reactor and the dc SPTL reactance will limit this component of the fault current. The following assumptions were made:

1. Fault is initiated at the beginning of commutation,
2. There is no commutation overlap,
3. Fault current is interrupted by blocking the firing of the subsequent valves,
4. Firing angle delay is zero,
5. Converters operate in 12-pulse mode, and
6. AC network reactance beyond the rectifier transformer is negligible.

The 12-pulse system, with its equivalent circuit for the computation of the fault current, is shown in Fig. 3-4. If the fault starts at $\theta_0 = \pi/3$ when the reference valve comes into conduction (Fig. 3-5), the fault current will continue to increase even if the sensing system is fast enough to block the next valve, which would have started conducting at $\theta_1 = \pi/2$. The fault current will continue to increase until the ac voltage in the loop reaches zero. The fault current will then decrease until it is zero when $\int v dt = 0$. If the next valve is not blocked the fault current will continue to rise until the new voltage around the loop is zero. Similarly, as the subsequent valves are not blocked, the fault current level will increase. A similar analysis has been published previously,neglecting the transformer reactance.[10]

TABLE 3-III

PARAMETERS OF THREE DC SPTLs

Design Parameters	Design A	B	C
Rated power, GW	2.5	5.0	7.5
Rated voltage, kV	100	200	300
Rated current, kA	25	25	25
Current density, A/mm^2			
in superconductor	15000	15000	15000
overall	90	90	90
Max. electrical stress, kV/mm	10	15	20
Inductance, nH/m	119	158	178
Capacitance, pF/m	234	175	156
Surge impedance, Ω	22.5	30.1	33.8
Diam of central channel, mm	25.0	25.0	25.0
i.d. of dielectric, mm	33.7	33.7	33.7
o.d. of dielectric, mm	61.0	74.3	82.1
o.d. of cable, mm	73.4	87.7	96.0
i.d. of enclosure, mm	82.7	96.1	103.8
o.d. of enclosure, mm	248.0	288.0	312.0
No. of subcables			
Inner conductor	20	20	20
Outer conductor	90	90	90

The temperature rise of the conductor was calculated on the conservative assumption that as soon as the fault starts, both the fault component of the current and the pre-fault steady-state current would flow through the copper matrix. Table 3-IV shows the limiting fault component of current permissible before the superconductor goes normal. The entry n_{max} in Table 3-IV denotes the maximum number of subsequent valves which may be permitted to conduct after the initiation of the fault. The total current is obtained by adding the steady-state current to the fault component of current, shown in the Table. The conductor temperature rise includes the contribution from the rectangular discharge current wave of the cable. Figure 3-6 shows the profiles for the fault current and conductor temperature rise for n = 2.

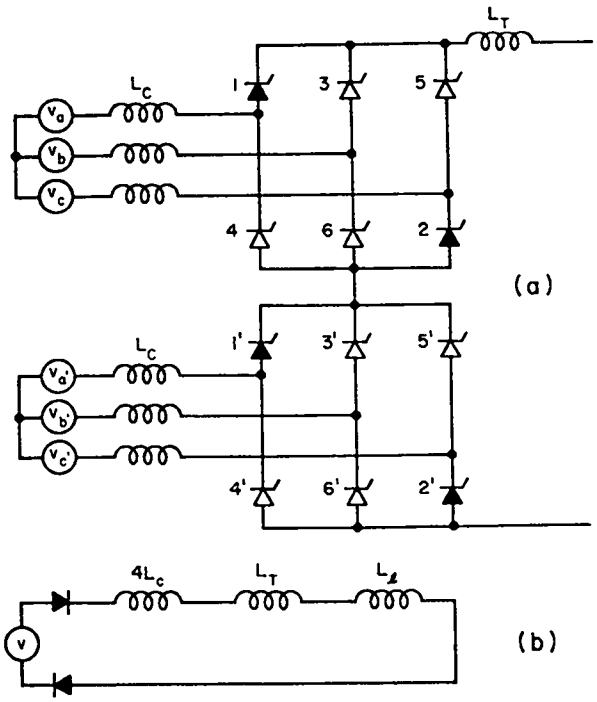

Fig. 3-4.
Representation of a 12-pulse rectifier bridge with fault at inverter end.

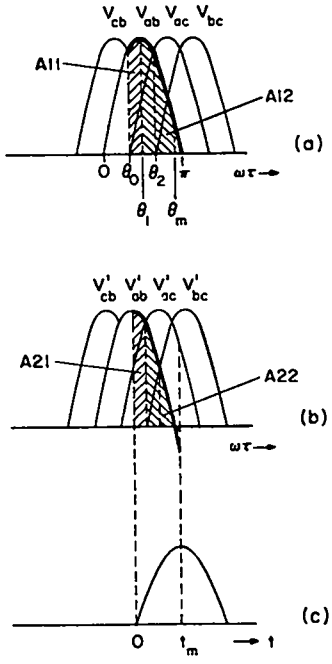

Fig. 3-5.
Voltage across 12-pulse rectifier bridge
and current profile under fault condition.

TABLE 3-IV

MAXIMUM ALLOWABLE FAULT COMPONENT OF CURRENT
IN DC SPTL WITH CONVERTER CONTROL
COMMUTATING REACTANCE, L_c = 0.18 p.u.

DC SPTL Design	Smoothing Reactor p.u.	n_{max}	Peak Fault Component of Current p.u.	Duration ms	Conductor Temperature Rise K
A	1	1	0.71	12.5	2.2
	2	2	0.64	15.3	2.4
	4	3	0.50	18.0	2.5
B	1	1	0.82	12.5	2.4
	2	2	0.72	15.3	2.6
	4	3	0.53	18.0	2.6
C	1	1	0.90	12.5	2.5
	2	1	0.59	12.5	2.1
	4	3	0.55	18.0	2.6

3.1.2.3. DC SPTL Fault Current With DC Circuit Breaker. DC power circuit breakers are not commercially available, but three types are being developed.[11-14] Although the modes of operation of these three types of circuit breakers are significantly different, they are similar in two basic priciples: first, the fault current is not limited during the initial period of sensing and contact opening; and second the total current is diverted to a nonlinear resistor during the final period of interruption. The time required from the initiation of contact opening to the current transfer into the nonlinear resistor is 3-4 ms for the first two types of breakers.[11-13] The third type of breakers requires 40-60 ms.[14] The initial delay period t_d of uncontrolled fault current is the sum of the relaying time, the contact opening time, and the time required to transfer current from the main circuit breaker to the nonlinear resistor.

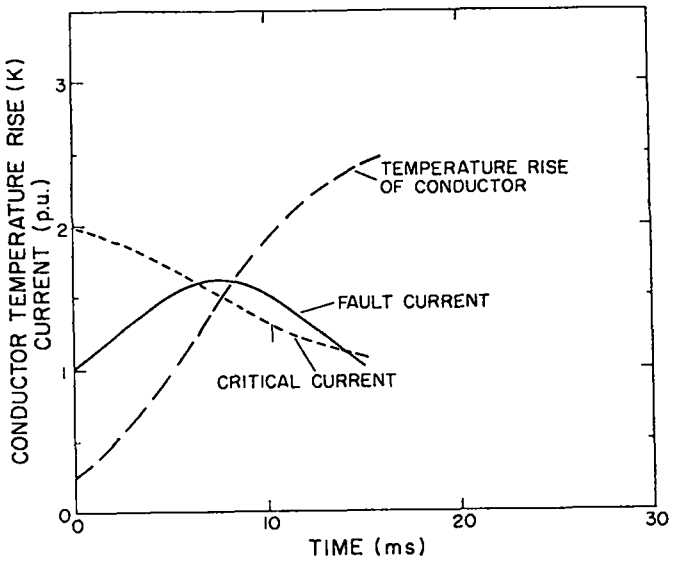

Fig. 3-6.
Profiles of fault current, critical current and conductor temperature rise. Fault cleared by valve control at n = 2, i.e., two subsequent valves are fired after fault is initiated; L_C = 0.18 p.u.; L_T = 2 p.u.

Computations of the fault current were made for two values of t_d -- 5 ms and 10 ms. The characteristics of the nonlinear resistor were assumed to be[15,16]:

$$v_a = k i_a^b, \tag{3-14}$$

where k,b = constants.

The current at the end of the initial period t_d is the peak of the total current i_{mt}, including the prefault load current. The current starts to decay, once it is transferred to the nonlinear resistor, according to the following relation:

$$L(di/dt) + ki^b = 0 \quad . \tag{3-15}$$

The solution of this equation is given by

$$i^{(1-b)} = i_{mt}^{(1-b)} - (k/L)\,(1-b)\,t \quad . \tag{3-16}$$

The constant k was derived on the assumption that $v_a = 1.7\ V_{dc}$ at i_{mt}. In actual applications, k can be adjusted to the desired value by series-parallel combination of the nonlinear resistor bank. A value of 0.05 was used for b, in agreement with Refs. 15 and 16. Table 3-V shows the fault component of the current and the conductor temperature rise for the three dc SPTL designs. The thermal recovery times are also shown in Table 3-V. The thermal recovery time is defined as the time required by the conductor to cool down to the temperature at which the critical current is 1 p.u. In other words, full power can be switched on to the dc SPTL after the lapse of the thermal recovery time. Figures 3-7 and 3-8 show the fault-current profile for the 100-kV, 2.5-GW dc SPTL and the conductor temperature rise for two values

TABLE 3-V

FAULT COMPONENT OF CURRENT IN DC SPTL

WITH DC CIRCUIT BREAKER

COMMUTATING REACTANCE, $L_c = 0.18$ p.u.

DC SPTL Design	Smoothing Reactor p.u.	Delay Time ms	Peak Fault Component of Current p.u.	Duration ms	Conductor Temperature Rise K	Thermal Recovery Time ms
A	1	5	0.72	12.5	1.6	0
	1	10	1.43	21.0	3.6	70
	2	5	0.50	14.5	1.5	0
	2	10	1.01	22.5	3.0	30
	4	5	0.32	18.0	1.4	0
	4	10	0.64	26.0	2.6	0
B	1	5	0.83	12.0	1.7	0
	1	10	1.67	20.0	4.0	100
	2	5	0.56	14.0	1.5	0
	2	10	1.12	22.0	3.2	40
	4	5	0.34	17.5	1.4	0
	4	10	0.68	25.5	2.6	3
C	1	5	0.91	12.0	1.8	0
	1	10	1.82	20.0	4.3	100
	2	5	0.59	13.5	1.6	0
	2	10	1.19	21.5	3.3	50
	4	5	0.35	17.0	1.5	0
	4	10	0.70	25.5	2.7	6

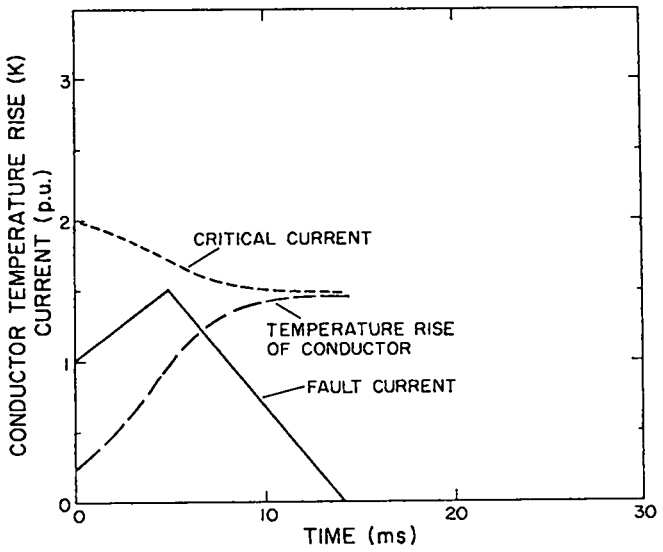

Fig. 3-7.
Profiles of fault current, critical current and conductor temperature rise. Fault cleared by dc circuit breaker at t_d = 5 ms; L_c = 0.18 p.u.; L_T = 2 p.u.

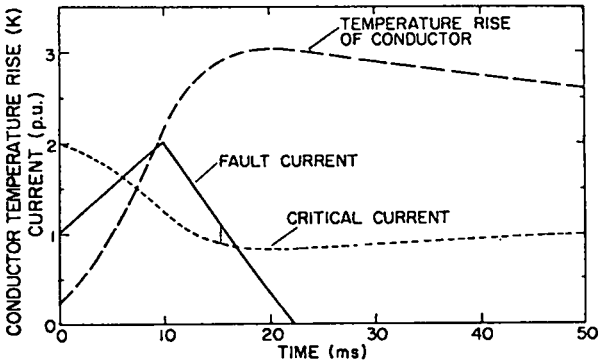

Fig. 3-8.
Profiles of fault current, critical current, conductor temperature rise and thermal recovery. Fault cleared by dc circuit breaker at t_d = 10 ms; L_c = 0.18 p.u.; L_T = 2 p.u.

of circuit breaker delay. The fault current profiles for the other two cables are almost coincidental with that for the 100-kV cable.

3.1.2.4. Thermal Response Model. The long-term (minutes and hours) thermal performance of the cable depends strongly on the specific wire and cable design and on the cryogenic heat transfer conditions. However, faults will take place essentially adiabatically. Therefore, the conservative assumption is that all energy is initially taken up in the enthalpy of the metallic

conductors. Under normal operating conditions the temperature of the line will vary by 2 K along its length (between the refrigeration stations) so that the thermal safety margin will be different at different points. Again, the conservative assumption is that all excursions start from the normal maximum temperature of 12 K. Finally, it is assumed (pessimistically) that all major disturbances will cause the superconductor to be driven into the normal state, because the associated rates of change of the magnetic field are between 20 and 50 T/s. As a result, both the fault component of the current and the normal pre-fault line current are assumed to be in the copper and heating it. The criterion for safe operation is that, at the end of the disturbance, the temperature should rise to a value lower than that at which the superconductor critical current is at least 1 p.u. For our model this temperature is 14.6 K.

For the heating calculations in the copper, we take the dc resistivity of 1×10^{-10} Ω-m, which also includes magneto-resistivity. A magnetic field diffusion "time constant" of about 0.3 ms can be used to characterize the penetration through a radius of 0.2 mm of such cryoconductor. From this we can estimate the frequency-dependent enhancement of the ac resistivity (including the proximity effect) to be 2 times for a 1-ms square wave, 1.5 times for 720-Hz ripple and 1.3 times for slower disturbances with half-periods of 10 to 50 ms. For steady-state heat losses due to all causes, a limit of 50 W/km has been used, which means that maximum ripple losses of 20 to 30 W/km are acceptable.

The thermal capacity per unit length of the helium refrigerant in the line is about two orders of magnitude larger than that of the metallic conductor. The conductor will therefore recool to the helium temperature with a time constant given by

$$\tau_r = mc_p/hA \ , \qquad (3\text{-}17)$$

where m = mass per unit length (kg/m), c_p = heat capacity per unit mass (J/kg•K), h = heat transfer coefficient ($W/m^2 \cdot K$), and A = heat transfer area (m^2).

The only uncertain quantity in the above equation is the value of the heat transfer coefficient, which depends on flow parameters, including velocity and turbulence. For a conservative h value of 5 $W/m^2 \cdot K$, τ_r becomes about 170 ms.

3.1.2.5. Discussion of Fault Current Study. Analysis of the fault current was performed under assumptions which produced conservative results. Nonzero firing angle delay and overlap angle will decrease the fault current level. Only the commutating reactance of the converter transformer was considered in the analysis. Inclusion of the ac system impedance would further reduce the fault current level. Modern control schemes for 12-pulse hvdc systems would not allow more than one commutation after a line-to-ground fault.[17] Therefore, fault currents beyond n = 1 need not be considered. Nevertheless, the present analysis considered n up to 10, the primary objective being to provide a simplified method in the understanding of the dc SPTL performance. Figure 3-6 shows that even with n = 2, the critical current I_c at the end of fault interruption is greater than 1 p.u., meaning that the dc SPTL will be able to carry full power immediately after the fault.

Although no hvdc circuit breakers are commercially available, it is expected that in the future dc breakers will play a major role in the hvdc transmission of power. Analysis was performed with two assumed delay times of the breaker--5 ms and 10 ms. A breaker with delay time less than 5 ms may not be practical. Similarly, a breaker with a delay time longer than 10 ms will not be very useful without assistance from valve control. Figure 3-7 shows that I_c is nearly 1.5 p.u. when the fault is interrupted by a breaker with t_d = 5 ms. Full power can be turned on the dc SPTL immediately after the fault is cleared. However, it t_d = 10 ms (Fig. 3-8), partial power may be restored to the dc SPTL. If it is required that full power be restored immediately after a fault is cleared by a 10-ms breaker, then the dc SPTL could be redesigned with more cryostabilizer. Engineering compromises can also be made where partial power is immediately switched on and full power is gradually attained as the conductor is cooled by helium.

It is evident from Table 3-V that the recovery time for the dc SPTL is very short--less than 100 ms for the assumptions made in this study. For transient faults, at least this time interval will be required for the deionization of the arc at the fault.

3.1.3. Overvoltage Study.[18,19] The dc superconducting cable of LASL design (Fig. 2-1) consists of four concentric cylinders. The innermost cylinder (conductor 1) carries the load current and consists of subcables made up of wires of multifilamentary Nb_3Sn superconductor embedded in a copper matrix. The second cylinder (conductor 2), which carries the return current,

also consists of copper-stabilized multifilamentary Nb_3Sn superconductor. The cryogenic enclosure is composed of the third and fourth concentric cylinders. The inner cylinder (conductor 3) of the cryogenic enclosure is made of stainless steel and the outer cylinder (conductor 4) of carbon steel. The space between conductors 1 and 2 is filled with wrapped tape dielectric to withstand the system voltage--steady-state dc and transient overvoltages. The space between conductors 2 and 3 is filled with supercritical helium at 1.38 MPa and 12 K. The space between conductors 3 and 4 is evacuated and filled with multilayer thermal insulation. Conductor 4 is isolated from earth by a thin layer of insulation.

When a transient voltage wave appears on conductor 1 of an n-conductor transmission line, the transient voltage splits into n component waves, each wave traveling with a specific velocity v_n.[20] Some of these component waves will be induced on the other conductors, creating a complex pattern of wave propagation. For a 4-conductor system (e.g., LASL coaxial design), the total number of component voltage waves will be four.

3.1.3.1. Method of Analysis. Although the return-current conductor (conductor 2) and the cryogenic enclosure (conductors 3 and 4) are nominally at ground potential for steady-state operation, this assumption may not be valid under transient conditions. To inhibit stray current from flowing through these "grounded" conductors, one end of each of these conductors will be kept isolated from ground either by keeping one terminal open or connecting it to earth through a capacitor or through a surge arrester. Furthermore, even when one terminal of each of these three conductors is grounded, there will always be a finite grounding resistance between the conductor and the earth. Therefore, the analysis should include the resistance of each conductor and the terminal grounding conditions.

The analysis becomes simple if it is assumed that the earth is perfect, i.e., an earth of infinite electrical conductivity. In practice, this ideal condition is never met. The problem becomes more complex if the long cable is laid not only in regions of divergent earth resistivities but also in layers of earth of different resistivities. Moreover, lack of precise knowledge of the earth resistivity precludes exact numerical computations. In spite of these difficulties, it is worthwhile to study the effect of imperfect earth in order to assess how attenuation and distortion of voltage waves in a cable take place.

3.1.3.1.1. Rudenburg-Hayashi Model of Transient Impedances. Transient phenomena, such as switching and lightning surges, are usually analyzed using the Laplace transform. Therefore, it is desirable to express the transient impedances in terms of the Laplace-transform operator s.

Rudenberg's analysis of imperfect earth has been extended by Hayashi so that the earth-correction terms can be expressed in terms of the operator s.[21,22] Rudenberg has represented an underground cable by laying its center conductor on the ground level at the center of a groove of a semicircular shape of radius h from which the earth has been scooped out, h being the distance of the center conductor of the original cable from earth (Fig. 3-9). The ground impedance as a function of the Laplace transform operator s can then be expressed as

$$Z_g(s) = \delta_{g1} s^{1/2} - \delta_{g2} + \delta_{g3} s^{-1/2} - \ldots \qquad (3\text{-}18)$$

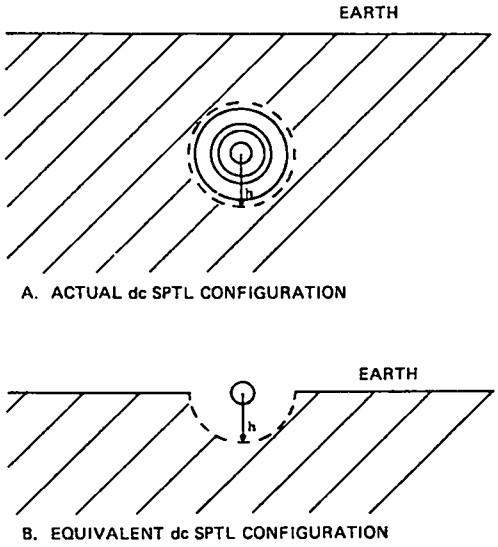

Fig. 3-9.
Rudenberg's model of cable in imperfect earth.

For fast transients, only the first two terms are important, where $\delta_{g1} = \sqrt{10\ R_g} \times 10^{-4}$, $\delta g_2 = R_g/4$, $R_g = 2\rho_g/h^2$, ρ_g = soil resistivity ($\Omega \cdot m$), h = distance of center conductor of cable from ground (m).

Similarly, the transient impedance of the cable conductor can be expressed as

$$Z_c(s) = \delta_{c1} s^{1/2} + \delta_{c2} + \ldots , \tag{3-19}$$

where $\delta_{c1} = \sqrt{10\ R_c} \times 10^{-4}$, $\delta_{c2} = R_c/4$, and R_c = dc resistance of the conductor (Ω).

For a cable consisting of n concentric cylinders, the earth-correction impedance matrix will then be

$$[\delta] = s^{1/2} [\delta_1] + [\delta_2] , \tag{3-20}$$

where

$$[\delta_1] = \begin{bmatrix} (\delta_{c11} + \delta_{g11}) & \delta_{g11} \cdots \cdots \delta_{g11} \\ \delta_{g11} & \\ \vdots & \\ \delta_{g11} \cdots \cdots \cdots \cdots & (\delta_{c1n} + \delta_{g11}) \end{bmatrix}$$

and

$$[\delta_2] = \begin{bmatrix} (\delta_{c21} - \delta_{g21}) & -\delta_{g21} \cdots \cdots -\delta_{g21} \\ -\delta_{g21} & \\ \vdots & \\ -\delta_{g21} \cdots \cdots \cdots \cdots & (\delta_{c2n} - \delta_{g21}) \end{bmatrix}$$

3.1.3.1.2. Solution of Transmission-Line Equations. The Laplace transform of the transmission-line voltage equations can be written in matrix form as

$$\partial^2[\bar{V}]/\partial x^2 = (s^2[L][C] + s^{3/2}[\delta_1][C] + s[\delta_2][C])[\bar{V}] = [Q]^2[\bar{V}] \qquad (3\text{-}21)$$

where

$$[Q]^2 = (s^2[L][C] + s^{3/2}[\delta_1][C] + s[\delta_2][C]) \ ,$$

[L] and [C] are the inductance and capacitance matrices of the n-conductor cable, and $[\delta_1]$ and $[\delta_2]$ are given by Eq. (3-20). The solution of Eq. (3-21) is given by

$$\bar{V} = \exp(-[Q]x)[\bar{V}_o] = \left\{\exp(-s[M]^{1/2}x)\exp(-\sqrt{s}[B_1]x/2)\exp(-[B_2]x/2)\right\}\cdot[V_o], \qquad (3\text{-}22$$

where

$$[M] = [L][C],$$
$$[B_1] = [M]^{1/2}[M]^{-1}[\delta_1][C],$$
$$[B_2] = [M]^{1/2}[M]^{-1}[\delta_2][C], \text{ and}$$
$$[\bar{V}_o] = [\bar{V}] \text{ at } x = 0.$$

Each of the three exponential terms needs to be expanded by Sylvester's expansion theorem[22], giving

$$\exp(-s[M]^{1/2}x) = \sum_{r=1}^{n_1} \exp(-sq_{1r}x)[a_{1r}] \ , \qquad (3\text{-}23)$$

$$\exp(-\sqrt{s}[B_1]x/2 = \sum_{r=1}^{n_2} \exp(-\sqrt{s}\, q_{2r}x/2)[a_{2r}] \ , \text{ and} \qquad (3\text{-}24)$$

$$\exp(-[B_2]x/2) = \sum_{r=1}^{n_3} \exp(-q_{3r}x/2)[a_{3r}], \qquad (3\text{-}25)$$

where

$$[a_{1r}] = \prod_{\substack{p=1,\ldots n_1 \\ p \neq r}} \left(\frac{q_{1p}^2[U] - [M]}{q_{1p}^2 - q_{1r}^2} \right)^{d_{1p}} ,$$

$$[a_{2r}] = \prod_{\substack{p=1,\ldots n_2 \\ p = r}} \left(\frac{q_{2p}[U] - [M]}{q_{2p} - q_{2r}} \right)^{d_{2p}} ,$$

$$[a_{3r}] = \prod_{\substack{p=1,\ldots n_3 \\ p = r}} \left(\frac{q_{3p}[U] - [M]}{q_{3p} - q_{3r}} \right)^{d_{3p}} ,$$

q^2_{1r} ($r = 1,\ldots n_1$) are distinct eigenvalues of [M], q_{2r} and q_{3r} are distinct eigenvalues of $[B_1]$ and $[B_2]$ respectively, [U] = identity matrix, d_{1p} = order of degeneracy of q_{ip} eigenvalue (i = 1, 2, 3), and

$$d_{11} + \ldots + d_{n1} = d_{21} + \ldots + d_{n2} = d_{31} + \ldots + d_{n3} = n$$

3.1.3.1.3. Boundary Conditions. The length of the cable has been assumed to be semi-infinite in this study; therefore, there would be no reflections from the far end. A voltage V_{01} is injected into conductor 1 at x=0, while the other conductors are either grounded through a grounding resistance R_g or left open. In this case, $V_{02}\ldots V$ need to be evaluated. These values can be obtained, for known grounding resistances, by solving for the currents at x=0.

The Laplace transform of the current matrix is given by

$$[\bar{I}] = s[C] \int [\bar{V}]dx \quad , \tag{3-26}$$

where $[\bar{V}]$ is obtained from Eqs. (3-22) through (3-25).

3.1.3.1.4. Final Solution. The closed-form solution for the voltage waves, in time domain, is shown in the following equation.

$$[V(t)] = \left\{ \sum_{k=1}^{n_1} [a_{1K}] \sum_{\ell=1}^{n_2} [a_{2\ell}] \operatorname{erfc}(q_2 x/4\sqrt{t-q_{1K}x}) \cdot u(t-q_{1K}x) \right\} \cdot \left\{ \sum_{m=1}^{n_3} [a_{3m}] \exp(-q_{3m}x/2) \right\} [V_o(t)] \quad , \tag{3-27}$$

where $u(t-q_{1K}x)$ = delayed unit function.

3.1.3.1.5. Cable Parameters. Computation of the voltage waves requires that the resistance matrix [δ], the inductance matrix [L], and the capacitance matrix [C] of the cable be known. As discussed before, the [δ] -matrix was computed by Hayashi's method.

The [L]-matrix was evaluated by computing Maxwell's electromagnetic coefficients from the following set of equations,

$$\phi_r = L_{r1} i_1 + \ldots\ldots + L_{rs} i_s + \ldots\ldots + L_{rn} i_n \quad , \tag{3-28}$$

where, $L_{rs} = L_{sr}$, ϕ_r = total magnetic flux linking conductor r, i_r = current flowing through conductor r, and r = 1,....., n.
The transient current was assumed to flow along the outer surface of the conductor. The permeability μ of a magnetic material was assumed equal to that of free space μ_o when a steep-front transient is applied. The coefficients of inductance L_{rs} are then given by, for $r \leqslant s$, and in units H/m,

$$L_{rs} = (\mu_o/2\pi) \ln (h/r_{so}) \quad , \tag{3-29}$$

where $\mu_o = 4\pi \times 10^{-7}$ (H/m), h = distance of earth from center of cable (m), and r_{so} = outer radius of conductor s (m).

The [C]-matrix was evaluated by computing Maxwell's electrostatic coefficients from the following set of equations:

$$Q_r = p_{r1} e_1 + \ldots\ldots + p_{rs} e_s + \ldots\ldots + p_{rn} e_n \tag{3-30}$$
$$p_{rs} = p_{sr},$$

where Q_r = electrostatic charge on conductor r, e_r = potential of conductor r, and r = 1,....., n.
The coefficients p_{rs} are then given by

$$p_{rn} = \ell n(h/r_{no})/2\pi\varepsilon_n \quad \text{for } r \leqslant n$$
$$p_{r(n-1)} = p_{nn} + \ell n(r_{ni}/r_{(n-1)o})/2\pi\varepsilon_{(n-1)} \quad \text{for } r \leqslant (n-1) \tag{3-31}$$

where ε_n = permittivity of conductor n (F/m), r_{ni} = inner radius of conductor n (m), and r_{no} = outer radius of conductor n (m).
The [C]-matrix is then given by

$$[C] = [p]^{-1} \tag{3-32}$$

3.1.3.2. Computation of Voltage Waves.

3.1.3.2.1. Computation. A numerical Fortran computer program was developed to solve the voltage equations for a given cable configuration. The voltage waves on each conductor of the cable, as per unit of the applied voltage, are computed at time and distance coordinates specified by the user.

The data put into the program are the number of conductors in the cable, their dc resistances and radii, the dielectric constants of the materials between the conductors, the known initial voltages, the distances between the center of conductors and earth, the earth resistivity, and the terminal resistances between the conductors and earth at x = 0.

The code includes a graphics package which plots two-dimensional graphs of the wavefronts at specified distances.

3.1.3.2.2. Cable Parameters. Surge responses of several types (superconducting and conventional) dc cables were analyzed. Table 3-VI shows the pertinent parameters of the cables.

Four-Conductor Superconducting Cable. The conceptual design of this cable is shown in Fig. 2-1, and has been described before. Most of the computations was performed on a 100-kV design with the following assumptions:

1. The transient current was expelled from the superconductor into the stabilizing copper,

2. The dielectric constant of the annular vacuum space in the cryogenic enclosure is unity, i.e., $k_3 = 1$,
3. The four conductors are perfect concentric cylinders, and
4. The cable is semi-infinite in length.

Figures 3-10 to 3-14 show the step responses of a 100-kV four-conductor dc superconducting cable under various system conditions. To determine the effect of conductor resistances, one specific case was studied where none of the four conductors had any resistance (Fig. 3-13). Because the vacuum space inside the cryogenic enclosure is filled with multilayer thermal insulation, its dielectric constant (k_3) will be higher than unity. A dielectric constant of three ($k_3 = 3$) was included in another case to ascertain its effect on the voltage across the space inside the cryogenic enclosure (Fig. 3-14).

The space inside the cryogenic enclosure is designed on the basis of allowable heat leak and is independent of the voltage rating of the cable. Therefore, a higher voltage (300-kV) cable was included in order to study the effect of cable voltage rating on the voltage across the enclosure space. Figures 3-16 and 3-17 show the step response of a 300-kV four-conductor dc superconducting cable.

TABLE 3-VI

PERTINENT PARAMETERS OF CABLES

	4-Conductor 100-/300-kV Superconducting Cable	3-Conductor 100-/600-kV Superconducting Cable	3-Conductor 250-kV Conventional Cable	2-Conductor 250-kV Conventional Cable
Outer radius of conductor 1, r_{10} (mm)	22.7/19.6	40.0	16.7	16.7
DC resistance of conductor 1, R_{c1} (μΩ/m)	0.2/0.55	1009.3	33.14	33.14
Inner radius of conductor 2, r_{2i} (mm)	28.3/42.15	100.0	31.6	31.6
Outer radius of conductor 2, r_{20} (mm)	35.0/48.45	102.0	35.5	35.5
DC resistance of conductor 2, R_{c2} (μΩ/m)	0.2/0.55	13.6	286.53	286.53
Inner radius of conductor 3, r_{3i} (mm)	45.0/54.9	105.4/124.1	44.1	-
Outer radius of conductor 3, r_{30} (mm)	49.0/58.9	106.4/125.1	49.5	-
DC resistance of conductor 3, R_{c3} (μΩ/m)	440.0/363.6	332.2/282.3	114.83	-
Inner radius of conductor 4, r_{4i} (mm)	90.0/161.0	-	-	-
Outer radius of conductor 4, r_{40} (mm)	94.0/165.0	-	-	-
DC resistance of conductor 4, R_{c4} (μΩ/m)	43.0/24.4	-	-	-
Distance of cable center to earth, h (mm)	98.0/177.7	110.4/129.1	55.4	41.5
Dielectric constants : k_1	2.2	1.0	3.0	3.0
k_2	1.0	3.0	3.0	3.0
k_3	1.0	3.0	3.0	-
k_4	3.0	-	-	-

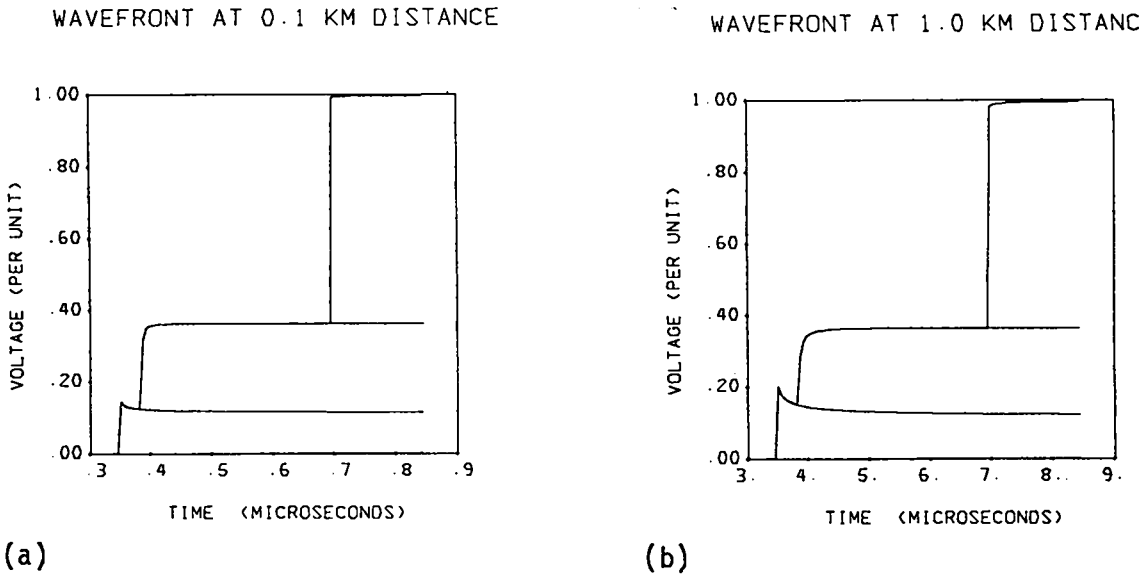

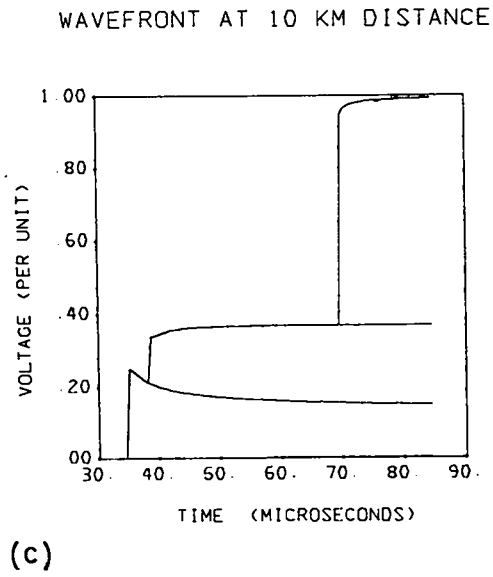

Fig. 3-10.
Step response of a semi-infinite 100-kV four-conductor dc superconducting cable. $R_g = 10\,\Omega$ at x=0; $\rho_g = 100\,\Omega$-m. (a) x = 100 m; (b) x = 1 km; (c) x = 10 km. Four, three, two, and one component waves travel along conductors 1, 2, 3, and 4, respectively. The component wave which is present on all four conductors is highly attenuated and is not discernible in the figures.

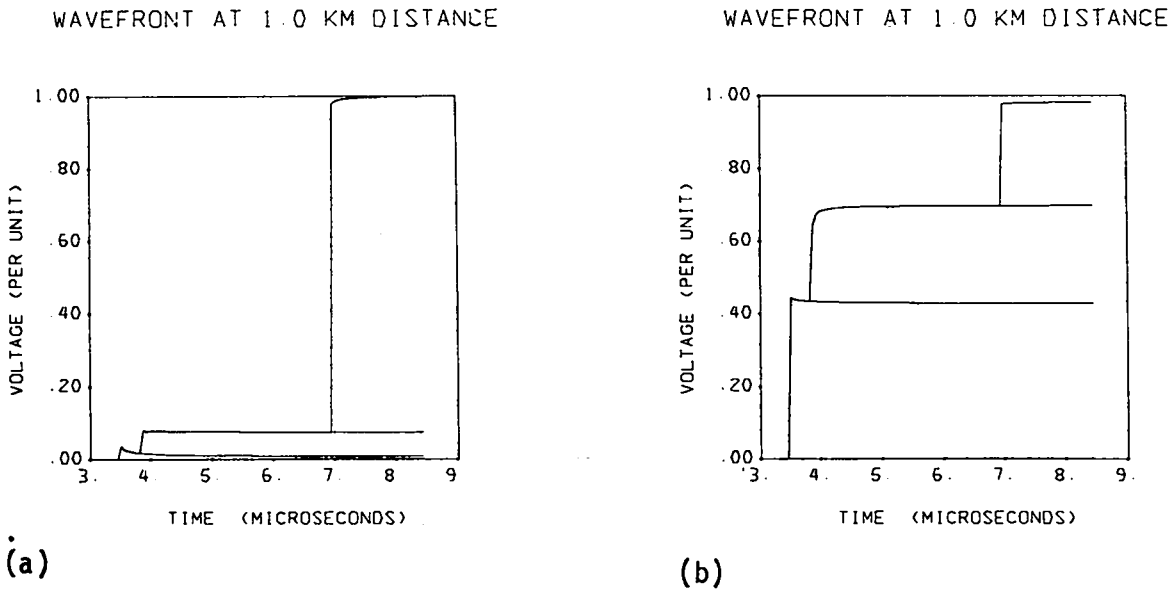

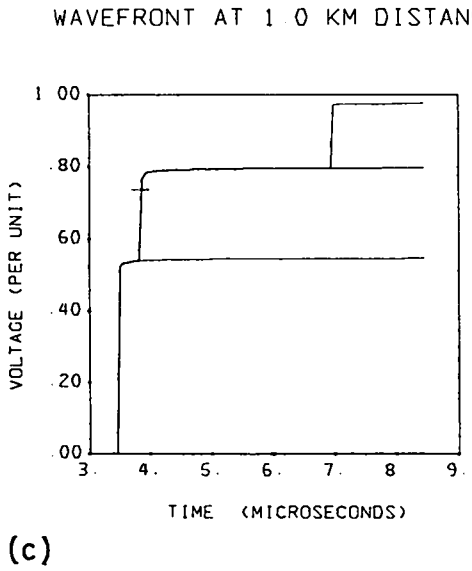

Fig. 3-11.
Step response of a semi-infinite, 100-kV, four-conductor dc superconducting cable at x = 1 km. Effect of grounding resistance R_g at x = 0. Earth resistivity $\rho_g = 100\ \Omega \cdot m$. (a) $R_g = 1\Omega$; (b) $R_g = 100\ \Omega$; (c) $R_g = \infty$. Four, three, two, and one component waves travel along conductors 1, 2, 3, and 4, respectively. The component wave which is present on all four conductors is highly attenuated and is not discernable in the figures.

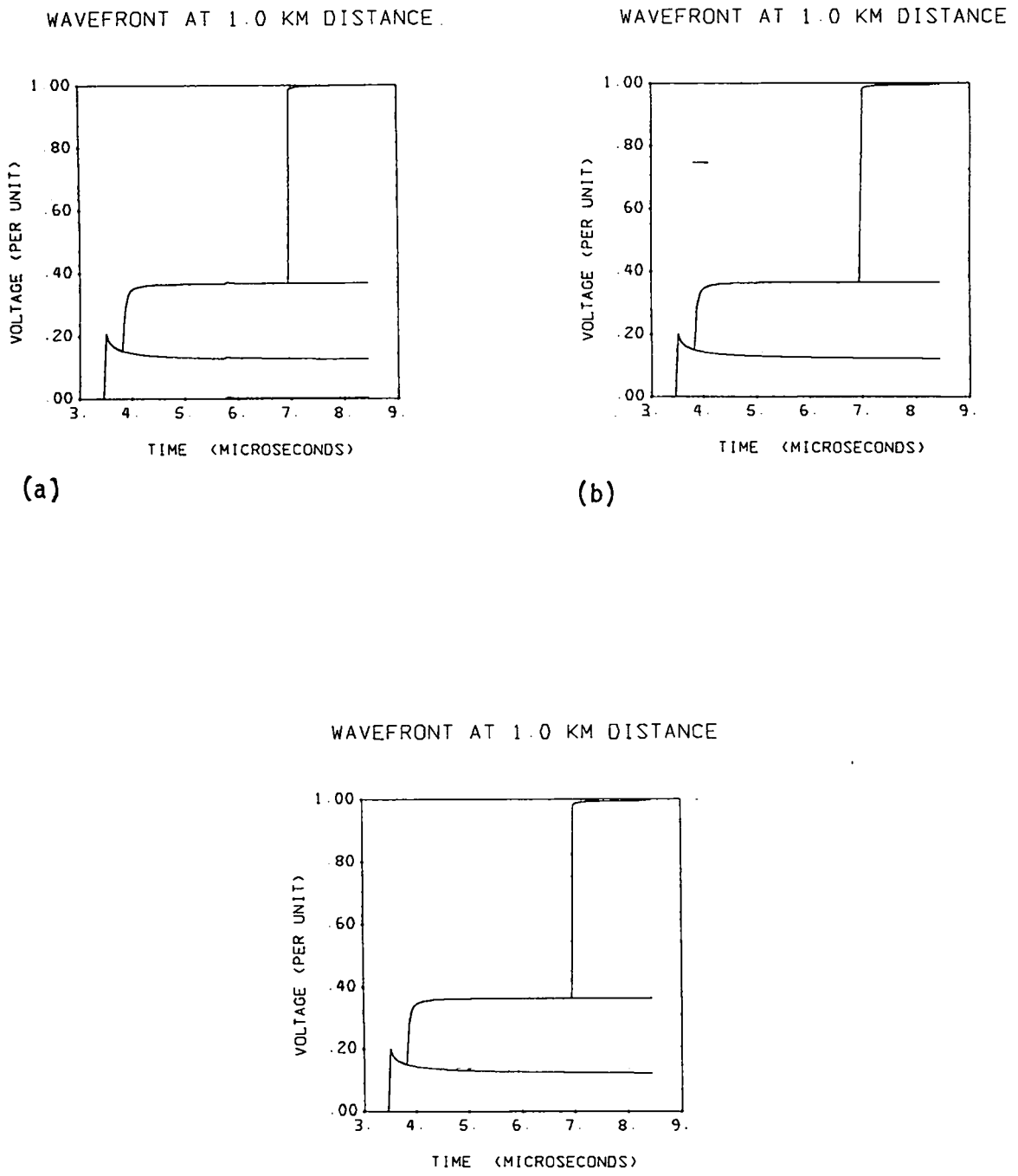

Fig. 3-12.
Step response of a semi-infinite, 100-kV, four-conductor dc superconducting cable at x = 1 km. Effect of earth resistivity ρ_g. Grounding resistance R_g = 10 Ω at x = 0. (a) ρ_g = 0; (b) ρ_g = 1 Ωm; (c) ρ_g = 1000 Ω•m.

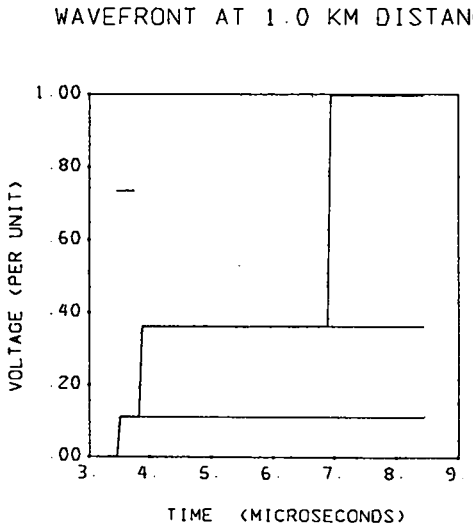

Fig. 3-13.
Step response of a semi-infinite, 100-kV, four-conductor dc superconducting cable at x = 1 km. Conductor resistances neglected. R_g = 10 Ω at x = 0; ρ_g = 100 Ω•m.

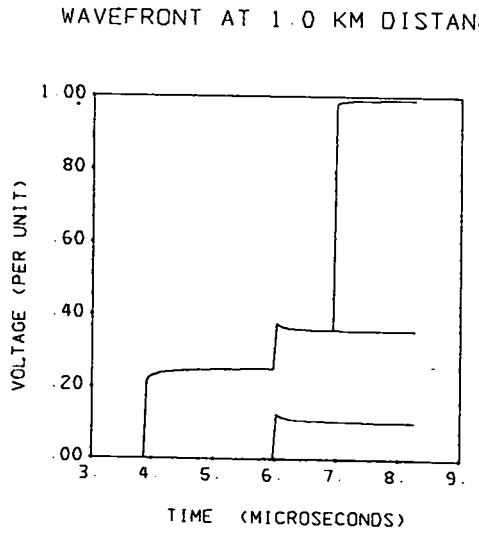

Fig. 3-14.
Step response of a semi-infinite, 100-kV, four-conductor dc superconducting cable at x = 1 km. Effect of dielectric constant. R_g = 10 Ω at x = 0; ρ_g = 100Ω• m; k_3 = 3.

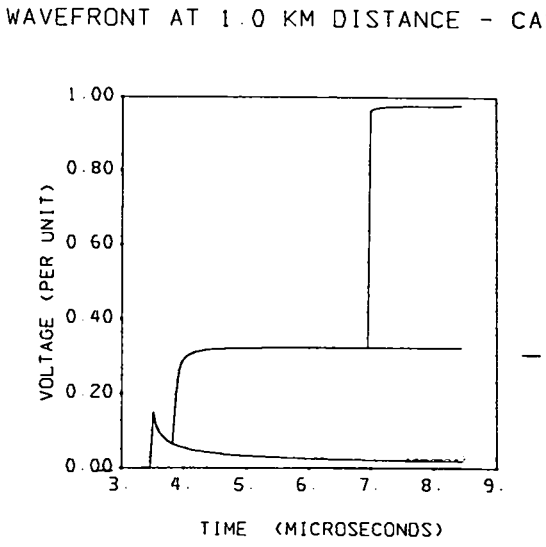

(a)

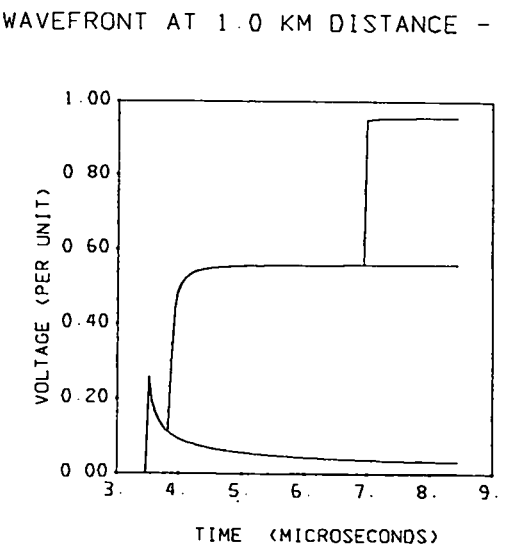

(b)

Fig. 3-15.
Step response of a semi-infinite, 100-kV, four-conductor dc superconducting cable at x = 1 km. Conductors 3 and 4 are connected together at x = 0. Conductor 2 and the common point of conductors 3 and 4 are grounded through R_g at x = 0. ρ_g = 100 Ω•m; (a) R_g = 10 Ω; (b) R_g = ∞.

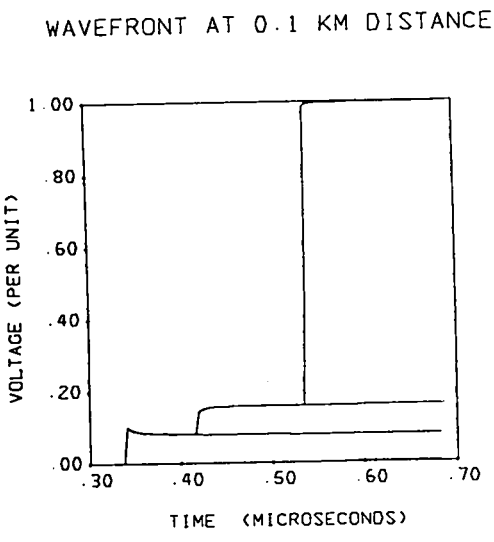

(a)

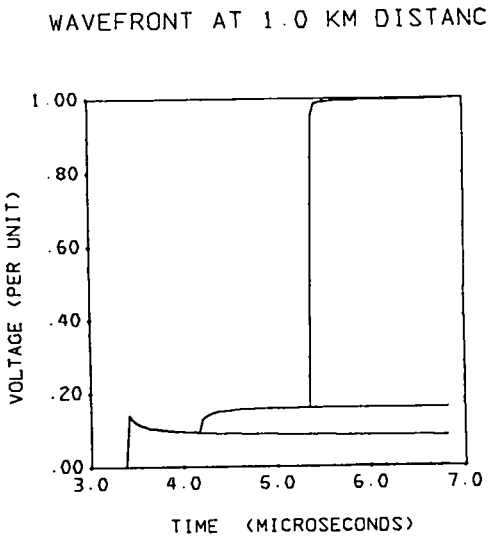

(b)

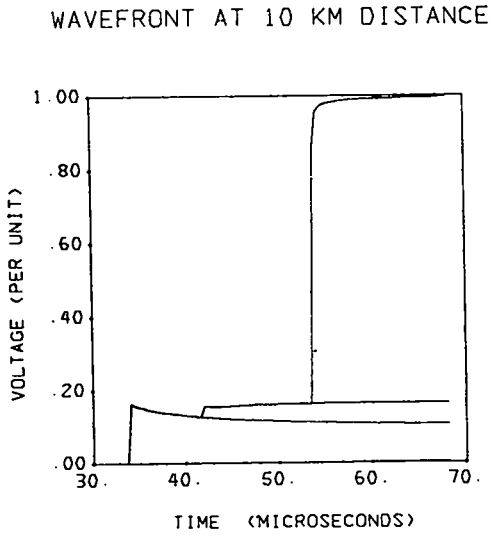

(c)

Fig. 3-16.
Step response of a semi-infinite, 300-kV, four-conductor dc superconducting cable. R_g = 10 Ω at x = 0; ρ_g = 100 Ω·m. (a) x = 100 m; (b) x = 1 km; (c) x = 10 km.

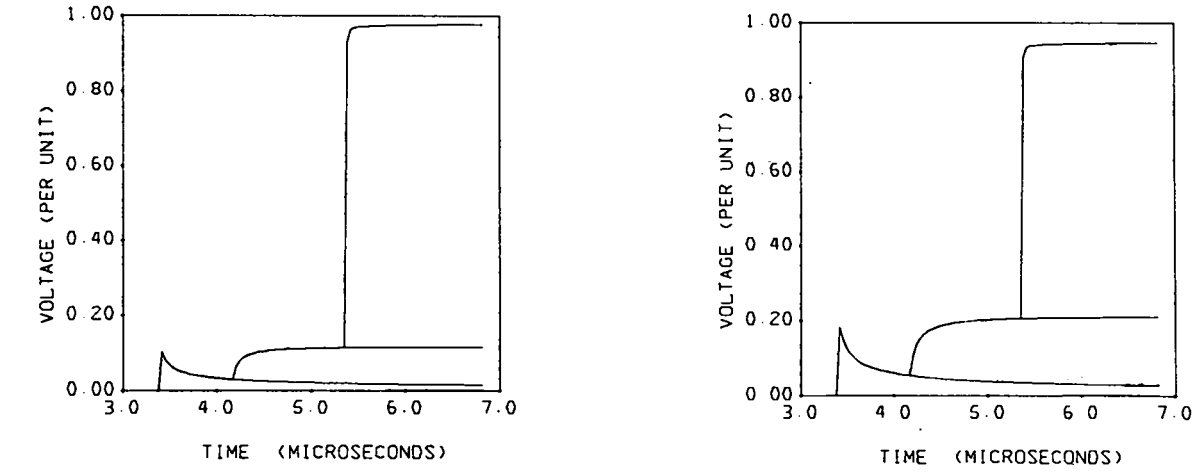

(a) (b)

Fig. 3-17. Step response of a semi-infinite, 300-kV, four-conductor dc supercoducting cable at x = 1 km. Conductors 3 and 4 are connected together at x = 0. Conductor 2 and the common point of conductors 3 and 4 are grounded through R_g at x = 0. ρ_g = 100 Ω•m. (a) R_g = 10 Ω; (b) R_g = ∞.

In each case, the applied voltage wave on conductor 1 is split into four component waves traveling at unequal velocities. All four component waves are present on conductor 1. Three component waves travel on conductor 2; two waves on conductor 3, and one single voltage wave of small magnitude travels on conductor 4 (nearest to earth). That component wave (of small magnitude) which is present on all four conductors at x = 0 is highly attenuated within a short distance from the origin. This wave is not discernable in any of the figures except Fig. 3-12a, which represents zero earth resistivity (ρ_g =0).

Three-Conductor Superconducting Cable. The three-conductor superconducting cable is an alternate design, more suitable for lower power ratings (Fig. 2-2). The dielectric is at ambient temperature, being thermally isolated from the high-voltage superconductor by the cryogenic enclosure. The inner cylinder (stainless steel) of the cryogenic enclosure is intimately connected to the high-voltage superconductor throughout the length of the cable. Therefore, this combination constitutes conductor 1. The outer cylinder (copper) of the cryogenic enclosure is connected to conductor 1 at the terminals. A lead sheath (not shown in the figure) that encloses the dielectric is conductor 3. The electrical load circuit is completed through another similar cable.

The transient current is assumed to be expelled by the superconductor into the stainless-steel cylinder. Two voltage ratings (100 kV and 600 kV) were considered for this study.

Figures 3-18 and 3-19 show the step responses of cables under various system conditions. The applied voltage wave on conductor 1 is split into three component waves traveling at unequal velocities. All three component waves are present on conductor 1. Two component waves travel on conductor 2, and one single wave of small magnitude travels on conductor 3. Similar to the four-conductor superconducting cable system, the component wave present on all three conductors is of small magnitude at the origin and is highly attenuated within a short distance. This component is not discernable in any of the figures.

Two- and Three-Conductor Conventional Cables. The model for the three-conductor conventional cable was derived from the 250-kV dc submarine cable laid between the north and south islands of New Zealand.[23] Conductors 1, 2, and 3 are assumed to be concentric cylinders made up of copper, lead, and galvanized steel, respectively.

The two-conductor model for this study is similar to the three-conductor model but without the galvanized-steel armour.

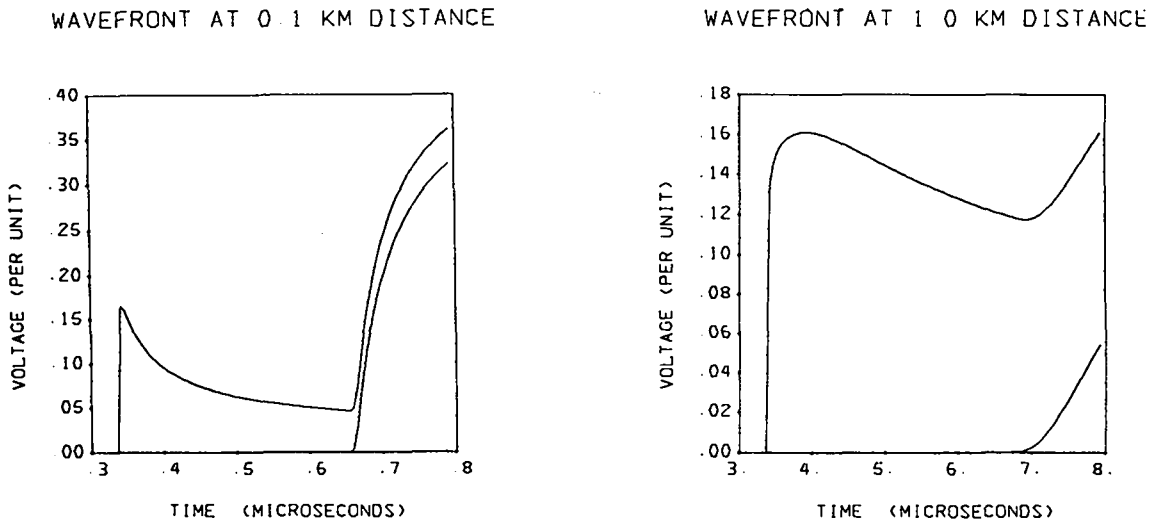

Fig. 3-18.
Step response of a semi-infinite, 100-kV, three-conductor dc superconducting cable. R_g = 10 Ω at x = 0; ρ_g = 100 Ω·m. (a) x = 100 m; (b) x = 1 km. Three, two, and one component waves travel along conductors 1, 2, and 3, respectively. The component wave which is present on all three conductors is highly attenuated and is not discernable in the figures.

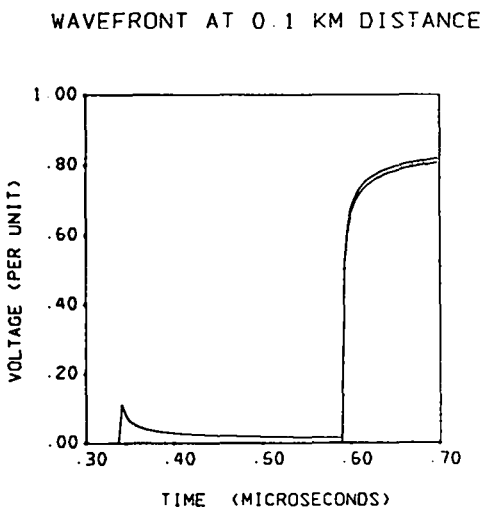

(a)

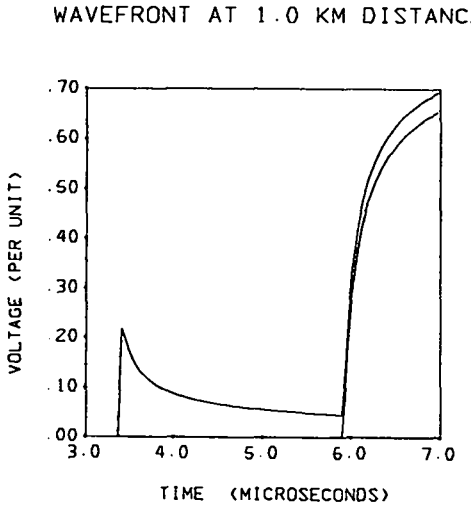

(b)

Fig. 3-19. Step response of a semi-infinite, 600-kV, three-conductor dc superconducting cable. R_g = 10 Ω at x = 0; ρ_g = 100 Ω• m. (a) x = 100 m; (b) x = 1 km.

Figures 3-20 to 3-23 show the step responses of 250-kV two- and three-conductor dc conventional cables. The three-conductor cable carries three component voltage waves, and the two-conductor cable carries two component waves. In each system, one component wave is very small in magnitude and is highly attenuated to a negligible value within a short distance from the origin.

3.1.3.2.3. System Parameters. The earth resistivity was varied from 0 to 1000 Ω•m for all of the cable designs studied. The grounding resistance of each "grounded" conductor at x = 0 was varied from 1 to ∞.

3.1.3.3. Interpretation of Data. With reference to Fig. 3-10, the original wave is split into four component waves traveling at unequal velocities. All four component waves are present on conductor 1. The number of component waves decreases progressively from conductor 1 to conductor 4. One single voltage wave of small magnitude travels on conductor 4 (nearest to earth). This component wave, which is present on all four conductors at x = 0, is highly attenuated within a short distance from the origin. This wave is not discernable in the figures.

The voltage between each conductor and ground changes abruptly as the component voltage waves arrive at a point along the cable at different times. For instance, conductor 1 experiences abrupt voltage changes at 3.45, 3.86,

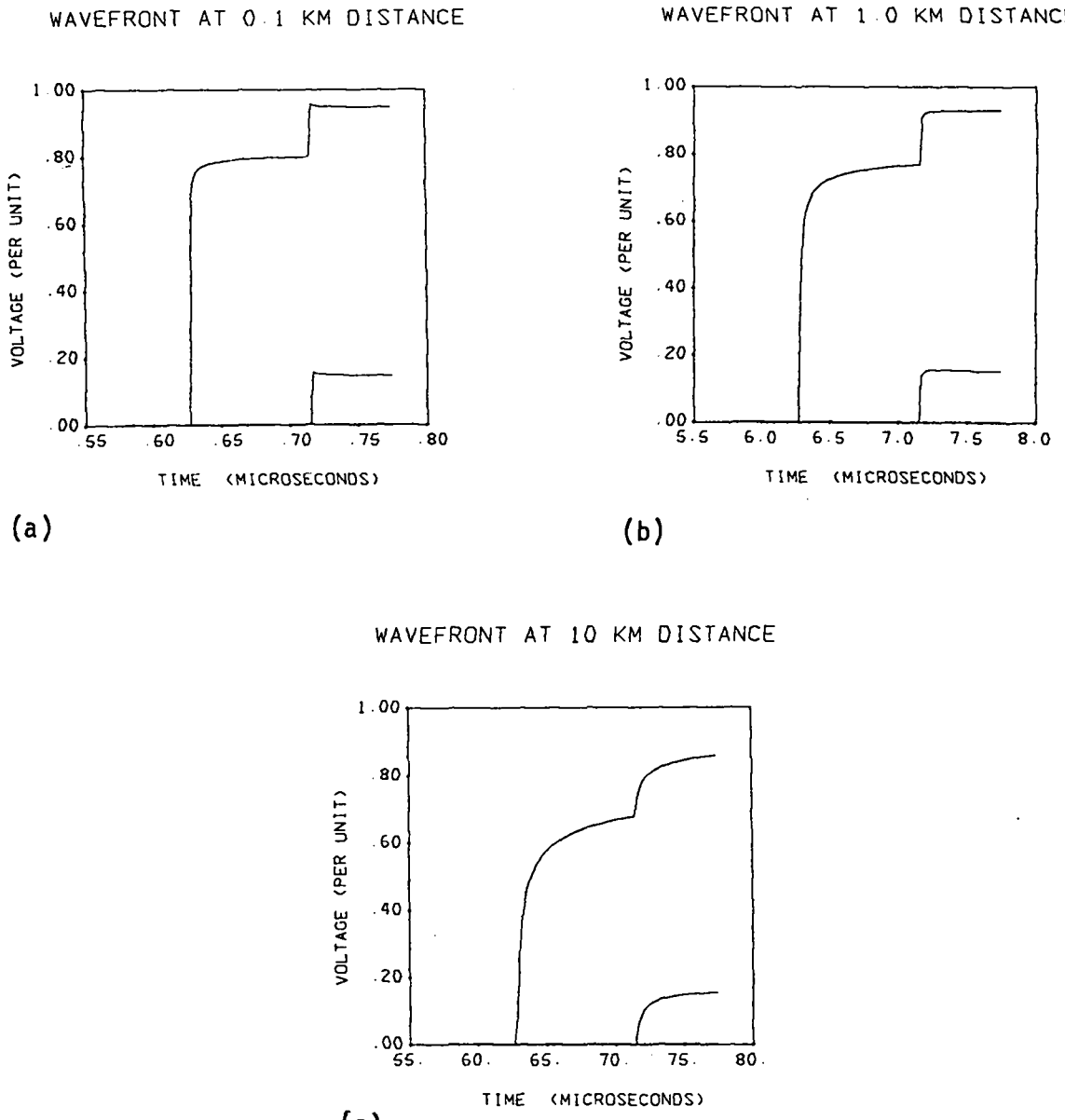

Fig. 3-20.
Step response of a semi-infinite, 250-kV, three-conductor dc submarine cable. R_g = 10 Ω at x = 0; ρ_g = 100 Ω• m. (a) x = 100 m; (b) x = 1 km; (c) x = 10 km.

5.77, and 6.93 μs as the four component waves arrive at x = 1 km (Fig. 3-10b). Similarly, three component waves arrive on conductor 2 at 3.45, 3.86, and 5.77 μs; two component waves on conductor 3 at 3.45 and 5.77 μs; and, one single wave on conductor 4 at 5.77 μs. The component wave (of small magnitude) which arrives at x = 1 km on all four conductors at 5.77 μs is highly attenuated within a short distance from the origin. This wave is not discernible in the figures.

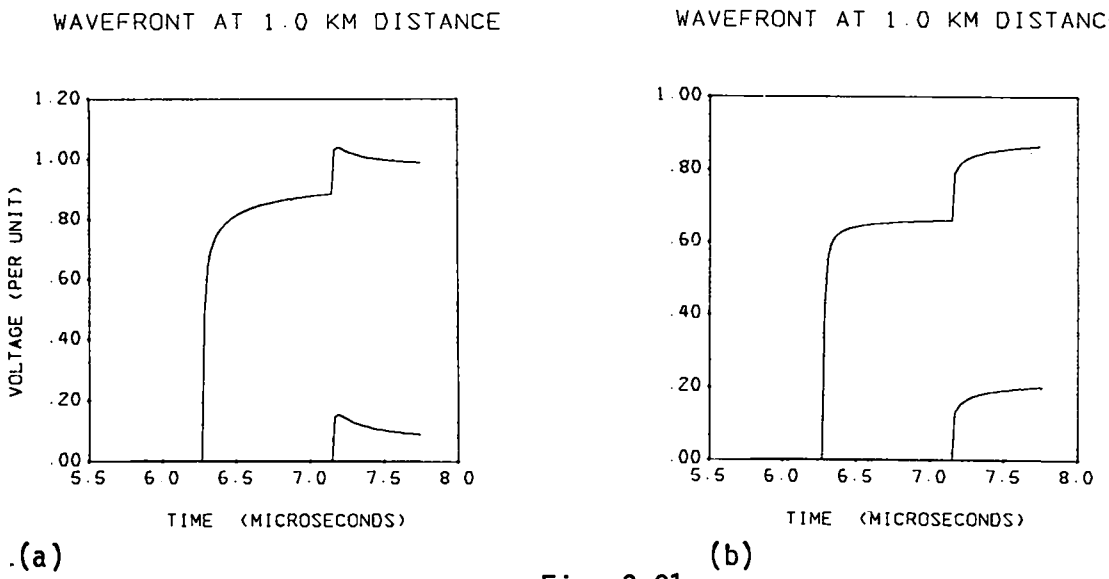

Fig. 3-21.
Step response of a semi-infinite, 250-kV, three-conductor dc submarine cable at x = 1 km. Effect of grounding resistance R_g at x = 0. Earth resistivity ρ_g = 100 Ω· m. (a) R_g = 1 Ω; (b) R_g = 100 Ω.

The primary voltage wave on conductor 3 (stainless steel) attenuates significantly with time. With increase in distance along the cable, the peak value of this wave increases, although the attenuation rate with time increases also. In general, the front time of the component waves increases with distance along the cable.

The voltage difference between each pair of conductors can also be ascertained from Fig. 3-10. At x = 1 km (Fig. 3-10b), no voltage difference appears between conductors 1, 2, and 3 until the second wave arrives on conductors 1 and 2 at 3.86 μs. Conductors 1 and 2 remain at equal voltages until the fourth wave arrives on conductor 1 at 6.93 μs, when about 0.65 p.u. is developed across conductors 1 and 2. The voltage spike developed across the cryogenic enclosure (between conductors 3 and 4) at x = 1 km is about 0.20 p.u. For a 100-kV cable (BIL = 250 kV), 50 kV of transient voltage will thus be impressed across the cryogenic enclosure. About 0.24 p.u. (i.e. 59.5 kV) will be impressed across the helium space between conductors 2 and 3. The major dielectric (between conductors 1 and 2) will carry only 0.65 p.u. (i.e. 162.5 kV).

The voltage stress across the cryogenic enclosure can be relieved by reducing the BIL (hence the steady-state voltage rating) of the cable. Other alternative solutions such as metallic shorts across the enclosure at regular

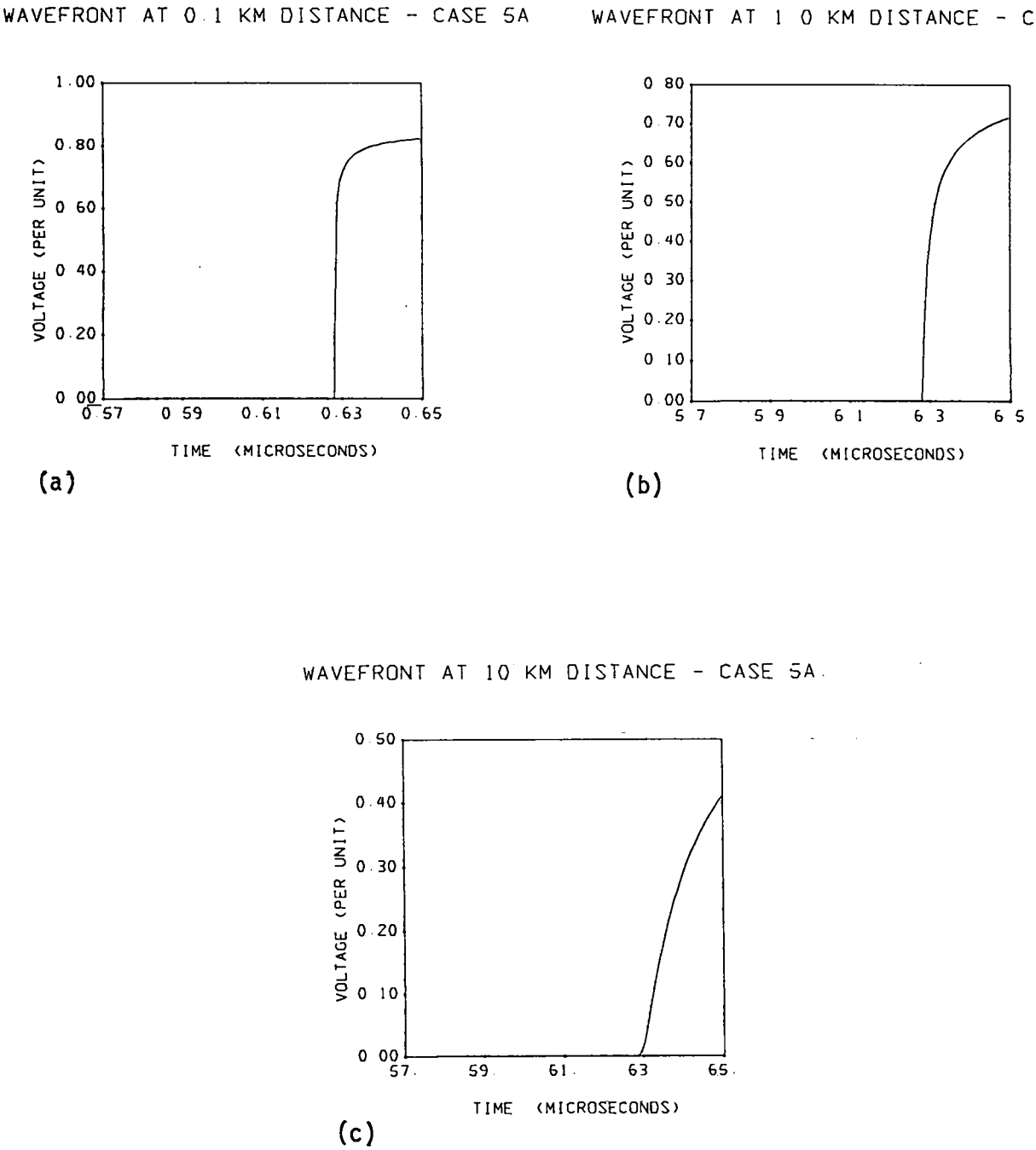

Fig. 3-22.
Step response of a semi-infinite, 250-kV, two-conductor dc cable. $R_g = 10\,\Omega$ at $x = 0$; $\rho_g = 100\,\Omega \cdot m$. (a) $x = 100$ m; (b) $x = 1$ km; (c) $x = 10$ km. Conductors 1 and 2 carry two and one component waves, respectively. The component wave which is present on both conductors is highly attenuated and is not discernable in the figures.

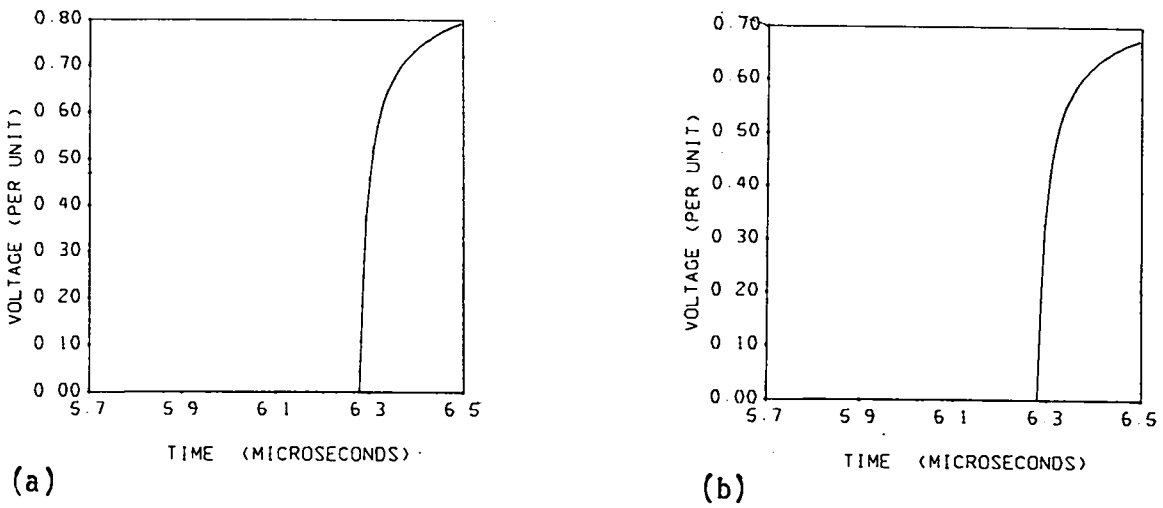

Fig. 3-23.
Step response of a semi-infinite 250-kV, two-conductor, dc cable at x = 1 km. Effect of grounding resistance R_g at x = 0. Earth resistivity ρ_g = 100 Ω·m. (a) R_g = 1Ω ; (b) R_g = 100 Ω.

intervals and design optimization in the cable and system can also reduce this voltage stress.

3.1.3.4. Limitations of the Analysis. The δ-matrices were evaluated by considering only the first two terms of the Eqs. (3-18) and (3-19) in order to keep the analysis simple and manageable. As a consequence, this analysis is valid at the wavefront of transients. To define the time period in which the results are valid, extensive computations were carried out by comparing results from the first terms of Eqs. (3-18) and (3-19), with those from the first two terms.

It was found that one of the eigenvalues (q_{3m}) of the B_2-matrix in Eq. (3-25) was negative. This will increase the corresponding exponential term in Eq. (3-27) with increase in distance along the cable. It was also found that all but one resultant matrix, $[a_{1K}][a_{2\ell}][a_{3m}]$, which is multiplied by this exponential term, is null. It was essential that this particular matrix is non-zero so that the initial conditions at x = 0 are consistent. This term was evaluated by using the exponential equivalent of erfc(y) for large values of y, i.e.,

$$\text{erfc}(y) = \exp(-y^2)/y\sqrt{\pi}, \qquad (3\text{-}33)$$

where $y = q_{2\ell}\, x/4\sqrt{t-q_{1K}x}$. The time limit was set such that $y^2 \geq q_{3m}\, x/2$. By simplifying the algebra, one gets

$$(t-t_{1k}) \geq q_{2\ell}^2/8q_{3m} \quad , \tag{3-34}$$

where, t = time limit, $t_{1K} = 1/q_{1K}$, and q_{1K}, $q_{2\ell}$ and q_{3m} are the eigenvalues corresponding to the non-zero matrix $[a_{1K}]\,[a_{2\ell}]\,[a_{3m}]$.

More terms of Eqs. (3-18) and (3-19) should be included if results at longer times are desired. As the front time is of concern in most applications, inclusion of just the first two terms of Eqs. (3-18) and (3-19) should be sufficient, considering the elegance, simplicity, and economy in computation time of the method described.

3.1.3.5. Discussion of Overvoltage Study.

3.1.3.5.1. Effect of Grounding Resistance. Figure 3-11 shows the effect of grounding resistance on the voltage propagation in the 100-kV, four-conductor dc superconducting cable. A lower grounding resistance would stress the major dielectric nearer to its design stress and would stress the cryogenic enclosure less. However, it should be borne in mind that conductors 2, 3, and 4 will be kept open or connected to earth through a nonlinear resistance at one end of the cable. The cable will be vulnerable if the surge enters through that end.

Figure 3-15 shows the effect when the two concentric cylinders (conductors 3 and 4) of the cryogenic enclosure are connected together at x = 0. The effect of connecting conductors 2 and 3 at x = 0, when R_g = 10 Ω, is to reduce the peak electrical stress across the thermal insulation by a small amount (Figs. 3-10b and 3-15a), although this reduction is significant when $R_g = \infty$ (Figs. 3-11c and 3-15b). In either case, the reduction of electrical stress across the thermal insulation is achieved by a substantial increase of electrical stress across the helium between conductors 2 and 3. As helium is primarily being used as a cooling medium only, this shift in electrical stress is also not welcome.

Figures 3-21 and 3-23 show the effect of grounding resistance on the conventional cables. Higher grounding resistances tend to attenuate and distort the wavefronts. For the three-conductor conventional cable (Fig. 3-21), the voltage on conductor 3 away from the origin is neglibible in all cases. The voltage peak on conductor 2 is reduced by decreasing the grounding

resistance. The attenuation rate is also increased when the grounding resistance is less. Just the opposite occurs for the voltage on conductor 1. For the two-conductor conventional cable (Fig. 3-23), the voltage on conductor 2 is negligible. The voltage on conductor 1 is attenuated more with higher grounding resistance.

3.1.3.5.2. Effect of Earth Resistivity. Figure 3-12 shows the effect of earth resistivity on the voltage propagation in the 100-kV, four-conductor dc superconducting cable. The earth resistivity affects only the voltage on conductor 4. This was also found to be true for other types of cables.

3.1.3.5.3. Effect of Conductor Resistance. The effect of neglecting the conductor resistances is shown in Fig. 3-13. When compared with Fig. 3-10b, it is evident that the effect of conductor resistances is to increase the stress on the cryogenic enclosure. The conductor resistances also slow down the wavefront.

3.1.3.5.4. Effect of Dielectric Constant. In most cases in this study, the dielectric constant of the annular space in the cryogenic enclosure was assumed to be unity. In practice, this vacuum space will be filled with thermal insulation. Assuming a dielectric constant of 3, computations were made of the voltage distribution in the 100-kV four-conductor dc superconducting cable (Fig. 3-14). As expected, the velocity of the major component wave on conductor 3 was decreased without changing the interconductor voltage differences substantially.

3.1.3.5.5. Effect of Voltage Rating of Cable. The wavefronts on a 300-kV, four-conductor dc superconducting cable are shown in Fig. 3-16. In this case, the major dielectric is stressed more nearly to its design value, and the helium space between conductors 2 and 3 is stressed less. The cryogenic enclosure is also stressed less on a per unit basis. However, assuming a BIL of 750 kV for this 300-kV cable, the highest voltages across the major dielectric, the helium space, and the cryogenic enclosure will be 647, 56, and 103 kV, respectively. This is in contrast with 162.5, 59.5, and 50 kV for the 100-kV design. The cryogenic enclosure of the 300-kV design is stressed about twice as much as that of the 100-kV design. This is not surprising considering the fact that the cryogenic enclosure is designed mainly on heat-leak specifications.

3.1.3.5.6. Three-Conductor dc Superconducting Cable. This cable (Fig. 2-2) is an alternate design that is more suitable for lower power ratings.

The inner cylinder of the cryogenic enclosure is intimately connected to the high-voltage conductor (conductor 1) throughout the length of the cable. The outer cylinder (conductor 2) of the cryogenic enclosure is connected to conductor 1 at both ends of the cable. Therefore, the two cylinders of the cryogenic enclosure are at the system voltage under steady-state conditions. Under transients, a voltage difference develops across the cryogenic enclosure (Figs. 3-18 and 3-19). As with the four-conductor case, the voltage across the cryogenic enclosure is smaller for a cable of lower voltage rating.

3.1.3.5.7. DC Conventional Cables. Computations for dc conventional cables were performed for the purpose of comparison. As Figs. 3-20 and 3-21 show, a considerable amount of voltage may develop between the lead sheath and the steel armour of the three-conductor submarine cable. Smaller grounding resistances at the terminals help in reducing this voltage difference. It is of interest to note in Fig. 3-21a that the voltage on conductor 1 exceeds 1 p.u. However, the voltage across the major dielectric does not exceed 1 p.u.

Wavefronts for a two-conductor cable of the same voltage rating (250 kV) are shown in Figs. 3-22 and 3-23. The voltage waves attenuate and slope off as they travel along the cable (Fig. 3-22). Higher terminal grounding resistance also attenuates the wavefronts (Fig. 3-23).

3.1.4. Conclusions to Electrical System Studies.

1. Methods of analysis have been developed to determine the performance of a dc superconducting cable under
   a. harmonic currents superimposed on dc load currents,
   b. fault currents and
   c. transient overvoltages.
2. Although a properly designed dc superconducting cable will be able to withstand the expected ripple losses and to meet the fault-current requirements, each specific design should be analyzed.
3. Transient voltages will not stress the major dielectric of the cable system to its full BIL capability.
4. Surge protection, cable design optimization, and system coordination will be required to limit transient voltages across electrically weak parts of the system (e.g., helium coolant and cryogenic enclosure), which are designed to perform non-electrical functions.

3.2. Dielectric Studies

The ultimate objective of our dielectric studies was to select the most promising material in terms of high dielectric strength and long life. To attain this objective, several problem areas need to be considered, among which are the statistical nature of breakdown; the effect of previous history (memory); electric field distortion by localized trapped charges; electrode area effect; aging; dielectric thickness; and mechanical properties when cycled to cryogenic temperatures.

Extensive data are available on cryogenic dielectrics for operation under ac conditions, but few data exist for operations under dc conditions. The electrical requirements of a dielectric under dc stress are different from those under ac stress; that is, for ac operation, the corona inception voltage and the dielectric losses are the limiting constraints; for dc applications, the polarity-reversal stress is the limiting factor. The aging mechanisms for the two types of application will also be different for long-term stress applications.

In our tests, periods of from 5 to 6 h were required to cool dielectric materials from room temperature to 12 K and as much time to warm again. The actual electrical test at cryogenic temperatures lasts for 30 min. To obtain statistically significant data would require many years of testing all candidate materials under various electrical conditions; therefore, we first performed screening tests on sheets of dielectric materials under uniform dc electric field. From the results, several dielectric materials were selected for cable sample tests under various electrical conditions (e.g., impulse, switching surge, polarity reversal). The data from the screening tests also provided basic information on the behavior of dielectric materials at cryogenic temperatures under dc stress. The equipment used for these tests is described in Sec. 3.5.

3.2.1. Screening Tests.

3.2.1.1. Dielectric Specimens. Of the 12 dielectric materials selected for screening tests (Table 3-VII), most were 3-mil (76.2-μm) thick. However, Cryovac could be obtained only in 1.5-mil (38.1-μm), Pink Poly in 4-mil (101.60-μm), and PP/C (a composite made up of cellulose paper in the outer two layers and polypropylene in the middle layer) in 5-mil (127-μm) thicknesses. The 5-mil-thick (127-μm) cellulose paper B was selected for direct comparison with the PP/C.

Oil-impregnated cellulose paper is ideal from the manufacturing standpoint because it is the standard dielectric for all high-voltage cables. Moreover, the oil-impregnated paper is significantly stronger at liquid nitrogen temperature under dc, impulse, and polarity reversal than at room temperature.[24] However, it had not been tested previously at temperatures near those of the dc SPTL operation, i.e., greater than 5.2 K but less than 20 K. Therefore, we tested the two types of cellulose paper, copaco paper and PP/C at cryogenic temperatures after impregnation with mineral oil (Univolt 60).

3.2.1.2. Test Parameters. Most of the tests were performed at 12 K with the samples under a helium pressure of 1.38 MPa, the operating conditions of the dc superconducting cable being designed by LASL. Additional tests were performed on the selected systems at 18 K, 83 K, and 298 K with helium pressures of 0.69 MPa and 1.38 MPa. Both polarities of dc were supplied by a filtered HVDC source with a 1 kV/s ramp rate of voltage application until breakdown.

The voltage measurement was accurate to ±1% and pressure measurements accurate to ±7 kPa. The accuracy of the temperature measurement was as follows: ±50 mK for 12 K and 18 K, ±0.5 K for 83 K and 298 K.

TABLE 3-VII

LIST OF DIELECTRIC MATERIALS FOR CRYOGENIC TESTS

Trade Name	Type of Material
Cellulose Paper, A(76.2 μm)	Air resistance = 7500-10 000 Gurley-Sec; Density = 1.15 g/cm^3; water finish
Cellulose Paper, B(127 μm)	Air resistance = 3000-6000 Gurley-Sec; Density = 1.10 g/cm^3; water finish
Copaco Paper (127 μm)	Rag paper
Cryovac, D929, (38.1 μm)	Cross-linked medium-density polythylene
Kapton, 300 H (76.2 μm)	Polyimide
Mylar, 300 WC (76.2 μm)	Polyester
Nomex, 410 (76.2 μm)	Fibrous-spunbonded polyamide
Pink Poly, RC AS 1 200 (101.6 μm)	Polyethylene, containing organic antistat
PP/C (127 μm)	Cellulose paper-polypropylene-cellulose paper
Teflon, FEP (76.2 μm)	Polytetrafluorethylene
Udel (76.2 μm)	Polysulfone
Valeron, U.O.P. 3096 (76.2 μm)	High-density polyethylene

3.2.1.3. Design of Equipment. The main part of the cryostat (Fig. 3-24) providing the environment for the dielectric specimens, is a copper cylindrical chamber, 210-cm long and 15-cm diam, which can be safely pressurized up to 2.1 MPa. The cylinder is cooled by flowing either liquid nitrogen or cold, gaseous helium through coils soldered along the outer surface. A second copper cylinder, 21.8-cm diam, is placed concentrically around the first. Liquid nitrogen, flowing through soldered coils, provides shielding against heat influx. A 27.4-cm-diam steel cylinder provides the vacuum jacket and external support. The annular space between the cylinders is filled with multilayer thermal insulation and is continuously evacuated by a diffusion pump. A hole in the floor accommodates the cryostat.

The bushing (Fig. 3-25) was designed so that connections could be made to the multi-electrode dielectric sample holder by manipulating an actuating rod and a moving arm from outside the cryostat. The actuating rod is inserted through the central hollow conductor that provides the voltage. Tightly wound Mylar sheets serve as the major insulation between the high-voltage conductor and the ground, which is concentrically placed stainless steel tubing. At the

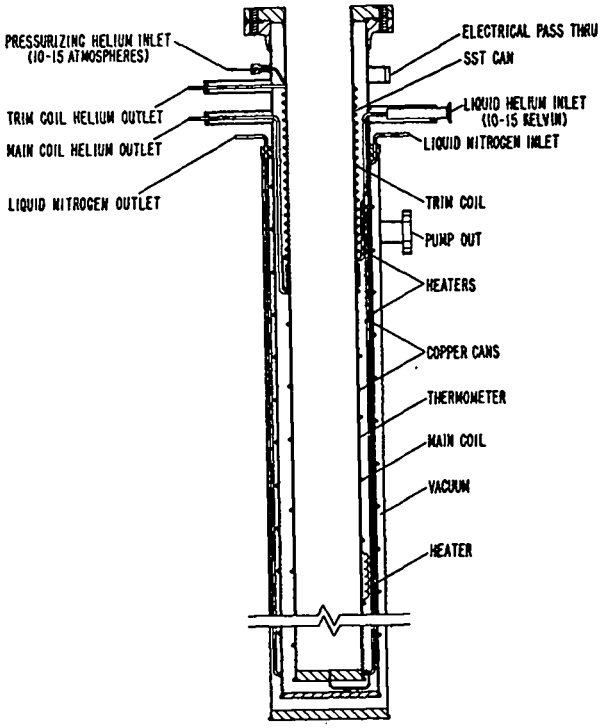

Fig. 3-24.
Outline drawing of test cryostat.

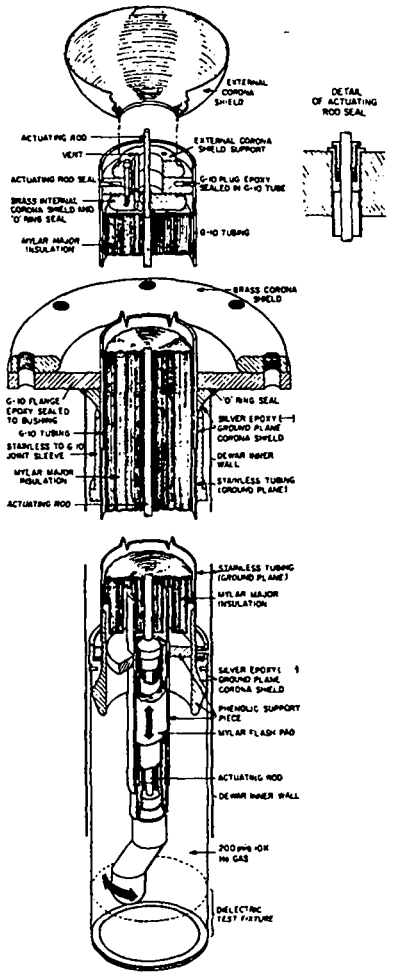

Fig. 3-25.
Outline drawing of bushing.

upper (room temperature) part of the bushing, the Mylar insulation is held in place by G-10 (glass-reinforced epoxy) tubing. A coating of silver epoxy controls the electric stress.

Because dielectric samples require hours to cool and warm, a multi-electrode dielectric sample holder was designed to speed up accumulation of data. This Plexiglas sample holder contains six pairs of stainless steel electrodes, seated in accurately aligned holes. Electrical contacts are made to each of the six upper electrodes by a rotating electrode attached to the actuating rod in the bushing. Each electrode has an overall diameter of 15.88 mm, a flat surface of 6.45-mm diam, and contour radius of 4.76 mm. The sample holder is attached by screws to a stainless steel cylinder (13.9-mm diam) connected at its upper end to the ground plane of the bushing. The sample holder and the rotating electrode are shown in Fig. 3-26.

The cryostat contains three heaters - two around the 13.9-mm-diam stainless steel cylinder, the third around the innermost cylinder of the cryostat. These heaters control the temperature and warm the cryostat to room temperature so that the dielectric samples can be changed.

A 1/8-W carbon-resistor thermometer was used to measure the 12-K and 18-K temperatures, and a copper-constantan thermocouple was used from 83 to 298 K.

Figure 3-27 shows the test set up.

3.2.1.4. Test Procedures. Before each test, the electrodes were cleansed with freon in an ultrasonic cleaner. They were also polished in a drill press with 1μ aluminum oxide and water. The dielectric samples, consisting of two 13.33-cm-diam sheets, were first tested for electrostatic charges on the surface by a Simco Type SS-1 locator, and charges were neutralized by polonium irradiation (Staticmaster from Nuclear Products Co.) before installation in the sample holder.

After the sample holder had been fitted to the bushing and the bushing installed inside the cryostat, the test assembly was evacuated for 15 min to about 66.8 Pa (0.5 torr) before the test assembly was flushed several times with helium. The cryostat was then pressurized and precooled by passing

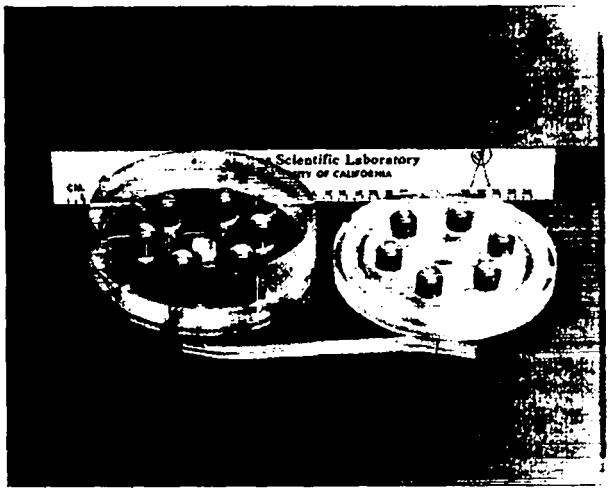

Fig. 3-26.
Six-electrode sample holder for multiple breakdown tests.

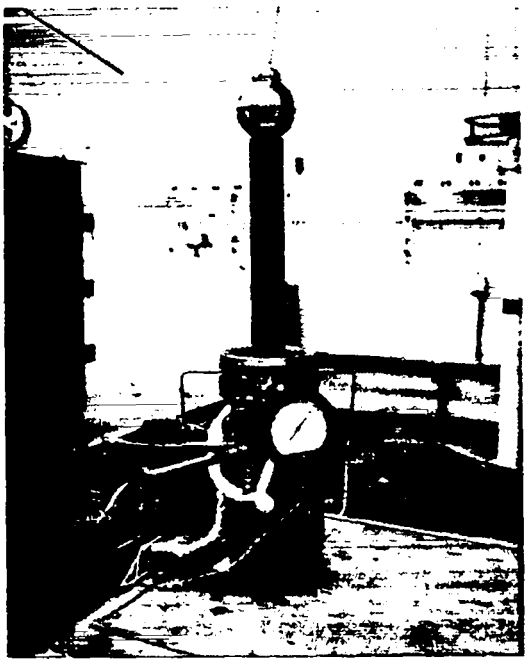

Fig. 3-27.
Test set up.

liquid nitrogen through the main cooling coils. For tests at 12 K, the cryostat was further cooled by passing cold gaseous helium through the main cooling coils. The temperature of the sample was held at 12 K (±50 mK) by an automatic temperature controller. The voltage-breakdown tests began after the sample had been in the pressurized helium environment at the required temperature for at least 15 min.

Voltage could be applied and polarity alternately reversed to any of the six electrode pairs by rotating an indexed rod from outside the cryostat. Voltages were applied to the numbered electrode pairs in the order 1,3,5,2,4, and 6.

Two sets of experiments (each with six breakdowns) were performed at 12 K and 1.38 MPa on each of the 14 dielectric samples; one set started with positive-polarity voltage and the other with negative-polarity voltage. Three replications of all sets were performed, each being completely randomized with the help of a Random Number Table.

A second series of tests was performed after five dielectric systems were selected as suitable for the cable-sample tests. The samples were tested in the form of sheets at 18 K, 83 K, and 298 K under 0.69 MPa and 1.38 MPa of helium, as well as at 12 K and 0.69 MPa of helium to determine the effects of temperature and pressure on the dc breakdown voltage levels. Two sets of tests (each with six breakdowns) were performed on the five samples. All sets of tests were randomized; Tables 3-VIII to 3-XII show the summarized results.

A third series of tests was performed with Copaco paper, the samples of which were obtained late in the testing program. The temperature and pressure variables were randomized during this series of tests. The results are shown in Tables 3-XIII and 3-XIV.

3.2.1.5. Analysis of Screening-Test Results and Discussion. Surface charges were a concern, particularly for the plastic dielectric materials. Although these charges were neutralized by polonium irradiation before the dielectric materials were placed in the sample holder, tests showed that they reappeared within a few hours. The paths of the surface discharges could be identified by dark streamer patterns on the dielectric surface.

The surface charge could also be correlated with surface discharges and flashovers when voltage was applied. On Kapton, surface flashovers were sometimes accompanied by black carbonized paths. Of all the plastic materials, Pink Poly showed the least amount of surface charges and accompanying discharges. Tables 3-VIII to 3-XIV show the ratio of puncture to surface flashover for

TABLE 3-VIII

DC BREAKDOWN VOLTAGE AND ELECTRIC FIELD AT 12 K AND 1.38 MPa OF HELIUM

Material	Mean kV(kV/mm)	Lowest Value kV(kV/mm)	Stand. Dev. kV(kV/mm)	No. of Measurements	Distribution	No. of Failures by Puncture/ Flashover
Cellulose Paper[a]	11.08 (72.70)	9.0 (59.06)	1.43 (9.38)	34	LN	34/0
Oil-Impregnated Cellulose Paper[a]	30.39 (199.41)	22.8 (149.61)	4.73 (31.04)	34	LN/W	34/0
Cellulose Paper[b]	15.22 (59.92)	12.0 (47.24)	1.65 (6.50)	36	W	36/0
Oil-Impregnated Cellulose Paper[b]	44.20 (174.02)	34.8 (137.01)	4.62 (18.19)	36	N	36/0
Cryovac[c]	40.63 (533.20)	24.0 (314.96)	6.88 (90.29)	35	W	21/14
Kapton[a]	54.67 (358.73)	36.0 (236.22)	13.05 (85.63)	36	LN	4/32
Mylar[a]	47.00 (308.40)	30.0 (196.85)	5.86 (38.45)	36	LN	5/31
Nomex[a]	14.10 (92.52)	10.2 (66.93)	2.22 (14.57)	35	E	35/0
Pink Poly[d]	43.93 (216.19)	27.6 (135.83)	6.28 (30.91)	33	N	33/0
PP/C[b]	31.08 (122.36)	27.0 (106.30)	2.34 (9.21)	35	LN	35/0
Oil-Impregnated PP/C[b]	46.37 (182.56)	33.6 (132.28)	6.33 (24.92)	35	N	35/0
Teflon[a]	47.70 (312.99)	36.0 (236.22)	4.84 (31.76)	36	W	18/18
Udel[a]	47.76 (313.39)	36.0 (236.22)	6.70 (43.96)	32	E	15/17
Valeron[a]	46.32 (303.94)	30.0 (196.85)	4.82 (31.63)	35	W	30/5

[a] Two nominal 76.2-μm-thick sheets.

[b] Two nominal 127-μm-thick sheets.

[c] Two nominal 38.1-μm-thick sheets.

[d] Two nominal 101.6-μm-thick sheets.

E = Extreme value (Type I) distribution.

LN = Lognormal distribution.

N = Normal (Gaussian) distribution.

W = Weibull distribution.

TABLE 3-IX

DC BREAKDOWN VOLTAGE AND ELECTRIC FIELD AT 12 K AND 0.69 MPa OF HELIUM

Material	Mean kV(kV/mm)	Lowest Value kV(kV/mm)	Stand. Dev. kV(kV/mm)	No. of Measurements	No. of Failures by Puncture/ Flashover
Cellulose Paper[a]	10.65(41.93)	9.0(35.43)	0.73(2.87)	12	12/0
Oil-Impregnated Cellulose Paper[a]	35.30(138.98)	27.6(108.66)	3.84(15.12)	12	12/0
PP/C[a]	26.45(104.13)	19.6(77.17)	3.49(13.74)	12	12/0
Pink Poly[b]	37.09(186.52)	30.6(150.59)	4.74(23.33)	11	10/1
Valeron[c]	39.30(257.87)	31.8(208.66)	2.93(19.23)	12	1/11

[a] Two nominal 127-μm-thick sheets.

[b] Two nominal 101.6-μm-thick sheets.

[c] Two nominal 76.2-μm-thick sheets.

TABLE 3-X
DC BREAKDOWN VOLTAGE AND ELECTRIC FIELD
AT 18 K AND 0.69 MPa AND 1.38 MPa OF HELIUM

Material	Mean kV(kV/mm)	Lowest Value kV(kV/mm)	Stand. Dev. kV(kV/mm)	No. of Measurements	No. of Failures by Puncture/ Flashover
Cellulose Paper[a]	9.98(39.29)[c]	9.0(35.43)	0.77(3.03)	11	11/0
	12.50(49.21)[d]	10.8(42.52)	1.47(5.79)	12	12/0
Oil-Impregnated Cellulose Paper[a]	31.83(125.31)[c]	24.0(94.49)	4.29(16.89)	12	9/3
	43.15(169.88)[d]	35.4(139.37)	6.21(24.45)	12	12/0
PP/C[a]	21.58(84.96)[c]	17.4(68.50)	2.50(9.84)	12	12/0
	26.20(103.15)[d]	21.0(82.68)	3.31(13.03)	12	12/0
Pink Poly[b]	47.30(232.78)[c]	33.6(165.35)	9.57(47.10)	12	1/11
	44.30(218.01)[d]	36.0(177.17)	5.71(28.10)	12	7/5

[a] Two nominal 127-μm-thick sheets

[b] Two nominal 101.6-μm-thick sheets

[c] At 0.69 MPa

[d] At 1.38 MPa

TABLE 3-XI
DC BREAKDOWN VOLTAGE AND ELECTRIC FIELD
AT 83 K UNDER 0.69 MPa AND 1.38 MPa OF HELIUM

Material	Mean kV(kV/mm)	Lowest Value kV(kV/mm)	Stand. Dev. kV(kV/mm)	No. of Measurements	No. of Failures by Puncture/ Flashover
Cellulose Paper[a]	6.50(25.59)[d]	5.4(21.26)	0.84(3.31)	12	12/0
	8.40(33.07)[e]	6.0(23.62)	1.95(7.68)	11	11/0
Oil-Impregnated Cellulose Paper[a]	31.95(125.79)[d]	27.6(108.66)	2.61(10.28)	10	6/4
	33.60(132.28)[e]	15.6(61.42)	6.62(26.06)	12	10/2
PP/C[a]	21.11(83.11)[d]	17.4(68.50)	3.02(11.89)	11	11/0
	27.76(109.29)[e]	18.6(73.23)	5.47(21.54)	11	11/0
Pink Poly[b]	53.93(265.40)[d]	43.2(212.60)	7.50(36.91)	12	0/12
	70.58(347.34)[e]	51.6(73.23)	11.53(56.74)	11	1/10
Valeron[c]	46.20(303.15)[d]	37.2(244.09)	5.64(37.01)	12	1/11
	55.72(365.62)[e]	40.8(267.72)	9.37(61.48)	12	7/5

[a] Two nominal 127-μm-thick sheets

[b] Two nominal 101.6-μm-thick sheets

[c] Two nominal 76.2-μm-thick sheets

[d] At 0.69 MPa

[e] At 1.38 MPa

TABLE 3-XII

DC BREAKDOWN VOLTAGE AND ELECTRIC FIELD AT 298 K UNDER 0.69 MPa AND 1.38 MPa OF HELIUM

Material	Mean kV(kV/mm)	Lowest Value kV(kV/mm)	Stand. Dev. kV(kV/mm)	No. of Measurements	No. of Failures by Puncture/ Flashover
Cellulose Paper[a]	6.25(24.61)[d]	4.2(16.54)	1.52(5.98)	12	12/0
	8.10(31.89)[e]	4.8(18.90)	2.34(9.21)	12	12/0
Oil-Impregnated Cellulose Paper[a]	25.35(99.80)[d]	15.0(59.06)	4.73(18.62)	12	1/11
	28.80(113.39)[e]	18.6(73.23)	6.90(27.17)	12	8/4
PP/C[a]	19.55(76.97)[d]	12.0(47.24)	5.08(20.00)	12	4/8
	24.40(96.06)[e]	20.4(80.32)	3.57(14.06)	12	8/4
Pink Poly[b]	22.95(112.94)[d]	21.0(103.35)	1.76(8.66)	12	0/12
	31.60(155.51)[e]	22.2(109.25)	6.63(32.63)	12	3/9
Valeron[c]	23.00(150.92)[d]	11.4(74.80)	5.32(34.91)	12	1/11
	38.84(254.86)[e]	24.6(161.42)	5.71(37.47)	11	5/6

[a] Two nominal 127-μm-thick sheets.

[b] Two nominal 101.6-μm-thick sheets.

[c] Two nominal 76.2-μm-thick sheets.

[d] At 0.69 MPa.

[e] At 1.38 MPa.

TABLE 3-XIII

DC BREAKDOWN VOLTAGE AND ELECTRIC FIELD OF COPACO PAPER (WITH AND WITHOUT OIL IMPREGNATION) AT 0.69 MPa OF HELIUM

Material	Mean kV(kV/mm)	Lowest Value kV(kV/mm)	Stand. Dev. kV(kV/mm)	No. of Measurements	No. of Failures by Puncture/ Flashover
Copaco Without Oil-Impregnation	12.30(48.43)[a]	9.0(35.43)	1.61(6.34)	12	12/0
	14.25(56.10)[b]	12.0(47.24)	1.12(4.41)	12	12/0
	16.00(62.99)[c]	15.0(59.06)	0.78(3.07)	12	12/0
	18.25(71.85)[d]	16.2(63.78)	1.48(5.83)	12	12/0
Copaco With Oil Impregnation	16.85(66.34)[a]	15.0(59.06)	1.24(4.88)	12	0/12
	37.55(147.83)[b]	30.6(120.47)	4.94(19.45)	12	1/11
	---	---	---	--	---
	44.70(175.98)[d]	33.6(132.28)	7.31(28.78)	12	1/11

[a] At 298 K.

[b] At 83 K.

[c] At 18 K.

[d] At 12 K.

TABLE 3-XIV

DC BREAKDOWN VOLTAGE AND ELECTRIC FIELD OF COPACO PAPER (WITH AND WITHOUT OIL IMPREGNATION) AT 1.38 MPa OF HELIUM

Material	Mean kV(kV/mm)	Lowest Value kV(kV/mm)	Stand. Dev. kV(kV/mm)	No. of Measurements	No. of Failures by Puncture/ Flashover
Copaco Without Oil-Impregnation	11.33(44.61)[a]	9.0(35.43)	1.34(5.28)	12	12/0
	15.75(62.01)[b]	13.2(51.97)	1.54(6.06)	12	12/0
	20.53(80.83)[c]	18.6(73.23)	1.44(5.67)	12	12/0
	24.85(97.83)[d]	21.6(85.04)	6.08(23.94)	12	12/0
Copaco With Oil Impregnation	25.65(100.98)[a]	22.2(87.40)	2.84(11.18)	12	0/12
	48.55(191.14)[b]	39.0(153.54)	4.36(17.17)	12	0/12
	---	---	---	--	---
	56.52(222.52)[d]	46.8(184.25)	4.51(17.76)	10	4/6

[a] At 298 K.
[b] At 83 K.
[c] At 18 K.
[d] At 12 K.

all materials tested. Comparison of these tables shows that higher pressure or lower temperature tends to suppress the surface discharges.

Often, breakdown resulted in multiple punctures of the test sample (Fig. 3-28). Puncture was associated with fractures for several of the dielectric materials. Some of these materials showed microfractures (Fig. 3-29) and others (e.g., Pink Poly) showed gross fractures. To determine whether the cool-down process produced the fractures, Pink Poly was cooled to 12 K at 1.38 MPa of helium using the voltage breakdown test procedure. When it was warmed without the application of voltage, no mechanical distress of the material was observed. Tapes of all 12 dielectric materials were immersed in liquid nitrogen. Although these tapes became stiffer, none broke when bent. Tapes of these materials were also wound on aluminum mandrels and plunged into liquid nitrogen. They showed no damage. This was also true of cellulose paper impregnated with Univolt 60. However, Univolt 60, when frozen in liquid nitrogen, became brittle like glass.

An investigation was made of four types of probability distributions to find the best fit in describing the breakdown voltage. The normal (Gaussian),

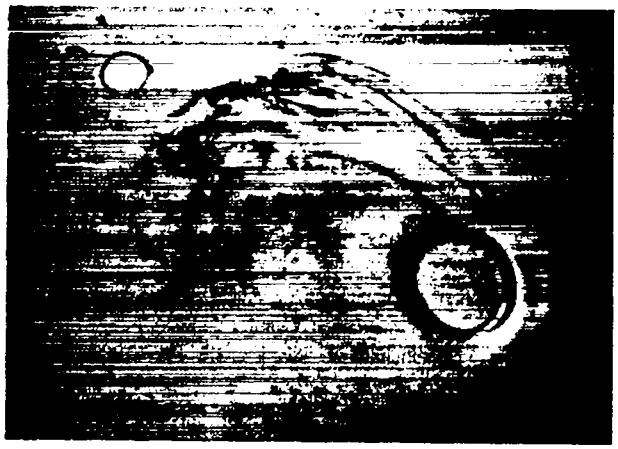

Fig. 3-28.
Photomicrograph of punctures on Teflon caused by voltage breakdown (75x).

Fig. 3-29.
Photomicrograph of microfactures surrounding puncture on Teflon caused by voltage breakdown (300x).

log-normal, Weibull, and extreme value (type I) distributions were selected for study.[25] The maximum distances between the sample cumulative distribution function (c.d.f.) and the respective theoretical c.d.f.'s were used as measured to form the basis of comparison between distributions. These are similar to Kolmogorov-type statistics.[26] No attempt was made to attach significance levels; they were used only for comparison purposes.

Maximum likelihood estimates of the Weibull and extreme value parameters were used to compute the respective c.d.f.'s. The sample mean and standard deviation (bias-corrected) provided the theoretical normal c.d.f. The theoretical lognormal c.d.f. was obtained by taking natural logarithms of the data, finding the corresponding normal c.d.f., and then making the appropriate transformation.

Figure 3-30 shows the empirical c.d.f. and the four theoretical c.d.f.'s for two sheets of 127-μm cellulose paper. The maximum absolute difference between the empirical c.d.f. and each theoretical c.d.f. is also given. The Weibull distribution best fits the data for cellulose paper under these experimental conditions.

Column 6 of Table 3-VIII indicates the type of statistical distribution for each of the dielectric materials tested at 12 K under 1.38 MPa of helium pressure. No single distribution appears to be favored over the others. Six

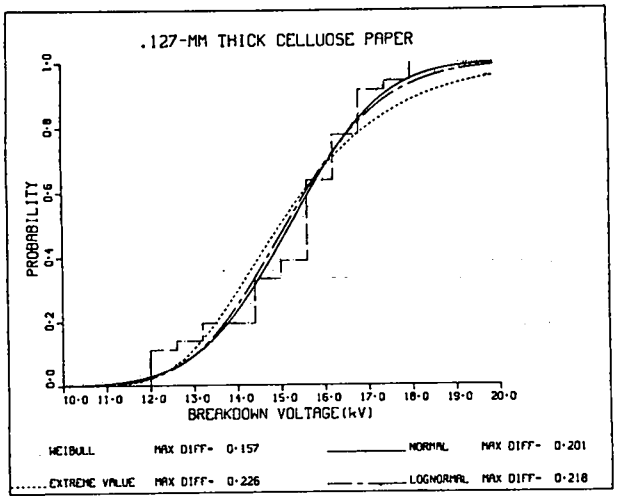

Fig. 3-30.
Comparison of sample breakdown voltage cumulative distribution function (c.d.f.) with four types of c.d.f.'s. Two layers of 127-μm-thick cellulose paper at 12 K and 1.38 MPa of helium.

of the 14 materials experienced both puncture and flashover. Perhaps no c.d.f. should have been tried; however, data for the eight materials that experienced 100% puncture also failed to support any particular type of c.d.f. Considerably more work needs to be done before anything definitive can be stated concerning the statistical distribution of breakdown.

A common mistake in data analysis is to attempt to determine the probability distribution of a universe from which a sample was taken by simply examining frequency distributions, histograms, or plots on various types of probability paper. A simple computer simulation exercise was conducted to illustrate this point. Pseudorandom samples of sizes 20, 36, 50, and 100 were taken from Gaussian distributions with standard deviations of 2.0, 4.0, and 6.0. Ten replications were made for each situation and histograms drawn for each replication. The histograms for standard deviation of 4.0 are shown in Figs. 3-31 through 3-34. The purpose of these figures is simply to show that even though samples are taken from a known distribution (Gaussian for this example) we are likely to observe sample distributions bearing little resemblance to the parent distribution. For example, 4 of the 10 histograms in Fig. 3-31 are not even approximately bell-shaped.

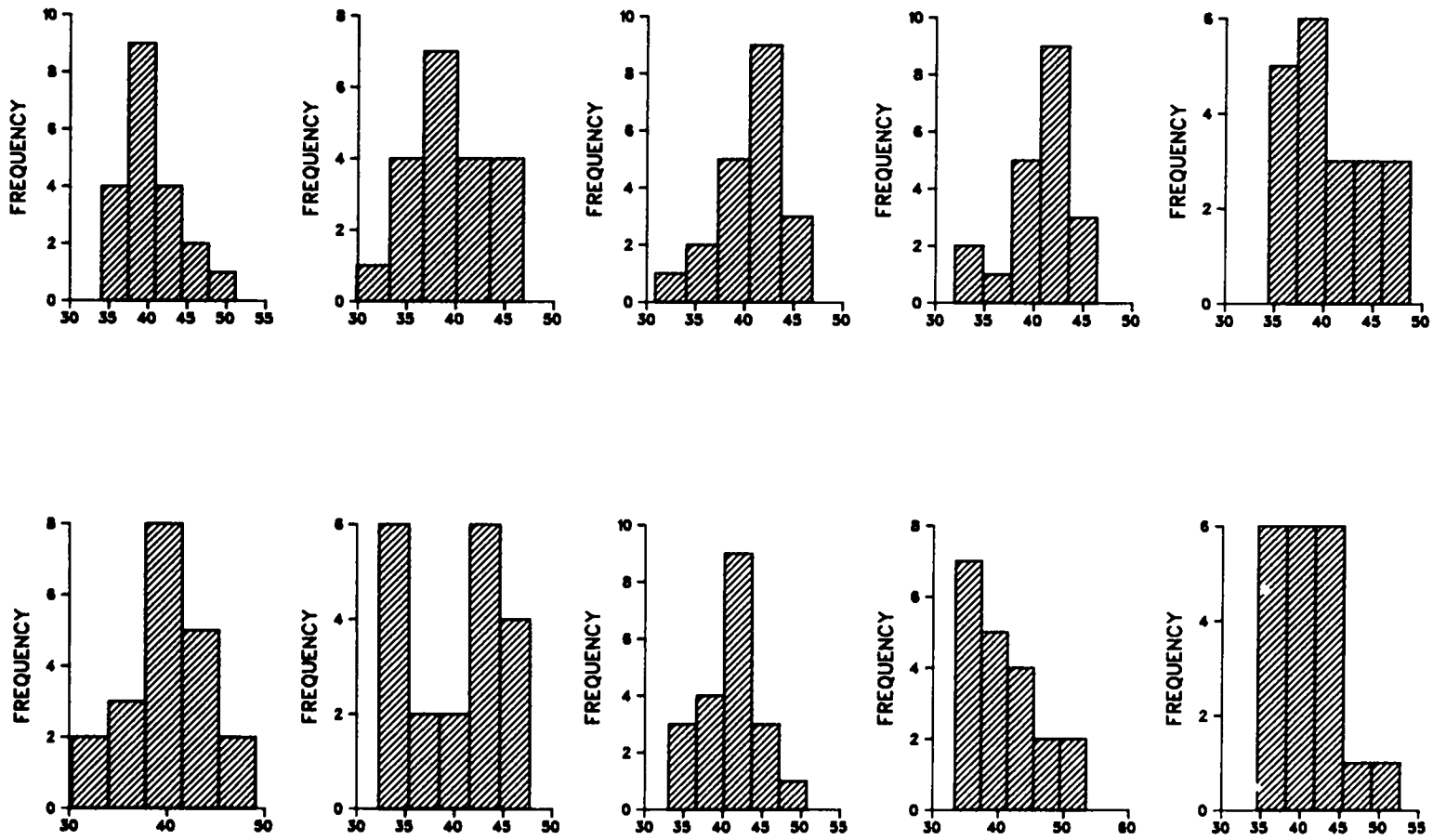

Fig. 3-31.
Ten independent histograms of randomly generated samples from a Gaussian distribution.
Sample size = 20, standard deviation = 4.0.

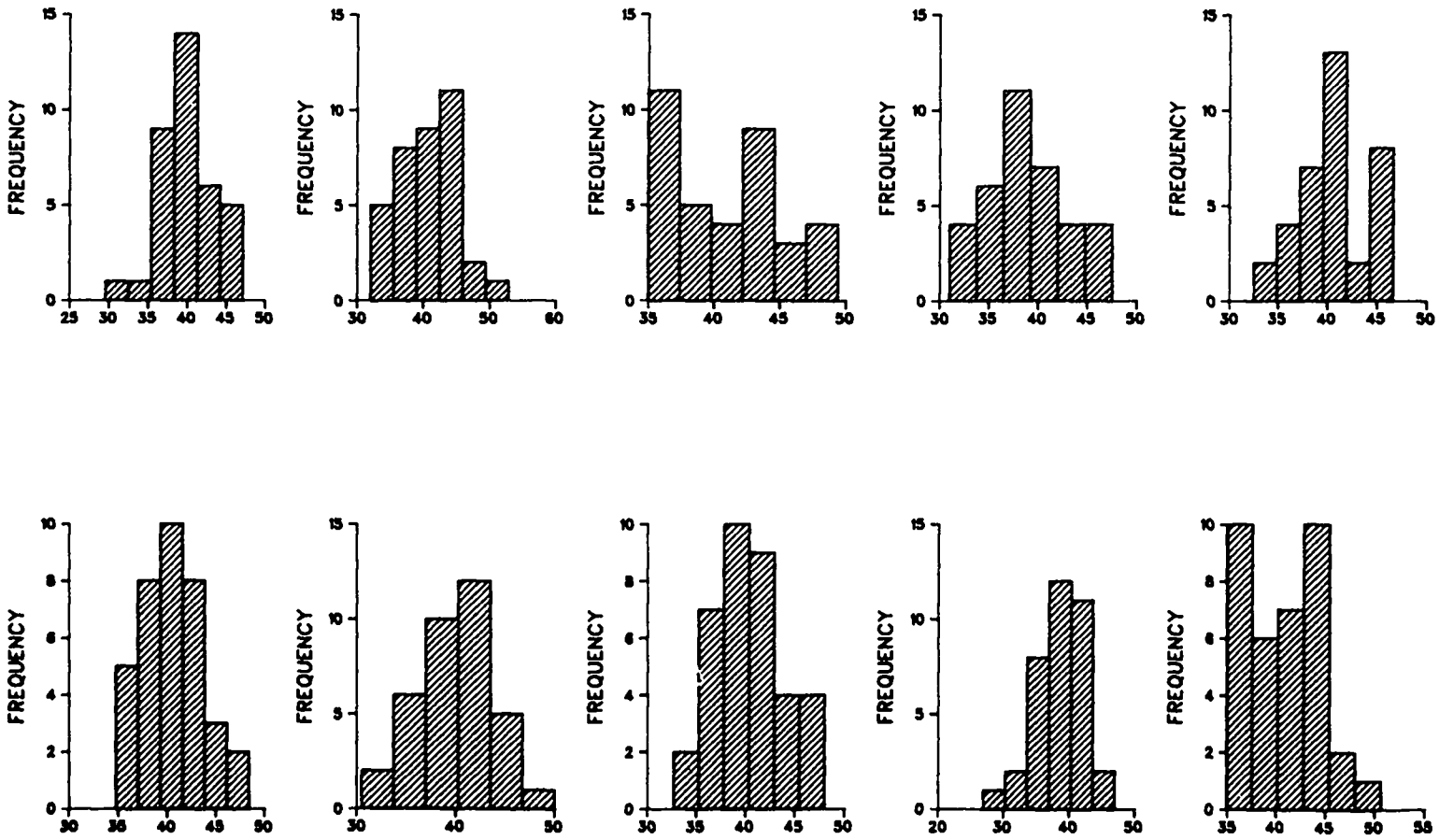

Fig. 3-32.
Ten independent histograms of randomly generated samples from a Gaussian distribution. Sample size = 36; standard deviation = 4.0.

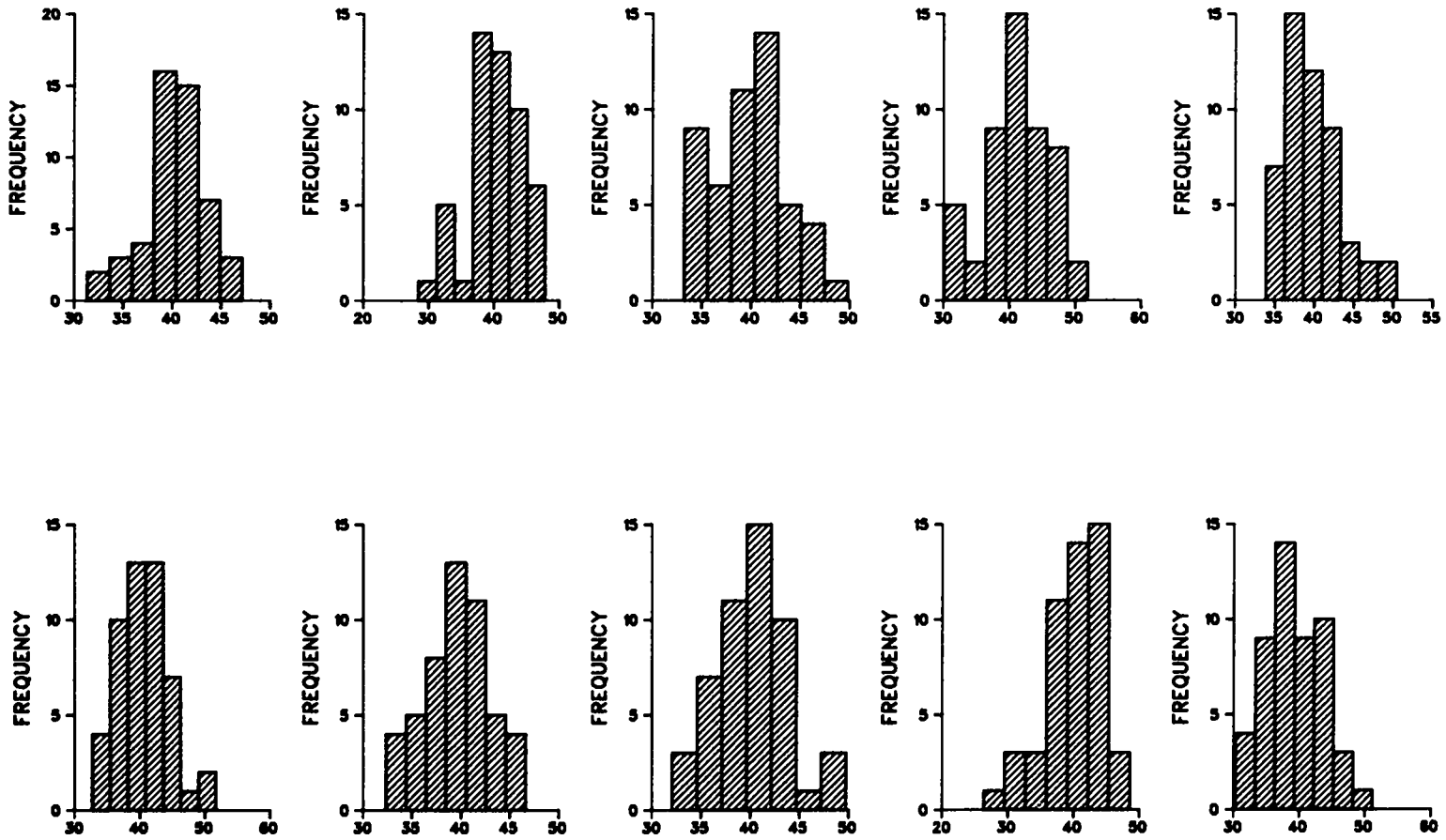

Fig. 3-33.
Ten independent histograms of randomly generated samples from a Gaussian distribution.
Sample size = 50; standard deviation = 4.0.

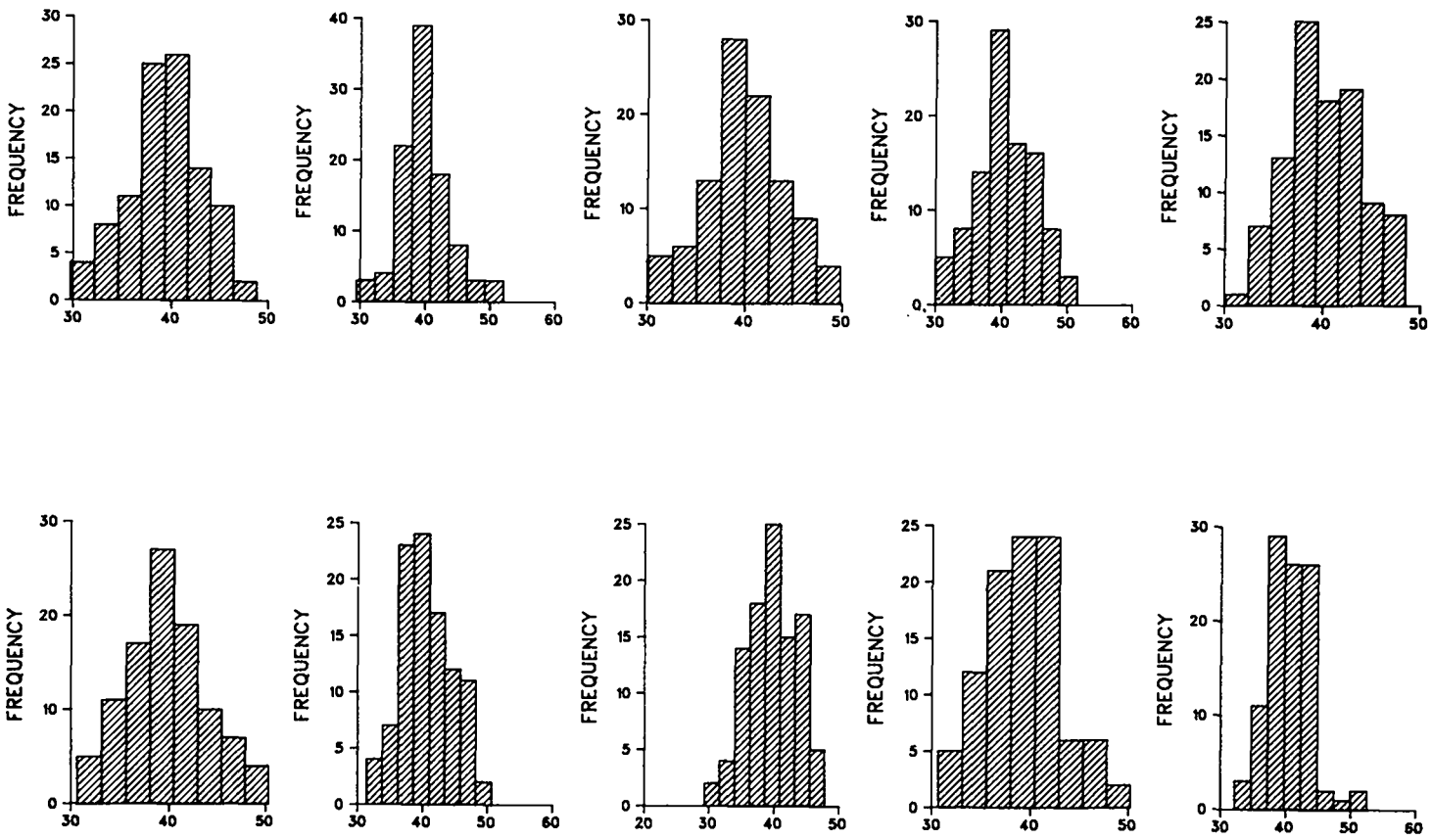

Fig. 3-34.
Ten independent histograms of randomly generated samples from a Gaussian distribution. Sample size = 100; standard deviation = 4.0.

The effects of temperature and pressure on the breakdown voltage for five selected materials (Figs. 3-35 and 3-36) were studied. For cellulose paper (with and without impregnation with Univolt 60) and PP/C, dependence of puncture breakdown on temperature followed the relationship,

$$E = E_0 \exp(a/T) \quad , \tag{3-35}$$

where E = breakdown electric field (kV/mm), T = temperature (K), and E_0 and a are constants. For these three materials, E_0 and a were computed and the values are shown in Table 3-XV. For Pink Poly and Valeron, the breakdown electric field increased to a peak at 83 K. The reason for such abnormal behavior is not readily understood. Because the data were taken at only three temperatures, neither the exact temperature at which the peak occurred nor the magnitude of the peak electrical strength could be obtained. However, a peak electrical strength certainly exists for Pink Poly and Valeron. In computing the data for Figs. 3-35 and 3-36, only the puncture breakdown values were considered for those cases where 50% or more of the breakdowns were caused by puncture. For those cases where 50% or more of the breakdowns were caused by surface flashovers, all numerical results, including puncture and surface flashover, were considered and the assumption made that the average of puncture breakdown would be higher than that shown.

Higher pressure generally increased the breakdown strength of a material. For cellulose paper and PP/C, this effect can be explained by considering the porous nature of a cellulose paper matrix (Fig. 3-37); helium gas at higher pressure in the pores of the material matrix would improve breakdown strength. For plastic materials (Fig. 3-38), there are two possible reasons for this apparent improvement in breakdown strength. Two sheets of the dielectric material were used as the test samples. Because helium gas was trapped between the two sheets, higher gas pressure should have improved the breakdown strength. In addition, surface flashover should have prevented puncture for some of the plastic materials. As pressure increased, flashover strength improved, and the apparent breakdown strength of the plastic materials showed higher values at high pressures.

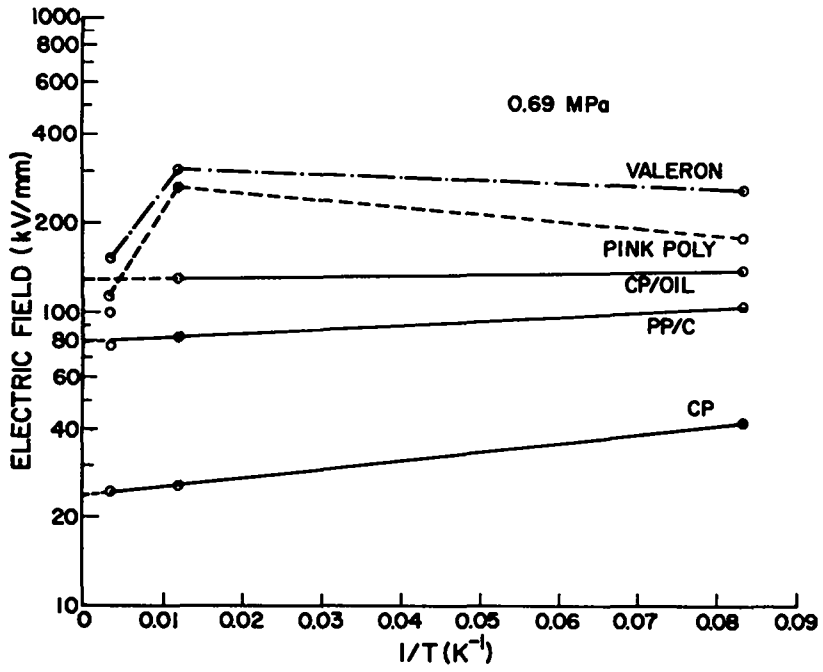

Fig. 3-35.
Relationship between breakdown electric field and temperature for five dielectric materials at 0.69 MPa of helium.

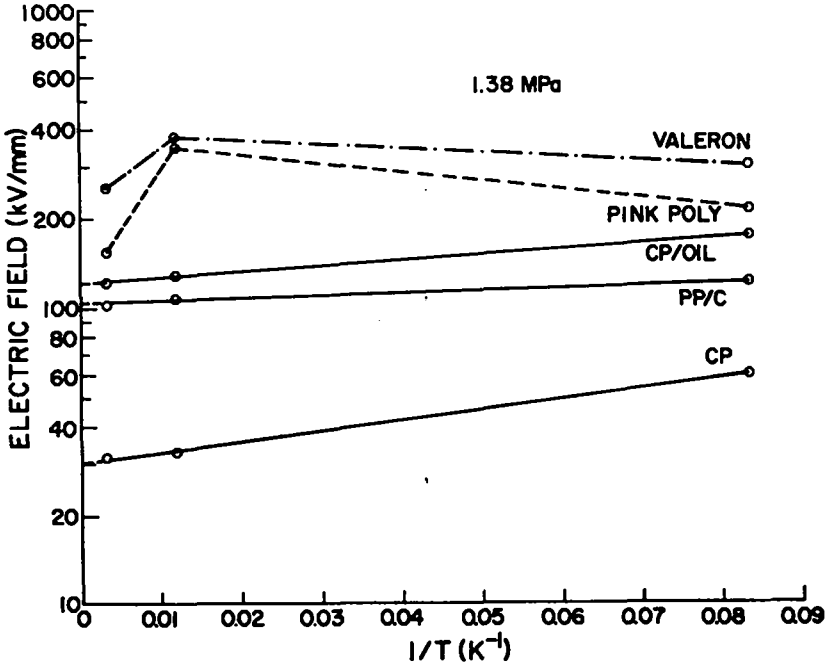

Fig. 3-36.
Relationship between breakdown electric field and temperature for five dielectric materials at 1.38 MPa of helium.

TABLE 3-XV

PARAMETERS FOR $E = E_0 \exp(a/T)$

Material	Pressure (MPa)	E_0 (kV/mm)	a (K)
Cellulose Paper	0.69	23.8	6.80
Cellulose Paper	1.38	30.1	8.27
Oil-Impregnated Cellulose Paper	0.69	129.0	0.89
Oil-Impregnated Cellulose Paper	1.38	122.0	4.26
PP/C	0.69	79.0	3.32
PP/C	1.38	104.5	1.89

Fig. 3-37.
Photograph (by scanning electron microscope) of cellulose paper (400x).

Fig. 3-38.
Photograph (by scanning electron microscope) of Pink Poly (400x).

Two discrepancies in the collected data should be noted. At 18 K, Pink Poly has a higher average breakdown voltage (47.30 kV) at 0.69 MPa of helium than that (44.30 kV) at 1.38 MPa (Table 3-X). We obtained similar results by repeating these two sets of tests. Similarly, Copaco paper, without oil impregnation at 298 K, had a higher averge breakdown voltage (12.30 kV) at 0.69-MPa helium than that (11.33 kV) at 1.38 MPa (Tables 3-XII and 3-XIV).

3.2.2. Cable-Sample Tests. On the basis of the results of the screening tests, we selected five dielectric materials for further testing in actual

cable configuration. The criteria for selection included high electrical breakdown strength and minimal surface discharges. These materials were cellulose paper, Copaco paper, Pink Poly, PP/C, and Valeron. Although cellulose paper showed the lowest breakdown strength, it was selected because it is the standard dielectric material for high-voltage cables. Pink Poly was tested at the Brookhaven National Laboratory (BNL) for its mechanical properties, where BNL researchers found that Pink Poly would not be suitable as a lapped dielectric for cables. PP/C tapes in small quantities could not be obtained from the vendor. The manufacturer of Valeron has stopped further production.

We originally planned to reduce the number of candidate dielectric materials based on the data from the dielectric screening tests. An extensive test program was planned with these few selected dielectric materials in tapes (cable samples) to determine the effects of length of cable (5 cm, 50 cm, and 500 cm), type (dc, impulse, switching surge and polarity reversal) and duration of dc voltage on the dielectric breakdown strength of the dc SPTL. We also planned to study the effects of dc corona in the operation of dc SPTL. A high-voltage cryostat was built to test cable samples up to the limits of our high voltage laboratory (300 kV dc). However, the program had to be rescheduled because of the early termination of the dc SPTL program. To compile meaningful data within a year's time, tests were continued in the original cryostat (Fig. 3-24), which was not suitable for operation above 100 kV. Only one length (10 cm) of the cable sample was selected for tests, and most of the tests were performed with negative impulse (1.2 x 50-μs) voltage waves.

3.2.2.1. Dielectric Specimens. Five of the 12 dielectric materials (Table 3-VII) were selected for tests on cable samples: 76.2-μm thick cellulose paper, 127-μm thick cellulose paper, 127-μm thick Copaco paper, 76.2-μm thick Mylar and 101.6-μm thick Pink Poly. Tapes (2.54-cm wide) of these materials were procured for the tests.

Our data from the dielectric screening tests showed that Mylar and Pink Poly have much higher electrical strength than the other three selected materials. However, cables manufactured purely from plastic tapes will have mechanical constraints in their bending ability. In order to maximize the electrical strength and to minimize the mechanical constraint, we decided to run a few experiments with cable samples in which the dielectric is built up from

one layer of plastic tape imbedded in several layers of 127-μm thick cellulose paper. The ratio of the thickness between cellulose paper and plastic tapes was varied to determine its effect on the electrical breakdown strength of the cable samples.

3.2.2.2. Preparation of Cable Samples. The dielectric tapes were first cleaned by a comercial dielectric tape cleaner, which directed ionized air onto the tape surface to loosen charged dirt particles; the tape surface was then brushed and the loosened dirt removed by a vacuum system.

The cable samples were then made by wrapping the dielectric tapes on a 4.45-cm o.d. aluminum tube, with 3.18 mm butt gaps and a registration of 33/67. A total of 32 to 34 layers of the 76.2-μm-thick dielectric tape were applied to complete the sample; similarly, 18 to 19 layers in the case of the 127-μm-thick dielectric tapes. Two layers of 127-μm-thick and 2.54-cm-wide carbon-black tapes were used as the ground shield. No conductor shield was used (except for a few cases) because the 4.45-cm-o.d. aluminum tube was polished and cleaned to provide a smooth surface before the dielectric tape was wrapped around it. An aluminum foil was tightly wrapped around the carbon-black paper (ground shield). Each cable sample was nominally 10-cm long, along which the thickness of the dielectric build-up was uniform. Cloth-based phenolic stress cones, machined to a log-log contour, were fitted to both ends of the 10-cm-long cable sample to prevent axial flashover. A four-section aluminum ground electrode was then fitted on to the cable sample, including the stress cones. The combination of ground electrode and the stress cones was designed to a specification of 1 kV/mm axial stress along the stress cones and 12.5 kV/mm stress in the surrounding helium at an applied voltage of 100 kV. The design is described in Section 3.4.3 Figure 3-39 shows the various parts of the cable sample, and Fig. 3-40 shows the completed sample being lowered into the cryostat.

3.2.2.3. Test Parameters. Preliminary tests showed that the cable samples at 12 K and 1.38 MPa of helium pressure have lower dielectric strength under negative impulse (1.2 x 50-μs) voltage waves than under dc voltage. Hence, most of the tests were performed with negative impulse voltages. The tests were later extended to 83 K and 298 K, at 1.38 MPa of helium pressure. Tables 3-XVI and 3-XVII show the summary of the test results with cellulose papers and Copaco paper. Tables 3-XVIII and 3-XIX show the results with composite dielectric materials (cellulose paper/Mylar and cellulose paper/Pink Poly) mixed in various proportions.

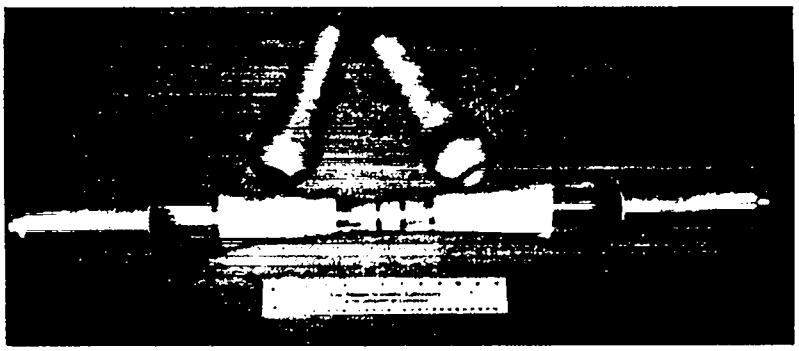

Fig. 3-39.
Parts of cable sample during manufacture.

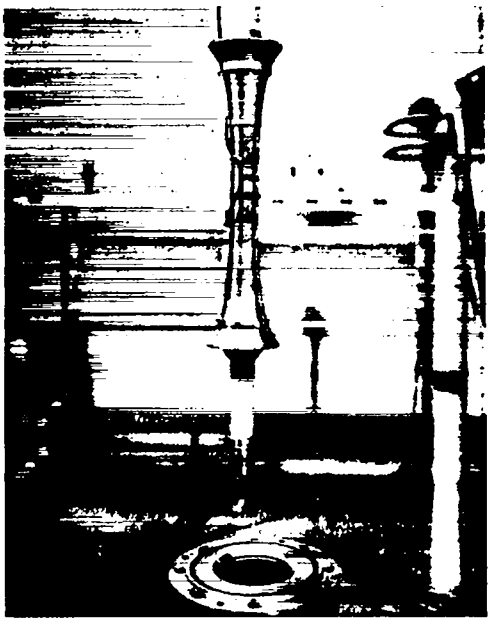

Fig. 3-40.
Cable sample being lowered into cryostat.

3.2.2.4. Analysis and Discussion: Our results of the cable-sample tests corroborate qualitatively the results of the dielectric screening tests; the 127-μm Copaco paper has the highest dielectric strength and the 127-μm cellulose paper the lowest when compared among the two cellulose papers and the Copaco paper. However, the dielectric screening tests showed that Copaco paper had significantly higher strength than the 76.2-μm cellulose paper, whereas the cable-sample tests showed that this difference is marginal. Another difference between the two test series is that the dielectric strengths

TABLE 3-XVI

IMPULSE BREAKDOWN STRENGTH OF CABLE SAMPLES UNDER NEGATIVE-POLARITY IMPULSE OF 1.2 x 50-μs WAVESHAPE: PRESSURE = 1.38 MPa OF HELIUM; NUMBER OF REPLICATIONS = 5

Material	Impulse Breakdown Strength (kV/mm)*		
	12 K	83 K	298 K
76.2-μm Cellulose paper	52.04	28.53	20.30
	4.95	2.25	0.72
	46.91	24.73	19.23
172-μm Cellulose paper	40.74	21.91	14.50
	1.71	1.18	1.14
	38.64	20.13	12.66
127-μm Copaco paper	54.63	36.39	23.06
	2.08	1.26	0.60
	48.11	35.28	22.57

*The three figures for each entry represent, in order, average value, standard deviation, and lowest value.

TABLE 3-XVII

DC BREAKDOWN STRENGTH OF CABLE SAMPLES UNDER NEGATIVE POLARITY, AT A HELIUM PRESSURE OF 1.38 MPa AND A TEMPERATURE OF 12 K

Material	Mean kV/mm	Lowest Value kV/mm	Stand. Dev. kV/mm	No. of Measurements
76.2-μm Cellulose paper	62.70	56.67	8.53	2
127-μm Cellulose paper	43.52	39.42	3.44	5
127-μm Copaco paper	62.86*	-	-	1

*Two other attempts resulted in breakdown under the stress cones at stresses of 56.79 and 59.29 kV/mm, respectively.

TABLE 3-XVIII

BREAKDOWN STRENGTH OF CABLE SAMPLES COMPRISING MIXTURE OF 127-μm CELLULOSE PAPER AND 76.2-μm MYLAR TAPES AT 12 K AND 1.38 MPa OF HELIUM PRESSURE

Type of Voltage	Ratio of Thickness (mm) Cellulose Paper/Mylar	Breakdown Strength kV/mm
Negative Impulse	2.286/0.152	40.72[1]
	1.778/0.381	45.67[1]
	1.905/0.457	44.37[1]
	1.778/0.610	47.63[1]
Negative DC	2.032/0.381	45.84[1]
	1.397/0.914	65.49[2]

1. Broke within cable section
2. Broke inside a stress cone

TABLE 3-XIX

BREAKDOWN STRENGTH OF CABLE SAMPLES COMPRISING MIXTURE OF 127-μm CELLULOSE PAPER AND 101.6-μm PINK POLY TAPES AT 12 K AND 1.38 MPa OF HELIUM PRESSURE

Type of Voltage	Ratio of Thickness (mm) Cellulose Paper/Pink Poly	Breakdown Strength kV/mm
Negative Impulse	2.286/0.203	39.63[1]
	1.905/0.508	39.03[1]
	1.905/0.508	40.82[1]
	1.651/0.508	43.10[1]
	1.778/0.711	48.96[2]
Negative DC	1.905/0.508	45.84[2]

1. Broke within cable section
2. Broke inside a stress cone

of all the three materials are significantly lower for the cable-sample tests than those for the screening tests. This was expected; thicker dielectrics and butt gaps reduce the dielectric strength of a material.

It is of interest to note that the impulse breakdown strengths of the dielectric materials were lower than their dc breakdown strengths at 12 K and 1.38 MPa of helium pressure. Similar observations were made previously by Hossam-Eldin and Salvage in a study of oil-impregnated paper cable at liquid-nitrogen temperature.[24]

The dependence on temperature of impulse breakdown strength of the cable samples with cellulose and Copaco papers was found to follow the relationship (Fig. 3-41):

$$E = E'_0(1/T)^b \ , \tag{3-36}$$

where E = impulse breakdown strength (kV/mm), T = temperature in Kelvin (K), and E'_0 and b are constants. This is somewhat different from the relationship found in the dielectric screening tests for uniform dc electric fields (Eq. 3-35, Figs. 3-35 and 3-36). The computed values of E'_0 and b are shown in Table 3-XX.

Unfortunately, the relationship E vs (1/T) could not be determined for the cable samples under dc stress because of heavy partial discharges at higher temperatures.

In order to increase the electrical strength of the dielectric without being limited by the mechanical inflexibility of plastic-tape cables, we built up the layered dielectric by composite dielectrics made up of one layer of Mylar or Pink Poly and several layers of 127-μm cellulose paper. The ratio of cellulose paper to plastic tapes was varied to observe the effect on the

TABLE 3-XX

PARAMETERS FOR $E = E'_0(1/T)^b$

Material	E'_0	b
76.2-μm Cellulose paper	110.31	0.30
127-μm Cellulose paper	90.40	0.32
127-μm Copaco paper	116.26	0.26

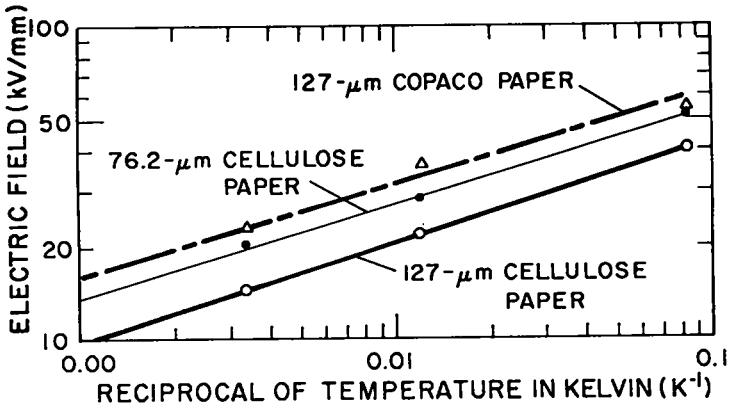

Fig. 3-41.
Relationship between impulse breakdown electric field and temperature for cable samples at 1.38 MPa of helium pressure.

electrical breakdown strength. Tables 3-XVIII and 3-XIX show a trend towards higher electrical strength as the proportion of the plastic tape was increased. The limitations were the cryostat and the stress cones. The stress cones were designed for 100 kV operation. The tests were pushed upwards to 160 kV. We believe that by mixing Mylar or Pink Poly tapes with 76.2-μm cellulose paper tape a breakdown strength of 70 kV/mm can be achieved at 12 K and 1.38 MPa of helium pressure. Finally, PP/C is another material which shows promise for applications in a dc superconducting cable.

3.2.3. Electrical Resistivity Measurement.

The steady-state voltage of a dc cable is distributed across its dielectric system in direct proportion to the volume resistances of the various dielectric components. Hence, it is necessary to know the electrical resistivities of the dielectric materials to be used in a new system. We decided to measure the electrical resistivity of several candidates for dielectric materials in the dc SPTL program because such data at cryogenic temperatures were not available. The measurements were performed on four types of dielectric materials: 76.2 μm-thick Mylar (DuPont); 76.2-μm thick high-density cellulose paper (Crocker); 127-μm-thick cellulose paper (Crocker); 127-μm-thick Copaco paper (Cottrell).

3.2.3.1. Experimental Procedure. Electrodes were made on a 30.48-cm x 34.93-cm sheet of the dielectric material by spraying a 19.69-cm x 24.13-cm rectangular area with silver paint. The guard electrode was similarly painted on a 2.54-cm wide rectangular strip of the sheet surrounding the main electrode

on the low-voltage side of the sheet. The outer edge of the main electrode and the inner edge of the guard electrode were separated by a 6.35-mm wide surface of the dielectric material on all four sides. The sample was then tightly wrapped around a stainless steel cylinder, which served as the high-voltage terminal. The stainless steel cylinder was then screwed on to the lower end of a bushing and lowered into the cryostat. The guard electrode was connected to the cryostat wall. The signal from the low voltage main electrode was brought outside through an air-insulated coaxial cable to minimize extraneous leakage. The experimental set-up is shown in Fig. 3-42.

The dielectric samples were stored in the sample preparation room where the relative humidity was between 40 to 50 per cent. Cellulose paper and Copaco paper being hygroscopic, the samples, after being prepared, were evacuated overnight inside the cryostat at an ambient temperature of about 33^{o}C. The cryostat was then filled with helium at 1.38 MPa of pressure, and a dc voltage of +218 volts (three 67.5-volt batteries connected in series) was applied. The leakage current was measured 1 h after voltage was first applied. The cryostat was then cooled by liquid nitrogen while the voltage was kept on. The leakage current was measured at several temperatures during the cool-down process.

An electrometer (Keithley model 642) was mostly used to measure the leakage current. A micro-ammeter (RCA type WV-84C) was used at higher temperatures when the leakage current was beyond the range of the electrometer. Table 3-XXI shows the summary of results.

3.2.3.2. Analysis and Discussion. The meter readings fluctuated widely at lower temperatures. An average was taken from these readings. These fluctuations may be caused by even a slight motion or vibration within the measuring system. This vibration might have come from the pumps for the vacuum jacket of the cryostat. The vacuum pumps were mounted on the same structure as the cryostat for the sake of compactness and mobility.

The electrical resistivity was plotted against temperature on semi-log paper (Fig. 3-43). For the cellulose papers and the Copaco paper, the relationship follows a straight line at higher temperatures; the slope changes abruptly at a critical temperature. For Mylar, no straight-line relationship was observed within the range of temperatures used for the experiment.

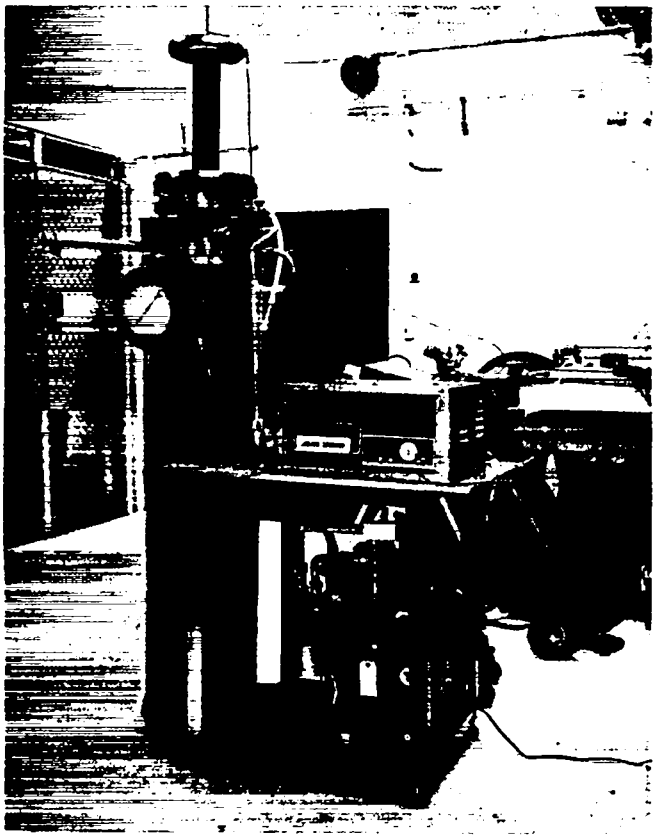

Fig. 3-42.
Photograph of experimental set-up for electrical resistivity measurement at low temperatures.

TABLE 3-XXI

ELECTRICAL RESISTIVITY OF DIELECTRIC MATERIALS

76.2-μm Mylar		76.2-μm Cellulose Paper		127-μm Cellulose Paper		127-μm Copaco Paper	
Temperature	Resistivity	Temperature	Resistivity	Temperature	Resistivity	Temperature	Resistivity
K	Ω-cm	K	Ω-cm	K	Ω-cm	K	Ω-cm
297.56	4.25×10^{18}	299.34	2.09×10^{14}	296.88	8.58×10^{16}	296.63	9.71×10^{12}
166.23	1.36×10^{18}	277.10	1.36×10^{16}	283.23	8.96×10^{17}	281.97	1.46×10^{14}
88.67	9.06×10^{19}	273.00	3.40×10^{16}	273.00	2.72×10^{18}	273.18	6.27×10^{14}
		120.18	6.79×10^{17}	159.52	8.15×10^{18}	230.83	2.72×10^{18}
		88.72	4.53×10^{19}	88.72	2.72×10^{19}	171.89	5.44×10^{18}
						88.78	1.63×10^{19}

Note: DC voltage = +218 V, supplied from three series-connected 67.5-V batteries.

The straight-line part of the electrical resistivity vs. temperature, follows the equation:

$$\rho = \rho_0 \exp(-\alpha T) \tag{3-37}$$

where ρ = electrical resistivity at temperature T ($\Omega \cdot$ cm), and ρ_0 and α are constants. The constants ρ_0 and α were evaluated, as shown in Table 3-XXII.

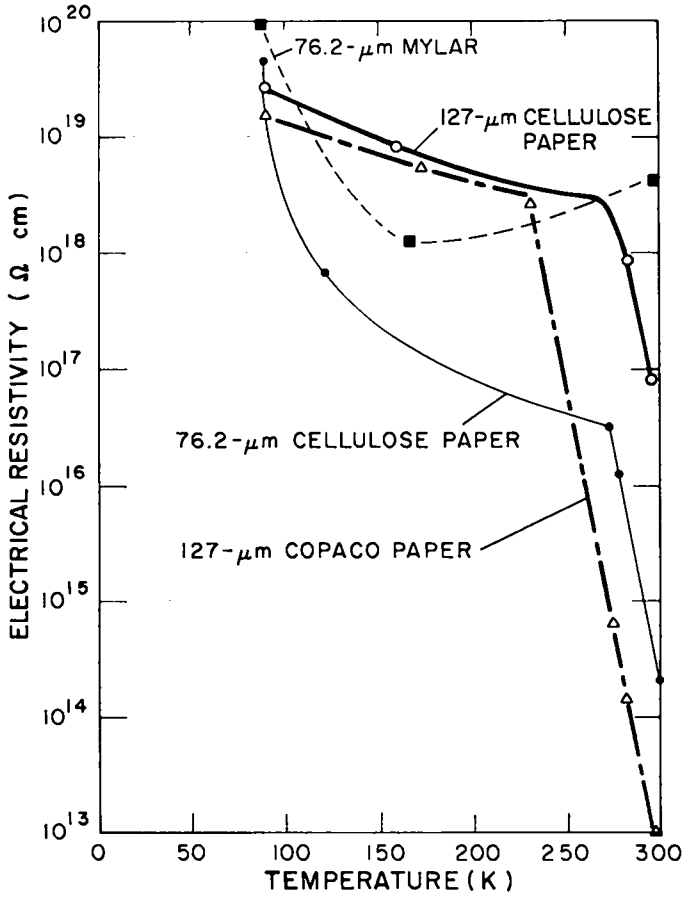

Fig. 3-43.
Variation of electrical resistivity with temperature for four dielectric materials.

TABLE 3-XXII

PARAMETERS FOR $\rho = \rho_0 \exp(-\alpha T)$

Material	ρ_0	α	Electric Field, kV/mm
76.2-μm Cellulose Paper	2.82×10^{39}	0.193	2.86
127-μm Cellulose Paper	3.93×10^{35}	0.145	1.72
127-μm Copaco Paper	7.64×10^{35}	0.178	1.72

It should be noticed that the effect of electrical field on the electrical resistivity has been neglected. The magnitude of ρ_0 is dependent on electric field; however, the magnitude of α should be invariant. The values of α, as measured by us, are higher than those published, e.g., 0.1 in Ref. 27 and 0.083 to 0.103 in Ref. 28. However, the published data pertain to cable models wrapped with oil-impregnated cellulose paper tape.

3.3. Bushing Development.

A high-voltage termination for operation at cryogenic temperatures and at high pressures is a critical item for the success of the dc SPTL program. A 100-kV bushing was required for the initial dielectric screening tests, and a 300-kV bushing for cable sample tests and tests on cable splices, stress cones, etc. In the future, high-current, high-voltage terminations would be required for the dc SPTL. The design criteria of such a termination will be based on the requirements that:

1. it shall withstand the rated dc voltage continuosly, and transient overvoltages occasionally,
2. it shall also withstand thermal stresses, axially and radially,
3. heat leak through the termination be minimum, and
4. all its constituents shall withstand severe thermal cycling, from 12 K to ambient temperature, without mechanical or structural failure.

Because no such terminations were commercially available, an in-house development program was initiated. The high voltage test facility is described in Sec. 3.5.

3.3.1. 100-kV Bushing Development. Because this bushing was of immediate need, two parallel approaches were pursued:

1. Fiber-glass reinforced plastic (FRP) bushing, and
2. Epoxy bushing.

3.3.1.1. FRP Bushing. The design details of this bushing are shown in Fig. 3-25. A photograph is shown in Fig. 3-44. This bushing was tested at a pressure of 311 psia (2.14 MPa); it also passed a 15-min voltage withstand test at 105 kV dc with each polarity.

The pressure containment was accomplished by a 1-in. (25.4-mm) thick G-10 (glass-reinforced epoxy) flange. A 4.5-in. (114.3-mm) o.d. x 3/16-inch (4.76-mm) wall G-10 tube penetrates through the G-10 flange and is held in place with epoxy. A 25.4-mm thick G-10 plug is both epoxy-glued and pegged into the end of the G-10 pipe.

The electrical design was based on the fact that the electrically weakest area will be near the flange, which will be approximately at room temperature. It was set as a design goal that the working electrical stresses in Mylar and helium (at room temperature) should not exceed 8 kV/mm and 3 kV/mm, respectively. The cylindrical ground surface of the bushing was 4.5 in. (11.43 cm) in diameter, which was limited by the inner diameter of the Dewar wall. The electrical stress relief was mainly accomplished by tightly rolling 10-mil (0.25-mm) Mylar sheets over the center conductor made of a stainless steel tube. The build-up of the Mylar was such that it would fit tightly into the cylindrical ground surface made up of the 11.43-cm stainless steel tube. In spite of the tight fit of the Mylar roll inside the grounded stainless steel tube, it was realized that there will inevitably be a very

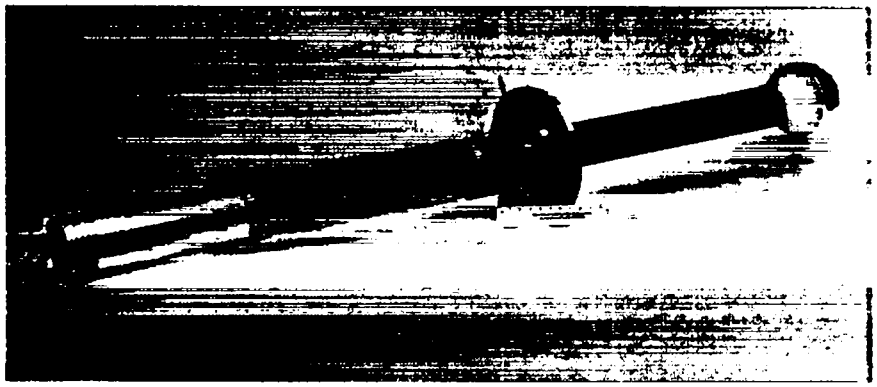

Fig. 3-44.
100-kV FRP bushing.

small helium-gas gap in between. The diameter (12.7 mm) of the center conductor was selected such that the electrical stress across the room-temperature helium near the ground surface was within the allowable limit of 3 kV/mm. The following equations were used to calculate the electrical stresses:

$$E_1 = \frac{V}{r_1[K\ell n\ (r_3/r_2) + \ell n\ (r_2/r_1)]} \tag{3-36}$$

and

$$E_2 = KE_1\ (r_1/r_2)\ , \tag{3-37}$$

where E_1 = electrical stresses on the surface of inner conductor (in Mylar); E_2 = electrical stress on the outer surface of Mylar roll (in helium); V = applied voltage; r_1 = radius of inner conductor; r_2 = radius of Mylar roll; r_3 = radius of ground cylinder; and K = dielectric constant of Mylar. For the calculations, it was assumed that V = 100 KV, $r_2 = r_3 = 52.3$ mm, and K = 3.25. r_1 was taken as a variable to calculate the minimum stress. A value of $r_1 = 6.35$ mm was finally chosen to produce $E_1 = 7.46$ kV/mm and $E_2 = 2.94$ kV/mm, which are within the set design limits.

Ground planes were painted on the surface of paper-phenolic pieces which were shaped appropriately for corona shielding. Silver epoxy was judged to be much superior to silver paint for this purpose; silver paint flakes off in a cryogenic environment and is damaged easily by abrasion. The epoxy also makes strong structural joints; two such joints are where the stainless steel tube is joined to the G-10 tube and where the ground plane is extended from the stainless steel tube out to the dewar wall.

The phenolic support piece (actually concentric paper-phenolic tubes epoxied to a 12.7-mm-thick phenolic disk) serves two functions. It centers the test fixture in he test chamber and provides a long creep path to the test chamber wall. Since the insulation in the test chamber is gas only, Mylar is wrapped around the upper part of the test fixture to suppress any corona at this point. The electrical strength of the bushing has been tested to 105 kV dc of both polarities with no breakdown or apparent corona.

The cryogenic thermal qualities of the bushing have not been tested quantitatively, but Mylar has a lower thermal conductivity than any of the cryogenic epoxies. The bushing has been regularly used for the dielectric screening tests as well as the cable-sample tests; thus, it has been subjected to hundreds of thermal cycles from room temperature to 12 K at 1.38 MPa of helium pressure. It has not shown any problem in cooling down or any external frosting. There is reason to believe that this bushing would have superior cryogenic properties compared to an epoxy bushing constructed to the same electrical specifications.

3.3.1.2. Epoxy Bushings. For corona-free testing of dielectric samples at cryogenic temperatures at high voltages, a Mylar-wrapped bushing would probably be inadequate because of the helium gas entrapped between the layers of Mylar. With an epoxy bushing, however, all gas can be excluded from the high-voltage stress field between the ground plane and the center conductor of the bushing. Two designs of epoxy bushings were investigated.

First Design. In this design, we used the low-viscosity, room-temperature cure system of catalyst 24 LV and epoxy 2850 FT, both manufactured by Emerson and Cumings. This epoxy system is known to have excellent high-voltage and low-temperature properties as well as a thermal expansion coefficient that matches that of aluminum below room temperature.

The design was based on calculations performed with a computer code, developed by R. Holsinger of LASL Group P-11, which computes the potential and electric field for two-dimensional and cylindrically symmetrical systems. It is also able to include dielectric constants other than unity. Design parameters were set to working stresses of 10 kV/mm on the helium gas at 20 atm (2 MPa) and 10 K, and the creepage stress along the epoxy-helium interface of 400 V/mm. The most difficult design parameter to achieve was the creepage limit with only a 5 3/4-in. (146-mm) bore available in the cryostat. The design, shown in Fig. 3-45, achieved the creepage parameter and was tailored to achieve the strike limit with the minimum amount of epoxy. Its construction involved an aluminum spinning, the contour of which produced the minimum surface electric field at the transition from ground plane to epoxy and was still thin enough to prevent serious heat leak to the cryogenic environment.

A vacuum-tight water-cooled mold system was fabricated to enable vacuum degassing of the epoxy-catalyst mix and also to prevent excessive temperature rise. Mixed epoxy was poured in 12 10-lb (4.5-kg) batches into the mold.

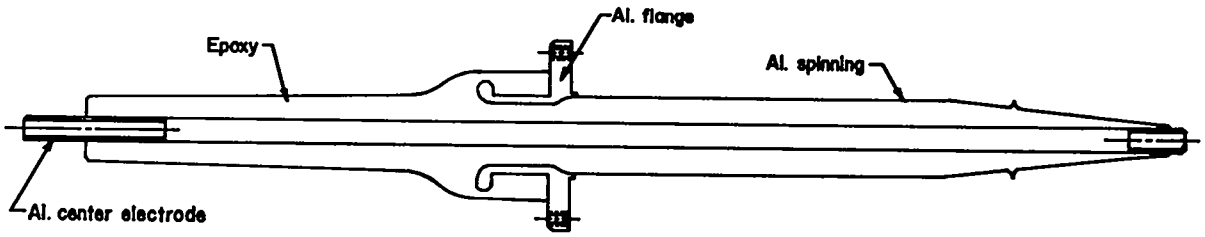

Fig. 3-45.
Outline drawing of the first design for the 100-kV epoxy bushing.

A radiograph of the casting showed numerous voids within the bulk of the bushing. It should be pointed out that the temperature of the epoxy mix rose to 95°C at several points on the outside surface as the epoxy cured. Since the recommended maximum temperature is near 50°C, it is estimated that the voids were formed because of this excessive temperature rise. As the sections cast were thick (5-8 cm), no additional cooling could have prevented thermal runaway; the heat transfer through the thickness of epoxy used was inadequate.

Second Design. Several innovations were incorporated in this second design of the epoxy bushing as a result of our previous experience in the design of epoxy bushings for operation at cryogenic temperatures.

Areas of concern in the construction of an epoxy bushing are:

1. The epoxy material must be compatible with cryogenic and high-voltage criteria;
2. The casting must be void-free; and
3. The integrity of the joints between epoxy and ground plane and high-voltage conducting surfaces must be maintained.

Several epoxy systems were screened for high-voltage reliability after thermal cycling. Two systems appeared to be acceptable. One system, a mixture of Shell Epon resins highly filled with powdered alumina is mechanically resilient, although difficult to prepare; the second system is Emerson Cumings Stycast 2850 FT blue. It was decided to cast the first sample with the Emerson Cumings resin as it has proven to be reliable in other cryogenic applications.

To insure void-free casting, we decided to vacuum outgas the epoxy in the mold and then to gel the epoxy on a slow cure schedule under pressure (0.69 MPa). To allow time for mixing, outgassing, and pressure cycling,

catalyst 11 (heat cure) was chosen. The resin was allowed to gel at room temperature (about 3 days) and then was postcured at 60°C.

During thermal cycling of epoxy test samples we discovered that even though the thermal expansion coefficients of epoxy and aluminum are matched closely, rates of cooling may not be matched. After cycling, the epoxy separated from the aluminum leaving a gas gap in the high-field epoxy-aluminum interface. This cannot be tolerated if we require a reliable, corona-free bushing. To remedy this fault, we decided to cast both high-voltage and ground planes in the body of the epoxy using a conductive cloth or screen. This makes a threefold improvement in the behavior of the epoxy bushing:

1. Electrically conductive cloth has lower thermal conductivity than aluminum, thus reducing heat leak to cryogenic environment;

2. Cool-down rate is determined almost entirely by epoxy, thus introducing less stress in the casting; and

3. Ground and high-voltage planes are cast in an epoxy matrix which precludes separation.

Other features of the bushing are:

1. To reduce overall height of the external standoff, the bushing has skirts. This would maintain adequate creep and flashover lengths.

2. Mounting hardware was not cast into the epoxy but was external and bolted on after casting, to reduce internal stresses in the casting. Figure 3-46 shows the outline drawing of this bushing, and Fig. 3-47 its photograph.

Each skirt was cast individually and checked for voids by radiography. The skirts were then cemented together and the rest of the bushing cast in one operation. The completed bushing was checked for voids by radiography. A void was found at the upper end. However, as this was shielded by the high-voltage terminal, no electric stress will exist within this void. Radiography also showed small cracks on each side of the casting near the epoxy-fill region adjacent to the ground-corona shield terminal.

This epoxy bushing was then subjected to thermal cycles and high-voltage dc tests. During the first cooling, we discovered a leak at the flange of the bushing. The leak was repaired after five cycles of cooling to 12 K at 1.38 MPa of helium pressure and subsequent warming to room temperature.

The Biddle balanced-bridge corona detector was used to monitor corona activities in the bushing. Because the test bushing was grounded directly to the cryostat, the corona detector was used in the single-ended mode, with the

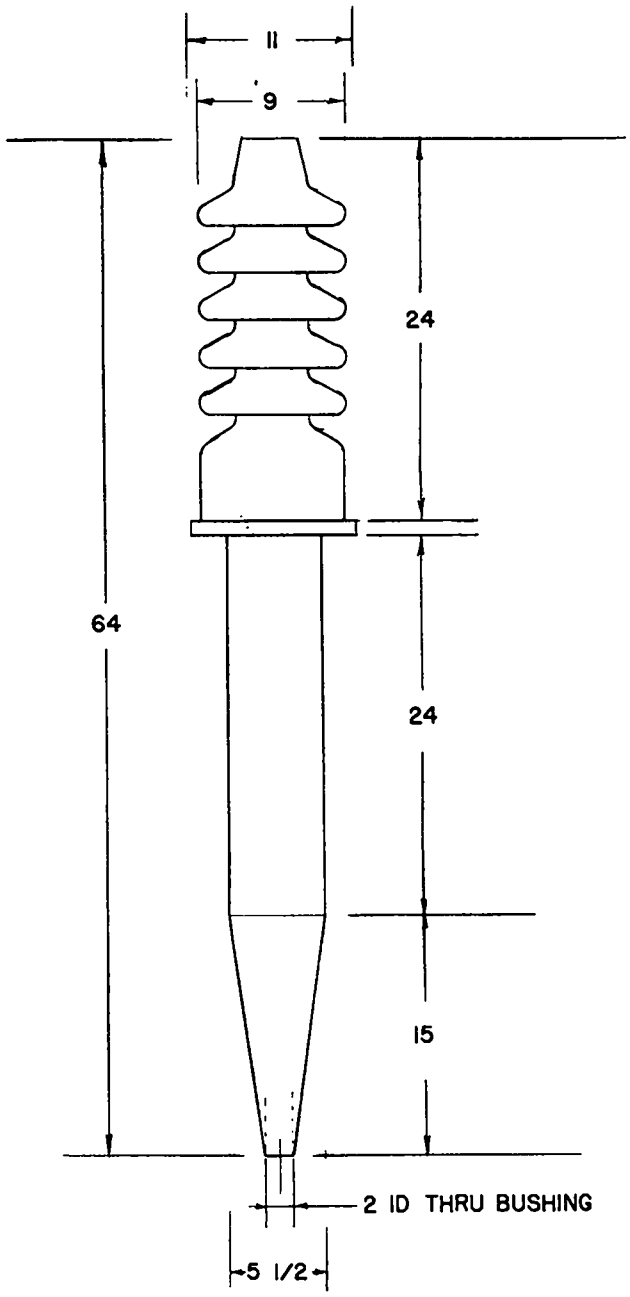

Fig. 3-46.
Outline drawing of the second design for the 100-kV epoxy bushing.

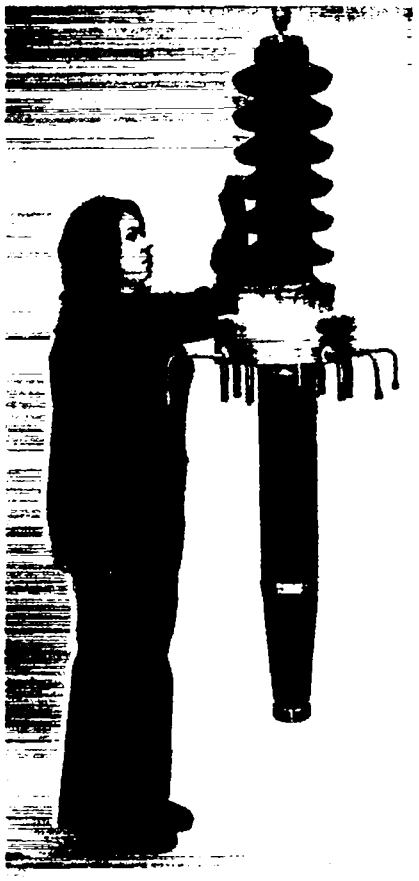

Fig. 3-47.
The 100-kV epoxy bushing.

corona signals taken from a tap on the 1000-pF filter capacitor of the high-voltage direct-current (HVDC) supply.

After the bushing was cooled to 12 K at 1.38 MPa of helium pressure, voltage was applied in steps and the corona activity monitored. After a few preliminary tests with both polarities of voltage, we decided that the negative-polarity voltage gives the lower breakdown results. Therefore, the final tests were performed with only the negative-polarity voltage.

During ramping (1 kV/s) of the voltage, we monitored a considerable amount of corona activity with the corona detector. This activity diminished when the voltage was held constant. Corona activity, in the form of occasional spikes, started at the 100-kV level. At the 201-kV level, the corona was continuous, and the temperature and the pressure of the cryostat began to rise. The voltage was held constant at 228-kV for 10 min; however, the temperature and the pressure rose so rapidly that the test had to be discontinued. The cryostat is too small to perform reliable tests above 100-kV dc.

It appears that the corona starts at the helium space between bushing and the cryostat wall; otherwise, the temperature and the pressure in the cryostat would not have risen. After being subjected to 40 more thermal cycles between liquid nitrogen temperature and room temperature, this bushing was installed in the cryostat for further voltage tests. The leak at the flange of the bushing reappeared but was repaired, following which the bushing was cooled to 12 K at 1.38 MPa of helium pressure. DC voltage was applied to

the bushing at 1 kV/sec rate up to 201 kV (each polarity) and held for 5 min. The negative-polarity voltage was then raised until the bushing flashed over outside at -255 kV. Similarly, the positive-polarity voltage was raised to +291 kV before the test was discontinued because of visible corona on the rope supporting the tubular bus to the bushing. It should be borne in mind that the elevation of LASL is about 3 km above sea level. The barametric pressure that day was 588.0 torr.

Impulse tests with 1.2 x 50-μs waves were then performed on the bushing at various temperatures and pressures. Table 3-XXIII shows the results.

3.3.2. Epoxy-Mylar Bushing. For operation at 300 kV or higher voltages, the dimensions of an epoxy bushing become large if the electric stress is kept below 8 kV/mm for reliable service. A large bushing will produce a heat leak to the cryostat because this bushing will have a relatively good thermal conductivity to prevent high thermal stresses across it. Bushings can be made from other dielectric materials, such as Mylar, Kapton, polyurethane, etc. Because these dielectric materials can withstand high electric stresses, the bushings made of these materials will have smaller dimensions. Since these bushings will be made of layers of these dielectric materials, helium gas will be trapped between layers, producing corona and eventual breakdown. If, however, the wrapped dielectric can be impregnated with a material having higher dielectric constant (e.g., heavily filled epoxy resin), gaps of helium gas will be avoided. Moreover, because of the higher dielectric constant of epoxy, the electric stress will be concentrated on the layers of the wrapped dielectric which can tolerate higher stresses than epoxy.

We made a small model of an epoxy-Mylar bushing (Figs. 3-48 and 3-49), using Emerson Cumings 2850 FT epoxy resin. The diameter of the inner conductor is 44.45 mm and that of the outer ring 57.15 mm. The dielectric between these two concentric electrodes is composed of alternate layers of 0.127-mm-thick Mylar (dielectric constant k=3) and 0.178-mm epoxy (k=7). This bushing was immersed in transformer oil to prevent surface flashover and then tested at 250-kV dc for 1 h. After much corona activity on the insulator surface and turbulence in the oil for the first 20 min, the corona subsequently subsided. After 1 h, we raised the voltage to 300-kV dc, where a flashover occurred after about 3 min.

TABLE 3-XXIII

RESULTS OF NEGATIVE IMPULSE (1.2 x 50-μs) TESTS ON 100-kV EPOXY BUSHING

Temperature K	Pressure MPa	Flashover Voltage kV	Remarks
300	0.078 (air) Air at Atoms Pressure	-35.3	Surface flashover on bushing inside cryostat (creepage path = 27 cm)
300	1.38 (helium)	-67.3	Surface flashover on bushing inside cryostat
12	0.69 (helium)	-201.0	Surface flashover on bushing inside cryostat
12	1.38 (helium)	-284.0	Surface flashover across outside skirts of bushing. Bushing damaged.

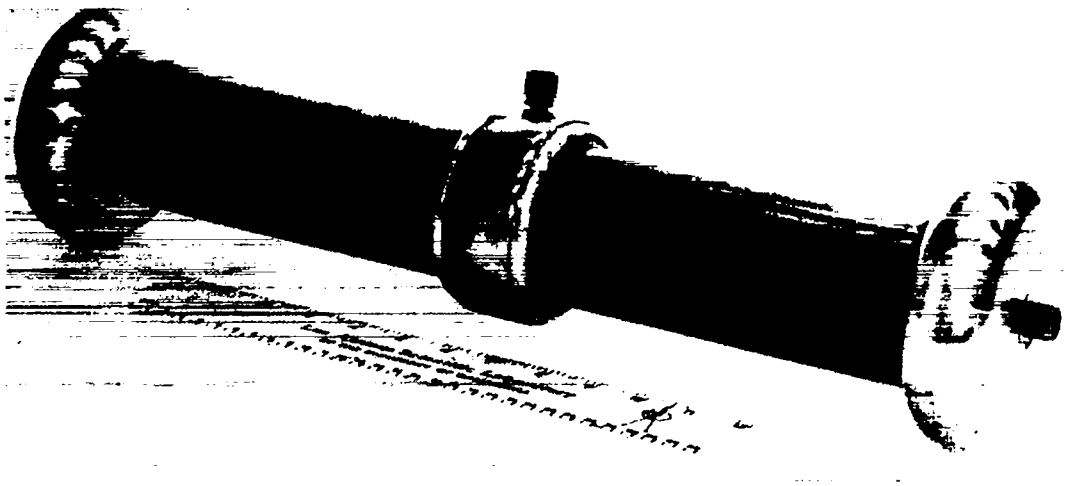

Fig. 3-48.
Photograph of the epoxy-Mylar bushing model with composite dielectrics.

The electric field across the first layer of epoxy at the surface of the inner conductor was calculated to be 29.92 kV/mm at 250 kV and 35.91 kV/mm at 300 kV. If only one dielectric material had been used, the corresponding electric stresses would have been 44.76 kV/mm and 53.71 kV/mm.

This test shows the superior performance of a properly designed composite dielectric. As the dielectric constant of epoxy (k=7) is higher than that of Mylar (k=3), the stress tends to be concentrated in Mylar, which is a better dielectric. This test data was used to design the 300-kV test bushing.

This 300-kV test bushing was going to be used with the horizontal cryostat for cable-sample tests. The dielectric located between the center conductor and the ground plane is made of layers of 0.254-mm Mylar embedded in 0.178-mm epoxy. The purpose of the Mylar in the epoxy is to relieve the electrical stress on the epoxy, a concept demonstrated in the test of the model bushing. Calculations show that the electric stress on the first layer of epoxy adjacent to the high-voltage inner conductor will be 7.87 kV/mm instead of 13.63 kV/mm, as would occur if only epoxy or Mylar were used. This type of hybrid design has several advantages for cryogenic high-voltage applications:

1. because of the smaller cross section of the bushing, the heat leak into the Dewar is reduced;
2. Mylar wrap will prevent radial cracks in the body of the bushing; and
3. the smaller cross section will allow reduced casting size and weight that makes the casting easier and more reliable.

Another new feature of the bushing is the casting of the ground-potential electric-stress shield from polyurethane foam instead of machining it from glass-epoxy laminate (G-10). This would relieve shrinkage and thermal stress in the epoxy around the stress shield. The G-10 casting in the 100-kV bushing produced cracks.

Still another new feature is the inner conductor lined with polyurethane foam to isolate thermally the inner wall of the bushing. This would reduce the large thermal gradient from the cold inner wall to the room-temperature outer wall of the bushing. The foam is situated inside the Faraday shield to protect it from any voltage stress.

We cast the 300-kV test bushing with the Shell Epon epoxy instead of the Emerson and Cummings 2850 FT. Although the Shell Epon epoxy is more difficult to mix, it penetrates the Mylar wrap more easily because of its lower viscosity at casting temperature. The 0.254-mm Mylar is wrapped with a 0.178-mm gap between layers. This and the vacuum-fill process allowed the epoxy to fill all void in the body of the bushing. An outline drawing of this bushing is shown in Fig. 3-50 and a photograph of the completed bushing in Fig. 3-51. An x-ray examination of this bushing showed no air voids within the composite dielectric.

The vacuum-fill process is shown in Fig. 3-52. First, both the mold and epoxy in the small vacuum pot were heated to approximately 27°C. The epoxy was then catalyzed and mixed. The mixture was thoroughly outgassed by evacuating the small vacuum pot. Meanwhile, the vacuum-pressure tank containing the warm mold was pumped to a residual pressure of 26.7 Pa. Atmospheric pressure of air was then admitted to the vacuum pot and the valve on the fill pipe opened. The outgassed epoxy was thus forced into the bushing mold. After the mold was filled, we bolted the pressure lid to the vacuum-pressure tank that was then pressurized to about 765 kPa. The bushing was allowed to jell at room temperature for about 24 h and then was postcured at about 60°C.

The 300-kV test bushing was installed in the existing cryostat and cooled to 12 K at 1.38 MPa of helium. We applied negative-polarity dc voltage at 1 kV/s-rate to -300 kV. This voltage was held constant for approximately 2 min, when the high-voltage terminal of the HVDC generator flashed over.

The cool-down time of this bushing was shorter than that of the 100-kV epoxy bushing. This increased cooling rate may be caused by lower heat leak through the Mylar layers. This was advantageous during cable-sample tests, because it reduced the cool-down time to such an extent that one breakdown test per day could be performed.

This bushing was initially used to perform cable-sample tests in the vertical (100-kV) cryostat. After about 50 cooldowns, the lowest skirt of the bushing showed a crack. Inspection showed cracks on the polyurethane foam also. Radiography further showed extensive cracks in the foam as well as in the surrounding Mylar layers. These cracks were contained only in the lower part of the bushing which experienced thermal cycling.

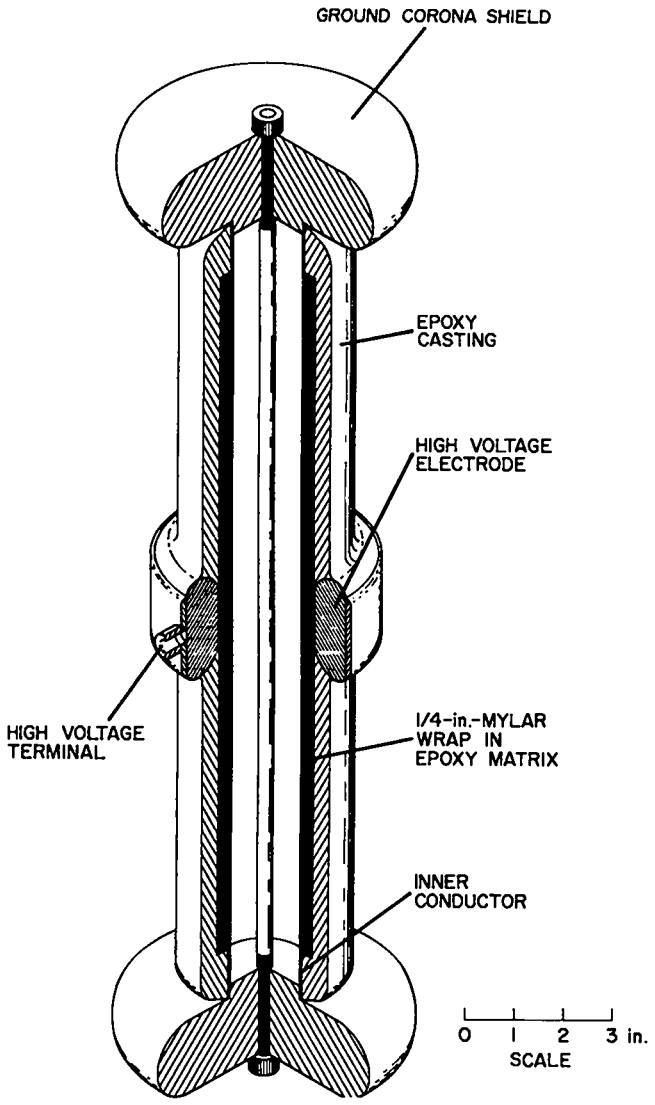

Fig. 3-49.
Cut-away view of Epoxy-Mylar bushing model.

3.3.3. 50-kV Epoxy-Mylar Bushing. Two 50-kV epoxy-Mylar bushings were fabricated (Figs. 3-53 and 3-54). Their design is similar to that of the 300-kV test bushing; however, we have improved the fabrication technique. Also, we selected the Emerson and Cummings 2850 FT epoxy instead of the Shell Epon epoxy previously used in the 300-kV test bushing. Because the vertical cryostat has been the limiting factor, the 100-kV and 300-kV test bushings could not be tested to destruction to determine the design safety factors. One of the two 50-kV bushings was intended to be tested to destruction with the present cryostat. The second 50-kV bushing was to be used to measure electrical resistivity of the selected dielectric materials.

3.4. Electrical Stress Analysis. Essential to the successful design of high-voltage apparatus is a thorough understanding of the electric electric field distributions in the apparatus. Of immediate concern to the dc SPTL program was the design of the following:

1. multiple-electrode systems for dielectric screening tests and cable-sample tests;
2. stress-relief cones for cable-sample tests; and
3. high-voltage bushings to lead test voltages into the test cryostats.

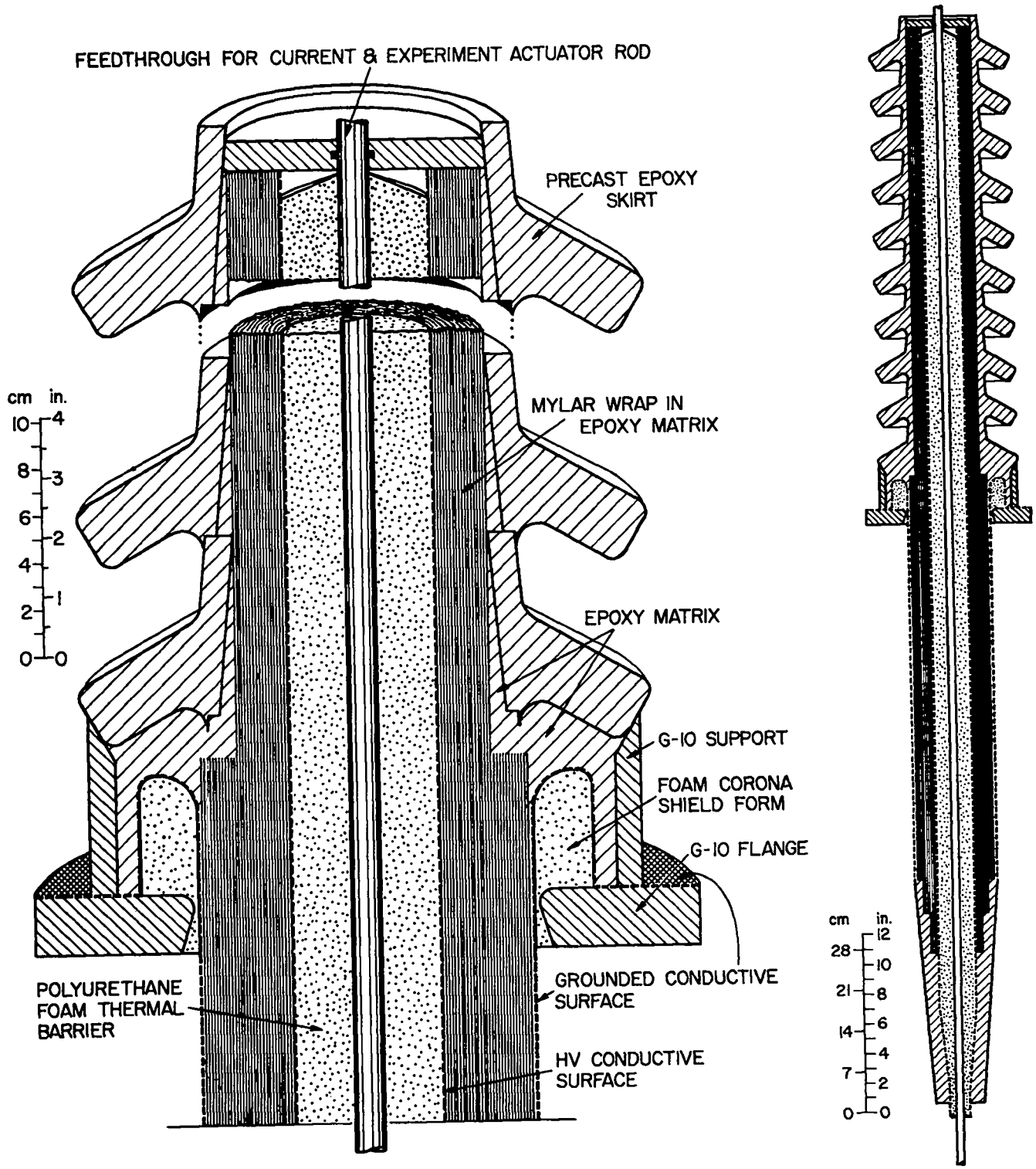

Fig. 3-50.
Outline drawing of 300-kV epoxy-Mylar bushing.

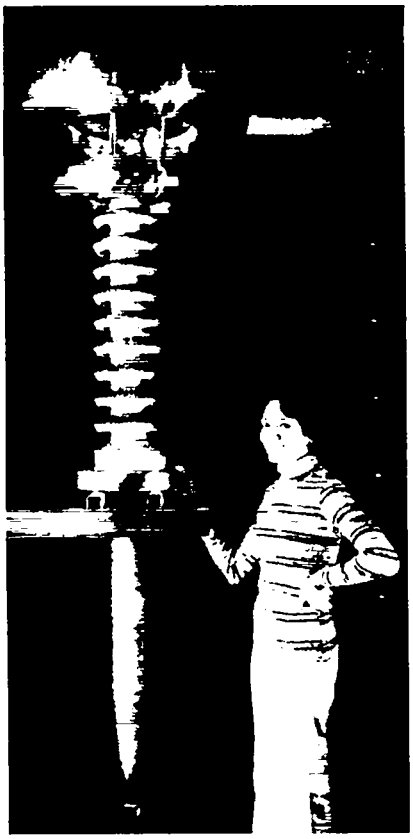

Fig. 3-51.
300-kV dc epoxy-Mylar bushing.

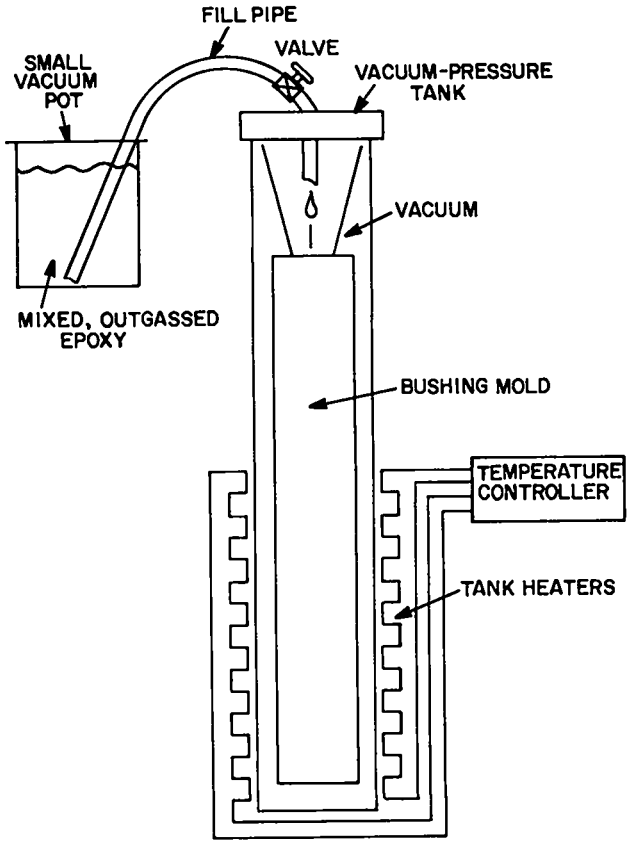

Fig. 3-52.
Schematic of vacuum-fill process for casting epoxy bushings.

The electric field distributions in SPTL equipment is too complex to be solved by hand computations. Consequently, we used digital computer simulations to calculate the electric fields. At the beginning, however, we used an electrolytic tank method to study electric fields and to check the calculations.

According to the computer method, a conducting object (e.g., an electrode) may be replaced by a number of discrete electric charges situated within its contour. The values and the locations of the charges are such as to make the contour an equipotential surface of the given value and to leave the external electric field unchanged. Once the charges and their locations have been determined, the electric field outside the contour may readily be found. The computer analyses were performed for several configurations by W. F. Westendorp, a consultant.

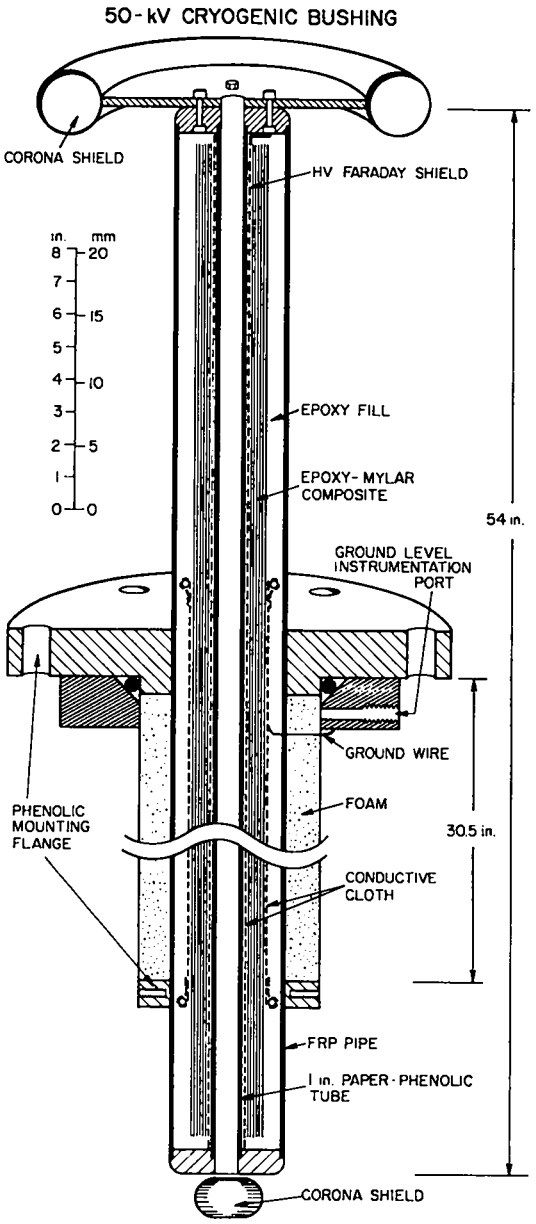

Fig. 3-53.
Outline of drawing of 50-kV epoxy-Mylar bushing.

Fig. 3-54.
The 50-kV epoxy-Mylar bushing.

3.4.1. Electric Field of the Six-Electrode Dielectric Sample Holder.

The six-electrode sample holder (Fig. 3-26), which was used in the dielectric screening tests, was simulated first. We calculated the electric fields tangential to the surface of the dielectric sample. The following assumptions were made:

1. The top electrode is at +50% of the applied potential, the bottom electrode at -50%, and a neutral plane is in the middle; and

2. the thickness of the dielectric sample is 0.152 mm, its dielectric constant being 3.3.

We determined the potentials at various radial distances along the surface of the dielectric sample. The electric field at various points along the dielectric surface was then computed from the gradients of surface potentials. A plot of the surface potential is shown in Fig. 3-55. The highest tangential stress (462 V/mm/applied kV) is at the edge of the electrode.

3.4.2. Analysis of Multiple-Breakdown on Single-Cable Sample. Because of the long cooling and subsequent warming times required for dielectric testing at cryogenic temperatures, the possibility of multiple breakdowns in one single cool-down procedure is extremely interesting. The six-electrode system for our dielectric screening tests allowed us to get the required data within a relatively short period of time.

The first multiple-breakdown attempt on cable samples was tried by designing a scale model of a ring-shaped ground electrode embedded inside an epoxy ring (Fig. 3-56). Our intent was to install such an electrode system at regular intervals along the length of the cable sample so that breakdown tests could be performed at several points along the test section during one cool-down procedure. We calculated, by the digital computer, the electrical stresses in the epoxy, along the surface of the wound dielectric, and in helium using the charge-simulation technique. For an applied voltage of 50 kV, the highest stresses in these media were found to be 47.24 kV/mm, 5.91 kV/mm, and 20.47 kV/mm, respectively. These figures show that the epoxy ring provides a significant stress relief. Although further improvement in the reduction of stress is possible, it may be difficult to achieve the required tolerances in machining and casting of epoxy; therefore, the study on multiple-breakdown apparatus should be continued.

3.4.3. Electric Field of a Cable Termination. Continuation of the dielectrics program will require 100-kV cable samples prepared for tests up to 300-kV dc. Electrode systems will have to be designed so that punctures occur through the bulk of the dielectric sample, and not as flashovers across the dielectric surface, during overstressing of the cable sample by the application of voltage.

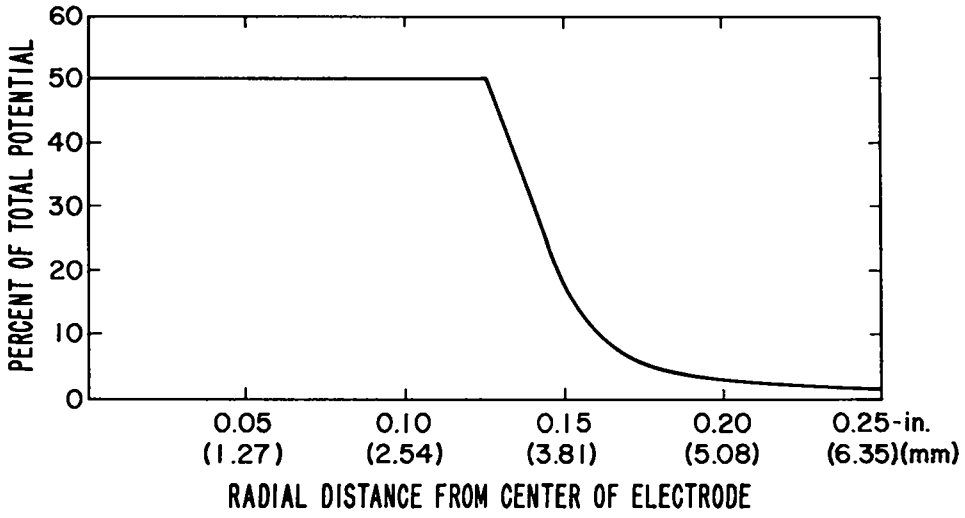

Fig. 3-55.
Voltage profile along the surface of the dielectric sheet sample.
(Six-electrode sample holder for dielectric screening tests.)

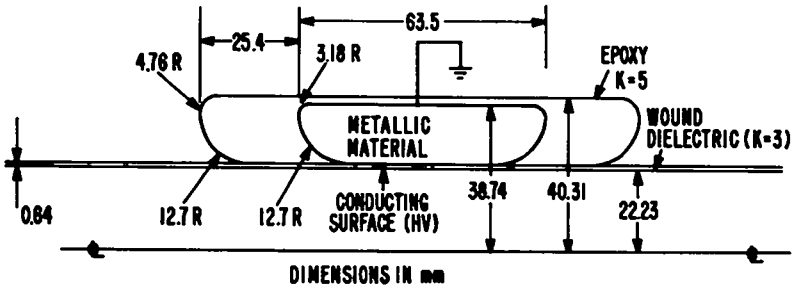

Fig. 3-56.
Schematic of electrode system for multiple-breakdown tests on cable samples.

A 300-kV termination was designed and is schematically shown in Fig. 3-57. The stepping of the dielectric is shown by the dotted line and the stress-control cone by the dashed line. Both the stepping and the stress-control cone start at x=0. The termination is of cylindrical symmetry and is immersed in helium at 12 K and 1.38 MPa.

The electrical stresses in the x-direction within the dielectric and the total stresses in the helium were calculated with the digital computer. These stresses were found to be unacceptably high. For instance, at x = 10 mm, the E_x on the dielectric surface was 3.27 kV/mm, and the total stress at the stress-control cone was 130.18 kV/mm for a 300-kV application.

A similar cable termination was simulated on the electrolytic tank. The scale of the electrolytic-tank model was 16:1. The photographs of this model are shown in Fig. 3-58 and 3-59. The summary result is shown in Fig. 3-60. The insert in Fig. 3-60 shows the schematic of the electrolytic-tank model. Because of the 16:1 scale of the model and the curvature of the ground electrode, the electric stresses at x=-109.2 mm on the electrolytic-tank model will correspond to the stresses at x=10 mm from the edge of the stepping for the actual termination. The E_x on the dielectric surface at this point was measured to be 5.5 kV/mm. The maximum measured electrical stress in helium was found to be 93 kV/mm. The stress would be even higher at the edges of the ground electrode.

The electrical stresses, as measured by the electrolytic tank and calculated by the digital computer, were much higher than the assumed design stresses. Therefore, the original design analysis was scrutinized. In the original evaluation we had used Short's analysis on cable joints.[29] We concluded that Short's analysis needed modifications because the resultant stresses in helium were not calculated. Corrected calculations now showed that the electrical stress at the stress-control cone at x=10 mm will be 138.63 kV/mm as compared with the digital-computer calculation of 130.18 kV/mm.

The breakdown strength of helium at 12 K and 1.38 MPa is approximately 35 kV/mm.[30] Therefore, the design stress of 12.5 kV/mm in helium is adequate. However, the design value of 0.5 kV/mm for the axial stress in the taped dielectric is an assumption that needs to be verified.

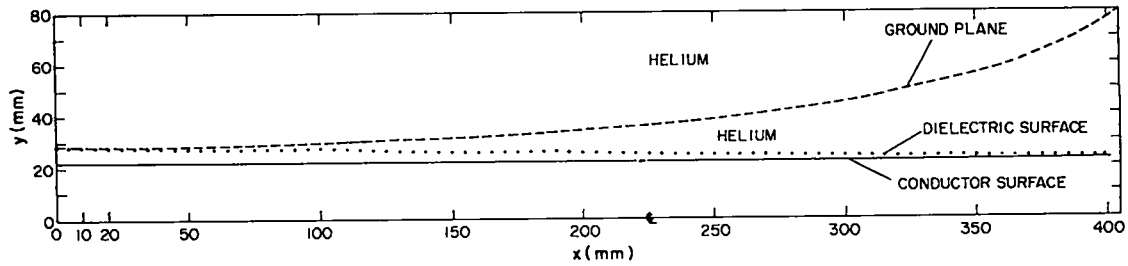

Fig. 3-57.
First design of a 300-kV termination for cable-sample tests.

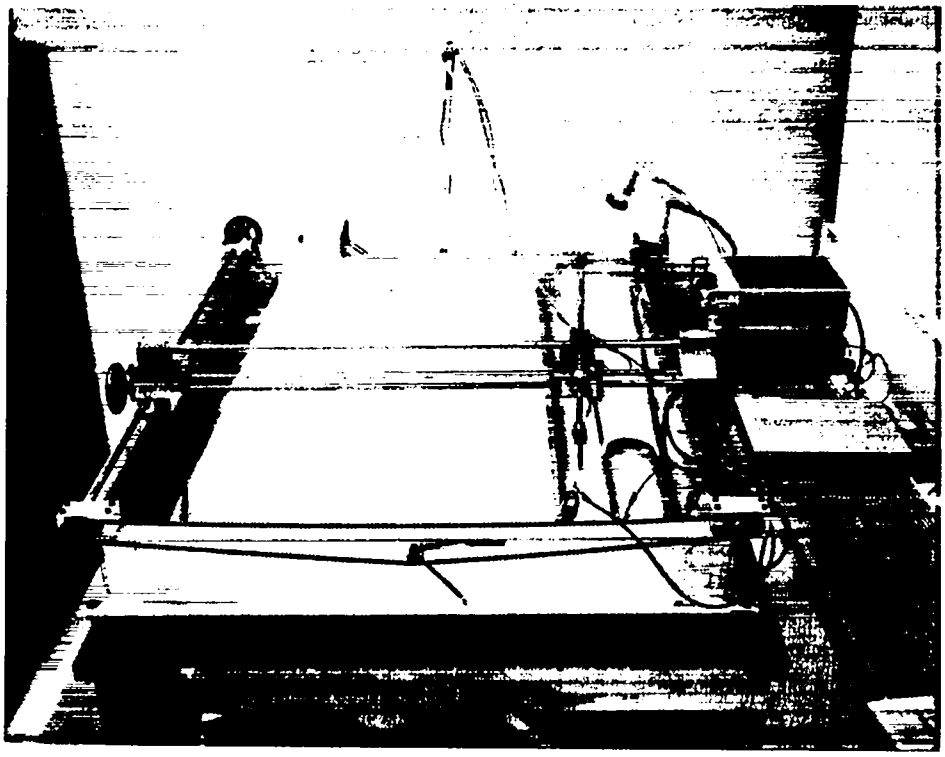

Fig. 3-58.
Electrolytic tank with the cable-termination model.

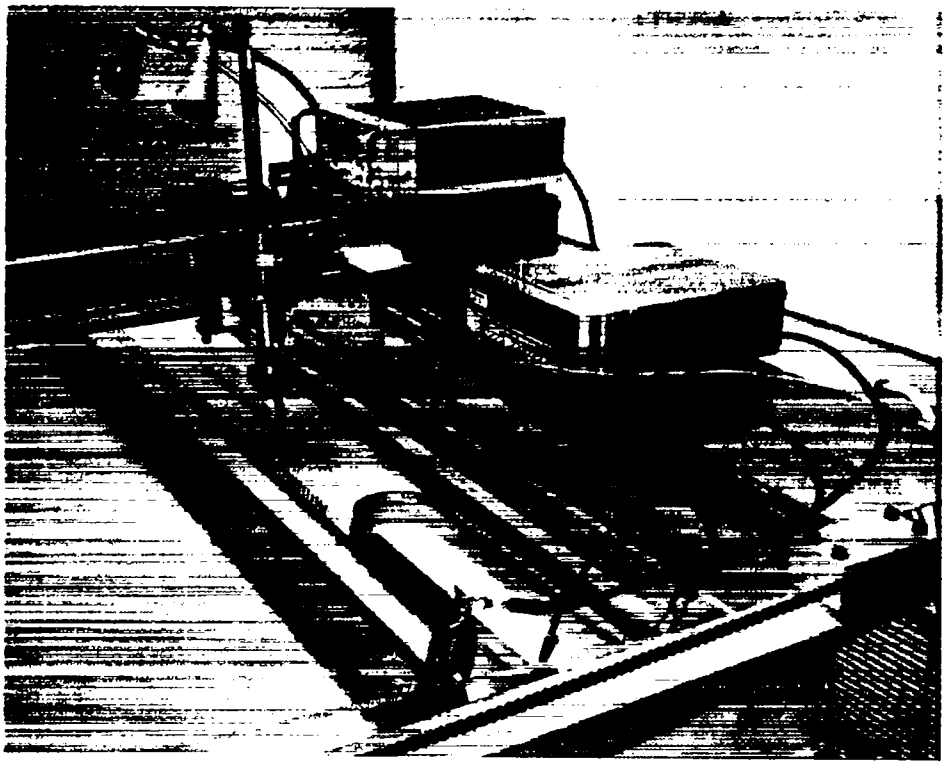

Fig. 3-59.
Close-up view of the cable-termination model in the electrolytic tank.

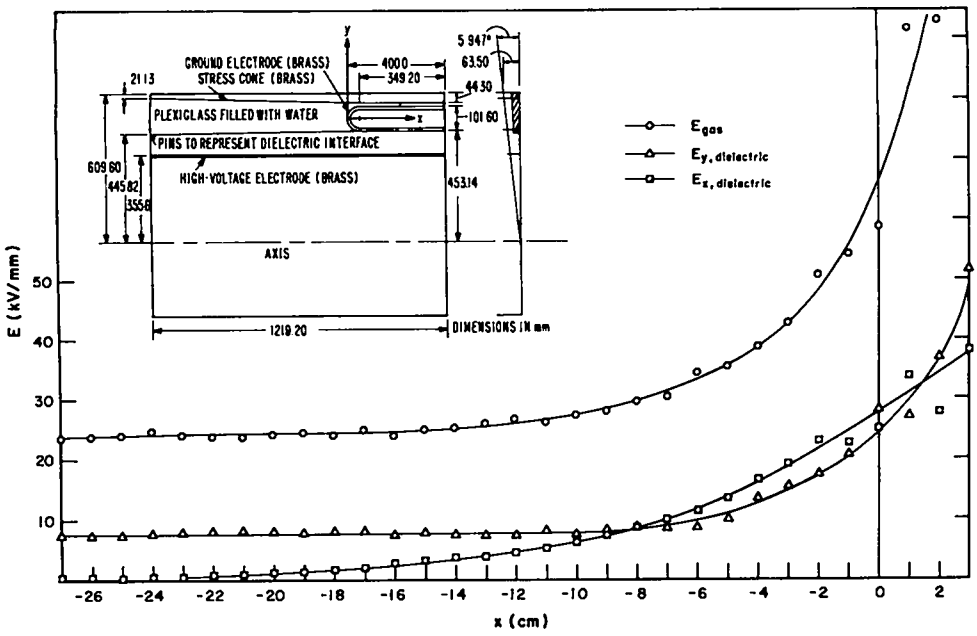

Fig. 3-60.
Electrical stresses at the surface of the stepping and in the surrounding helium for cable-termination design (applied voltage = 300 kV).

A second termination was designed to be used in the horizontal cryostat during cable-sample tests and to withstand up to 300kV. The design requirements limit the axial stress in the taped dielectric to 0.5 kV/mm and the stress in helium to 12.5 kV/mm. This design was verified by a computer study using the charge simulation method, performed by W. F. Westendorp, consultant. The profile of the termination is shown in Fig. 3-61. The computer calculation shows that the highest axial stress in the taped dielectric will be 0.52 kV/mm and the highest stress in helium will be 12.55 kV/mm, which come very close to the design requirements.

A cable sample with stress cones on both ends was manufactured to determine the axial breakdown strength of cellulose paper tape. To prevent breakdown across the dielectric in the radial direction, the radial design stress was 10 kV/mm at 100 kV. The axial design stress at 100 kV was selected as 2 kV/mm to encourage axial flashover below 100 kV of applied voltage. The helium stress at 100 kV was designed to be 12.5 kV/mm.

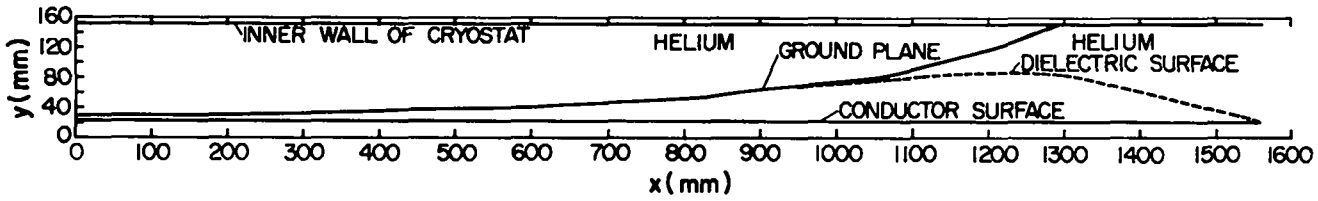

Fig. 3-61.
Profile of a termination to withstand 300 kV.

The main part of the dielectric, 4 cm long, consisted of layers of 2.54-cm-wide and 127-μm-thick cellulose paper. The stress cones at both ends were built up from a 6335-mm-long tapered sheet (0.203-μm-thick waxed cellulose paper).

The cable sample was cooled to 12 K at 1.38 MPa of helium and held there for about 3 h before dc voltage was applied at 1 kV/s to 100 kV. Both polarities of the dc voltage were held for 5 min. There were some indications of corona although we could not ascertain the source. After dismantling, the tapered sheets (stress cones) were examined for corona tracking. No sign of distress was observed.

A similar cable sample was manufactured for impulse testing with 1.2 x 50-μs voltage waves at 12 K and 1.38 MPa of helium pressure. The only difference between this and the previous sample was that the stress cone was machined out of cloth-based phenolic (Fig. 3-39). The objective was to reduce the preparation time for the test cable samples. The stress cone flashed over at -212 kV and +234 kV of negativeand positive-polarity impulse waves, respectively.

Another cable sample was manufactured with design stresses of 10 kV/mm and 1 kV/mm in the radial and axial directions, respectively, at 100 kV of applied voltage. One of the two stress cones broke along its axis at -172.4 kV of negative-polarity impulse waves. This design was finally selected for cable-sample testing in the 100-kV cryostat.

3.4.4. Electric Field at the Ground Flange of Bushings. The grounded flange in a bushing (Fig. 3-50) produces a discontinuity and, hence, a concentration of electrical stress. A cylindrical collar is generally designed around this grounded flange to diffuse the stress concentration. The ideal design would be one in which the electrical field at any point on this

grounded electrode would be lower than that at the high-voltage conductor. A contour of the grounded collar was designed to follow the equation of a modified hyperbolic spiral. Computation of the electrical field at this collar showed that the highest field could be limited to 90% of the field at the high-voltage electrode. This contour was used for the design of the 50-kV bushings (Sec. 3.3.3.).

3.5. Equipment and Instrumentation.

Study of dielectric properties of materials in cryogenic environments is difficult and time consuming. The laboratory must contain not only the usual high-voltage equipment but also other ancillary instrumentation to monitor parameters under controlled cryogenic environments. Because such a laboratory was not available to the Group, a laboratory was built to carry on the dielectric study. This laboratory consists mainly of three areas:

1. high-voltage bay,
2. sample preparation room and
3. screen room.

3.5.1. High-Voltage Bay. This is a fenced-in, interlocked area (Fig. 3-62) which contains a 300-kV, 10-mA, filtered dc power supply; a 600-kV, 60-kJ impulse generator; resistive and capacitive voltage dividers; and the cryostat which contains the dielectric sample to be tested. The dc power supply can provide voltages of either polarity. The impulse generator can produce both the lightning wave (1.2 x 50-μs wave) and the switching surge (250 x 2500-μs wave), also of either polarity.

The interlock system was designed such that the 300-kV dc power supply and the 600-kV impulse generator cannot be energized if the gate of the fenced-in area is open. To energize the high-voltage equipment, this gate has to be closed and the interlock key has to be in the "on" position on the control panel of the screen room.

To avoid any possible damage to the instrumentation and control circuits, steps were taken to isolate and protect these circuits. To accomplish this, an auxiliary 24-V dc supply was installed and protected with transient voltage suppressors. Remote controls are operated with 24-V relay contacts, thus isolating the screen-room electronics from possible sparkover or surge damages. All wiring external to the screen room was installed in conduits or steel ducting. Instrumentation wiring is both shielded and installed in conduits. All safety and warning devices were installed utilizing the 24-V relay interface.

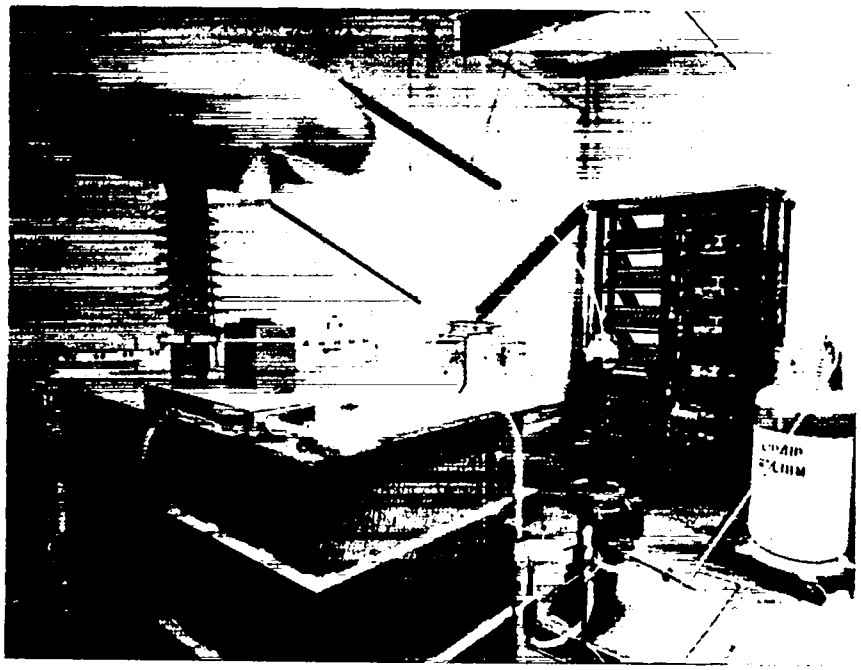

Fig. 3-62.
High-voltage laboratory for the dc SPTL program.

3.5.2. Sample Preparation Room. This is an air-conditioned room (Fig. 3-63) which contains the Insulator Test System (ITS), the dielectric taping machine, the dielectric tape cleaner (Simco) and other ancillary equipment.

3.5.2.1. Insulator Test System (ITS). This system (shown at the back of Fig. 3-63) automatically inspects rolls of dielectric tape for thickness and pin holes. These conditions are monitored and continuously recorded for a permanent record of each roll of tape. The functional and block diagrams of this tester are shown in Figs. 3-64 and 3-65.

The tape, in widths of 1.9 to 2.54 cm in rolls, will snap into the tester. Drive of the tape through the system is done by means of rubber drive rollers.

Thickness of the tape is measured by a beta transmission gauging circuit. ^{147}Pm betas (230 keV) have been shown to provide measurement of the tape thickness to within $\pm$ 1% of the total thickness.

Fig. 3-63.
Dielectric sample preparation room.

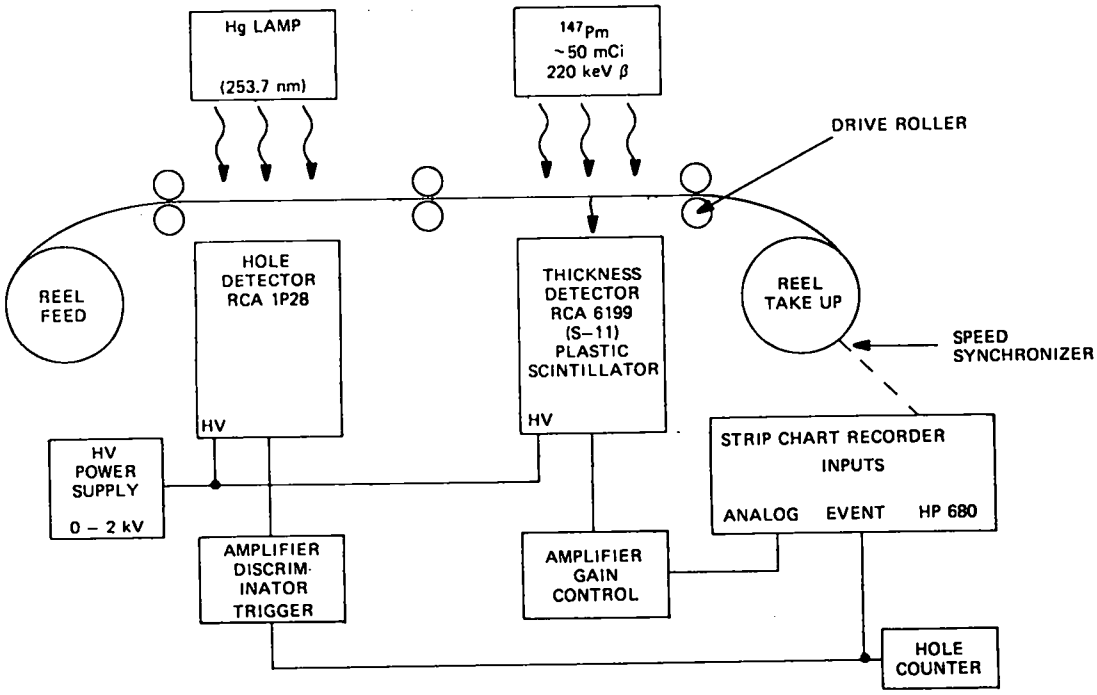

Fig. 3-64.
Functional diagram of the Insulator Test System (ITS).

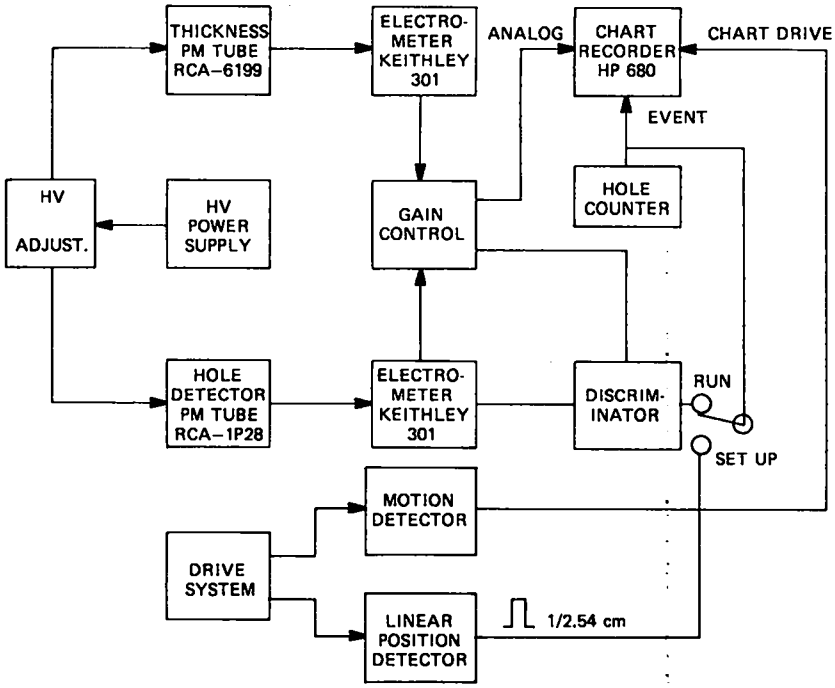

Fig. 3-65.
Block diagram of the Insulator Test System (ITS).

The ^{147}Pm source is mounted above the tape, which in turn passes over an aperture (22.9 mm x 3.18 mm width). The betas that pass through the tape are detected by a photomultiplier (RCA-6199), which produces a current proportional to the detected betas. This signal is amplified and fed to a strip chart recorder.

A miniature mercury lamp is used as the light source for the detection of pin holes. The mercury line at 254 nm was selected as being the optimum. The insulators being considered are opaque at this wavelength. An optical interference filter, with 19% transmission at 254 nm and less than 0.1% transmission at 300 nm, is used between the sample and the detector. The detector is a 1P28 Photomultiplier tube. Response of the system to holes 0.1 mm or larger indicate that these will routinely be recorded. Difficulty in producing holes less than 0.1 mm in the insulator material have made calibration of the system for holes in this range impractical at this time. The signal generated by the system indicates that detection of much smaller holes is possible.

The above system can be used for all but one of the dielectric tapes selected for the dielectric screening tests; the only exception is Cryovac,

which is transparent to the 245-nm light. For this material, a light source consisting of two CW laser diodes with a peak emission at 850 nm was chosen. An RCA Type 7102 Photomultiplier, which has an S-1 spectral response, was chosen as the detector. A wide-band pass optical filter (700 nm to 900 nm) will also be used to limit the spectrum to the desired wavelength.

The detector electronics are designed to allow the setting of discrimination levels to compensate for the different average transmission of the light through the various samples.

Once a discrimination level has been set for an insulator type, a hole will trigger a pulse that will cause an event marker on the strip chart recorder, which also records the thickness. At the same time, a circuit is tripped to indicate that a hole has been detected. The presence of a hole is simultaneously recorded on the chart recorder and a counter.

The chart recorder and tape transport speeds are synchronized by the operator before the start of an inspection. The event marker on the chart recorder is switched to detect linear motion of the transport by a circuit that transmits a pulse each 2.54 cm of tape travel. The tape transport speed is then adjusted to match the chart recorder speed or, if desired, increased to reduce the chart record length by a known scale with respect to the tape length.

The tape transport system automatically detects the end of a reel of tape and shuts the system off so that the system once set up and started is left unattended for the duration of the inspection.

The ITS was designed and built by LASL Group M-1 (Non-Destructive Testing).

3.5.2.2. Dielectric Taping Machine. This machine, shown at right of Fig. 3-63, consists of two basic assemblies: the first holds the cylindrical conductor, while the second holds and dispenses the dielectric tape. This machine is designed so that as the cylindrical conductor is rotated at constant speed, the tape holder will travel along the length of the conductor dispensing the dielectric tape at the proper pitch, butt gap, and tension. Dielectric tapes can be wound on a conductor of length up to 5 m. This machine was designed and built by LASL Group J-7.

3.5.3. Screen Room. The screen room (Fig. 3-66) consists of a 2.4-m x 2.4-m x 2.4-m (8'x8'x8') double-walled enclosure made of copper mesh (Model D2H2 of Ace Engineering). It contains the following equipment:

1. control console for the 300-kV dc power supply,
2. control console for the 600-kV impulse generator,
3. bridge type partial discharge detector (Biddle Type 5700-03),
4. pulse height analyzer (Tracor Northern, NS-710A),
5. tape casette unit for pulse height analyzer, NS111-A),
6. impulse peak voltmeter (Haefely type 64M),
7. waveform recorder (Biomation model 8100),
8. data acquisition system for Biomation 8100 (William Palmer Industries, Model DCR/10),
9. cathode-ray tube display accessary (Biomation Model 350)
10. high-voltage surge-test cathode ray oscilloscope (Tektronix 507),
11. dual-beam cathode ray oscilloscope (Tektronix 551)
12. cryostat temperature controller and monitor,
13. cryostat temperature monitor, and
14. cryostat pressure monitor.

Description of some of the special equipments follows.

3.5.3.1. Partial Discharge Measurement. Partial discharges in a dielectric system under ac voltage occur during each half cycle of the voltage wave. Under dc voltage, partial discharges occur at much longer intervals (sometimes hours) depending upon the complex RC time constant of the dielectric system. It is, therefore, difficult to analyze partial discharges under dc voltage. It is important to minimize the effects of external electrical noise on the instrumentation. We selected the bridge-type partial discharge detector to balance out the effects of external electrical noise; the pulse height analyzer records the frequency of the discharges of various magnitudes in 1024 channels; the data is stored in the magnetic tape casette unit and can be retrieved and read out.

3.5.3.2. Impulse Voltage Measurement. The impulse voltage is measured in three different ways:

1. impulse peak voltmeter (Haefely type 64 M),
2. cathode ray oscilloscopes (Tektronix 507 and 551), and
3. waveform recorder (Biomation 8100).

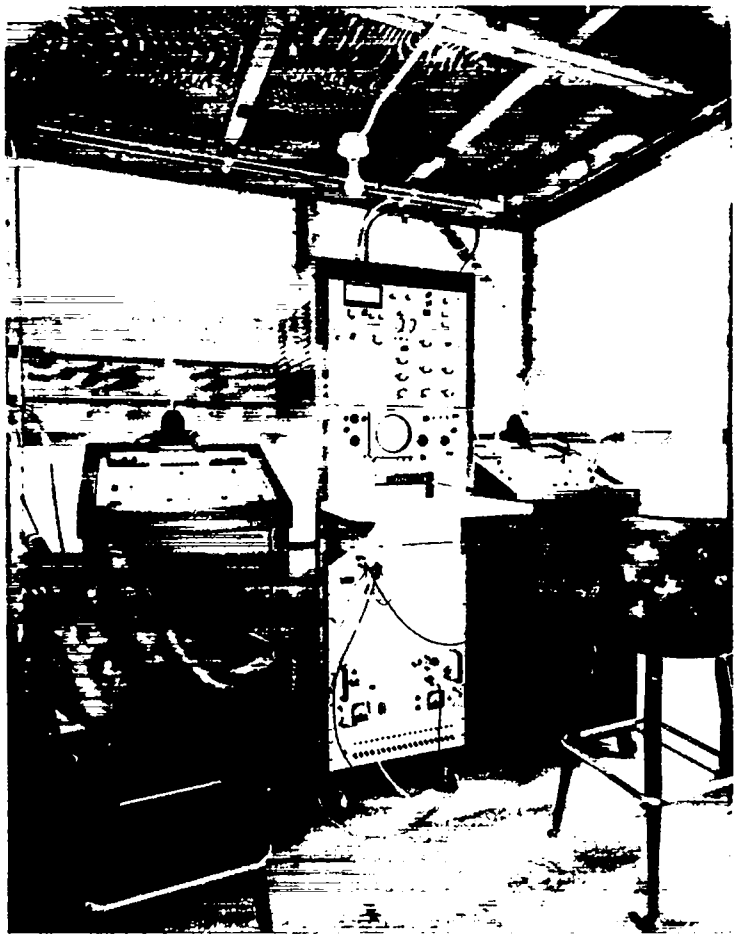

Fig. 3-66.
Control center for the high-voltage laboratory.

The cathode ray oscilloscopes were intended to be used for set-up and for special tests. However, the surge-test oscilloscope has been used most of the time to record the 1.2 x 50-μs voltage waves.

The impulse peak voltmeter and the surge-test oscilloscope are connected in parallel to the 75-Ω low-voltage arm of the 1000:1 resistive voltage divider through a 75-Ω triax cable. While the cathode ray oscilloscope gives information on the wave shape and time to breakdown, the impulse peak voltmeter gives instant reading of the peak of the impulse wave.

The waveform recorder records an impulse wave in 2048 channels at a selectable interval, the shortest being 10 ns. The data are stored in a magnetic tape cassette by a data acquisition system (DCR/10) designed by the William Palmer Industries. The DCR/10 has been factory-programmed to read, edit, and format the data from the Biomation 8100 waveform recorder. It

precisely duplicates a number of tape encoding techniques to assure digital computer compatibility. The cassettes produced by this unit are read directly by any Texas Instruments 733 ASR Data Terminal. Up to 14 waveforms may be recorded on each side of a magnetic tape cassette. A 50-Ω ladder-type attenuator (100:1) was designed to be used with the 1000:1 voltage divider to attenuate 500-kV output from the impulse generator and apply 5 V to the Biomation 8100.

3.5.3.3. Cryostat Temperature Controller. This temperature controller (Fig. 3-67) was designed by us to serve many applications within the dc SPTL Program.

The controller includes the following five circuit functions:

1. differential instrumentation amplifier,
2. constant-current supply,
3. servo-loop amplifier,

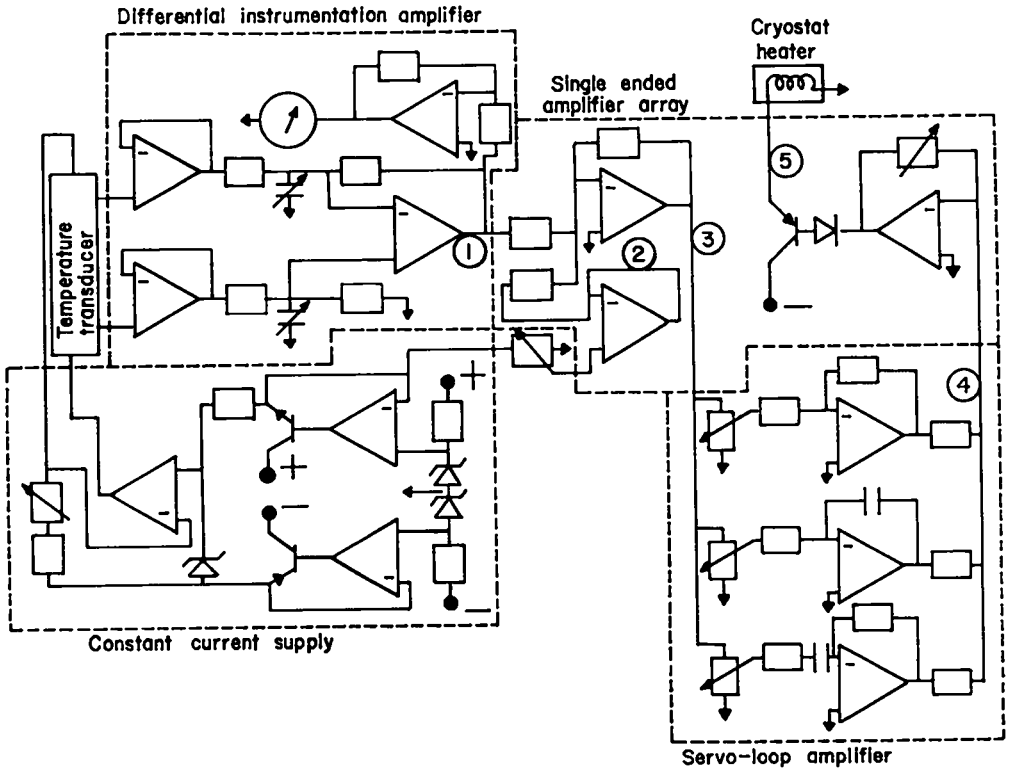

Fig. 3-67.
Schematic of primary components in a PID temperature controller.

4. single-ended amplifier array, and
5. computer interface.

Each board has common power connections and a card-edge connector for a standard Wyle card file, so that several boards can be combined to meet a given system requirement merely by plugging in the required cards and providing appropriate input and output connections to the card edge connector.

The differential instrumentation amplifier board is an ultra-high performance, 10^{12}-Ω input impedance, linear, noninverting voltage mirror. Its function is to sense the voltage difference between two terminals, neither of which need be at ground potential, and to provide a grounded output equal to that difference, accurate to a part in 10^6. It must have a common-mode rejection ratio greater than 150 dB and also provide a separate, variable-gain, grounded output to drive a recorder. Several such amplifiers would be used to provide parallel grounded outputs for the voltages generated in a typical experimental configuration by several temperature transducers connected in a series string and maintaining full isolation between input and output. Thus, the circuit functions as a high-quality buffer amplifier used to prevent a grounded instrument system from influencing readings taken from an ungrounded sensor string.

The constant current supply board has an output stable to 1 part in 10^6 and can provide a grounded, or virtually grounded, constant current of between 10^{-6} and 10^{-2} A for load voltages up to 8 V with an output impedance at 10^{-3} A of 9×10^9 Ω. It also provides approximate +9.3 V and -9.3 V reference voltages with stability of 0.001%/^{o}C and output impedance of 10^{-6} Ω. Its function is to power one or more resistance temperature transducers wired in series and to provide stable reference voltages for servo-control applications. Transducers, such as doped-germanium, silicon-diode, carbon, carbon-in-glass or platinum, are commonly used in low-temperature measurement and control systems and may be used with constant current excitations.

The servo-loop amplifier board is a stable PID signal processor. Its functioning is to generate an output signal proportional to the sum of the input voltage and the integral and the derivative of the input voltage. A proper mix of all three types of signals will enable the generation of an error signal from a temperature transducer, which will tend to stabilize temperature for almost any perturbation to the cryogenic system. Thus, inherently

unstable systems, such as the 300-m SPTL refrigerator-flow experiment, can be controlled. In generating the correction signal, the servo-loop amplifier processes any nonzero input signals, and, therefore, it is necessary to "buck" the signal from the temperature transducer with a set-point signal so that when the desired voltage appears at the transducer, the servo-loop sees zero input. This function, as well as several others, is performed by the single-ended amplifier array. This array is necessary for servo-loop amplifier operation and, hence, is also used in the control mode of the instrumentation package.

The function of the single-ended amplifier array board is to buffer and amplify signals generated by the other three boards in order to complete the temperature measurement and control package. Its application is best demonstrated by describing the temperature controller assembly. Connection of the constant current supply to the temperature-transducer current leads powers the transducer so that a temperature dependent voltage difference appears across its voltage leads. The differential instrumentation amplifier acts as a buffer and provides a gain-one grounded output equal to that voltage difference. This voltage appears at point 1 of Fig. 3-67. The +9.3 V reference voltage of the constant current supply is reduced by an external voltage divider to be the negative of the voltage the transducer should produce at the desired control point. This dividend voltage (set-point voltage) is buffered by the gain-one voltage follower of the single-ended amplifier array board and appears at point 2. The voltages at point 1 (thermometer voltage) and point 2 (set point voltage) are summed and amplified by the precision-summing amplifier, also on the single-ended amplifier array board. The result appears at point 3, where it is fed to the servo-loop amplifier, and then to the rectifying amplifier of the single-ended amplifier array, where it is amplified, inverted, rectified, and fed to the cryostat control heater at point 5 in such a way as to do the following. If the thermometer voltage is greater than the inverted set-point voltage (too cold), negative voltage appears at point 3, and a positive voltage, equal to the amplified sum of the proportional integral and derivative voltages, appears at point 4. Therefore, the voltage appearing at point 5 is a negative voltage, which results in power to the heater, thereby warming the thermometer. If the thermometer voltage is less than the inverted set-point voltage (too warm), the positive voltage generated by the servo-loop array is blocked by the final diode, and no voltage appears at the

heater, thereby enabling the cryogens in the system to cool the thermometer. Thus, a complete control function is provided by the four circuit boards described above.

A fifth digital interface board enables a computer to control the set-point voltage and hence the temperature of the system.

3.5.3.4. Cryostat Temperature Monitor. Although the temperature controller has a temperature sensor incorporated in it, we fabricated several temperature monitors for use independent of the controller. A 1/8-W carbon resistor was used as the temperature transducer to measure the range between 12 and 18 K. A constant-current supply was used to pass 100 μA through this resistor. The temperature-dependent voltage drop across this resistor was measured by a separate pair of voltage leads in a mullivoltmeter. The actual temperature was read from a tape, which was previously made during calibration of the carbon resistor at various temperatures. A copper-constantan thermocouple was used to measure temperatures near room temperature and 83 K.

3.5.3.5. Cryostat Pressure Monitor. The helium pressure in the cryostat during dielectric tests is measured by a Bourdon-tube pressure gauge attached to the cryostat wall. If the absolute pressure could be measured electrically it could be read in the control room on a digital voltmeter and record the pressure fluctuations during the breakdown tests. The block diagram of a pressure transducer system to accomplish this is shown in Fig. 3-68. The pressure transducer (National Semiconductor LX1730A) measures absolute pressure (0 to 2.07 MPa) and consists of four functional elements: the diaphragm and pressure reference, piezoresistive sensor, signal discriminator, and signal amplifier and processor. The first three functional elements are contained in a single silicon die and the fourth is provided by linear IC operational amplifiers. The transducer is located in the same outflow tube (at room temperature) as the Bourdon tube indicating pressure gauge.

The output of the pressure transducer is fed to an instrumentation amplifier (Analog Devices AD522) selected particularly for its excellent performance in an operating environment characterized by low signal-to-noise ratios and for its reasonable cost. It provides output offset voltage drift of less than 10 $\mu V/^{o}C$, input offset voltage drift of less than 0.5 $\mu V/^{o}C$, common mode rejection ratio above 80 dB at unity gain, maximum gain nonlinearity of 0.001% at G = 1, and typical input impedance of $10^{9}\ \Omega$. The output from this

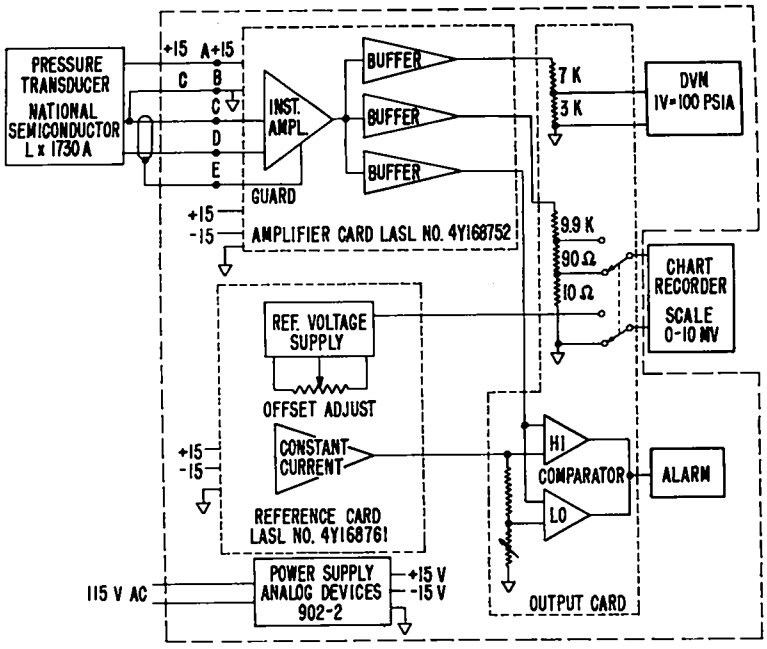

Fig. 3-68.
Schematic of the pressure transducer system.

instrumentation amplifier is then taken to three output functions through separate buffer amplifiers for isolation. The first output feeds a digital voltmeter for direct readout; the second output feeds a chart recorder for continuous monitoring of the pressure; the third output feeds the alarm circuit, which is activated if the actual pressure deviates from the desired pressure by a preset amount.

3.6 References

1. P. Chowdhuri and H. L. Laquer, "Some Electrical Characteristics of a dc Superconducting Cable," IEEE Trans. on Power Apparatus and Systems PAS-97, 399-408 (1978).

2. D. H. Welle, A. G. Phadke and D. K. Reitan, "Evaluation of Harmonic Levels on an HVDC Transmission Line," Proc. American Power Conference, Vol. 29, 1967, pp. 1100-1108.

3. C. Adamson and N. G. Hingorani, High Voltage Direct Current Transmission, (Garraway, London, 1960).

4. E. W. Kimbark, Direct Current Transmission, Vol. 1 (Wiley-Interscience, New York, 1971).

5. J. Reeve and J. A. Baron, "Harmonic DC Line Voltages Arising from HVDC Power Conversion," IEEE Transactions on Power Apparatus and Systems PAS-89, 1619-1624 (1970).

6. C. P. Bean, "Magnetization of Hard Superconductors," Phys. Rev. Lett. 8, 250-253 (1962).

7. H. London, "Alternating Current Losses in Superconductors of the Second Kind," Phys. Lett., 6, 162-165 (1963).

8. S. Ramo and J. R. Whinnery, Fields and Waves in Modern Radio, (John Wiley and Sons, Inc., New York, 1964).

9. M. F. Gardner and J. L. Barnes, Transients in Linear Systems, (John Wiley, New York, 1942).

10. H. A. Peterson, A. G. Phadke, and D. K. Reitan, "Transients in EHVDC Power Systems: Part I-Rectifier Fault Currents," IEEE Transactions on Power Apparatus and Systems PAS-88, 981-989 (1969).

11. A. N. Greenwood and T. H. Lee, "Theory and Application of the Commutation Principle for HVDC Circuit Breaker," IEEE Transactions on Power Apparatus and Systems PAS-91, 1570-1574 (1972).

12. A. N. Greenwood, P. Barkan, and W. C. Kracht, "HVDC Vacuum Circuit Breaker," IEEE Transactions on Power Apparatus and Systems PAS-91, 1575-1588 (1972).

13. G. A. Hofmann, G. L. LaBarbera, N. E. Reed, and L. A. Shillong, "A High Speed HVDC Circuit Breaker with Crossed-Field Interrupters," IEEE Transactions on Power Apparatus and Systems PAS-95, 1182-1193 (1976).

14. A. Ekstrom, H. Haertel, H. P. Lips, W. Schultz, P. Joss, H. Holfeld, and D. Kind, "Design and Testing of an HVDC Circuit Breaker," CIGRE paper no. 13-06, Paris, 1976.

15. E. C. Sakshaug, J. S. Kresge, and S. A. Miske, Jr., "A New Concept in Station Arrester Design," IEEE Transactions on Power Apparatus and Systems PAS-96, 647-656 (1977).

16. J. P. Bowles, L. Vaughan, and N. G. Hingorani, "Specifications of HVDC Circuit-Breakers for Different System Applications," CIGRE paper no. 13-09, Paris, 1976.

17. H. Martensen in discussion of ref. (10)

18. P. Chowdhuri and M. A. Mahaffy, "Wave Propagation in a dc Superconducting Cable Part I: Analysis," paper No. A 79 409-4, presented at the 1979 Summer Meeting of IEEE Power Engineering Society, Vancouver, July 1979.

19. P. Chowdhuri and M. A. Mahaffy, "Wave Propagation in a dc Superconducting Cable Part II: Parametric Effects," paper No. A 79 410-2, presented at the 1979 Summer Meeting of IEEE Power Engineering Society, Vancouver, July 1979.

20. L. V. Bewley, Traveling Waves on Transmission Systems. (John Wiley & Sons, New York, 1951).

21. R. Rudenberg, Transient Performance of Electrical Power Systems, (McGraw-Hill, New York, 1950).

22. S. Hayashi, Surges on Transmission Systems, (Denki-Shoin, Kyoto, 1955).

23. A. L. Williams, E. L. Davey, and J. N. Gibson, "The 250-kV DC Submarine Power-Cable Interconnection Between the North and South Islands of New Zealand," Proc. IEE (England) 113, 121-123 (1966).

24. A. A. Hossam-Eldin and B. Salvage, "A Liquid Nitrogen-Cooled, High-Voltage, Direct-Current Cable," Proc. International Conference on High Voltage DC and/or AC Power Transmission, England, 1973 IEE Conference Publication No. 107, pp. 47-57.

25. H. L. Johnson and S. Kotz, Distributions in Statistics, Univariate Distributions - 1 (Houghton Mifflin, Boston, 1970).

26. W. J. Conover, Practical Nonparametric Statistics (John Wiley & Sons, New York, 1971).

27. G. Bahder, G. S. Eager, G. W. Seman, F. E. Fischer and H. Chu, "Development of ± 400 kV/± 600 kV High and Medium-Pressure Oil-Filled Paper-Insulated dc Power Cable System," IEEE Trans. on Power Apparatus & Systems PAS-97, 2045-2056 (1978).

28. E. M. Allam and A. L. McKean, "Design of an Optimized ± 600 kV dc Cable System," paper no. F79 766-7 presented at the IEEE PES Summer Meeting, Vancouver, July 1979.

29. H. D. Short, "A Theoretical and Practical Approach to the Design of High-Voltage Cable Joints," AIEE Transactions 68, 1275-1283 (1949).

30. R. J. Meats, "Pressurized-Helium Breakdown at Low Temperatures," Proc. IEE 119, 760-766, (June 1972).

4. CRYOGENIC ENGINEERING

Careful studies and estimates of the performance of cryogenic components must be made in order to design a prototype dc SPTL. A thorough understanding is needed of the heat transfer and fluid flow processes as well as of the static and dynamic performances of major components. Accordingly, we have been engaged in evaluating the performance of dc SPTL cryogenic components as well as in performing experiments and analysis in the area of fluid flow and heat transfer. These phenomena are important for studies of the response of the refrigeration system to thermal upsets, system cool down, and the propagation of normal zones in the conductor.

The cryogenic engineering effort also includes the design, fabrication, and checkout of many of the specialized pieces of equipment needed in all phases of the program.

4.1. 20-m Test Bed

The purpose of constructing a test bed was to provide an accessible vacuum and cryogenic environment for the testing of the electrical, thermal, and mechanical characteristics of superconducting transmission line conductors made of various materials and geometries.

4.1.1. Test Bed Construction. The test bed, shown in Fig. 4.1, consists of an aluminum vacuum box 0.81-m wide, 0.34-m deep, and 9.38-m long with a double O-ring sealing a removable lid. Cylinders 1 m in diameter and 0.2-m deep are attached to both ends of the vacuum box. Electrical, vacuum, instrumentation, and cryogenic fluid penetrations are made in these cylinders. The superconducting sample to be tested is enclosed in a copper tube, approximately 2 cm in diam and 20-m long, shaped as a hairpin. Connections for helium fluid refrigerant (which flows through the copper tube) and for electrical leads (potheads) are made at the open end of the hairpin. The tube is mounted within a liquid-nitrogen-cooled shield, and the entire system is contained within the evacuated aluminum box.

As for a superconducting power transmission line system, the 20-m test bed pothead terminals must supply a large current through leads spanning temperatures between 300 and 4 K. The need to bias the lines to high voltage is also a consideration. High voltage standoff between the terminals and nearby ground points can be achieved by using high voltage insulation techniques; no new major difficulties should arise because of the large thermal gradient present, although care must be exercised in constructing the terminal from

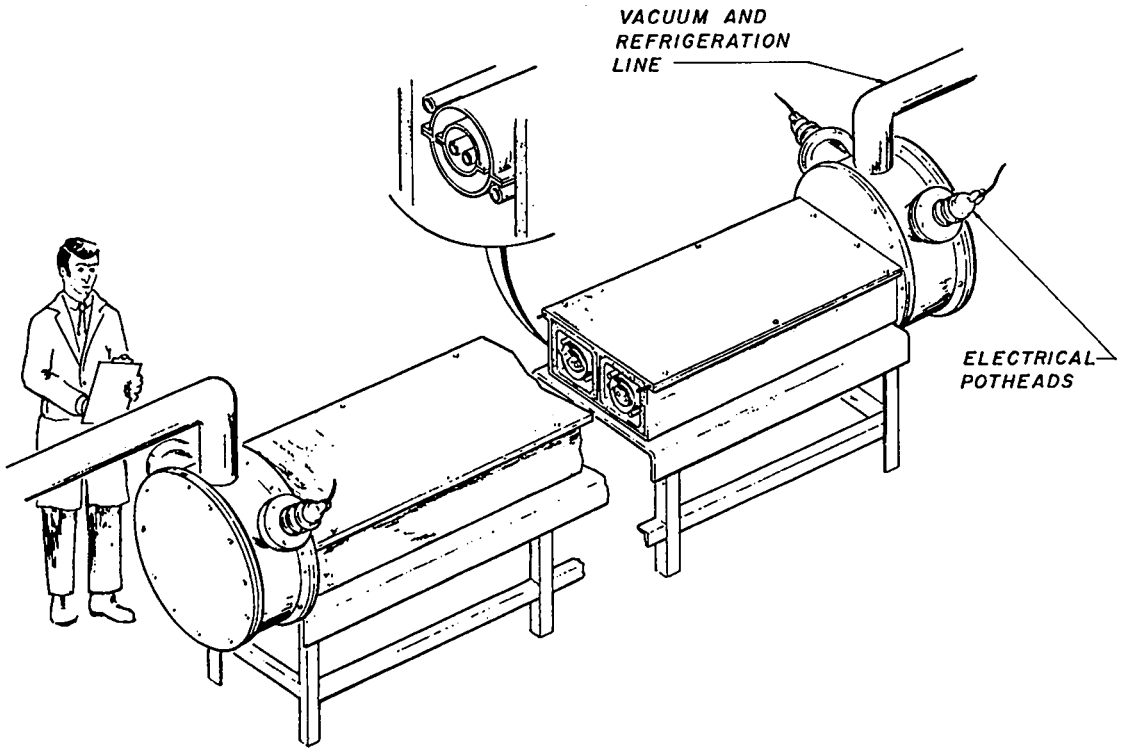

Fig. 4-1.
Test bed for superconducting power transmission studies.

materials with mutually compatible thermal expansion coefficients. However, the need to transport high current into the cryogenic environment while maintaining low thermal influx produces conflicting requirements. Heat flow from the current-carrying leads is due to two causes: thermal conduction along and electrical joule heating in the leads. To minimize thermal conduction losses, the leads should be made long and thin; but if joule heating is to be minimized, short, thick leads are needed. The total heat input into the cryogen is minimized by optimizing conductor material and sizing and by designing the leads as electrical current-carrying heat exchangers. Helium vapor passes through porous conductors and provides continuous heat exchange so that the refrigeration from the cold gas is recovered. Such vapor-cooled leads capable of carrying over 10,000 amperes are commercially available from American Magnetic Inc. and are incorporated in the test bed. These leads can carry 8 kA continuously and 12 kA for short periods of time. Glass insulators are installed between the potheads to keep all the current flowing in the sample (see Fig. 4-2).

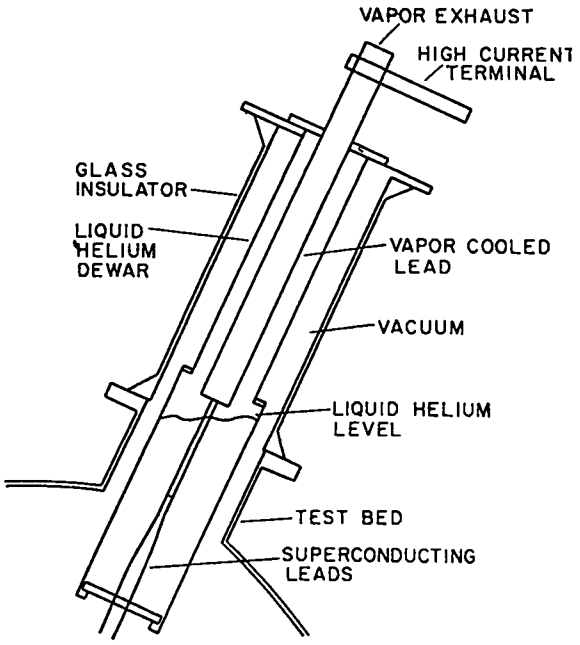

Fig. 4-2.
High current pothead.

4.1.2. Test Bed Operation.

Liquid helium near atmospheric pressure was used in the reservoirs at the bottom of the current leads. Vaporization of this liquid provides the refrigeration to intercept the thermal conduction and joule heating in the leads. A separate supply of liquid helium, also near atmospheric pressure, was used to cool the superconducting sample. Liquid was transferred from a Dewar vessel, admitted to one end of the hairpin sample while passing through a heated section, and withdrawn at the other end. Control of the cold helium transfer rate and the heater power provides temperature adjustment of the superconducting sample.

Seven thermometers and voltage taps were located along the sample length. Other thermometers and voltage taps monitored the current lead operation. A heater wrapped on the coolant tube midway along the sample provided a means of initiating a normal zone. Figure 4-3 shows a photograph of the test bed operating in the above mode.

The temperature-current characteristic and the behavior of normal zones were observed for three samples (details of the experiments are given in Sec. 5.8). However, it was observed that the creation of a normal zone produced a local high pressure volume that blew the helium coolant away from the normal zone in both directions affecting the local heat transfer rate and normal zone propagation rate.

The liquid transfer method of cooling the sample was replaced by the installation of a helium refrigerator that provided a sample environment of turbulent flowing supercritical helium, a more realistic situation considering that any final cable would be cooled in this manner. An electronic temperature controller was installed at the same time.

Fig. 4-3.
The 20-m test bed.

Records of the helium temperature as a function of time during and after a heat pulse demonstrate the dynamic effect of the pulse. Figure 4-4 shows that a local heat pulse has driven the superconductor normal, and the base current of about 1500 A has caused I^2R heating in the stabilizing copper during the time between the pulse and current shutoff. The recording shows a rapid rise in helium temperature of about 2 K and an exponential recovery taking 8 min until the controller holds the temperature at its original 5.78 K.

4.2. CTI Model 1400 Refrigerator

A CTI Model 1400 helium refrigerator/liquefier with a capacity of 70 W of refrigeration at 4.2 K or 26 ℓ/h liquefaction rate was purchased to support the experimental program. This machine was later modified to produce over 150 W of refrigeration when operating near 10 K by replacing the expansion valve with an additional expansion engine and by increasing the compressor capacity.

4.2.1. Installation and Acceptance Testing. The CTI Model 1400 helium liquefier/refrigerator was received at LASL on October 7, 1975. The

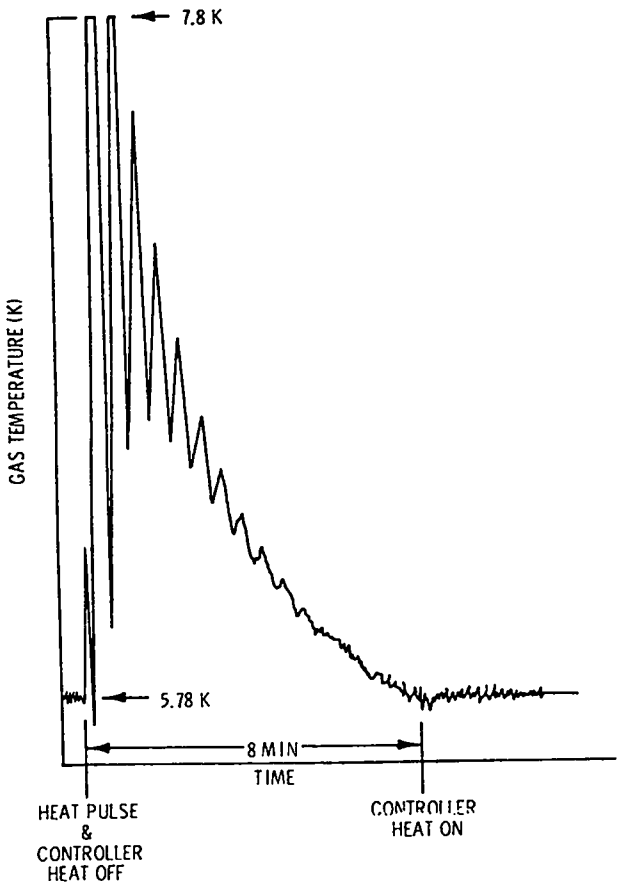

Fig. 4-4.
Typical refrigerator and cooling channel thermal response to normal zone creation in the superconductor.

installation of the utilities and interconnecting plumbing for the refrigerator was completed on December 1, 1975. Familiarization and training of LASL operators by a CTI field engineer began on December 2, 1975. A 500-ℓ Dewar was purchased and installed with the refrigerator. Acceptance testing of the refrigerator was interrupted because of excessive impurities in the helium supply but was resumed after a tube trailer of Grade A helium was obtained. The refrigerator met the liquefaction specification (25 ℓ/h) but not the refrigeration requirement (70 W in an external Dewar), although it had been able to do so at the manufacturer's plant. It is believed that this failure was a result of an incompatibility between the 500-ℓ Dewar and the remote delivery tube (RDT) from the refrigerator to the Dewar. The refrigerator held 70 W at 4.5 K in a test load that was connected to the refrigerator instead of the 500-ℓ Dewar. As the specifications for refrigeration were met with a test load simulating the intended application, the machine was accepted.

4.2.2. Performance Evaluation. The CTI Model 1400 refrigerator/liquefier is designed to produce liquid at 4.5 K. The performance of this machine as a gaseous helium refrigerator near 10 K was not well known and was not guaranteed. Because we required operation at 10 K it was necessary to evaluate refrigerator performance under this condition.

A schematic diagram of the refrigerator and its connection to the load is shown in Fig. 4-5. All components above and including heat exchanger 1 (Hx #1) are standard refrigerator components, whereas those components connecting the refrigerator to the load are special. The valves were supplied by the manufacturer but the orifice flow meter and temperature controller were constructed at LASL. Expander 3, located at the test section outlet, was adapted from a surplus Collins refrigerator.

Two different test sections were used to provide a load for the refrigerator. A 1.1-cm-i.d. tube, 1-m long, was used for preliminary testing. Another test section was built from 500 m of 4.8-mm-i.d. copper tube wound (each loop thermally isolated) in a racetrack configuration in a liquid nitrogen

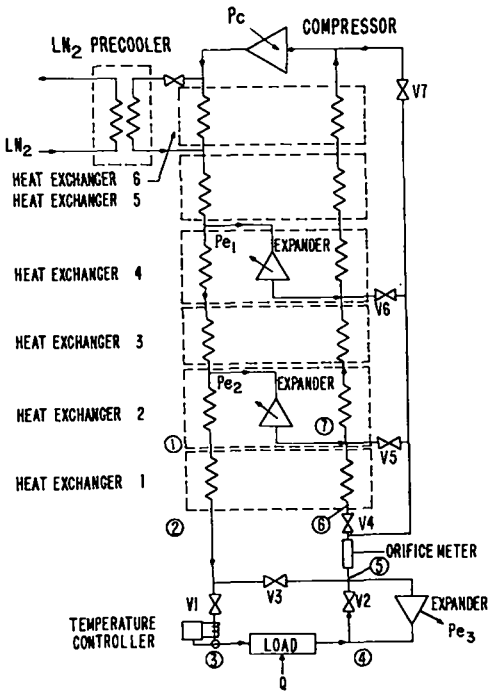

Fig. 4-5.
CTI Model 1400 helium refrigerator and test section flow schematic. P_c = compressor input power. P_e = expander output power.

nitrogen shielded vacuum box (20-m test bed). The long test section was chosen to simulate a power transmission cable with a cooling channel length-to-diameter ratio of 10^5. Both test sections could be heated electrically. The temperature at the inlet of the test section was controlled by a proportional, integral, differential electronic temperature controller equipped with a separate heater. Most of the refrigeration load was applied by the electrical heater in the test sections, with the remaining load coming from the thermal influx and the temperature controller.

Refrigerator performance data were obtained between 4.4 and 16 K for five modes of operation:

1. A bypass mode was performed with valve V5 open and V4, V6 and V7 closed, and with expansion occurring across either V1 or V2. In this mode Hx 1 is fully bypassed. However, some data were taken with V4 open causing Hx 1 to be partially bypassed. All of the other modes of operation given below were with V4 open and V5 closed, thus forcing full flow through Hx 1.
2. A low-pressure, short test section mode of operation was achieved by expansion across V1, causing the test section to operate at an absolute pressure near 100 kPa. Two-phase flow (near 4.5 K) occurred in this mode when the load was less than 75 W; however, increasing the load depletes the liquid and produces a temperature rise.
3. A high-pressure, short test section mode of operation was achieved by expansion across V2, causing the test section to operate at near 1.2 MPa and above 6 K (supercritical conditions).
4. The long test section was operated to produce a large pressure loss in the load with final expansion occurring across valve V2. The inlet pressure was maintained above 1.0 MPa.
5. The long test section was again used with similar pressures, but final expansion was performed in expander 3.

Modes 1 to 3, having little pressure loss, typically resulted in a temperature rise of 1 to 4 K across the test section, with mass flow rates of 3 to 5 g/s. However, modes 4 and 5 resulted in a pressure loss of 400 to 500 kPa accompanied by a temperature reduction of about 0.5 K at the test section exit because Joule-Thomson (JT) cooling occurred throughout the load. The refrigeration obtained is reported below as a function of the maximum temperature experienced in the test section.

The performance of the refrigerator with JT expansion was calculated from the overall energy balance

$$Q = m\,(h_6 - h_2) \quad , \tag{4-1}$$

where m is the mass flow rate, h_6 is the enthalpy at the refrigeration return conditions at point 6 (see Fig. 4-5) and h_2 is the enthalpy at the refrigerator exit conditions at point 2. Helium gas thermometers, silicon diode thermometers, and pressure gauges were used to measure the temperature and pressure at points 2 and 6 for enthalpy determination. The orifice flow meter was first calibrated with water to determine its discharge coefficient. The helium mass flow rate was then inferred by using this coefficient and the helium density as determined by the pressure and temperature measurements.

When the final expansion was performed with expander 3, the refrigerator performance was calculated from

$$Q = m\,(h_6 - h_2) + m\,(h_4 - h_5) \quad , \tag{4-2}$$

where h_4 is the enthalpy before expander 3, and h_5 is the enthalpy after expansion.

The refrigeration calculated by Eqs. (4-1) or (4-2) is the sum of the heater power and the thermal influx to the transfer lines and the test section. The thermal influx to the short test section is about 3 W while the thermal influx into the long test section and transfer lines varied between 65 and 85 W depending on the quality of the insulating vacuum.

The data for bypass mode 1 are given in Figs. 4-6 and 4-7 for low and high pressures in the load. These data are identified by the note "Hx #1 bypassed" or "Hx #1 partially bypassed" and result in the maximum obtainable refrigeration for operation with JT expansion at temperatures above 10 K. Valve V4 should be closed because any flow in the return side of Hx 1 degrades the performance. At temperatures below 10 K, valve V4 should be opened and V5 closed, resulting in the full utilization of Hx 1.

Data for mode 2 with JT expansion before the short test section are given in Fig. 4-6. The two-phase flow points are those at the far left. Increasing the compressor suction pressure increases the mass flow rate and compressor power, resulting in an increased 4.4 K performance (from 72 to 80 W). However, with 96 kPa suction pressure, increasing the load results in themal

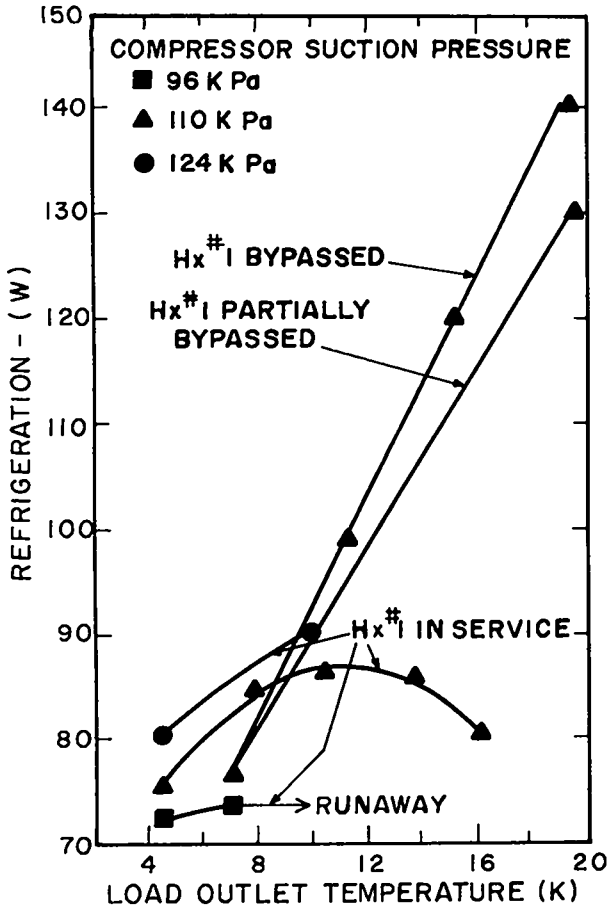

Fig. 4-6.
Refrigeration obtained with low pressure (∿ 120 kPa) in the short test section.

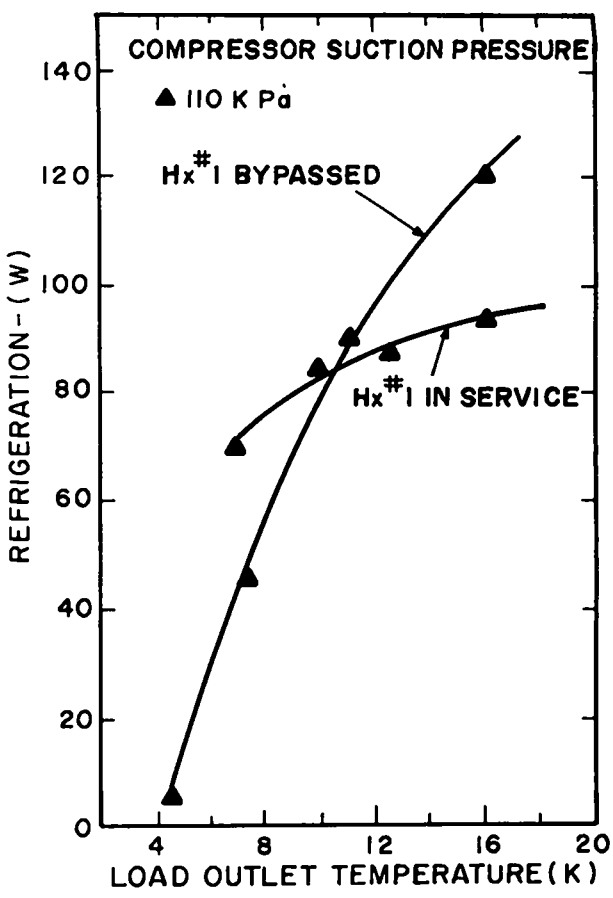

Fig. 4-7.
Refrigeration obtained with high pressure (∿ 1.2 MPa) in the short test section.

runaway in which the refrigerator and load warm to liquid nitrogen temperature and must be recooled. This is to be expected as operating a JT expansion above the critical temperature results in an increased irreversibility at the expansion valve, thus requiring more compressor power. Increasing the suction pressure to 110 kPa increases the compressor flow rate and power sufficiently to allow stable operation at least up to 16 K. Note that as the test section outlet temperature reaches the temperature of the expander exhaust at point 7 (near 8 K), losses occur in Hx 1 that degrade the refrigerator performance. Operation at 124 kPa suction pressure showed improved performance but overheated the compressors at temperatures above 14 K.

Data for mode 3 with JT expansion after the test section are shown in Fig. 4-7 and are identified by "Hx #1 in service." This and all further data were taken with the compressor suction pressure at or above 110 kPa. This mode gives nearly the same performance as the low pressure mode but is not as susceptible to degradation at high test section outlet temperatures because further cooling occurs at the JT expansion.

Data for mode 4 (shown in Fig. 4-8) with the long test section and JT final expansion, were taken with the compressor suction pressure varying from 110 to 130 kPa, accounting for the scatter and increased performance over those of Fig. 4-7. A typical data set represents a test section inlet pressure of 1.0 MPa, an inlet temperature of 10 K, an outlet pressure of 580 kPa, and an outlet temperature of 9.3 K with a flow rate of 4.5 g/s. The same performance can be obtained with a helium refrigerator utilizing JT expansion for either long or short test sections if the overall flow impedance, including the test section and the expansion valve (and thus the flow rates), are equal. However, the temperature and pressure distribution in the test section will be different for each case.

Figure 4-9 shows a temperature recording for mode 4 operation. As the recording proceeds, the flow impedance was increased by partially closing the

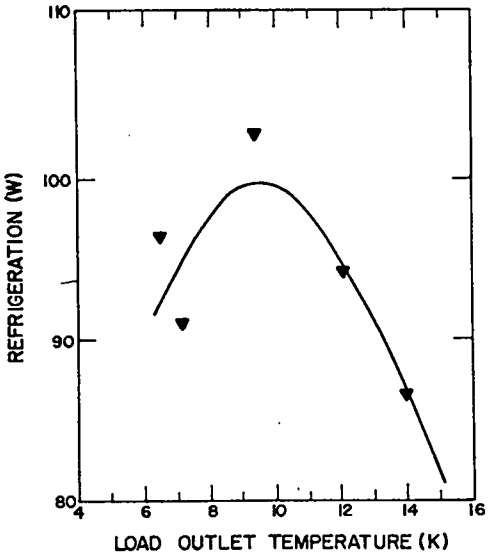

Fig. 4-8.
Refrigeration obtained within the long test section and final JT expansion.

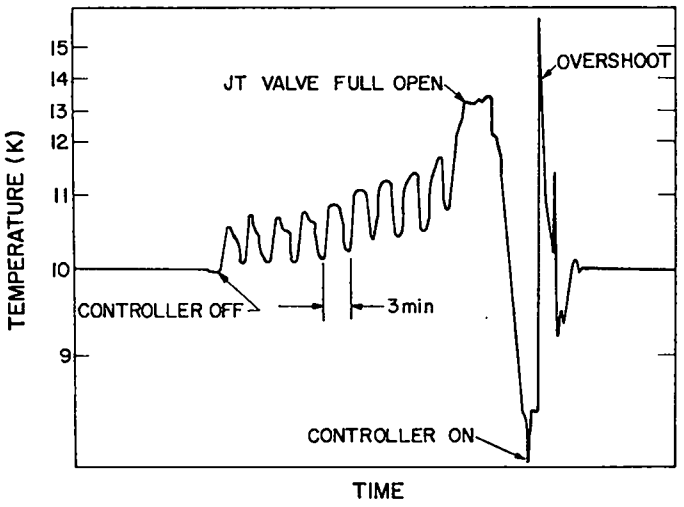

Fig. 4-9.
Temperature-time record as the expansion valve position is partially closed and then reopened.

expansion valve, thus reducing the flow rate in the test section. When the flow rate was reduced to 3 g/s, the temperature controller shut off because the refrigerator could no longer support the load. Density wave oscillations occurred as the test section warmed. The JT valve was then opened and temperature control reestablished.

The data for mode 5, with a large pressure loss in the long test section followed by expansion in expander 3, are shown in Fig. 4-10. This mode gives the maximum refrigeration. However, reducing the pressure loss would allow the expander to produce more work, increasing the refrigerator performance. The loss in performance at lower temperatures is caused by the reduction of the expander efficiency at these temperatures. This expander has an efficiency of 65% with a 12 K inlet temperature and a speed of 500 RPM, but the efficiency drops off rapidly as the inlet temperature or speed is reduced.

The speed of the expanders in the CTI refrigerator (expanders 1 and 2) were kept as low as possible (55-79 RPM) throughout all tests. This was done to keep the temperature at point 7 as high as possible in an attempt to reduce the losses in heat exchanger 1 when operating near 10 K.

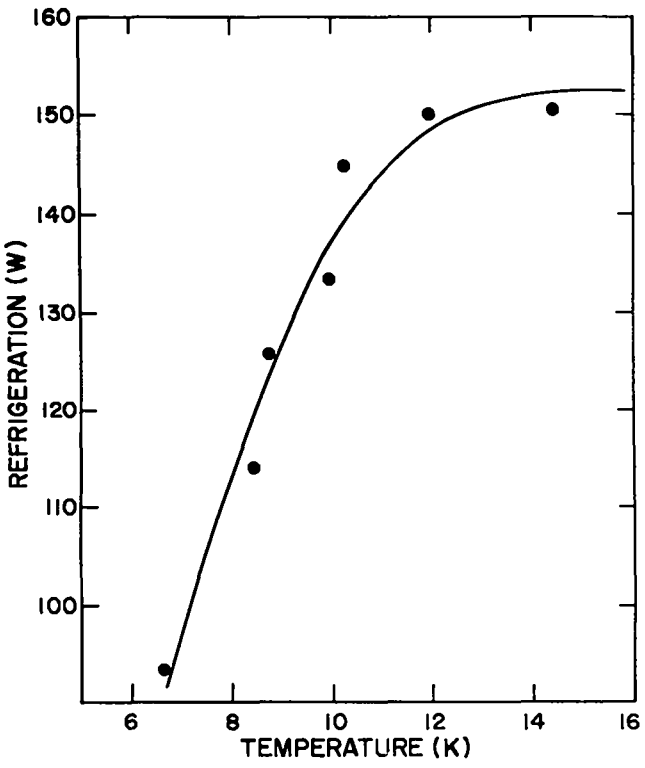

Fig. 4-10.
Refrigeration obtained with the long test section and a reciprocating expander.

It was found that the refrigerator cooled to operating temperature before the long test section could be brought to a uniform cold temperature. The condition existed where gas above 200 K returned from the long test section (at point 4) with Hx 1 cooled to below 50 K. Valve V4 was installed to keep the warm gas out of Hx 1. This gas was then returned to the compressor with V4 closed and V7 open.

The uncertainty in the performance measurements is thought to be ±5%.

The conclusions from this work regarding gaseous helium refrigerator operation are:

1. The compressor suction absolute pressure must be kept near 110 kPa for refrigerator operation above the liquid temperature.
2. Hx 1 should be bypassed when operating above 10 K.
3. The refrigerator can supply 90 W at 10 K with JT expansion, or at least 140 W at 10 K when the expansion valve is replaced by an expansion engine, and should supply even more refrigeration for test sections with lower pressure loss.
4. The same refrigeration performance can be obtained with a refrigerator using JT expansion for either long or short test sections if the flow rates and overall flow impedances (including the expansion valve and test section) are the same.
5. If a test section has a flow impedance that restricts the flow rate below the flow rate required by the refrigerator to achieve a specified performance level, the refrigerator performance will be reduced. Thus, manufacturers of supercritical helium refrigerators need to specify the flow impedance of the load.
6. It is necessary to control the inlet temperature to the test section when operating above the liquid temperature to avoid density wave oscillations and to achieve stable conditions.

4.2.3. Refrigerator Operation and Application. The CTI 1400 refrigerator has been used with the 20-m test bed for superconductor tests and for measuring the temperature profiles of a long tube and its associated pressure drop; with the model superconducting power transmission line for tests of current leads, dielectric and conductor cooling; and with the 2-m test bed for superconductor cooling. This machine has required very little maintenance. The piston seals have been replaced in the expanders and oil seals on the compressor oil circulating system have been replaced.

4.3. Steady State Thermal Analysis of Counterflow Cooling Scheme

The construction of an enclosure to contain a coaxial superconducting cable is made simpler if the go and return helium cooling channels can both be contained within the enclosure inside diameter. This can be done by passing the go helium through the center of the cooling channel of the cable and the return helium through the annular space between the cable and the inside of the cryogenic enclosure. The two helium gas streams exchange heat across the cable (the main thermal impedance is the dielectric material separating the high- and low-voltage conductors). The system acts as if it were a counterflow heat exchanger with poor thermal conductance between streams. The differential equations that govern the heat transfer between gas streams are

$$mc_1 \frac{dT_1}{dx} = Q_1 - GT_1 + GT_2 \tag{4-3}$$

and

$$mc_2 \frac{dT_2}{dx} = Q_2 + GT_1 - GT_2 \quad , \tag{4-4}$$

where T = temperature (K), c = specific heat (J/g•K), m = mass flow rate (g/s), Q = heat flow per unit length (W/m), G = thermal conductance (W/m•K), and x = distance (m); the subscripts 1 and 2 denote respectively go and return helium. Solutions for these equations have been found by Edney, Fox and Gilbert[1] and by Morgan[2] for different boundary and initial conditions. We have verified and rearranged Morgan's solution and have chosen initial conditions appropriate for a dc SPTL.

The solution for the go helium stream is

$$T_1 = -\lambda x + \beta(1-e^{-\delta x}) + T_{10}e^{-\delta x}; \tag{4-5}$$

and the solution for the return stream is

$$T_2 = T_{20} - \frac{c_1}{c_2} T_{10} + \frac{c_1}{c_2} T_1 - \frac{Q_1 + Q_2}{m\, c_2} \quad x \quad , \tag{4-6}$$

where T_{10} = temperature of the go stream at x = 0, T_{20} = temperature of the return stream at x = 0,

$$\lambda = \frac{Q_1 + Q_2}{m\,(c_2 - c_1)} \quad , \tag{4-7}$$

$$\beta = \frac{Q\,c_2}{G(c_2 - c_1)} + \frac{c_2}{c_2 - c_1} T_{20} - \frac{c_1}{c_2 - c_1} T_{10} + \frac{(Q_1 + Q_2)\,c_2 c_1}{G(c_2 - c_1)^2} \quad , \tag{4-8}$$

and

$$\delta = \frac{G(c_2 - c_1)}{m\,c_2 c_1} \quad . \tag{4-9}$$

The thermal conductance is given by

$$G = 2\pi k / \ln \frac{r_2}{r_1} \quad , \tag{4-10}$$

where k = thermal conductivity of the dielectric material, r_2 = outer dielectric radius, and r_1 = inner dielectric radius.

The thermal conductance across the cable wires is relatively large and can be ignored. Values of k = 0.0002 W/cm•K, r_2 = 3.1 cm, and r_1 = 2.5 cm (typical values for a 100-kV, 5-GW cable design to an electrical stress of 20 MV/m) result in G = 0.58 W/m•k. Temperature profiles according to Eqs. (4-5) and (4-6) for two different initial conditions are shown in Figs. 4-11 and 4-12.

Both temperature profiles have a maximum temperature of 14 K and thus are equivalent from the viewpoint of temperature control in operating a Nb_3Sn cable. However, the mass flow rate and the refrigerator design are different for each case. Figure 4-11 shows a decreasing temperature with distance that might enhance superconductor stability, but here the flow rate and thus the cable and enclosure size and cost are larger than these quantities associated with the profile of Fig. 4-12. The profile of Fig. 4-11 requires an expander

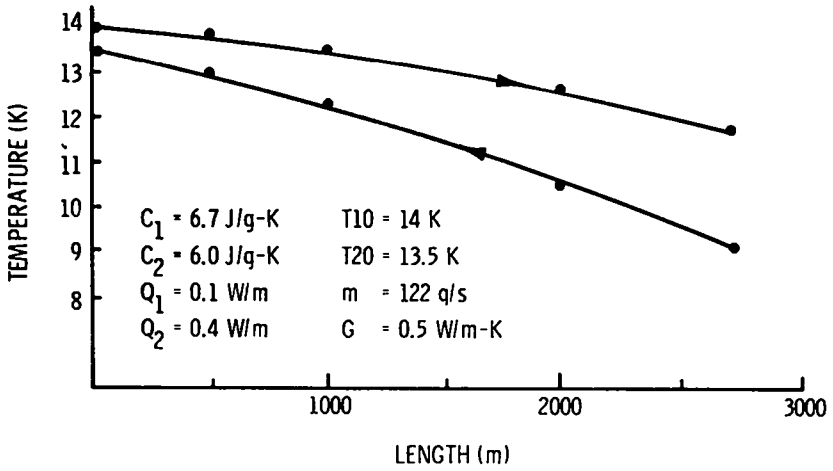

Fig. 4-11.
Temperature profile for go and return coolant streams in the model LASL cable with far end expansion.

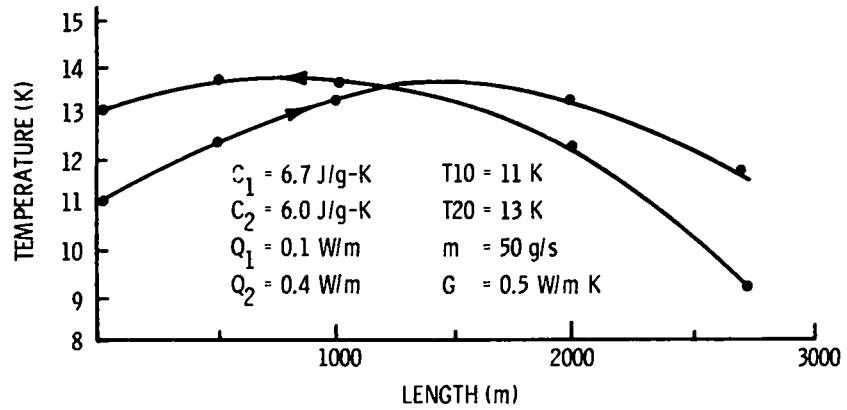

Fig. 4-12.
Temperature profile for go and return coolant streams in the model LASL cable with near and far end expansion.

to be located at $x = \ell$, while the profile of Fig. 4-12 requires an expander at both ends. The refrigerator must be designed to match the desired temperature profile.

4.4. Studies of Unidirectional Flow in Tubes of Large Aspect (L/D) Ratio

Although the LASL dc SPTL design concept involves a counterflowing helium cooling scheme with weak thermal contact between the go and return streams, it was thought prudent first to verify flow and pressure drop equations with single direction flow, as this may be the preferred cooldown arrangement. Accordingly, both computer studies and experimental investigations have been

performed on the transient and steady-state behavior of supercritical helium flowing in "smooth" tubes having large aspect ratios, length/diameter $\approx 1 \times 10^5$.

To achieve an aspect ratio near 10^5 and to match the flow capacity of the flow channel to the pressure and mass flow rate capabilities of the CTI 1400 refrigerator, it was necessary to select an inner diameter near 5 mm and a length near 500 m. By choosing nominal 6 mm o.d. water service copper tubing, (6.4 mm o.d. x 0.76 mm wall), having a measured inner diameter of 4.8 mm, it was also possible to approximate roughly the conductor-cross-sectional-area-to-flow-area ratio that exists in the inner bore of the SPTL design concept. The copper tubing, shipped in coiled 146-m (50 ft) lengths, was first straightened by pulling. No measurable distortion of the cross section occurred during this process. Fifty straight sections of approximately 9.5-m length each were prepared. To conserve tubing, some of these sections were assembled from shorter pieces. These sections were placed into the 20-m test bed in two assemblies of 25 sections each, held by polycarbonate spacers at 1-m intervals, as shown in the photograph in Fig. 4-13. The circuit of 25 turns of 20-m length each was completed by joining the straight sections

Fig. 4-13.
Straight section of 4.8-mm-i.d. x 504-m-long copper tube installed in the 20-m test bed.

with curved sections of approximately 0.5-m length each. See Fig. 4-14. Joints were made with copper tubing fittings over the presawn ends soldered with Sil-Fos brazing alloy. The gaps thus formed by the joints represent an enlargement in diameter of approximately 1 mm and are 1 mm long. The additional pressure drop due to the approximately 125 such joints is less than 0.1% of the total pressure drop and may be neglected. A larger, but still negligible extra pressure drop is caused by the curvature ($r \approx 25$ cm) of the bent sections, the effect being approximately 1%. Eleven carbon-in-glass thermometers were positioned along the flow path for purposes of measuring the temperature profiles. The sensing elements were placed within the flow stream in short (3-cm-long) expanded sections (1/2-in. nominal copper "Tee" fittings) and the leads were brought out via hermetic seals. The exact position of each thermometer was measured both physically and electrically along the completed 504.1-m length of the flow tube. The electrical measurements, made with the ratio function of a digital voltmeter with an external power supply across the ends of the flow tube, agreed with the physical measurements to within $\pm$ 2 cm. This close agreement attests to the uniformity of the 35 coils of copper tubing needed for the flow tube.

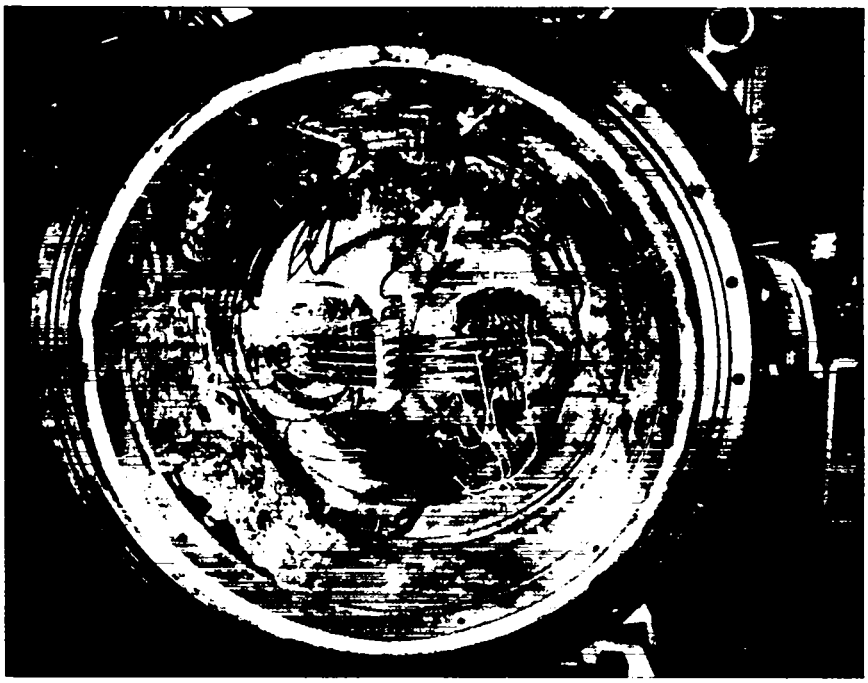

Fig. 4-14.
End of 20-m test bed showing 0.5-m diameter bend of tubing.

The flow tube was terminated on both ends by larger sections, which were connected to the supply and return ports of the refrigerator. Pressure taps were placed in these enlarged sections to measure the inlet and outlet pressure in the flow tube. A 1.0-Ω heater was wound around the inlet section to provide temperature regulation of the inflowing helium by an electronic proportional-integral-differential controller responding to the first thermometer on the flow tube, thermometer #0, located exactly at the 0.0-m position. A second heater of 45 Ω was wound over a 50-cm length beginning at the 43.9-m position and was used to introduce heat pulses to the flowing cryogen from a 0-36 V pulsed dc supply. The flow tube itself, being insulated from ground, was used as a uniform line heater. Current was supplied from a 2-V, 100-A dc pass bank controlled by a 36-V pulsed dc supply. Current leads were short sections of brass, optimized for 10 kA and connected to LN_2-cooled 8-kA cryogenic current leads installed in the test bed. The heat input to the flow tube resulting from the uncooled brass connections was calculated to be 0.06 W each (at zero current) and had no noticeable effect on the temperature profile of the flow tube except during cooling. The line heater enabled the effective heat leak to be varied over a wide range. A cryogenic valve was installed across the ends of the flow tube so that the refrigerator and transfer tubes could be precooled without affecting the initial flow tube temperature profile. An orifice meter was connected in series with the output section of the flow tube to measure the mass flow rate of helium. This meter was bypassed by the cryogenic shunt valve during precooling operations.

The voltage of the thermometer elements was scanned, converted to temperature, recorded, and plotted at regular time intervals as short as 6 s (but usually at 300 s) by the HP 3050A data acquisition system. Up to four selected thermometers also could be continuously monitored by analog strip chart recorders.

4.4.1. Mathematical Analysis. The mathematical model of the present, single-circuit, unidirectional flow problem is shown in Fig. 4-15. A steady-state analysis of such a geometry has been published by Arp.[3] Inasmuch as such a complete analysis is not a trivial problem for even a large computer, and the present analysis seeks to extend the problem to include time dependance, certain simplifying assumptions have been made. As in the work of Arp, radial gradients in the wall and the coolant gas have been ignored, and the

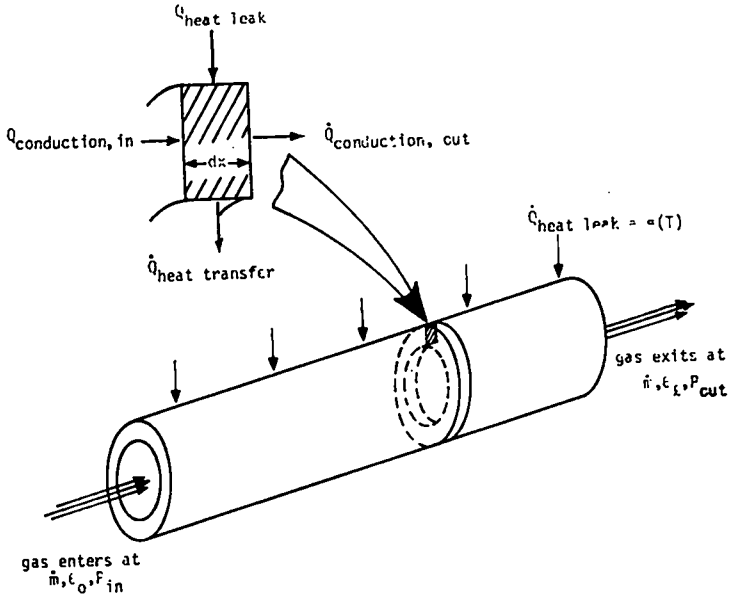

Fig. 4-15.
Schematic representation of the cryogenic flow tube.

mass flow rate of the gas has been taken to be independent of length (but not time). Simple functions were derived from published data on helium[4] to evaluate the thermal properties of the gas over the temperature and pressure ranges of interest. The tube was treated as if it were a homogeneous alloy of copper having a residual resistance ratio equal to 10.0, and the Wiedemann-Franz law was used to calculate the thermal conductivity from a simple fit of published data[5] on the electrical resistivity of copper alloys. Such assumptions and parameterization of physical properties have resulted in enormous time savings on the computer without seriously affecting the accuracy of the results. As can be seen in Table 4-I, the number of distinct thermal and physical properties which must be considered is still large.

We may set up the differential equations which define the response of the system by referring to an annular element dx of the tube as shown schematically in Fig. 4-15. For the wall element we have,

$$c_s \rho_s a_s \frac{\partial T}{\partial t} = \frac{\partial}{\partial x}\left(k_s a_s \frac{\partial T}{\partial x}\right) - hU(T-\theta) + \alpha \ , \qquad (4\text{-}11)$$

TABLE 4-I

NOTATION FOR CRYOGENIC FLOW TUBE STUDIES

Wall properties:

- temperature.....$T(x,t)$
- cross-sectional area.....a_s
- density.....ρ_s
- specific heat.....$c_s(T)$
- thermal conductivity.....$k_s(T)$

Coolant channel properties:

- perimeter.....U
- heat transfer coefficient.....$h(T,\theta,m)$
- friction factor.....f
- hydraulic diameter.....D

Gas properties:

- temperature.....$\theta(x,t)$
- pressure.....$P(m,f)$
- cross-sectional area.....a_g
- density.....$\rho_g(\theta,P)$
- specific heat (at constant pressure.....$c_p(\theta,P)$
- mass flow rate.....m
- velocity.....$v(m,\rho_g)$
- viscosity.....$\eta(\theta,P)$
- thermal conductivity.....$k_g(\theta,P)$
- Joule-Thompson coefficient.....$\mu(\theta,P)$

where $\frac{\partial}{\partial x}\left(k_s a_s \frac{\partial T}{\partial x}\right)$ represents the differential conduction heat rate entering the element; $hU(T-\theta)$ represents the rate of heat transfer to the coolant gas; and α represents the radiant heat leak rate to the wall surface; all per unit length.

For the coolant gas moving past the wall element with the velocity v, we ignore k_g and write

$$\frac{d\theta}{dt} = \frac{hU(T-\theta)}{c'\rho_g a_g} = \left(\frac{\partial\theta}{t}\right)_X + V\left(\frac{\partial\theta}{\partial X}\right)_t \quad . \tag{4-12}$$

Substituting $v = m/\rho_g a_g$, we may write

$$c'\rho_g a_g \left(\frac{\partial\theta}{\partial t}\right)_x = hU(T-\theta) - mc'\left(\frac{\partial\theta}{\partial x}\right)_t \quad . \tag{4-13}$$

The gas flow takes place neither at constant pressure nor constant volume. However, ignoring kinetic energy effects, the heat absorbed by the gas is equal to the change in enthalpy, dH, therefore

$$c' \equiv \frac{dH}{d\theta} = c_p\left(1 - \mu\,\frac{dP}{d\theta}\right) \quad , \tag{4-14}$$

where c_p is the specific heat at constant pressure $\left(\frac{\partial H}{\partial\theta}\right)_p$ and μ is the Joule-Thompson coefficient $\left(\frac{\partial\theta}{\partial P}\right)_H$. Combining Eqs. (4-12), (4-13), and (4-14) yields

$$c_p\rho_g a_g\left(\frac{\partial\theta}{\partial t}\right)_x = hU(T-\theta) + m\,c_p\left[\mu\,\frac{dP}{dx} - \left(\frac{\partial\theta}{\partial x}\right)_t\right] \quad . \tag{4-15}$$

To calculate the pressure derivative we again ignore kinetic energy effects and assume that the pressure drop is due only to frictional effects, whence

$$\frac{dP}{dx} = \frac{32\,f\,m^2}{\pi^2\,\rho_g\,D^5} \quad . \tag{4-16}$$

The dynamics of the system may thus be approximated by Eqs. (4-11), (4-15), and (4-16). To calculate the steady-state temperature and pressure profiles of the wall and the gas, one sets the time derivatives equal to zero and solves the three equations simultaneously, with appropriate boundary conditions. To analyze the transient behavior of the system, it is not necessary to solve the equations, per se. Rather, having arbitrarily specified initial temperature profiles for both wall and gas independently, we need only

evaluate the right-hand sides of Eqs. (4-11), (4-15), and (4-16) at appropriate time and distance intervals. This method lends itself well to high-speed computer techniques. In any case, computerized numerical techniques are necessary because of the extreme nonlinearity of the equations. The solutions are quite sensitive to the size of the time and distance steps and to the ratio $\Delta x/\Delta t$, which must be large relative to velocities inherent to the problem if instabilities are to be prevented. In general, the time interval Δt must be smaller than the thermal relaxation time of the gas to the wall.

At low temperatures, the gas and wall thermally equilibrate with a time constant of approximately 3 ms, and Δt must be set to ~ 2 ms to achieve accurate solutions. For cool-down and thermal pulse propagation analysis, where relatively sharp thermal fronts occur, Δx would have to have been set to ~ 2 cm to represent accurately the temperature profiles along the flow tube. (Note that $\Delta x/\Delta t = 1000$ cm/s is still greater than any observed velocities. Pulse propagation at 10 K occurs as fast as 400 cm/s, being nearly equal to the helium flow velocity.) To follow such behavior over 500 m of length, times as long as 2 h (cool down) would require 3.6×10^6 time iterations of 25 000 points, with numerous calculations for each point. For the pulse propagation studies, where the pulse traverses the flow tube in about 1 min, where "only" 3×10^4 time iterations would be needed, the estimated CDC 6600 computer time is over 14 days! Obviously, it has been necessary to find more approximate methods of calculation.

The heat transfer coefficient h has been evaluated using the classical Dittus-Boelter correlation

$$Nu = 0.023\ Re^{0.8}\ Pr^{0.4}\ , \tag{4-17}$$

where $Nu = hD/k_g$,

$$Re = \frac{mD}{a_g \eta}\ ,$$

and $Pr = c_p \eta / k_g$.

The magnitude of the values of h is large (0.2 W/cm^2·K); and when broad (σ = 1000 cm) Gaussian shaped pulses are considered, typical values of (T-θ) are

always less than several millikelvins. Therefore it is reasonable to assume ideal heat transfer in an attempt to simplify the mathematics. Combining Eqs. (4-11) and (4-15) to eliminate the term in $(T-\theta)$, and assuming ideal heat transfer, i.e., $\theta \rightarrow T$, $\left(\frac{\partial\theta}{\partial t}\right)_x \rightarrow \frac{\Delta T}{\Delta t}$ and $\left(\frac{\partial\theta}{\partial x}\right) \rightarrow \frac{\Delta T}{\Delta x}$,

we arrive at the following equation:

$$(c_s\rho_s a_x + c_p\rho_g a_g)\ \frac{\alpha T}{\alpha t} = \frac{\alpha}{\partial x}\left(k_s a_s \frac{\alpha T}{\alpha x}\right) + \alpha + m\, c_p\left(\mu \frac{dP}{dx} - \frac{\alpha T}{\alpha x}\right) \quad . \qquad (4\text{-}18)$$

Simultaneous numerical solutions of Eqs. (4-16) and (4-18) have been investigated with the aid of the computer, because the nonlinear nature of the equations has not been eliminated by the assumption of ideal heat transfer. The use of Eq. (4-18) allows one to analyze the response of the system with reasonable accuracy in a reasonable amount of computer time.

The steady-state temperature profiles were independently calculated by a computer code (HEHT3, provided by the National Bureau of Standards)[6] which solved the complete set of equations defined by Arp.[3] This code evaluates the variation of thermodynamic properties of the helium gas along the length of the tube, and does not ignore kinetic energy effects. The steady-state profiles calculated by this code are virtually indistinguishable from the steady-state profiles calculated from Eqs. (4-16) and (4-18) (where $\partial T/\partial t$ is set to zero) for the same input parameters. At first, it appeared that it would be necessary to assume approximately 50% higher values for the friction factor than would be predicted by the formula of Koo[7] for smooth tubes in order to bring the computed temperature profiles into agreement with the experimentally determined profiles for the measured mass flow rates, heat leaks, and pressure drops. However, subsequent recalibration of the mass flowmeter revealed an error in the flow measurement. With corrected values of the mass flow, good agreement is obtained between calculated and measured temperature profiles using the friction factors expected for smooth tubes.

4.4.2. Experimental Results of Unidirectional Flow in Tubes of Large Aspect Ratio - Steady State. Depending upon the total pressure drop, mass flow rate, inlet temperature and heat leak, various steady-state temperature profiles can be achieved over the length of the flow tube. Three such profiles and the computed profiles for pressure and temperature are shown in

Figs. 4-16, 4-17, and 4-18. Before recording the data presented in Fig. 4-18, we shortened the flow tube to 321 m, because an unlocatable leak had developed in the flow tube, causing the heat leak in the apparatus to rise to an unacceptable value. Although we thought that the capacity of the CTI 1400 refrigerator could cope with this leak if the tube were shortened, this was not necessary as the removed 183-m section contained the leak; and, in fact, it was then necessary to add approximately 20 W of line heating to balance the refrigerator. The data shown in Fig. 4-18 result from an attempt to balance the total heat leak to the system by the JT cooling effect associated with the pressure drop, so that a nearly isothermal temperature profile could be attained. With the values as shown in the figure caption, the temperature was held uniform to within 0.5 K along the entire length of the flow tube.

4.4.3. Experimental Results of Unidirectional Flow in Tubes of Large Aspect Ratio - Cool-down and Thermal Waves. Two different modes of cool-down were investigated. In the first mode, the radiation shields in the test bed were cooled with LN_2 the day before starting the experiment. The flow tube subsequently cooled uniformly to a temperature near 220 K by radiation and residual gas conduction. The refrigerator and the transfer lines were then

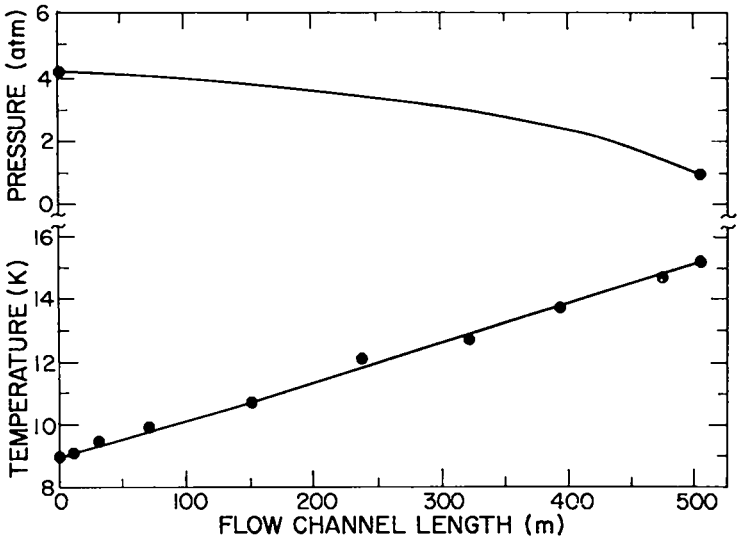

Fig. 4-16.
Pressure and temperature profiles with 0.32-MPa (3.2-atm) pressure loss. Computer input; m = 0.68 g/s, i.d. = 4.48 mm, Q = 0.062 W/m, P = 0.42 MPa (4.2 atm), T_{in} = 9.0 K, ● = data at 1704 on Nov. 12. Solid line is computed value.

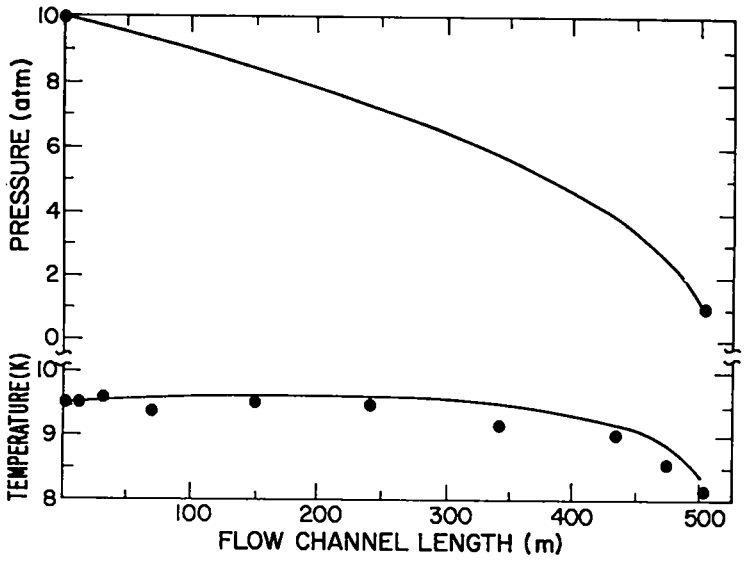

Fig. 4-17.
Pressure and temperature profiles with 0.9-MPa (9-atm) pressure loss. Computer input; m = 2.22 g/s Q = 0.062 W/m, P = 1.0 MPa (10 atm), and T_{in} = 9.5 K. ● = data measured at 0802 on Nov. 17, 1976. Solid line is computed value.

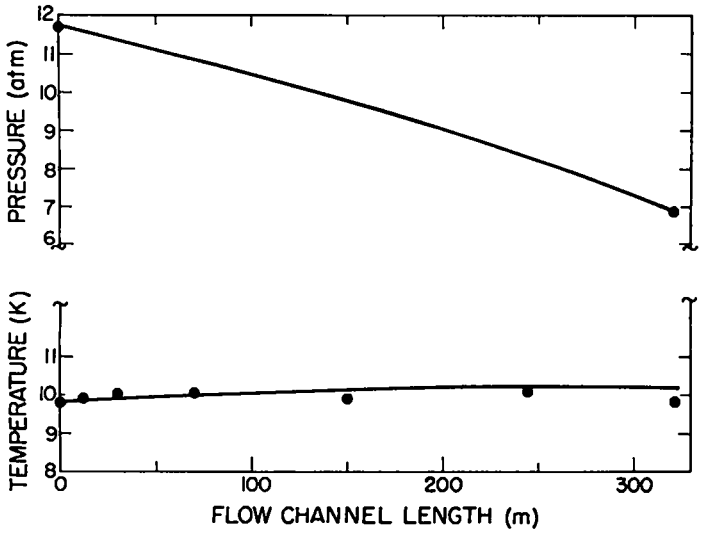

Fig. 4-18.
Pressure and temperature profiles with 0.5-MPa (4.8-atm) pressure loss. Computer input: m = 2.6 g/s, i.d. = 4.8 mm, Q = 0.09 W/m, P = 1.2 MPa (11.7 atm), T_{in} = 9.81 K, f = 0.003, Re = 3 to 4 x 10^5, ● = experimental data at 1505 on June 2, 1977. Solid line is computed value.

cooled to 4 K before allowing cold gas to enter the cooling channel. This step required 3 h.

Figure 4-19 is a representation of the plot obtained from the computerized data acquisition system during the cool-down experiment of Nov. 29, 1976. The original data show that the base line is not constant at 15 K but is being swept by thermal waves caused by temperature variations within the refrigerator. The actual base line varies from 4 K to 25 K, the amplitude of the refrigerator output temperature variation during cooling. The warm section of the line also varied somewhat in temperature, falling to approximately 205 K near the end of the cooling, presumably from conduction by small amounts of gas escaping the line through a small leak.

The principal features of this cool-down mode are a cold inlet section of the cooling channel (4-25 K), a sharp temperature rise with thermal gradient in excess of 100 K/m, and a warm final section of the cooling channel. This form of temperature profile propagates through the 500 m of cooling channel in 1.5 h with mass flow rates starting at 0.3 g/s and increasing to 1.5 g/s. The computer simulation of this experiment, shown in Fig. 4-20 and Fig. 4-21, compares the arrival times of the cold front as determined experimentally and analytically.

Figure 4-22 shows experimental temperature profiles in the second cool-down mode, when the refrigerator and the cooling channel are cooled simultaneously without liquid nitrogen shielding of the cooling channel. The inlet temperature of the cooling channel decreases with time as $T = 300 \exp(-t/75)$ min and the rest of the cooling channel follows with a gentle temperature gradient ($\sim$ 1 K/m). The cool down of the line took 3 h, which was the same as the time it took to precool the refrigerator and transfer line alone in the previous cool-down mode. Therefore the simultaneous channel-refrigerator cool down is to be preferred because the temperature gradients, and thus thermal stresses, as well as the overall time and refrigerator power requirement are less. When the refrigerator is cooled down by itself, the heat exchanger bypass valves must be initially open and the refrigeration that could be used to cool the cooling channel is lost.

The computer-generated temperature profiles shown in Fig. 4-23 are in good agreement with the experimentally determined profiles, on the assumption that approximately 20-min elapsed between when the refrigerator was first turned on and when the first significantly cooled gas reached the start of

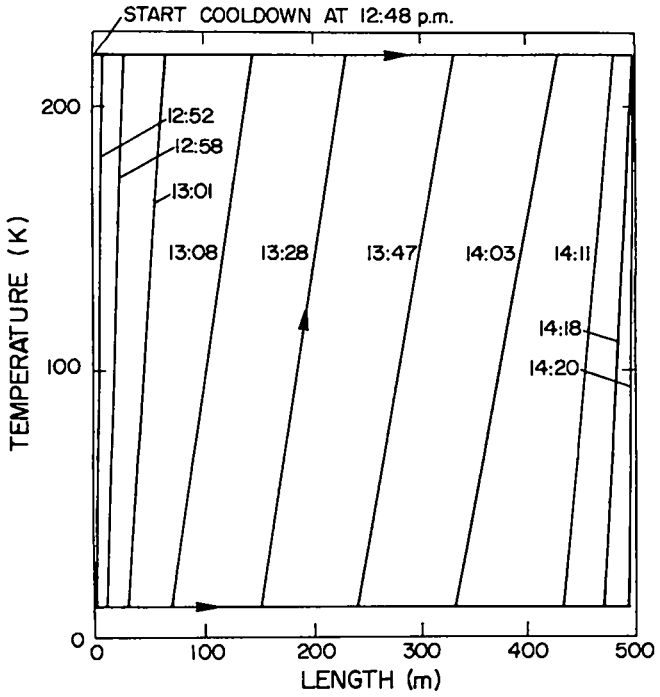

Fig. 4-19.
Line temperature profile with inlet gas at ≈15 K and precooled to 220 K by LN_2 shield. (Numbers on curves are clock time, Nov. 29, 1976.)

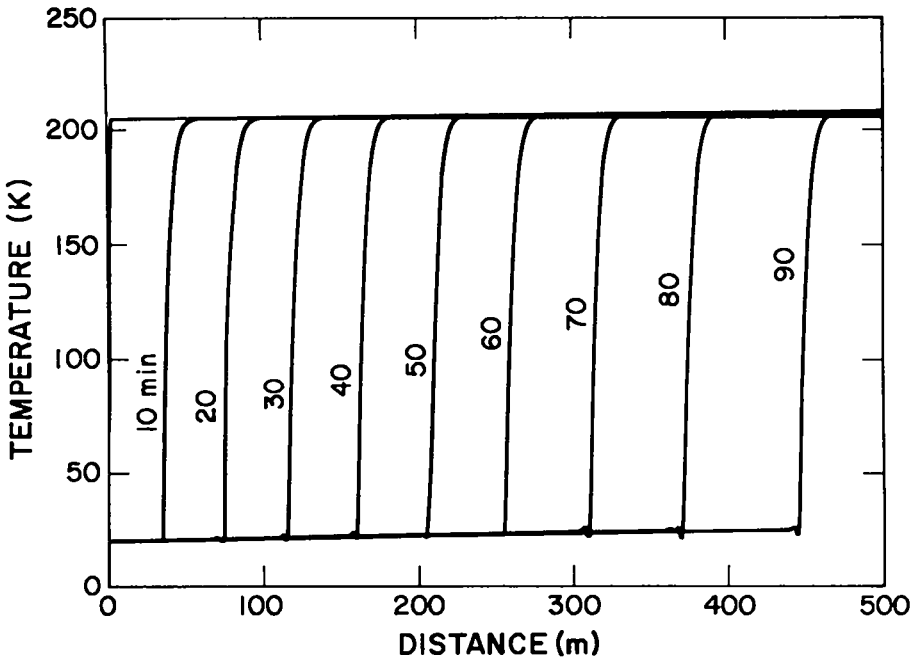

Fig. 4-20.
Computer simulation of the cool-down experiment for which actual data are shown in Fig. 4-19; T(t=0) = 205 K, θ(x=0) = 20 K, P_{inlet} = 0.9 MPa (9.0 atm), P_{outlet} = 0.15 MPa (1.5 atm).

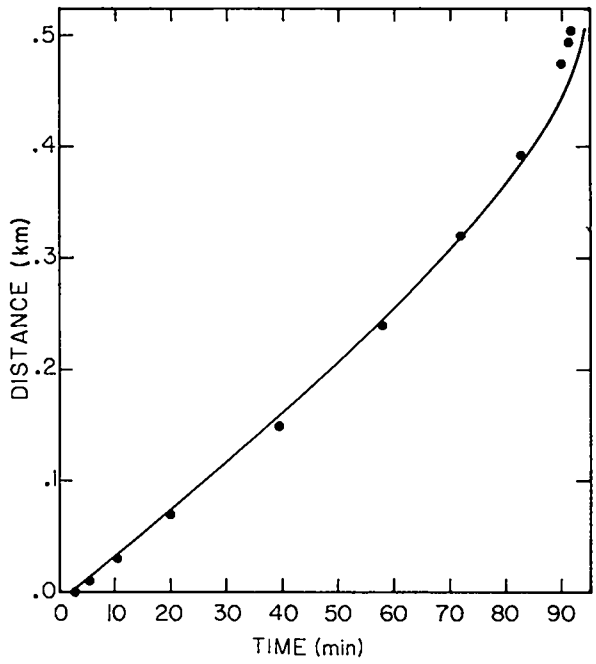

Fig. 4-21.
Arrival time of the cold front vs distance for the cooldown experiment of Nov. 29, 1976. Points represent the experimentally measured data. The solid line is from the computer simulation. This line was shifted forward to coincide with the arrival time of the cold front at the first thermometer. This lag occurs because the by-passed portion of the inlet tube was also warm initially.

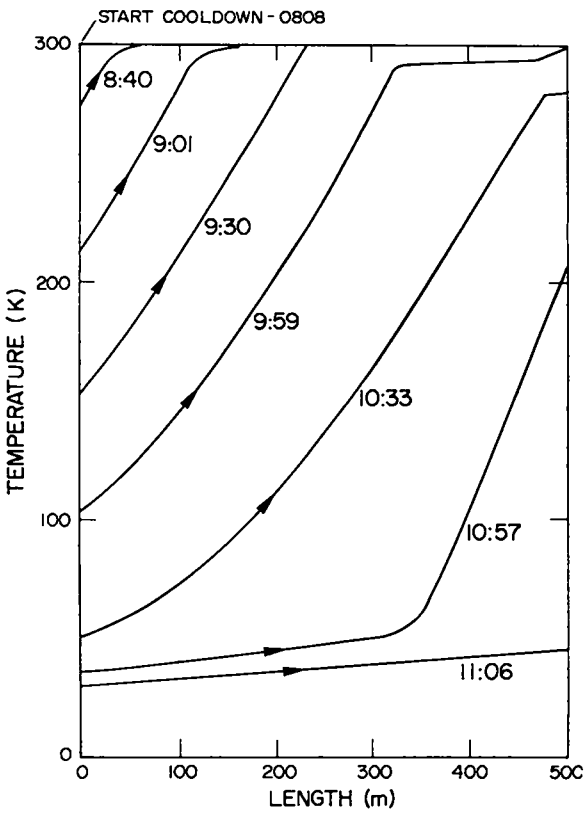

Fig. 4-22.
Line temperature profiles with simultaneous line - refrigerator cool down. Numbers on curves are clock time.

the flow tube. This assumption is in agreement with the experimental data for T(x=0) vs t.

Under various steady-state conditions, thermal pulses were introduced to the flow stream via the 50-cm-long pulse heater by applying up to 28.8 W of energy for times varying from a few milliseconds to 15 s. Thermal waves with amplitudes of approximately 2 K were generated and were seen to travel along the cooling channel at a velocity slightly less than the fluid velocity.

The thermal waves were swept out of the cooling channel, through the transfer lines, and into the low-temperature heat exchanger of the refrigerator. There they exchanged heat with the helium approaching the cooling channel, generating a new thermal wave that was in turn swept through the cooling

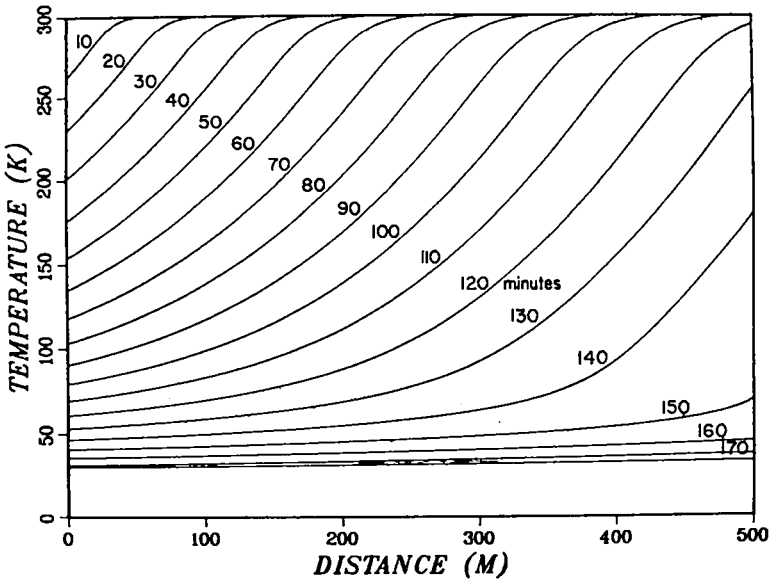

Fig. 4-23.
Computer simulation of the simultaneous cool-down of the flow tube and the refrigerator. $T(t=0) = 300$ K, $\theta(x=0) = 300\ e^{-t/75}$ min, but when $\theta(x=0)$ reached 30 K, it was thereafter held constant. $P_{inlet} = 1.3$ MPa (12.9 atm), $P_{outlet} = 0.09$ MPa (0.9 atm).

channel. Once initiated, a thermal wave proved hard to eliminate. In some experiments, a single wave traveled through the cooling channel more than six times before damping out. In other experiments, a single wave would upset the refrigerator, after which two or three thermal waves of larger amplitude were seen in the refrigerator output stream. It is clear that refrigerator stability and a method of damping thermal waves must be considered.

Computer simulations of thermal pulse propagation under steady-state conditions represented in Fig. 4-17 are shown in Fig. 4-24. These were the conditions under which the thermal pulses were seen to "reflect" from the bottom heat exchanger of the refrigerator and to make subsequent transits of the flow tube. Whereas the total "lap time" of the thermal pulses was approximately 150 s, Fig. 4-24 shows that the pulse requires approximately 85 s to traverse the flow tube itself; hence the remaining time is spent in traveling through the transfer tubes and the bottom heat exchanger. The thermal pulse is damped only slightly in passing through the flow tube (the majority of the broadening effect noted in Fig. 4-24 is due to the pressure drop and the corresponding expansion of the gas); and, under the assumption that the pulse is virtually

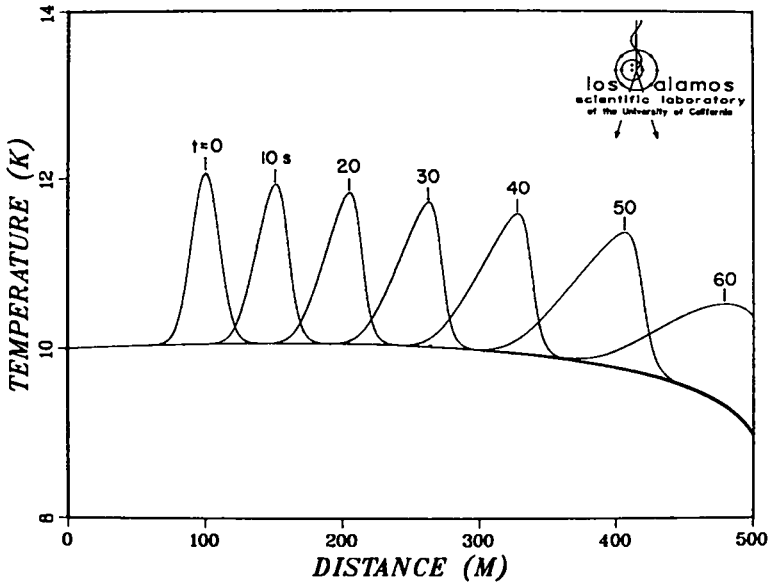

Fig. 4-24.
Computer simulation of thermal pulse propagation under steady-state conditions represented in Fig. 4-17. Here the pulse "heater" is centered over the 100-m position and has generated a Gaussian-shaped pulse of 2 K amplitude at time t = 0. The position of the pulse is shown at 20-s intervals. The cooling effect at the end of the flow tube is due to the JT effect.

totally "reflected" by the heat exchanger, it is apparent such a disturbance could make many transits of the system before becoming appreciably damped.

A more thorough investigation of thermal pulse propagation was performed under conditions similar to those reported in Fig. 4-16. The pressure dropped from 400 kPa at the beginning of the flow tube to approximately 110 kPa at the end, while the temperature along the tube increased from 7.0 K to 12.0 K, due to a radiant heat leak of 0.076 W/m. Energy pulses of 21.6 J (28.8 W x 0.75 s) generated narrow thermal pulses, which were closely monitored by the eight downstream thermometers. The experimental data are summarized in Table 4-II. The observed transit times (velocity) and pulse heights (damping) are in excellent agreement with the computer simulated experiment shown in Fig. 4-25. Broad pulses are used in the computer simulations to decrease the number of points needed for an accurate analysis (and hence to decrease the computation time). Since these broad pulses undergo considerable dispersion, it is slightly inaccurate to compare the propagation rates of the experiment

TABLE 4-II

PULSE PROPAGATION DATA

Thermometer Number	Location (m)	Steady State Temp. (K)	Pulse Height above Steady State (K)	Pulse Transit Time (s)
0	0.0	6.98	-	-
1	10.1	7.09	-	-
2	29.9	7.35	-	-
heater	43.9-44.4		(21.6 J)	0
3	69.7	7.65	2.0	13.5
4	149.7	8.32		46.7
5	239.9	9.35	1.9	76.3
6	321.2	10.00	1.8	96.9
7	392.9	10.66	1.6	111.6
8	473.8	11.58	1.5	123.6
9	494.5	12.01	1.5	126.0
10	504.1	11.97	1.5	127.2

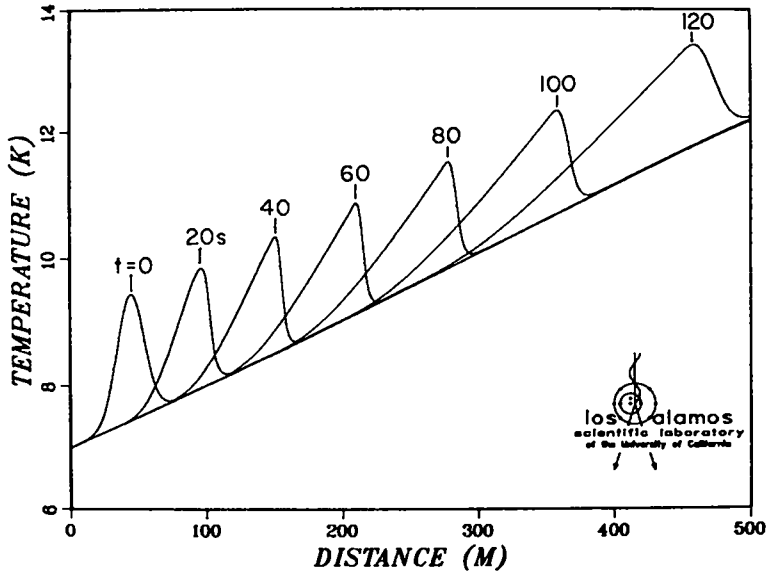

Fig. 4-25.
Computer simulation of thermal pulse propagation under steady-state conditions as reported in Fig. 4-16. The position of the pulse "heater" matches that of the experimental heater, but is wider and generates a Gaussian-shaped pulse.

to computer pulses by looking only at the peaks of the latter. The data in Table 4-II were therefore obtained by assuming that the narrow pulses would propagate with the same velocity as the center of thermal mass of the larger computer-generated pulses. We believe the dispersion in the computer-propagated pulses arises because in the computations the mass flow rate is held constant over the entire flow tube for each time interval. Hence the warmer gas flows faster, producing a thermal shock front. In reality, this is certainly not true, and, in fact, the experimental pulses are observed to have sharp trailing edges and broadened fronts, directly opposite to the computer predictions. A more accurate mathematical analysis would resolve this discrepancy but would require the inclusion of a momentum equation.

4.4.4. Computer Study of Prototype SPTL Cool down. A computer study of a possible cool-down mode was carried out for a 5000-m length of prototype cable (Case B, PECO study, see Sec. 6). This mode of cool-down permits the go and return channels of the cable to be connected in parallel; i.e., helium enters both channels at 2.0 MPa (20 atm) and exits at 0.8 MPa (8 atm) from both channels 5000 m downstream. The remote expander is thus bypassed, and the gas is collected in a transportable compressor-storage unit. The refrigerator is allowed to cool from 300 K to 10 K according to the equation $T_{inlet} = 300 \exp(-t/2)$, where t is in hours. Radial temperature gradients have been ignored, permitting a unidirectional, one-dimensional analysis. Total mass flow rates, again assumed to be uniform but time dependent, are quite high since in such a parallel connection the total pressure difference is applied over the length of the cable. Furthermore, when connected in parallel, the annular return channel carried 1.5 times as much mass flow as does the inner go channel. A practical limit of 200 g/s is set for the refrigerator. Without such a limitation, mass flow rates as high as 500 g/s are calculated for steady-state conditions (i.e., cool-down process completed) with inlet and outlet pressures of 2.0 MPa (20 atm) and 0.8 MPa (8 atm), respectively. However, mass flow rates do not reach 200 g/s until approximately 80% of the cable has been cooled, so that such a limitation has only a small effect on the total cool-down time. Temperature profiles at 6-h intervals are shown in Fig. 4-26, where it can be seen that the total cool-down time is approximately 66.5 h. Mass flow rates reached 200 g/s at the 60-h point, after which the outlet pressure increased steadily to a final value of 1.86 MPa (18.4 atm) when the cable was completely cooled. Note that this is a

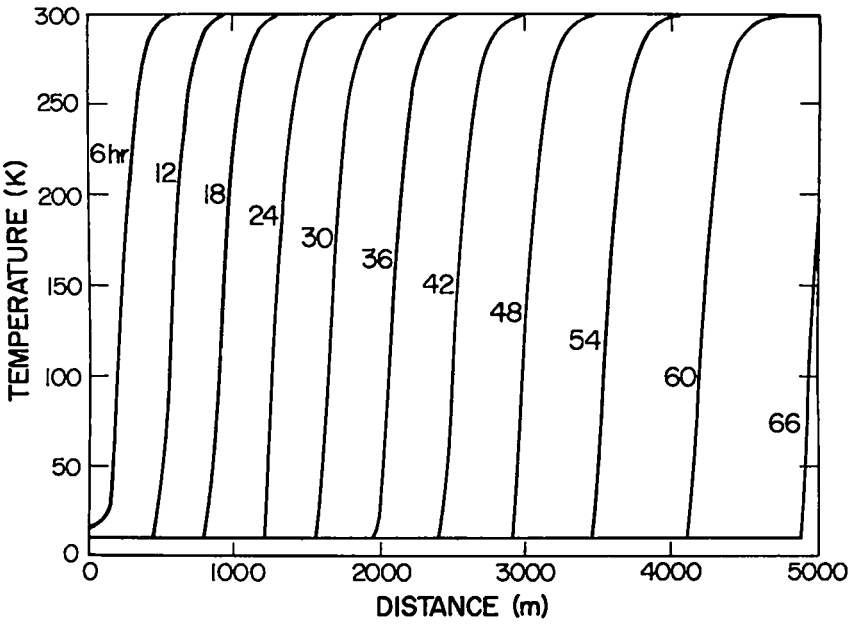

Fig. 4-26.
Temperature profiles during cool-down of a prototype SPTL where the cooling gas flows through both the inner and outer flow channels in parallel. A limit of 200 g/s has been placed on the output capacity of the refrigerator. Without this limit, mass flow rates near 500 g/s would occur after t = 60 h, and the total cool-down time would be 64.6 h.

relatively efficient cool-down mode, because only a small portion of the gas is recovered at temperatures below 300 K, i.e., only that portion which is collected during the last hour of cooldown contains unused refrigeration.

4.5. Current Leads

A pair of current leads, cooled by gaseous helium, were designed, constructed, and installed in the cryoflow loop described in Sec. 4.6 and used during superconducting cable tests.

The steady state behavior of a gaseous-helium-cooled current lead may be analyzed by considering at any given segment the heat balance between a) the differential heating via thermal conduction from neighboring segments, b) local joule heating, and c) cooling via heat transfer to the vapor flowing past the segment;

$$\frac{d}{dx}\left(k\ a \cdot \frac{dT}{dx}\right) + \frac{\rho}{a} I^2 - Uh\ (T-\theta) = 0 \quad , \tag{4-19}$$

where we neglect radial temperature gradients to allow a one-dimensional analysis. Here k is the thermal conductivity of the metal, a is the cross-sectional area of the metal wall, T is the temperature of the metal, θ is the temperature of the gas, x is the distance along the lead measured from the cold end, ρ is the electrical resistivity, I is the current, U is the wetted perimeter, and h is the heat transfer coefficient.

Heat transferred to the helium causes the gas temperature to increase with distance, and, ignoring kinetic energy terms, pressure drop, and JT effects, the heat balance equation for the vapor may be expressed as;

$$m\, c_p \frac{d\theta}{dx} - Uh\,(T-\theta) = 0 \quad , \tag{4-20}$$

where m = mass flow rate and c_p = specific heat at constant pressure of the helium coolant.

For a lead which is cooled by a refrigerator, the mass flow up the lead, m_1, is independent of the rate of heat flow Q_0 out of the lead at x = 0. To maintain the temperature T in the absence of a boiling liquid, however, the refrigerator must also accommodate Q_0 by a separate flow m_2 which is returned to the refrigerator at the bottom end of the coldest heat exchanger.

In general, the combination of Eqs. (4-19) and (4-20) cannot be solved analytically and numerical methods must be used. A useful, simplifying assumption is that the lead material obeys the Wiedemann-Franz Law

$$\rho(T) \cdot k(T) = L\, T, \tag{4-21}$$

where the Lorentz constant $L = 2.45 \times 10^{-8}\, \Omega\, W/k^2$. This is a good approximation for many copper alloys and will be employed in this study.

To facilitate the numerical calculations, a change of variables was made by defining a "thermal impedance" y such that

$$k\, a\, dy = dx \quad . \tag{4-22}$$

Using Eqs. (4-21) and (4-22) and substituting B = kahU and $M = mc_p$ we find that Eqs. (4-1) and (4-2) reduce to

$$\frac{d^2T}{dy^2} - B(T-\theta) + LTI^2 = 0 \qquad (4\text{-}23)$$

and

$$\frac{d\theta}{dy} = \frac{B}{M}(T-\theta) \quad . \qquad (4\text{-}24)$$

Using the Euler method, Eqs. (4-23), (4-24), and (4-22) can be approximated by the following numerical equations:

$$T_{i+1} = 2\,T_i - T_{i-1} + \Delta^2\,B_i(T_i-\theta_i) - \Delta^2\,L\,T_i\,I^2, \qquad (4\text{-}25)$$

$$\theta_{i+1} = \theta_i + \Delta B_i\,(T_i-\theta_i)/M_i, \text{ and} \qquad (4\text{-}26)$$

$$X_{i+1} = X_i + \Delta L\,T_i\,a_i/\rho_i, \qquad (4\text{-}27)$$

where Δ represents equally spaced steps in y.

Values of $\rho(T)$ were calculated from a functional fit to literature data on copper alloys:

where $\rho(T) = \sqrt{(C_1 + C_2 T^2)} + C_3$ (Ω cm)

$C_1 = 8.42269925 \times 10^{-13}$

$C_2 = 7.15805382 \times 10^{-17}$,

$C_3 = \dfrac{2.485376 \times 10^{-6} - 9.18376401 \times 10^{-7} \cdot RRR}{(RRR-1)}$, and

RRR = the residual resistance ratio.

The physical properties of helium gas, assumed to be at 1 atmosphere through the lead, were obtained from analytical fits of the data of McCarty[4] and are given here without attempting to justify the physical significance of the various terms:

thermal conductivity:

$k_g(\theta) = 1.5 \times 10^{-4} + 4.0 \times 10^{-6}\theta + 1.5 \times 10^{-5}\theta^{1/2}$ (W/cm·K),

viscosity:

$\eta(\theta) = 5.023 \times 10^{-6}\,\theta^{0.647}$ g/cm·s and heat capacity:

$C_p = 5.2$ (J/g·K) .

Values of the steady state heat transfer coefficient for turbulent helium gas have been evaluated from a modified Dittus-Boelter correlation as suggested by Yaskin et al.[8]

$$h = 0.023\ Re^{0.8} Pr^{0.4} (\theta/T)^{0.5} k_g/D$$

where

$$Re = m\ D/A_g \eta \quad \text{and} \quad Pr = c_p\ \eta/k_g \quad .$$

For Reynold's numbers below a critical value Re_{crit}, the flow will be laminar and one must use the gas conduction correlation[9]

$$hD/k_g = 4.36 \quad .$$

The performance or efficiency of a refrigerator cooled lead at a given current level is best rated in terms of the reversible refrigerator power requirements:

$$P = a(\theta_o)\ m_1 + b(\theta_o)\ Q_o \quad ,$$

where $a(\theta_o) = -166\ \theta_o + 5600$ is the change in the availability between 293 K and θ_o, and $b(\theta_o) = (293 - \theta_o)/\theta_o$ is the Carnot ratio. The cold end of the lead need not necessarily terminate in a liquid bath. The heat flow Q_o from the current lead to the low temperature environment may be intercepted by a heat exchanger to a gaseous helium stream, m_2, at temperature θ_o obtained from the refrigerator. The real power may be found by dividing by the refrigerator thermal efficiency, which ranges from 5 to 20% for most commercially available helium refrigerators.

A copper heat exchanger tube manufactured by the Spiral Tubing Corporation known as "Biloculine-PTO" was selected as the basic lead element. This heat exchanger tube is constructed from a copper tube twisted in such a manner to form extended fins and is inserted into a round outer copper tube. The round tube is swaged onto the twisted tube, forming three parallel twisted passages for the helium gas. In our use, the center passage of the inner tube is plugged.

Investigations of an element with the finite difference code showed that this element could carry 600 A or more and that additional copper soldered to the outside of the round tube to form a taper (with the larger amount of copper at the top) helps to reduce and broaden temperature peaks at low helium mass flow rates. Results of this investigation are shown in Fig. 4-27. The residual resistance ratios (RRR) for the Biloculine-PTO, the tapered copper, and the solder, shown in Fig. 4-27, are measured values of the material used to construct the lead. The locus of the optimum power as a function of mass flow rate is approximated by the equation P = 5750 m. The ratio m/I = 0.058 g/s•kA at these optimums, except for currents less than 300 A. The refrigeration needed at zero current reaches 100 W as a limit.

A pair of prototype current leads were fabricated for use in the LASL model dc superconducting power transmission line. The cooling capacity of the CTI Model 1400 refrigerator was sufficient to support the cryogenic flow circuit and a pair of current leads rated at not more than 5 kA. Hence each prototype lead was made from seven Biloculine-PTO elements. An "effective" taper of approximately five-fold in cross-sectional area was achieved by adding

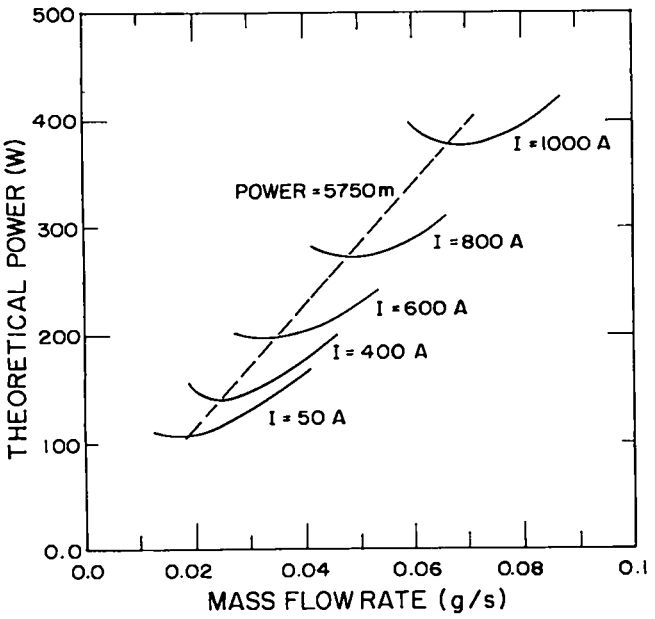

Fig. 4-27.
Investigation of optimum performance for a single lead. T_0 = 10 K, ℓ = 100 cm, copper RRR = 100, Biloculine-PTO RRR = 5, solder RRR = 8.

different lengths of pure copper rods (RRR 100) in parallel. For ease of fabrication, the six shortest rods, ranging in length from 4.1 cm to 43.8 cm, had diameters of 0.635 cm; six rods ranging from 50.2 cm to 72.4 cm long had diameters of 0.476 cm, and twenty-four rods ranging in length from 75.2 cm to 99.8 cm had diameters of 0.259 cm. The Biloculine-PTO elements were first silver-soldered into a heavy copper terminal lug at the top end. The bottom side of this terminal had a 0.3-cm-deep recess into which was silver soldered a 4.45-cm-o.d. tube. The upper 100.3-cm-long portion of the tube is thin-walled stainless steel, and the bottom 9.0-cm-long portion is copper, around which copper tubing coils had been added for heat exchange with the helium coolant stream from the refrigerator. The assembly was inverted and the copper rods were inserted, all coming to rest on the recessed face of the terminal lug. A manifold for directing the helium stream into the annular channels of the Biloculine-PTO was then silvered soldered to the Biloculine-PTO elements and to the 4.45-cm-o.d. copper tube. The 4.45-cm-o.d. composite tube was then heated and completely filled with soft solder through pre-cut vents. In this manner, the Biloculine-PTO elements and the copper rods are thermally and mechanically joined into a rigid structure. The free length of each prototype lead, i.e., that portion between the terminal lug and the copper-walled heat exchanger, is exactly 100.0 cm. Over this length, the cross-sectional areas of the Biloculine-PTO elements, copper rods, and soft solder are, (assuming the area of the copper rods to be a linear, not stepwise function of length), exactly seven times the values assumed in the calculations shown in Fig. 4-27.

Performance tests demonstrated that the refrigerator could support a pair of these leads operating at 4500 A continuously, with a cold end temperature T_o = 10 K. The measured voltage drop across the leads was as calculated. These leads were operated at 7000 A for a period of 10 min before T_o exceeded 13 K and the superconducting cable attached to the leads were driven normal, terminating the test.

4.6 Cryoflow Loop Tests

We have integrated the CTI Model 1400 refrigerator with an 18-m section of cryogenic enclosure to form the basic elements of a system for testing full-scale cryogenic components for a dc SPTL. The inlet and outlet tubes of the refrigerator both penetrate at the same end of the enclosure. For simplicity, we call this test system the "Cryoflow Loop," although as additional components

have been added, the complexity has increased to the point where the system has become a model for a low-voltage dc SPTL. Initial tests on the Cryoflow Loop studied the cryogenic performance of the enclosure itself. Then a conventional high-pressure-oil-filled cable together with a remote expander (at the far end with respect to refrigeration leads), were added to the system to provide a simulation of the counterflow cooling scheme proposed for the dc SPTL. Current leads were then added to the system, and, finally, superconducting subcables were installed to permit the dc SPTL model testing as well as testing of long lengths of superconductor under near operating conditions. These successive steps are described below.

4.6.1. Enclosure Performance. A 10-cm-i.d. by 17.7-m-long enclosure was obtained from Cryenco, Inc., installed, as shown in Fig. 4-28, and hooked into the CTI Model 1400 refrigerator. The 16.83-cm-o.d. enclosure is supported mainly in the open air, but one end penetrates the wall of the building, enters a braid-covered expansion joint, and terminates in a cylindrical section. The end cover plate of this section is removable for instrument and cable installation. Smaller cover plates for future current leads are visible on penetrations located vertically and at 45^{o} to the cylindrical section. Refrigeration piping rises vertically from the back of the cylinder and runs to the helium refrigerator, visible in the background of the photograph. The electronics rack holds temperature-measurement and temperature-control instrumentation. Figure 4-29 shows the helium refrigerator with the enclosure in the background.

The enclosure has seven carbon-in-glass thermometers distributed along its length. The locations of these thermometers and one set of readings are shown in Fig. 4-30.

The performance of the enclosure is derived from

$$Q = \dot{m}\, c_p \frac{\Delta T}{L} \quad , \tag{4-28}$$

where Q = thermal influx in W/m, m = the refrigerant mass flow rate, c_p = the specific heat, and ΔT = the temperature rise along the length L of the enclosure.

Thus the computation of the thermal influx depends on measuring the mass-flow rate and the temperature rise, as well as determining the specific

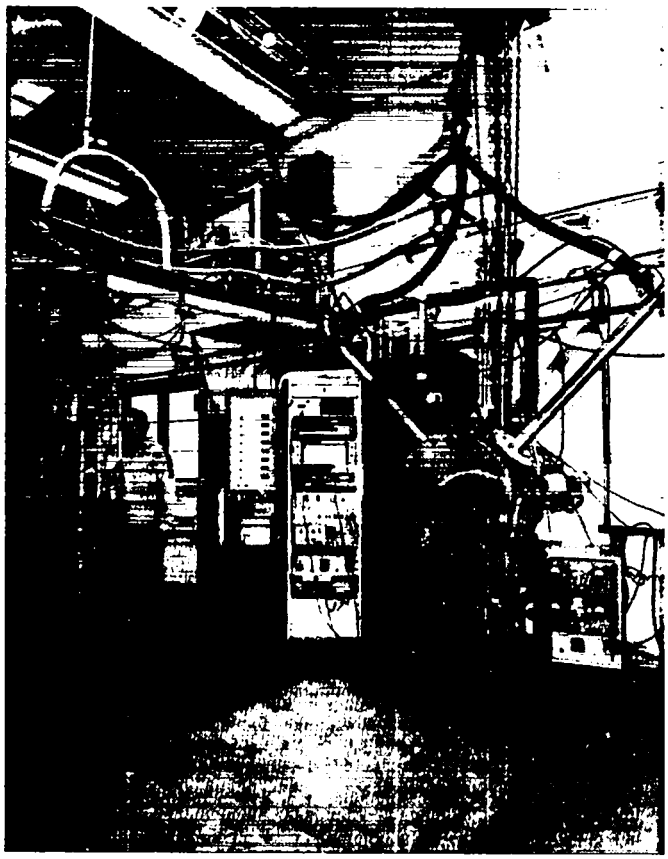

Fig. 4-28.
Cryenco enclosure installation.

heat of the gas. On the basis of our previous work on orifice meter development, the mass-flow was computed to be 1.86 g/s. The specific heat of the gas was obtained as 5.4 J/g•k from helium property tables[4] for a measured temperature of 11 K and a pressure of 1.48 atm. The slope of the line is 0.033 K/m, as plotted in Fig. 4-30, resulting in a heat leak value of 0.33 W/m.

This value of Q was reached after we operated the refrigeration system for eight days. The initial reading was 0.5 W/m, but was reduced to a range of 0.25 to 0.35 W/m after three days of operation. The input temperature within the enclosure could be controlled to within $\pm$ 0.05 K. The vacuum at the enclosure terminations varied between 10^{-6} and 10^{-7} torr, while the vacuum at the center (read on an external port) was 10^{-4} torr. The best estimate of the enclosure performance is 0.3 W/m; the design goal was 0.25 W/m with a guaranteed performance of 0.5 W/m.

Fig. 4-29.
CTI Model 1400 helium refrigerator.

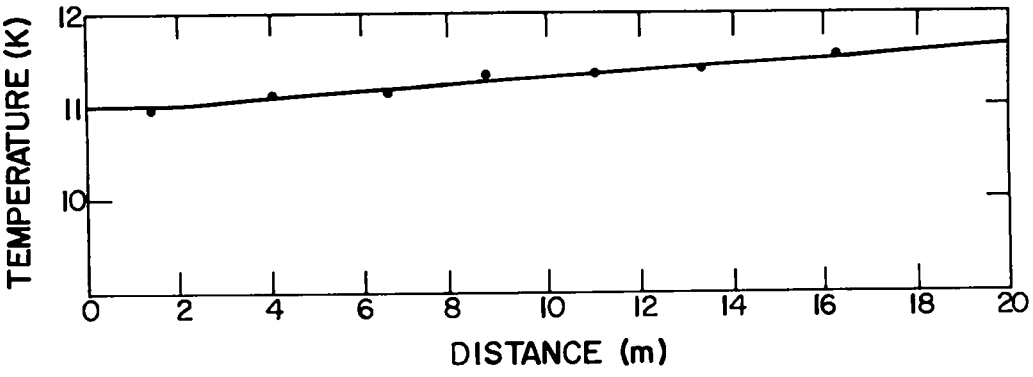

Fig. 4-30.
Thermometer location and a typical temperature profile for the Cryenco enclosure.

When a high-pressure-oil-filled cable (see Sec. 4.6.2.), with a mass of 13 kg/m, was loaded into the enclosure, measurements revealed that the thermal influx into the enclosure had increased to 1.3 W/m. The compressive load on the spacers and multilayer insulation must have reduced the effectiveness of the thermal insulation. It appears that more enclosure development work is required to find a supporting system that can withstand the load while maintaining the insulation properties of the enclosure.

4.6.2. Cable Effective Thermal Conductivity Determination. A 300 kV dc high-pressure-oil-filled cable manufactured by the Phelps Dodge Co., shown in Fig. 4-31, was drawn into the cryogenic enclosure. The inner copper tube and the outer lead sheath were joined at both ends so as to provide a seal between the helium gas and the oil impregnating the paper tapes forming the dielectric material of this cable. The oil-filled cable provided a thermal impedance that allowed us to check the experimental temperature profile against the theoretical one and to estimate the value of this thermal impedance.

A reciprocating expander was fitted at the end of the enclosure remote from the refrigerator. Ten-atmosphere, 10 K helium entered the cable and traveled down the center cooling channel before it was expanded to 1 atm and

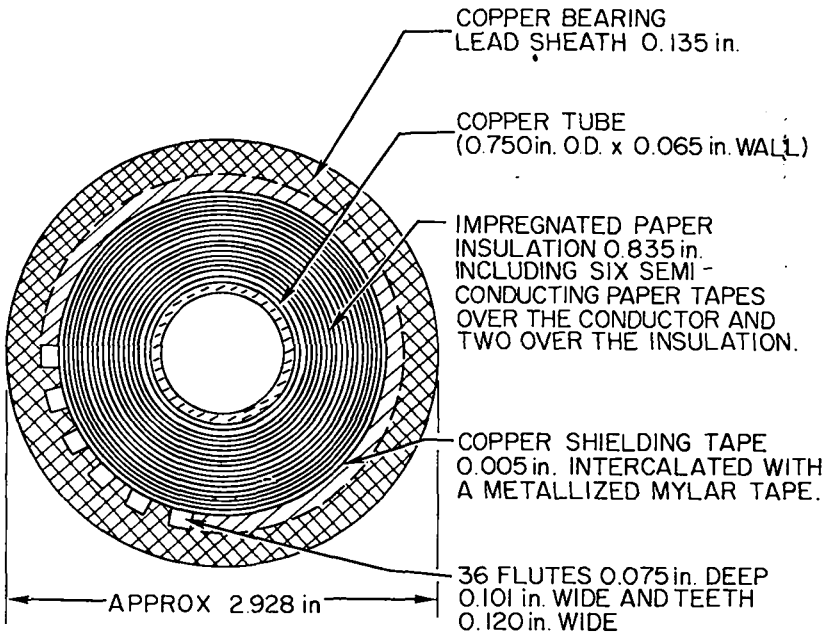

Fig. 4-31.
Phelps Dodge high pressure oil filled cable.

5.7 K. This low pressure helium returned in the annular gap between the enclosure and the cable, where it was heated by the thermal influx across the thermal insulation of the enclosure. This 3.0 g/s flow of helium left the enclosure at a temperature of 7.3 K and was returned to the refrigerator heat exchangers. The temperature profile of the helium throughout the cable is shown in Fig. 4-32 and is similar in shape to the profile of Fig. 4-11 because, again, only far-end expansion was used.

An analytical expression for the temperature profile is given by Eqs. (4-5) through (4-9). These equations were used with trial values of the thermal conductance to compare the analytical to the experimental results. It was found that only a thermal conductance value of 0.1 W/m K resulted in a fit everywhere within $\pm$ 0.1 K.

The effective thermal conductivity (includes inner copper tube, tapes, and outer lead sheath) was then calculated from the rearrangement of Eqs. (4-5) through (4-10) as

$$k = G \ln \frac{r_2}{r_1} / 2\pi \quad .$$

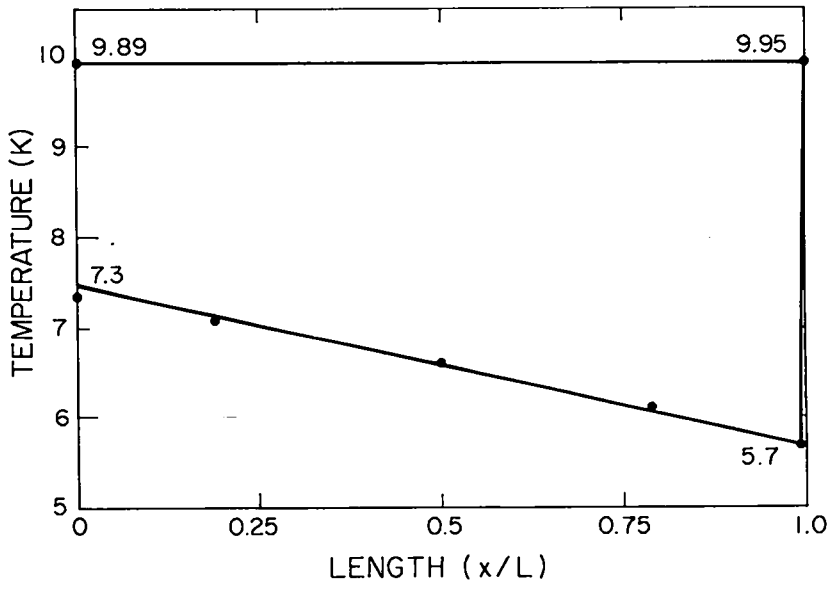

Fig. 4-32.
Temperature profile in the cryoflow loop containing a conventional high-voltage cable and a single superconducting subcable in the central helium cooling channel.

The results of this calculation are k = 0.036 W/m•K. This value is sufficiently low to make the proposed cooling scheme practical for long distance (> 20 km) applications.

4.6.3. Superconductor Cable and Subcable Tests in the Cryoflow Loop. Originally the goal of the dc SPTL program was to have been a demonstration test that would have been as close to actual use conditions as possible. This was intended to include a full current test and a separate high voltage test. With the reorientation of the program, we decided to come as close to this goal as possible with the materials and equipment on hand. Several intermediate tests have led to the testing of a cable consisting of three subcables, each of which, in turn, is composed of 19 individual strands of mf Nb_3Sn superconducting wire (see Sec. 5.4.2.).

An initial experiment was made with a single 18-m-long subcable reacted at 750°C for 64 h. The conventional high-voltage cable was left in the cryoflow loop and the superconducting subcable installed in the central 1.8-cm helium cooling channel. A return current path, also 18-m long, was made from the superconducting tapes previously tested in the 20-m test bed. These tapes were installed in the return helium space which is in the annular gap between the high-voltage-cable outside diameter and the enclosure inside diameter. The temperature of the return path was always colder than the cable under test in the central helium cooling channel (see the temperature profile in Fig.4-32), and the current-carrying capacity of the return path was intrinsically greater than that of the subcable. Thus the initiation of any normal zone occurred in the central cable under test. The temperature in the test section was held constant to within $\pm$ 0.1 K along the 18-m length, and the current was increased until the voltage reading across the sample indicated that the cable had become resistive. This voltage activated a circuit breaker that shut off the current and protected the cable.

The second run was made with three Supercon subcables installed in the central cooling channel. The tapes in the return helium space were replaced with three similar conductors. The cryoflow loop was then cooled to operating temperatures and the critical current determined as a function of the critical temperature.

The cryoflow loop can be cooled to a uniform temperature of 8 K in the test section when the current is off and no joule heating occurs in the current leads. However, joule heating in the current leads results in increasing

the test section operating temperature. It was found that the test section could be maintained at 5 kA and 12 K continuously, but lower temperatures and higher currents could be reached for operating periods of 5 to 10 minutes.

The results of the critical current vs temperature for both the one- and three-subcable tests are shown in Fig. 4-33. From the slopes of the 2 lines it can be shown that 3 cables operating in close proximity are able to carry 80% of three times the current of a single cable operating by itself.

Recovery of the subcables, after being driven normal, was rapid and without incident. Helium gas temperature at the outlet of the test section did not rise more than 1 or 2 K over the operating temperature during a quench, and the current could be reapplied within the time it took to reset the current source.

4.7. Equipment

The cryogenic engineering section has been responsible for the design, fabrication, and installation of several important pieces of equipment.

4.7.1. The 100-kV Dielectric Test Cryostat. Figure 4-34 shows a schematic diagram of a flow cryostat capable of providing a controlled environment of pressure and temperature during and after the cool-down process. Helium gas obtained from a LHe storage Dewar (or helium refrigerator)

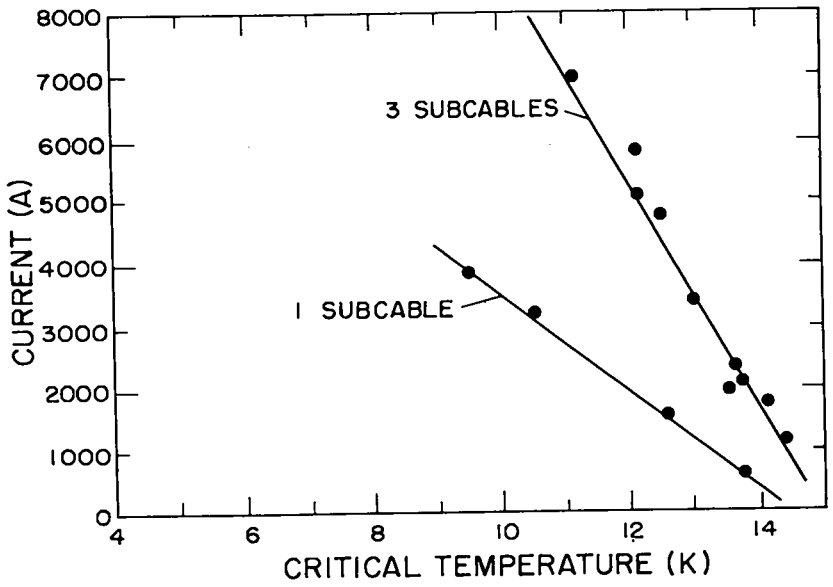

Fig. 4-33.
T_c characteristics for Supercon subcables.

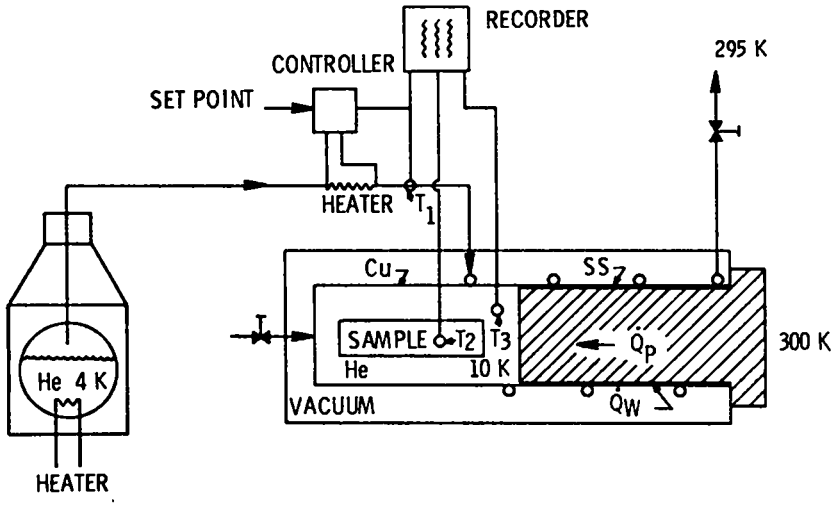

Fig. 4-34.
Schematic of dielectric test cryostat.

flows to a heater regulated to produce a gas temperature as demanded by the controller set point. This controlled-temperature gas enters a cooling coil wound around a copper cylinder with a stainless steel extension and leaves at room temperature. Heat conduction down the wall Q_W is intercepted by the helium gas stream; thus, the stainless steel tube acts as a gas cooled strut. An insulating plug fills the entrance of the stainless steel tube. Heat conduction through the plug is Q_p. The sample chamber at the end of the stainless steel tube and plug is insulated by vacuum and nitrogen shields (not shown).

The thermal stress occurring in a bar sample during cool-down is approximated by the expression,

$$\sigma_T = E\,(\alpha_1 - \alpha_2)\Delta T - \delta_2 \,, \tag{4-29}$$

where E = modulus of elasticity, α = thermal expansion coefficient, ΔT = temperature difference between ambient and operating conditions, δ = deformation of support. The subscripts 1 and 2 refer respectively to the sample under test and the supporting material. In order to avoid stresses in the sample that exceed the yield point during cooling, either the temperature gradient must be limited, or the support must have the same thermal expansion coefficient as the sample, or the support must deform under load. The deformation can be controlled by proper construction of the sample holder, while the temperature gradient can be controlled by the cryostat design and operation.

Figure 4-34 shows locations for three thermometers (T_1, T_2, and T_3) to measure and record the temperatures of the cooling gas, of the sample, and of the pressurizing helium. However, several thermometers must be attached to the sample during initial runs in order to monitor temperature gradients. Cooling rates can then be controlled to assure that the temperature gradients and resulting thermal stresses are small.

The results of calculations of Q_W for a gas-cooled strut are presented in Fig. 4-35. The dimensions of the length L and the Area A have been chosen to allow a thermal load of about 0.1 W with a liquid helium use of 1 to 2 ℓ/h.

A 2.4-m-long x 0.15-m-i.d. flow cryostat, intended for dielectric experiments up to 100 kV, has been assembled and tested. The results show that about 3 h of precooling with liquid nitrogen and 2 h of cooling with

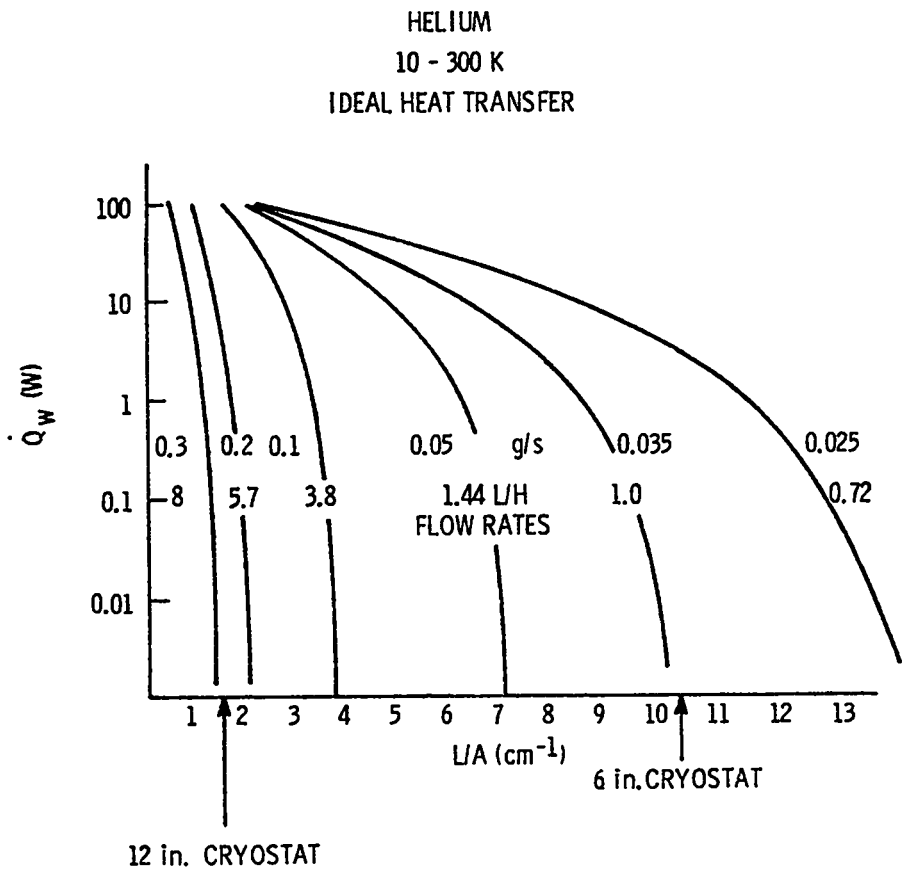

Fig. 4-35.
Heat influx down the cooled support tube of the dielectric test cryostat.

helium are required to reach a state of 10 K and 15 atm using 30 ℓ of liquid helium. This can be reduced to about 2 h total if the pressure is maintained at 1 atm. Most of the dielectric testing has been done in this cryostat, shown in Fig. 4-36.

A horizontal test of this cryostat showed that the heat leak through the connection in the gap between the bushing and the cryostat wall is excessive. The cryostat failed to reach operating temperature in this position.

4.7.2. The 300-kV Dielectric Test Cryostat. Breakdown in the 100-kV dielectric cryostat occurs between the electrode and the wall across the cold helium near 150 kV. Thus, this cryostat is used for nominal 100 kV work. Another cryostat, capable of operating at 300 kV, shown in Fig. 4-37, was constructed for higher voltage experiments. This cryostat has a horizontal test section, but the bushing is vertical to avoid the natural convection

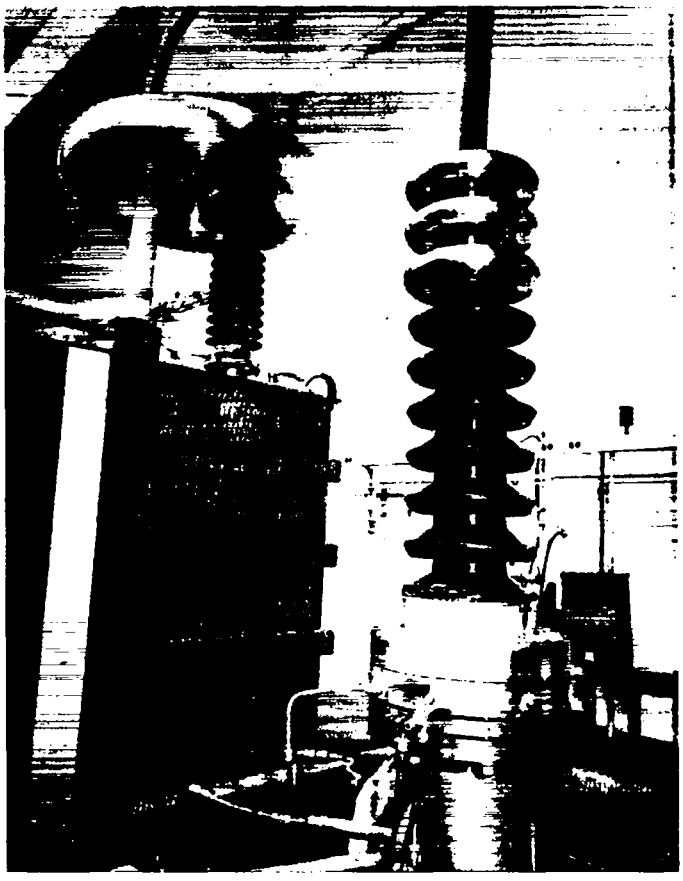

Fig. 4-36.
The 100-kV dielectric test cryostat.

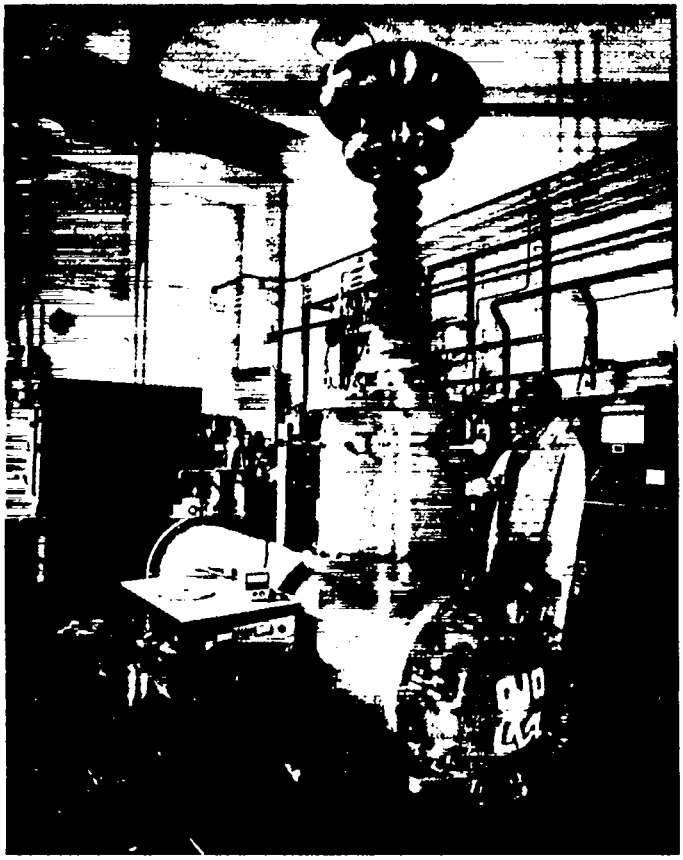

Fig. 4-37.
The 300-kV dieiectric test cryostat.

problem at the bushing. The sample is loaded horizontally through a cold seal developed especially for this tank. This 300-kV cryostat is now available but has not been placed in service because of the reduced program effort.

4.7.3. 2-m Test Bed. A 2-m test bed was designed and constructed to facilitate the testing of high-current cables and subcables up to 1.5 m in length, at temperatures from 4 to 18 K, using the CTI 1400 refrigerator for sample cooling. Present potheads will allow 10-kA operation, but 25-kA terminals have been designed, and critical components have been purchased. The philosophy of the 2-m test bed is to allow rapid change of samples and provide convenient, extensive instrumentation of temperature, voltage, current, joint resistance, and magnetic field. A new data acquisition system has been purchased primarily for use with this test system. An isometric drawing of the test bed is shown in Fig. 4-38. Unfortunately the decrease in program effort has made it impossible to make use of this test apparatus.

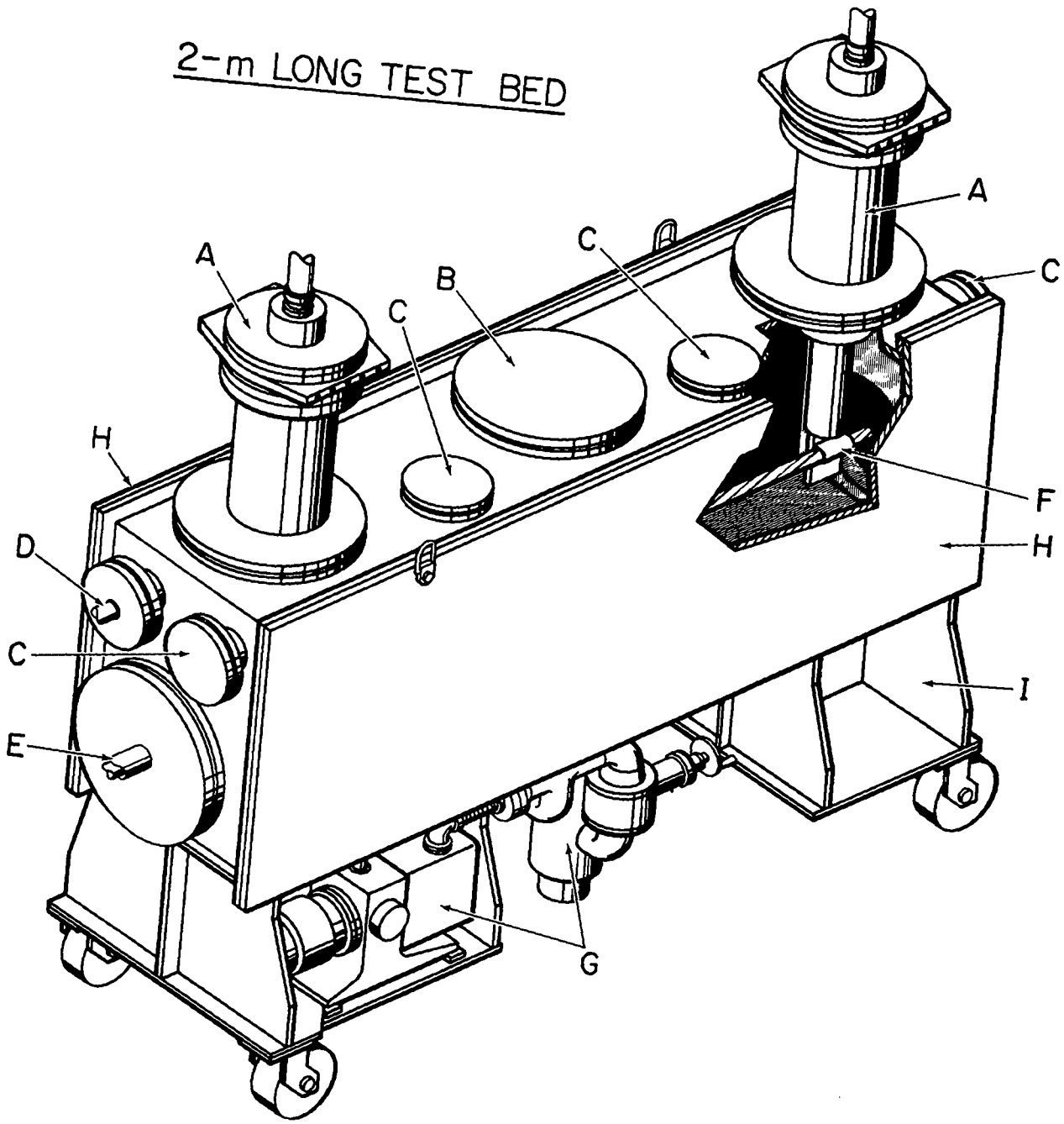

Fig. 4-38.
2-m vacuum chamber for testing cables to 25 kA at temperatures from 4 to 18 K. Components include A. pothead assembly with its helium dewar, vapor exhaust and high current header plate, B. port for installing a superconducting magnet to provide a transverse field on the test sample, C. instrumentation ports, D. liquid nitrogen inlet for cooling full radiation shield, E. inlet for helium cryogen from nearby refrigerator (sample cooling only), F. cutaway view showing connection of sample to high-current lead and outlet path of helium cryogen, G. self-contained high-vacuum system, H. double O-ring-sealed access door to provide full access to sample area, and I. instrument rack for monitoring vacuum in chamber.

4.8. References

1. K. Edney, M. Fox, and G. Gilbert, "Longitudinal Temperature Distribution in Low-Temperature Cables with Counterflow Cooling," Cryogenics 7, 355-358, (1967).

2. G. Morgan, Brookhaven National Laboratory, personal communication.

3. V. Arp, "Forced Flow, Single Phase Helium Cooling System," in Advances in Cryogenic Engineering, K. D. Timmerhaus, Ed. (Plenum Press, NY, 1972), Vol. 17, pp. 343-351.

4. R. D. McCarty, "Thermophysical Properties of Helium-4 from 2 to 1500 K with Pressures to 1000 Atmospheres," National Bureau of Standards (US), TN 631, (1972).

5. A. F. Clark, G. E. Childs, and G. H. Wallace, "Electrical Resistivity of Some Engineering Alloys at Low Temperatures," Cryogenics 10, 295 (1970).

6. V. Arp, National Bureau of Standards (US), personal communication.

7. E. C., Koo, D. Sci Thesis in Chemical Engineering, Massachusetts Institute of Technology, 1932.

8. L. A. Yaskin, M. C. Jones, V. M. Yeroshenko, P. V. Giarratano, and V. D. Arp, "A Correlation for Heat Transfer to Supercritical Helium in Turbulent Flow in Small Channels," Cryogenics 17, 549 (1977).

9. M. C. Jones, Colorado School of Mines, personal communication.

5. CABLE DEVELOPMENT

5.1. Introduction

The Cable Development Section of the LASL dc SPTL project has had the task of choosing a superconductor for the dc SPTL and developing it into a cable. The early stages of this task required tests and development of new superconductors. Once suitable parameters were established, Nb_3Sn was selected as the superconducting material, and the effort then shifted to engineering this material into a conductor suitable for a dc SPTL.

In the initial phase of superconductor selection, emphasis was placed on understanding the current-limiting mechanisms involved in carrying large currents with zero applied fields, as previous work on superconductors by others had concentrated on high-field behavior, as required for magnet fabrication. Our studies included determining the current and field distributions in the superconductor, measuring the critical current as a function of temperature and geometrical configuration of the conductor, calculating and testing the electrical stability of the conductor, and measuring the ac losses due to ripple. Also a study was carried out in conjunction with Intermagnetics General Corporation to optimize their Nb_3Sn tape for the self-field regime. This study involved varying several of their process parameters and comparing the critical current I_c with that of their standard tapes.

To make the measurements for the above studies development of new apparatus was required. The most important measurement was that of the critical current because it is an important parameter of the dc SPTL and because it is used as an indicator of the influence of other perturbations upon the conductor. The I_c measurement apparatus consisted of Dewar systems, pumps, high current power supplies, micro-voltmeters, and sample holders. The I_c measurement itself was a simple four probe resistance measurement. AC susceptibility equipment was used to determine the superconducting to normal transition temperature T_c and the temperature width of the transition ΔT_c. In some instances the measuring systems were computerized for convenience and efficiency.

The choice of a superconducting material was narrowed to the A-15 compounds Nb_3Sn, Nb_3Ge, $Nb_3(Al Ge)$ and V_3Si; and to NbTi and NbZr. This selection was made because of the high transition temperatures and large critical currents of the A-15 compounds and because of the ductility and reasonably

high T_c's and I_c's of NbTi and NbZr. Critical currents and transition temperatures were measured for commercially available samples of these materials as well as samples prepared at LASL. In general, most of the conductors performed satisfactorily. However, the final choice of Nb_3Sn was made because it has a relatively high T_c, has a large I_c at the planned operating temperature ($\sim$ 12 K), and is commercially available in both mf wire and tape geometries. The high transition temperature allows operating flexibility, increased refrigeration efficiency, and a larger margin of safety, while the large critical current reduces the amount of superconducting material needed and simplifies the conductor design. The biggest drawback to Nb_3Sn is its "glass-like" mechanical properties, requiring special techniques and care in the manufacture of the cable.

After the superconducting material was selected, small conductor component configurations were tested. These consisted of superconducting tapes on tubes, stacked tapes, tapes on flat copper strips, and concentric cables made of mf Nb_3Sn wire. Both the electrical and mechanical properties of the units were evaluated. The magnetic interaction among the individual superconducting units was also measured. As expected, the critical current densities of the superconductors in the conductor configurations was reduced from the values obtained when the superconductors were not interacting.

Once the conductor components were tested and their characteristics known, it was next a matter of assembling them into an economical cable of the desired power level. At present, there does not seem to be any one configuration that is best for all possible uses. One must have a specific case in order to select a "best" cable, but we have been able to provide recipes for doing this.

Over the life of the project the objectives have changed somewhat and, thus, so has the dc SPTL design. In the beginning, the goal was to transmit large blocks of power ($\geqslant$10 GW) in single cables. With this objective, technical and economical reasons dictated a coaxial design. After considerable investment of time and effort on the coaxial design, it became clear that it would be useful to design single circuits to carry only 1 to 3 GW. It is likely that the most economical design for a 10 GW cable and a 3 GW cable will <u>not</u> be the same. Our design for the lower power levels is to place each pole in its own cryogenic enclosure and to place the electrical insulation outside the cryogenic environment, at ambient conditions. This design has many

desirable features, particularly the fact that the electrical insulation can now be a conventional "field proven" type; thus, the operating voltage of the line can be easily matched to the electrical system.

With two types of lines, the coaxial system for high power per circuit cases and the isolated pole design for smaller power per circuit cases, it was necessary to develop two different conductor configurations. By a reasonable choice of the conductor design for each type of cable, the elementary superconducting unit in each case was made the same. This elementary unit, an approximately 5-mm-diam cable of mf Nb_3Sn wire and stabilizing copper wire, has been the subject of many electrical and mechanical tests, which culminated in an 18-m cryoflow loop test, as mentioned in Sec. 4.6.3.

In the following sections the work leading to this final design is described. Section 5.2 discusses the material development and elemental superconductor tests. Section 5.3 reviews the test and development of mf Nb_3Sn wire for use in a cable, and Sec. 5.4 decreases the work on the stabilized mf Nb_3Sn cable. Joints are discussed in Sec. 5.5.

5.2. Material and Elemental Superconductor Tests

In this section the work on plasma arc spraying of V_3Si, $Nb_3(Al Ge)$ and Nb_3Sn and the work on the chemical-vapor-deposition (CVD) produced Nb_3Ge is reviewed, and tests related to the current carrying properties of superconductors are discussed.

5.2.1. Plasma Arc Spraying of Nb_3Sn, $Nb_3(Al Ge)$ and V_3Si.

The spraying of a superconducting material onto a substrate was considered a viable fabrication option for a dc SPTL conductor. This process has the advantages that the conductor can be formed on any geometrical configuration and that superconducting joints can be easily fabricated.

In the plasma arc process a plasma is generated by striking a high-current arc between the electrodes while a gas is passed through the inter-electrode region. Arc voltages of 30 to 40 V and currents of several hundred amperes are typical for operation in an argon plasma. The high-temperature plasma exits through a nozzle at a high velocity, picking up the sample powder (the superconducting material) as it is injected into the core of the plasma by a gas stream. The powder is melted in the arc and the molten particles impact on a nearby cooler substrate.

Powders of V_3Si, Nb_3Sn and $Nb_3(Al Ge)$ were prepared and sprayed on tubular substrates. Some of these samples were then annealed (750^oC) and

the T_c and ΔT_c of all the samples were then measured. T_c's comparable to literature values were obtainable. However, critical current measurements on the samples were disappointingly low. This was probably due to the low density of the A-15 material produced and possibly due to stress caused by the mismatch between the coefficient of thermal expansion of the substrate and of the superconductor. Of the materials tested, V_3Si showed the most promise of producing a good arc-sprayed superconductor. A detailed account of the work can be found in the materials development sections of previous progress reports.[1-8]

5.2.2. Development of Nb_3Ge by Chemical Vapor Deposition. Nb_3Ge has the highest known transition temperature of all superconductors but is difficult to make and is not commercially available. However, because of its potential as a conductor, another program at LASL is investigating methods to develop the material by a CVD process. Early successes in the program indicated that the CVD process was capable of producing good quality material exhibiting low ac losses. Samples with T_c's of approximately 21 K and critical currents of 2×10^6 A/cm^2 at 14 K were regularly produced. After initial funding by the AEC the program was continued by EPRI. The material has been improved and 20-m lengths of tape have been produced. Also a 1-m coaxial ac transmission line section has been completed. A description of the early work is included in the materials sections of progress reports.[5-12] Except for a higher T_c Nb_3Ge has few advantages over Nb_3Sn for a dc SPTL.

5.2.3. Multilayered Nb_3Sn Extruded Conductor. A new type of extruded Nb_3Sn conductor was formed by extruding niobium, Cu-13%Sn, and pure copper in a spiral-layered "jelly roll" structure, followed by a heat treatment at 700°C for 24 h. A 2.0- to 2.5-μm layer of Nb_3Sn was formed by diffusion of tin into the niobium. The arrangement of the materials prevented tin from contaminating the pure copper used for stabilizing the conductor. The superconducting onset-temperature was 17.6 K as measured by magnetic susceptibility. The critical current was measured at 4 K using a flux transformer technique and, in the temperature range from T_c down to 15.5 K, using a directly coupled power supply. The results of the measurements are given in Table 5-I.

At 4 K the critical current was flux-jump limited. At 25 kA the current density in the Nb_3Sn layer is 1.2×10^5 A/cm^2, a value considerably lower than expected. Above 15.5 K the conductor showed no signs of instability,

TABLE 5-I

CRITICAL CURRENT AS A FUNCTION OF TEMPERATURE FOR JELLY ROLL CONDUCTOR

Temperature (K)	Critical Current (A)
17	10
16.5	165
16	340
15.5	990
4	25 000

and the I-V curves showed a very gradual transition from the superconducting to normal state. It is possible that the contact area between the normal current leads and the superconductor tube was not large enough to transfer the current without some local heating, resulting in a reduced I_c. This project was begun when only Nb_3Sn tapes were readily available. This scheme has little to offer when compared to the commercially available multifilamentary Nb_3Sn wires now available.

5.2.4. Magnetic Field Profiles of Current-Carrying Superconducting Tapes. The design and engineering of a dc SPTL must prevent failure of the conductor during electrical faults and overloads while minimizing use of materials and refrigerator power so that minimum cost and maximum efficiency are achieved. Both fault and surge stability of the conductor and ripple losses arising from the partially unfiltered output of a converter affect the line design and are dependent upon the way the current distributes itself inside the conductor. It is therefore useful to understand the details of current penetration for the large-transport-current-density, zero-applied-field case.

5.2.4.1. NbTi Tapes. Because the surface magnetic field in a type II superconductor carrying near critical current usually exceeds H_{c1}, it would seem reasonable to apply a Kim-type[13] critical state model to describe the magnetic fields and current distribution inside the conductor. However, it can be shown that no local or Kim-type critical state model can accurately describe partial flux penetration in a long straight type II superconductor in zero applied field[14] because such a model cannot provide zero magnetic field

inside the portion of the conductor where J = 0, a condition that must be satisfied by a superconductor if all currents are transport currents.

That the magnetic field B must be zero where the transport current density J is zero is supported by previous results for Nb_3Sn tapes,[15] where measurements were made with a Mossbauer effect magnetic field probe and Hall probes. Experimental data were well described by a constant-current-density shell model, the principal feature of which is a zero-current, zero-field hole. Attempts to fit a critical state model to the results failed. However, the Nb_3Sn used for the measurements suffered in that it was a layered structure having both Nb and Nb_3Sn components, and its performance degraded with cycling. Improved measurements required a homogeneous system; NbTi was a logical choice because of its ductility and availability as well as its moderately high critical current density J_c.

The apparatus used to obtain the data on NbTi was based on a previously established technique whereby a loop of the sample material was formed with a superconducting joint and then placed around a superconducting primary to form a dc transformer. Heaters on this secondary loop enabled us to drive it normal independent of the current in the primary. A germanium thermometer and heater on the loop combined with a temperature controller could be used to regulate the temperature of the sample to within 0.01 K over the range from 2 K to 14 K. By making the diameter of the sample much greater than its thickness, a reasonable approximation to a long straight tape conductor was achieved. Total persistent current in the sample loop was measured to a precision of 4 A and an accuracy of 8 A with a calibrated Hall probe ammeter located at the loop's center. Parallel and perpendicular components of the magnetic field were measured by two movable Hall probes that could be swept across the tape loop's surface to provide a field profile near the superconductor. The sample itself was made from 0.76-cm-thick rolled Nb 45% Ti plate with a measured T_c of 9.45 K. This plate was explosively bonded on one surface to an equal thickness of OFHC copper. The resulting sandwich was then rolled to two separate thicknesses of 0.183 cm and 0.091 cm, where the NbTi thicknesses were 0.091 cm and 0.045 cm, respectively. T_c of the material after bonding dropped to 9.19 K, presumably because of a 400°C anneal prior to the bonding operation. The sheets were then sheared into strips 1.96-cm wide and formed into loops 10-cm in diameter, with the NbTi on the outside. The superconducting joint was made by spot welding one or two additional

strips of unclad NbTi over the break in the loop. The area of the spot welds was much larger than the cross section of the tape.

In Fig. 5-1 we show the maximum persistent current achieved in a sample loop as a function of temperature. This current was obtained by maintaining the sample at a fixed temperature and inducing more current than could be carried in a persistent mode. After a rapid decay, the current reached a stable and reproducible value. At temperatures below 8.5 K, because of the added thickness of the joint, this current probably represented an accurate value for the critical current of the main tape because the maximum decay rate for the observed current indicated that the effective resistance of the loop was less than 10^{-13} Ω. This corresponded to a voltage drop of 10^{-11} V/cm for a straight section, a level well below the minimum detectable voltage drop used to determine I_c by other methods. Near T_c, however, spotwelding of the joint may have lowered the local T_c below that of the rest of the tape, and therefore currents above 8.5 K were probably joint limited.

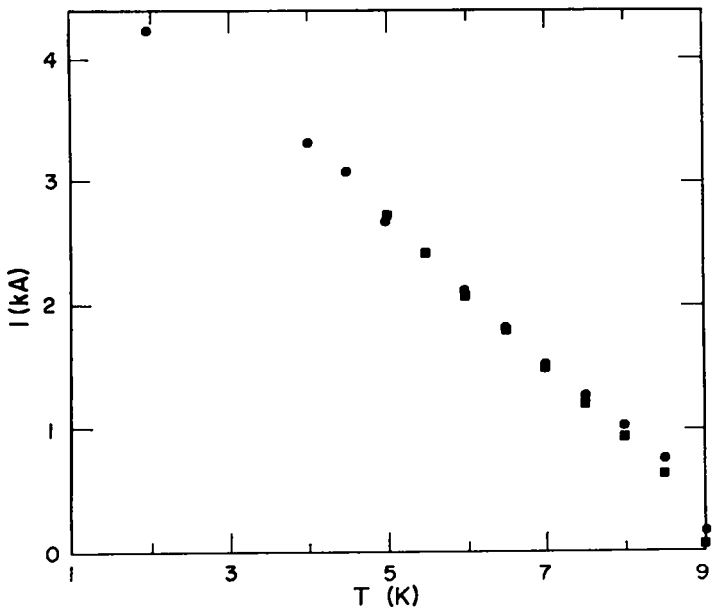

Fig. 5-1.
Maximum persistent current as a function of temperature for a 0.091-cm-thick NbTi, 0.092-cm-thick copper superconducting loop, 1.96 cm wide. The circles represent values obtained with no flux trapping present. The squares represent values obtained with some observable trapping. In both cases the final stable value of I was reached after a decay from a somewhat higher current. T_c measured for this material was 9.19 K; thermometry errors were about 0.1 K.

In Fig. 5-2 we show field profiles of the 0.091-cm-thick NbTi sample. Current was induced by, first, raising the temperature of the entire loop above T_c while maintaining current in the primary, then, lowering the temperature to 4 K, and, finally, reducing the primary current to zero very slowly. At the end of this procedure the observed current in the sample was 2690 A at 4 K, a value about 82% of I_c. By slowly increasing the tape's temperature until the persistent current just started to drop we obtained a critical current of 2680 A at 5.0 $\pm$ 0.1 K. The field profiles were obtained simultaneously with two Hall probes, one to scan the component of the field parallel to the surface of the sample, the other, the component perpendicular. Scan positioning accuracy was about $\pm$ 0.01 cm and field accuracy about 5×10^{-4} T, with repeatability to 2×10^{-4} T. Because the unclad side of the NbTi was almost in contact with the case of the small (0.06-cm x 0.008-cm active area) Hall probes, spatial resolution was sufficiently high to resolve the peaks almost fully.

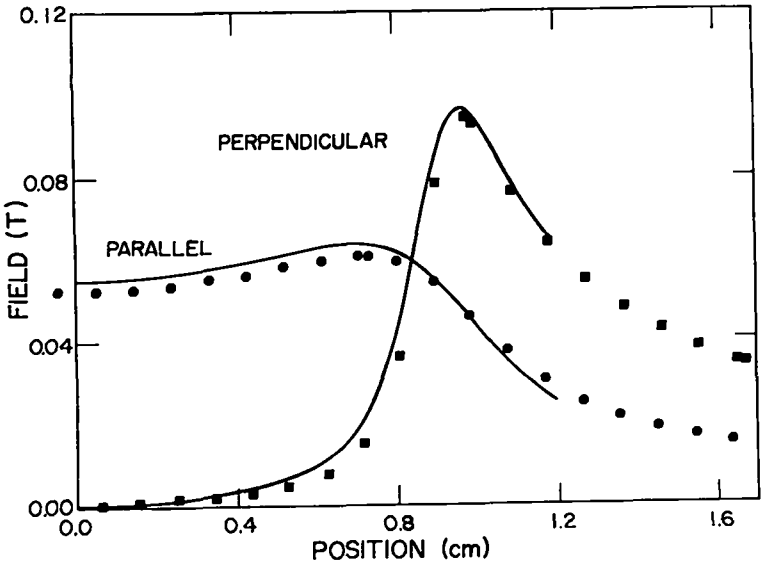

Fig. 5-2.
Magnetic field profiles of a NbTi superconducting loop carrying 2680 A at 5.0 K. The Hall probe used to measure the parallel component of the field was 0.25 cm from the surface of the NbTi, and that for the perpendicular component was 0.05 cm away. Data (shown as circles and squares) have been adjusted to compensate for the fact that measurements were taken on a loop and not an infinite straight conductor. The fits (solid lines) were to an elliptical shell model with total current equal to the measured current and with the inner ellipse 0.87 $\pm$ .02 times the outer ellipse (see text). No other parameters were adjustable. The center of the tape was at zero and the edge at 0.98 cm.

For the data of Fig. 5-2, the field profile was independent of temperature from 4 to 5 K. Scans taken from 5 to 8.5 K, shown in Fig. 5-3, displayed no observable change in shape and scaled accurately with the decrease in persistent current with rising temperature. Furthermore, the field profiles were observed to scale accurately with the persistent current induced both at 4 K with peak fields below H_{c1} and below 4 K, where the critical current no longer varied linearly with temperature. As temperature was increased above 8.5 K, the persistent current dropped from about 600 A to zero at 9.3 ± 0.1 K. In this region a slight decrease in spacing between the edge peaks of the perpendicular component of the field was observed, indicating that current had penetrated more deeply into the tape. Qualitatively this effect is consistent with a field profile partially governed by λ, the penetration depth, which varies rapidly only near T_c.

In Fig. 5-2 we also show a good fit of the data to an elliptical shell model[15] that approximates the actual current distribution of a tape as a region of constant current density bounded by two similar concentric ellipses, the outer one with a major axis equal to the tape's width and minor axis equal to the tape's thickness. The only adjustable parameter is the size of the inner ellipse. A property of this distribution, one which cannot be achieved by a critical state model (except for circular symmetry), is that where $J = 0$, $B = 0$. An application of this model to results for Nb_3Sn or NbTi gives a good fit to the data with a relatively large area void of current. It seems, therefore, that I_c was reached in both Nb_3Sn and NbTi tapes well before the tape was fully penetrated with current and that the unpenetrated fraction had both $J = 0$ and $B = 0$ simultaneously. Thus the shape of the unpenetrated region and the current distribution elsewhere are not well described by a local Kim-type critical state model. Clearly the ellipse model is a phenomenological one which only crudely approximates a tape. The physical phenomena which govern the size of the inner ellipse are not fully understood at this time; however, the success of the model should lead to a better understanding of the large transport current density, low field regime. Local flux trapping was observed during several runs on the 0.046-cm-thick NbTi loop. In Fig. 5-4 one field profile data set with trapping effects present is shown together with a fit to an extension of the ellipse model with two concentric elliptical shells with antiparallel currents.

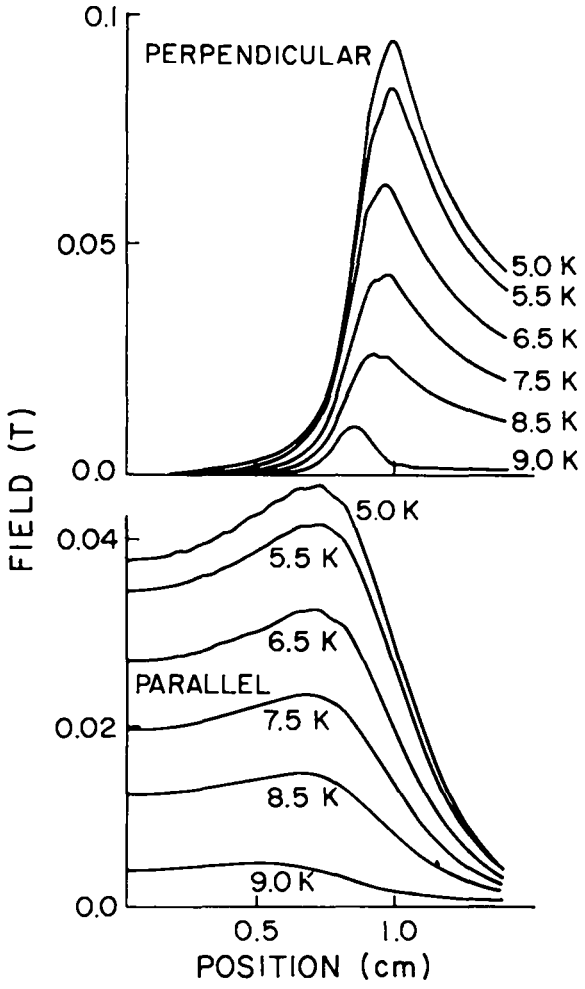

Fig. 5-3.
Magnetic field profiles as a function of temperature for the NbTi superconducting loop described for Fig. 5-1 with the Hall probes in the same position as described for Fig. 5-2. The current carried at each temperature is given in Fig. 5-1. The data at 5.0 K are identical to other scans (not shown) taken with the same total current at 4.5 K, 4 K, and 2 K. The data have not been adjusted for the effects of small stray fields from portions of the loop not close to the Hall probes, and the ripple noise in the curves is a result of runout in the lead screw used to move the Hall probes. All data have the correct symmetry about the center of the tape at 0; the edge of the tape is located 0.98 cm from its center. Other data, not shown, were taken at lower temperatures and higher currents with no deviation from the expected scaling behavior. Data taken at 4 K and at currents down to a small fraction of I_c also scaled with current. The only noticeable deviation from a current-scaling behavior was above 8.5 K, as is apparent.

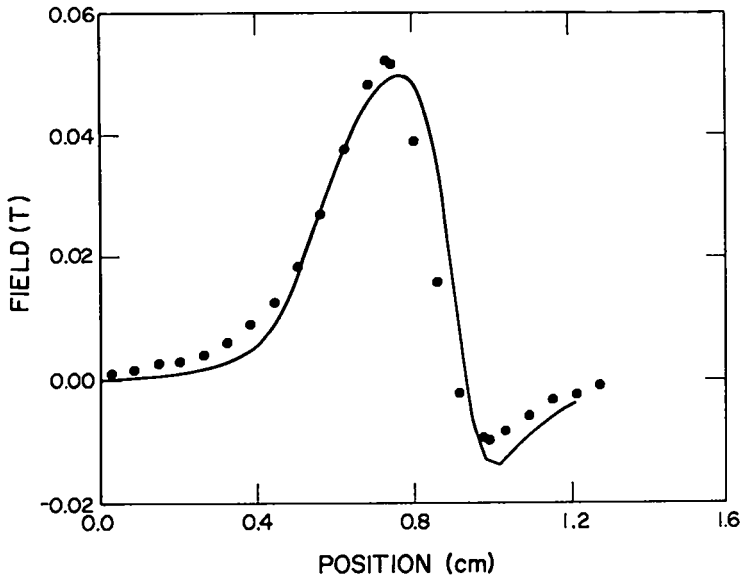

Fig. 5-4.
The perpendicular component of the magnetic field (circles) of a 0.046-cm-thick NbTi superconducting loop, 1.96-cm-wide, exhibiting symmetrical flux trapping at 4.0 K. The center of the tape was at zero, its edge at 0.98 cm, and the Hall probe was 0.06 cm from the surface of the NbTi. The net current carried was 180 A. The fit (solid line) used two elliptical shells, the inner one extending from 0.50 to 0.90 and the outer one extending from 0.90 to 1.00 times the outer elliptical boundary (see text). The outer shell carried a uniform current density 2.475 times the current density in the inner shell and antiparallel to it. The outer shell carried a net current opposite in direction to and 84% of the magnitude of the net current carried in the inner shell.

The conditions required to generate trapping are not fully understood, nor was it determined whether a return path existed at some point on the loop or whether the current distribution was necessarily circularly symmetric. It was clear that the observed field profile and analysis based on the ellipse model strongly suggested antiparallel components of J. In addition, trapping has been observed to lower I_c at higher temperatures, as shown in Fig. 5-4.

5.2.4.2. Nb_3Sn Tapes. In addition to the flux transformer technique for inducing large currents in tape loops, we have introduced current directly from an external power supply using Hall probes to measure field profiles in the 13.8 K-to-T_c regime. Probably the most important observation was a profile which implied that most of the current flowed near the surface of the tapes, leaving a field- and current-free region in the tape's center. The model for the current profile is being incorporated into studies of

superconducting stability and should have implications for the dc SPTL design. It was also observed that flux was trapped in the samples after removing the driving current even for the case of an external power supply. In the externally driven tapes this trapped flux field profile is in qualitative agreement with that found for the NbTi tape loops reported above despite the fact that in this measurement we certainly have an open loop. The data were inadequate to determine the complicated return path of the persistent current.

5.2.5. Critical Current - Geometrical Considerations. In order to determine the best configuration of the superconductor in a cable, measurements were made on simple geometries to determine the effect of width and thickness of the superconductor on the critical current. As shown in Figs. 5-5 and 5-6 the critical current is a linear function of the tape width for flat thin tape geometry both for temperatures near T_c and for much lower temperatures. This fact is important for scaling some of the early conductor designs. It is also interesting that even when these tapes are placed on a cylinder, the total current is a linear function of the conductor width. This is shown in Fig. 5-7.

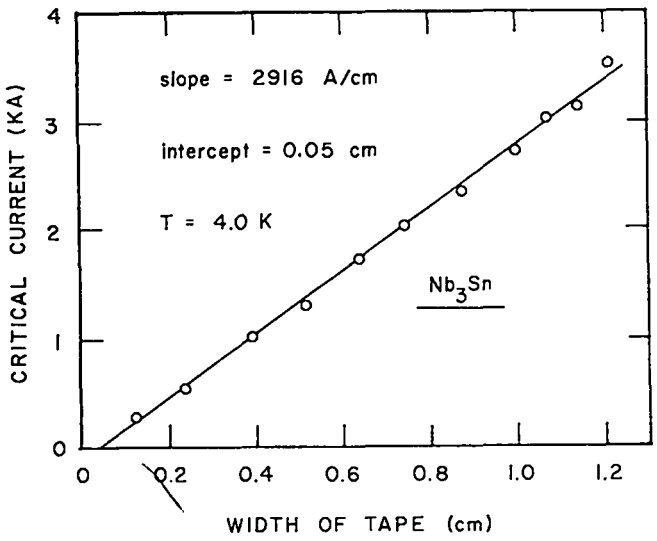

Fig. 5-5.
Critical current at 4 K as a function of tape width for single flat tape. Curve through the experimental points was calculated as explained in text.

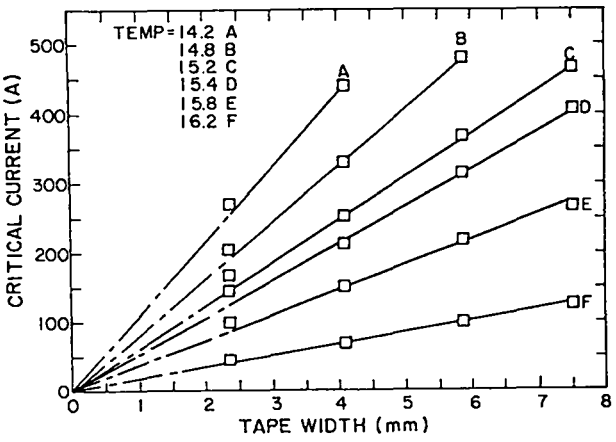

Fig. 5-6.
Critical current as a function of tape width for six isotherms derived from the data for sample No. IGC-B-4. Above 16.2 K a linear dependence was not obtained.

The critical current of the thin tapes did not have a simple linear relation to the thickness of the tape and, in fact, seemed to depend on the temperature range of the measurements. Near T_c ($T > 0.75\ T_c$) the critical current went through a maximum as thickness is varied; however, the current density showed a steady increase with decreasing thickness, improving by a factor of 5 over the range of thickness measured. This is in qualitative agreement with the results of Suenaga et al.[4] on solid-diffusion-formed Nb_3Sn multifilamentary wire samples. Though our results are similar we were unable to determine whether the causal factors were the same. Figure 5-8 is a plot of J_c vs temperature for five of the tape samples in which the Nb_3Sn layer thickness was varied. It can be seen that the thinner Nb_3Sn layers carry a higher current density and, as well, have a larger dJ_c/dT.

The critical current density vs Nb_3Sn layer thickness is plotted in Fig. 5-9 for four different temperatures. For the lower three temperatures, a straight line fit has been made corresponding to $J_c = J_o e^{-nt}$, where J_o is the intercept at zero thickness in A/cm^2, t is the total Nb_3Sn thickness in μm, and n is the slope of the $\ln(J_c(t))$-vs-t curve. For the 15 K curve, $J_c = 2.32 \times 10^6 e^{-0.0507t}$.

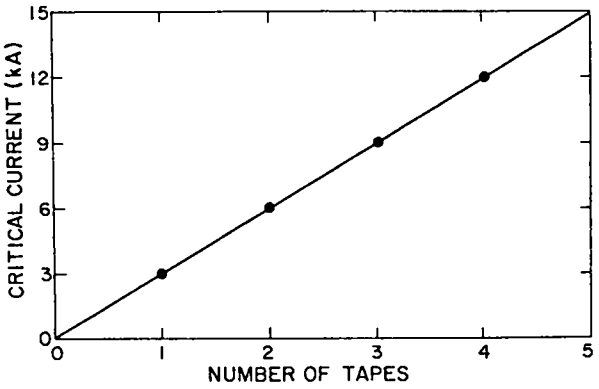

Fig. 5-7.
Critical current at 4 K for Nb_3Sn tapes soldered lengthwise along a cylindrical copper tube as a function of the number of tapes on the cylinder. Width of four tapes combined is equal to the perimeter of the cylinder.

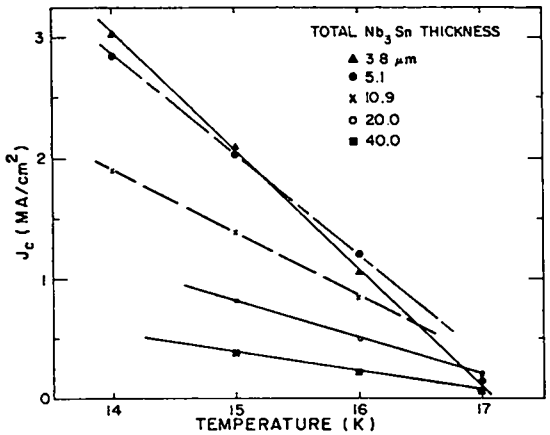

Fig. 5-8.
Critical current density as a function of temperature for Nb_3Sn tapes having five different thicknesses.

It is interesting to note that several of the tapes carried more than 10^6 A/cm^2, even at 15 K, and the thinnest tape carried more than 2.4 x 10^6 A/cm^2 at 14 K.

In Fig. 5-10 the critical current density at 4 K of several tapes is plotted as a function of the thickness of one of the Nb_3Sn layers. The current density ranges from 2 x 10^6 to 8 x 10^6 A/cm^2. The data appear to be separated into two groups, those with Nb_3Sn layers thicker than 4 μm and those with thinner layers. Tapes with the thinnest layers carry the largest current density, as was also seen at the higher temperatures. All tapes except those with heavy copper cladding are stability limited (flux-jump limited) so that the intrinsic or "true" critical current is not achieved. In the thinner tapes the superconductor seems to be approaching the "true" critical current of the sample.

Since the critical current in most of the samples is flux-jump limited, full penetration of the current into the sample was not achieved and the current is carried near the tape surface. This surface current distribution for the flat tape geometry would produce a critical current density inversely proportional to the superconductor thickness. The solid curve in Fig. 5-10

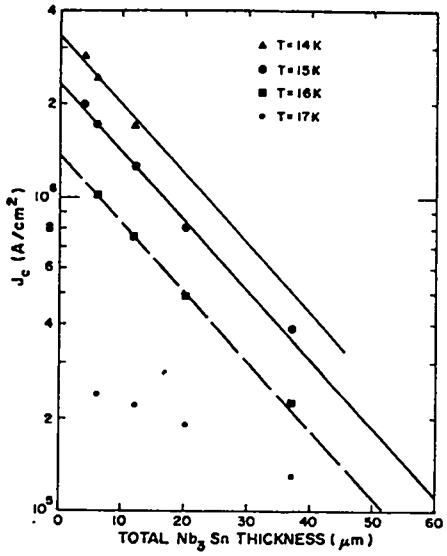

Fig. 5-9.
Critical current density as a function of Nb_3Sn layer thickness for four selected temperatures.

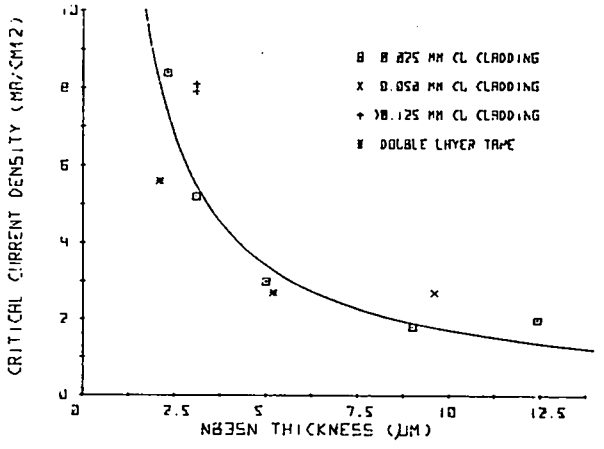

Fig. 5-10.
Critical current density at 4 K for a number of commercial tapes as a function of thickness of the Nb_3Sn layer.

is such an inverse thickness curve representing the equation

$$J_c(A/cm^2) = 1700\ (A/cm)/t(cm) \quad ,$$

where t is the thickness of a single Nb_3Sn layer. The curve is a reasonable fit to the 0.025-cm copper-clad tapes, especially in view of the fact that there are process variations from tape to tape as well as errors in the thickness and current measurements. (This indicates that the critical current per unit width is constant, as seen in the discussion above.) The heavier-copper clad tapes have critical current densities larger than would be predicted by the inverse thickness curve. This is due to the fact that the extra copper stabilizes the superconductor, allowing the current to penetrate further into the bulk of the sample.

The constant in the above equation, 1700 A/cm, is in good agreement with the value of 1400 A/cm, obtained from adiabatic stability calculations. The calculations indicate that the current-carrying layer for Nb_3Sn at 4 K must be 2.5 μm thick. For thicknesses greater than this value the tape is unstable and susceptible to flux jumps. The experimental data are consistent with this type of behavior.

5.2.6 Stacked Tape Experiments. A series of tests were performed on stacked Nb_3Sn tapes to determine the total critical current of tapes in close proximity and the current distribution in the individual tapes. For the tests, Nb_3Sn tape (IGC #751-11) was used throughout. The first set of runs involved three 25-cm tapes stacked and soldered together at the contacts, except that in the 7-cm region between the contacts the tapes were separated by sheets of mica 10^{-4} m thick. Two voltage probes 1 cm apart were soldered to each tape in the center of the region between the contacts. Using liquid hydrogen (boiling at reduced pressure) as the cryogen, measurements at several temperatures were made of the potential drop along each tape and between the tapes as a function of total current through the three tapes. The cryostat was then warmed and the upper tape was carefully removed so as not to damage the lower tapes. Data for two tapes were obtained and, finally, for a single tape.

In a second series, two tapes were soldered as before with mica separating the tapes in the region between the contacts; however, the soldering was done with only light clamping pressure at the contacts. The critical current

and the potential drop along the individual tapes and between the two tapes was then determined as a function of temperature. The cryostat was then warmed up and the tapes were resoldered to the contact blocks using more clamping pressure. After similar measurements were made, the upper tape was cut for a final set of measurements.

In a third series of experiments, three tapes were stacked and soldered over their entire length and $I_c(T)$ was determined. The same experiment was repeated for two tapes.

Finally, in a fourth series of experiments, different lengths of three tapes were stacked but staggered so that a length of each tape would be soldered to the normal metal contacts. As a reference, $I_c(T)$ of several sections of a single layer of tape was used.

The total critical currents as measured in the above experiments are shown in Table 5-II, where we list the average current per tape at I_c at several temperatures. Although there is scatter, the following general statements can be made: 1) stacking of tapes decreases the average critical current; 2) the smaller the separation between tapes the greater this decrease; and 3) soldering tapes together produces a critical current lower than that of the same number of tapes separated with insulating sheets. Since these experiments were done using Nb_3Sn tapes, the scatter probably results, in part, from damage during handling. Inhomogeneity in the tapes is also possible; however, measured I_c of individual tapes did not vary by more than 10%.

Figure 5-11 shows the voltage-current characteristics for two tapes separated by mica. The various traces are different combinations of the four voltage probes. The current given is the total through both tapes at a temperature of 17.0 K. The nonlinear behavior observed for probes 1-3 and 2-4 is characteristic of all runs with multiple tapes in this geometry. These nonlinearities indicate changes in the effective resistance of the joint, implying that layers of the superconducting tapes are becoming normal as I_c of that layer is exceeded. This causes a shift in the current distribution between the tapes. Critical behavior and current sharing of superconductors is complicated even for the simple situations studied here.

TABLE 5-II

CRITICAL CURRENT (A) PER TAPE IN STACKED TAPE EXPERIMENTS

Temp(K)	A	B	C	D	E
17.5	18	16	18	20	15
17.0	275	240	120	210	100
16.5	650	420	460	330	300
16.0	1010	620	650	-	-

A = Single tape

B = Double tape unsoldered

C = Double tape soldered

D = Triple tape unsoldered

E = Triple tape soldered

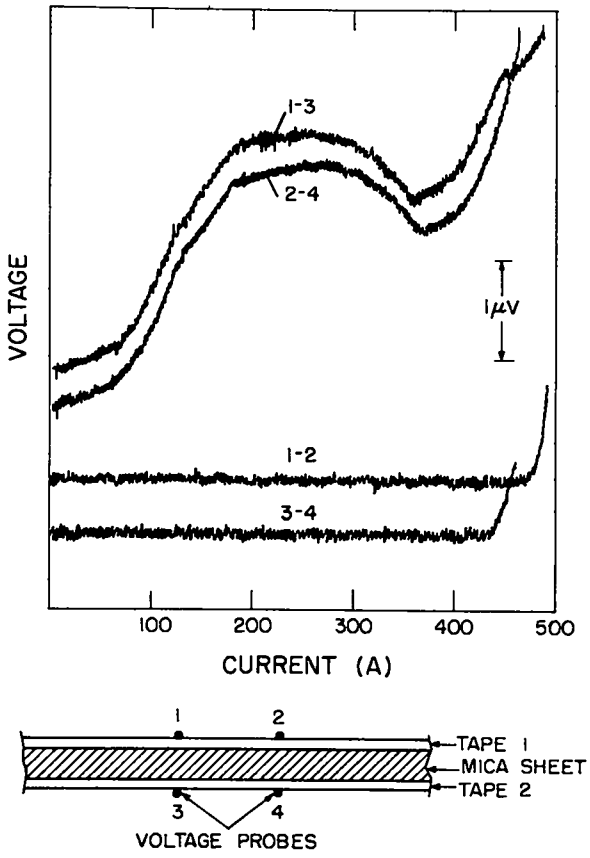

Fig. 5-11.
Voltage drop observed along and across two parallel superconducting tapes at 17.0 K as a function of the gross current. A cross section of the tape geometry is shown.

5.2.7. Ripple Losses. While our measurements to evaluate hysteretic losses associated with ripple currents on a dc transmission line have been made on Nb_3Ge, the influences of dc bias upon ac losses which we have observed are expected to be similar to those operating in any high-T_c superconducting material, such as Nb_3Sn. The effect of dc bias on losses at a given ac amplitude is twofold in that it is expected to diminish both J_c and $\Delta\sigma$, the surface barrier field.

In Fig. 5-12 the power loss vs induced ac current is plotted for various levels of dc bias for a Nb_3Ge sample, denoted as V444, in the polished and etched condition. It is apparent that a bias dc magnetic field H_{dc} of 400 Oe is sufficient to destroy most of the shielding at low ac current levels. At higher bias values the loss curves are also displaced upwards, indicating a nearly monotonic decrease in J_c as H_{dc} increases. With similar reasoning to that employed in the analysis of the temperature dependence of the losses,[5] we have utilized the Bean-London model to determine the dependence of J_c upon H_{dc}. All of the field dependence of the losses should be contained in $J_c(B)$, assuming $\Delta\sigma$ effects can be neglected; therefore, we have chosen to plot the inverse power loss P_L^{-1} as a function of B. The results are shown in Fig. 5-13, where J_c determined in this manner is plotted vs B, in arbitrary units, in order to illustrate the functional dependence upon B for various induced current levels. Complex behavior is evident at low values of the dc bias. However, at a sufficiently high dc bias, all of the curves approach a straight line with the same slope on the log plot. The slope of this line is roughly 0.4 and indicates a functional form of $J_c \propto B^{-0.4}$. The peculiar behavior observed for dc biases less than 1000 Oe is undoubtedly caused by the variations of $\Delta\sigma$ with H_{dc}. This conclusion was borne out by a careful investigation of dc bias dependence of $\Delta\sigma$ for sample V444 after polishing and etching. It was found that if $\Delta\sigma$ is assumed to be that value of field at which the power loss is equal to 0.1 W/cm^2 (see Fig. 5-12), then $\Delta\sigma$ is described accurately as being inversely proportional to the applied dc bias.

We show in Fig. 5-14 a plot of ac power loss at an induced current of 71 rms A/cm as a function of dc bias for sample V444 in the polished and etched condition. It can be seen that a dc bias of 400 Oe is sufficient to produce some measurable loss. Once the dc bias has exceeded 400 Oe, the losses increase monotonically. Such behavior is characteristic of the samples

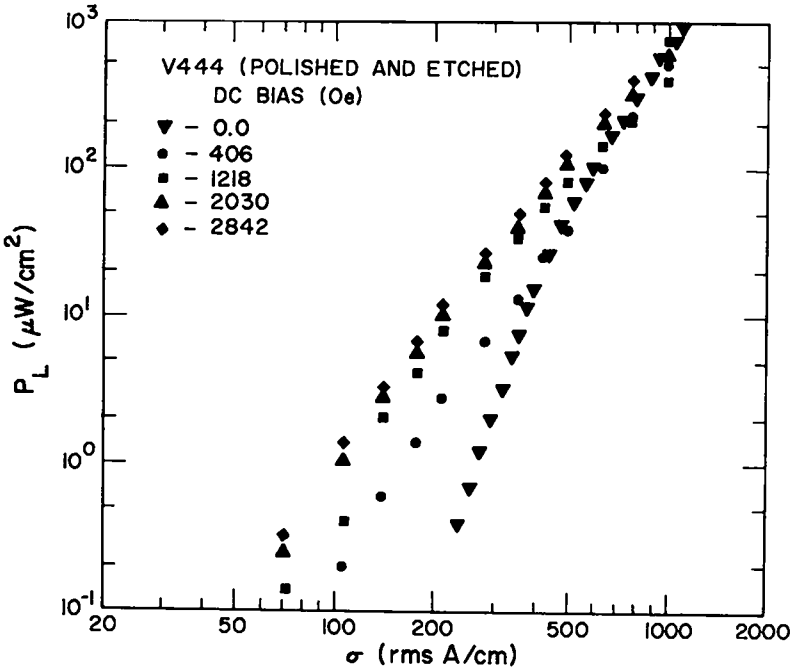

Fig. 5-12.
Measured as power loss at 4 K as a function of induced current for Nb_3Ge sample V444 after mechanically polishing and chemically etching the surface. Data taken at several different values of dc bias field.

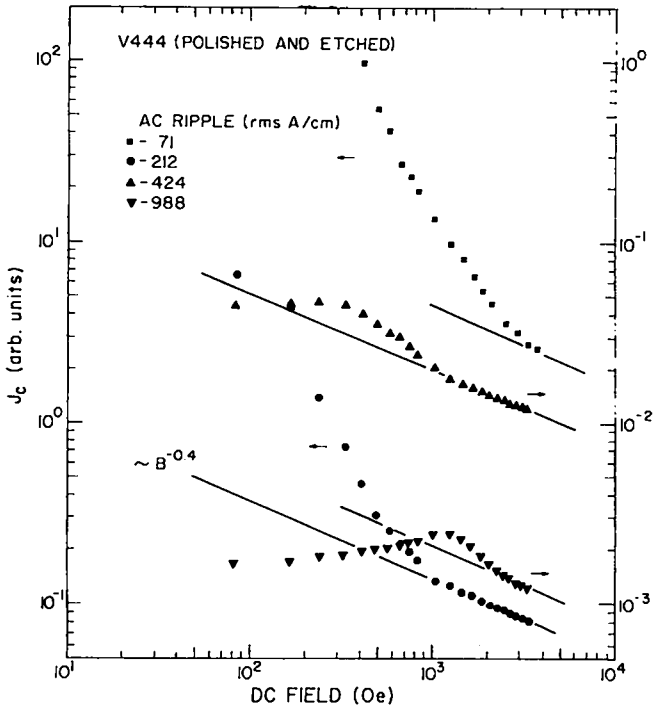

Fig. 5-13.
$J_c \sim$ (power loss)$^{-1}$ at 4 K as a function of bias field for sample V444 after polishing and etching. Data shown are for several different values of induced ac circumferential current.

investigated at low ripple currents. However, at high ripple currents, the power loss actually decreased initially as the dc bias was increased. The resulting minimum in the power loss was usually rather shallow and broad. This behavior is illustrated in Fig. 5-15 for sample V507T at various temperatures. The magnitude of the ac current has been held constant at 847 rms A/cm,

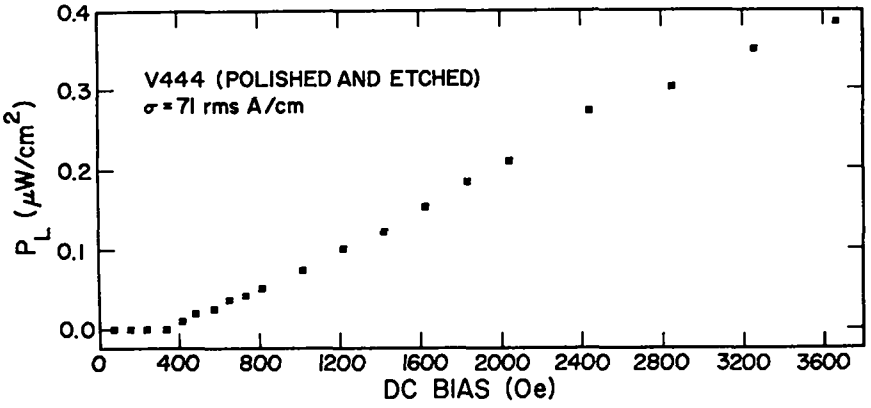

Fig. 5-14.
Measured power loss at 4 K and 71 rms A/cm as a function of dc bias for sample V444 after polishing and etching.

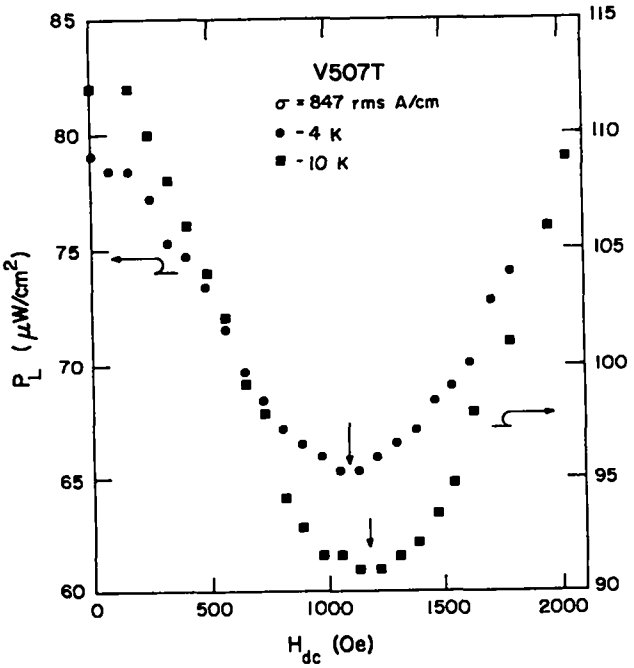

Fig. 5-15.
Measured ac power loss at 50 Hz, at a fixed value of induced ac circumferential current, σ, as a function of dc bias field, H_{dc}. Data are shown for Nb_3Ge sample V507T at 4 K and at 10 K.

which corresponds to a peak magnetic field of 1509 Oe. It is interesting to note that the minimum occurs at a field $H_{dc} \sim 1096$ Oe, corresponding to a value of the total applied field, $H_{min} = H_{dc} - H_{ac} \approx 413$ Oe at the negative swing of the ac cycle. This value is close to the magnitude of $\Delta\sigma$ (410 Oe) measured for this same sample at 4.0 K. This same correlation between $\Delta\sigma$ and the field at the lowest part of the ac cycle for the minimum power-loss condition is seen to hold at 10 K and had been observed at different values of the ac amplitude. The correlation breaks down at higher temperatures. This behavior can be described by a model which contains a rapid functional decrease of either J_c or $\Delta\sigma$ with increasing field values. The results of this work have been used as a guide for the assumptions made in predicting the ripple losses for a dc SPTL, with the conclusion that we expect these losses not to be significant for the LASL coaxial cable design.

5.2.8. Superconducting Stability. A very important aspect of any superconducting cable is its stability with respect to small thermal perturbations (which may be electrically or mechanically induced). We have looked at this problem from many viewpoints. Below are two theoretical treatments of different features of the problem and measurements on two different conductors.

5.2.8.1. Theoretical Study of Superconductor Stability in a Transmission Line Geometry. A fairly extensive theoretical study of the stability of the superconducting operating mode in a general transmission line geometry has been completed.[16] In this study the response of a device to a disturbance is analyzed, a disturbance being any event which releases energy at or in the superconductor, thus creating one or more limited normal conducting zones. A stable operating point (given by operating temperature T_o and current density J) is analogous to the bottom of a potential well into which a small ball will return after a not-too-large displacement; if the ball is moved beyond the unstable equilibrium point on the rim of the potential well it will escape the attracting influence of the potential well. The unstable equilibrium which limits the stability of a superconductor operating point is described in either of two ways.

a) The Minimum Propagating Zone (MPZ) addresses the question: "How big a normal zone in an otherwise superconducting surrounding can be tolerated so that the normal zone can still shrink and disappear instead of growing by itself?"

b) The Minimum Recovery Zone (MRZ) relates to the question: "What is the smallest superconducting zone, between adjoining normal zones, which will still grow?"

The two descriptions apply in different stability regimes as explained below.

In general, a superconductor remains superconducting up to its short sample critical current but will have its lowest stability at that point. The MPZ (whenever it can be defined) will approach zero at the short sample critical current. Reducing the current increases the MPZ eventually to a point where it is infinite (see point B in Fig. 5-16). The concept of the MPZ implies that the normal zone contacts an infinite superconducting zone. "Infinite" MPZ, therefore, actually means that half the device is normal and half is superconducting with one normal superconducting interface. The position of the interface makes no difference: a slightly lower current would shift the interface in the direction of the normal region, leading to full recovery of the superconducting operating mode; a slightly higher current would shift the interface in the opposite direction, leading to full normalcy of the device. In the case of several normal and superconducting zones, detailed analysis shows that the device can recover provided less than 50% is normal.

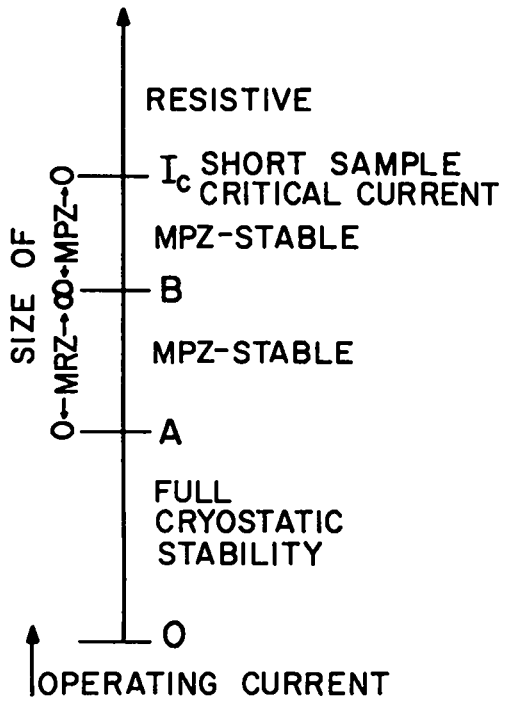

Fig. 5-16.
Schematic representation of various stability regimes of a composite superconductor carrying a current.

For currents lower than point B (Fig. 5-16) stability of the superconductor increases. Recovery can take place provided at least one zone larger than the MRZ is kept superconducting. The MRZ decreases with decreasing current and becomes zero for a certain current, schematically point A in Fig. 5-16. At, or below, this current level the device is said to have full cryostatic stability. Recovery can take place even after the entire length of superconductor is driven normal because the Joule heating in any part of the device is equal to or lower than the local cooling capacity. Full cryostatic stability is a very conservative stability criterion.

A knowledge of the MPZ gives information on the size of a localized disturbance which will cause a quench. In practice, quenches usually occur above point B but below short sample critical current. The margin, or difference between the normally occurring disturbances and the ones needed to create a MPZ, gives a quantitative stability margin, or operational safety factor.

A knowledge of the MRZ can help determine the proper width of cooling channels, the possible width of sections not in direct contact with the cryogen due to electrical insulation or force supports, and similar, usually periodic, design limitations.

The copper-to-superconductor ratio, in addition to several other parameters, influences the stability limits. Increasing th amount of copper (stabilizer) increases both limits A and B until, for a su icient amount of copper, both A and B coincide with the short sample critical current. In terms of overall current density, however, addition of copper brings a reduction of the short sample critical current density. The current density of limit B is also reduced but to a lesser degree, while A increases marginally.

In a particular device it may be advantageous to operate at a higher current density even though in a less than cryostatically stable mode. An important result of this stability study is to provide design options. An example follows. For a typical conductor the aforementioned stability limits may coincide with the short sample critical current density at a copper-to-superconductor (Cu:SC) ratio of 8:1. Reducing Cu:SC to 2:1 may increase the stability limit B to a 10% higher current density, while the short sample critical current density has tripled. Disturbances of the order of 0.1 J/cm^2 (energy release per unit area conductor cross section of a localized disturbance) cause quenches at 70% short sample performance, but the device can now operate to twice the initial (fully stable) short sample current density. In order to carry the same total current at twice the current density, only half as much copper but 50% more superconductor are needed. For prices of copper at 1.75 \$/kg and superconductor at 88 \$/kG, this corresponds to an increase of 36% in the cost of conductor material. Yet the increase in current density results in reduced cost of dielectric and cryogenic envelope and increased overcurrent capacity and flexibility of the final cable, factors which may offset the increased conductor cost.

Computer studies of the spread of single normal zones in a realistic coolant flow situation,[17] are related to these stability studies. Experimental verification of the theroetical studies has partially been made. More empirical experience of normally occurring disturbances and their statistical distribution in space, time, and size will be necessary to establish practical stability margins.

5.2.8.2. Adiabatic Stability. Adiabatic or intrinsic stabilization represents the most fundamental approach in that it finds an upper limit to the magnetization energy of a type II superconductor in the critical state[18,19], in relation to the specific heat. The theory[20,21] develops a criterion for maximum superconductor thickness x_m or diameter d as a function of critical current density J_c and specific heat per unit volume S. There can be no flux jumps as long as the film thickness x is less than

$$x_m = (10^9 \, ST_o)^{1/2}/4J_c \quad , \tag{1}$$

where

$$T_o = J_c/(-dJ_c/dT) \quad . \tag{2}$$

Because both J_c and S vary with the temperature, but with slopes of opposite signs, it should not be surprising that there is a maximum in the adiabatically stable critical current. This is, of course, simply another way of viewing the maximum flux jump field of Swartz and Bean.[21]

5.2.8.3. Stability Analysis of Test Bed Sample. The first mf Nb_3Sn sample measured in the 20-m test bed was a monolithic 67,507-filament, copper-stabilized conductor that was made by Airco and shown in cross section in Fig. 5-17. Abofe 13.8 K the critical current was that expected, based on short sample measurements at 4.2 K and on the measured T_c. At lower temperatures, the critical current increased rather slowly (see Fig. 5-18), and at 4 K the test bed sample carried only about one-third the short sample critical current. Such "degradation" is well known in superconducting magnets; a number of factors are involved but the explanation generally falls in the category of stabilization. Although the test bed configuration is hardly a magnet, the rather disappointing results found in Fig. 5-18 can be explained from the point of view of stability theory as follows:

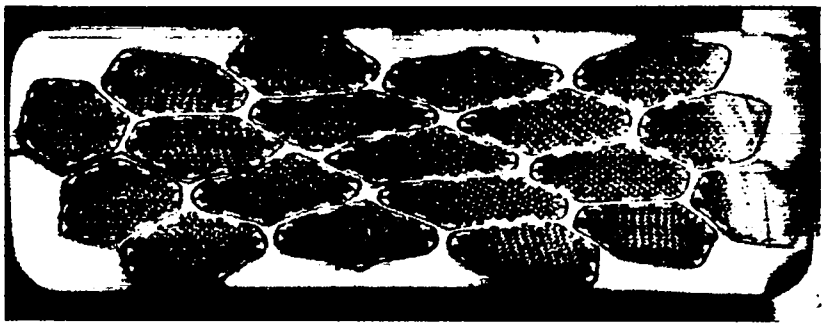

Fig. 5-17.
Photomicrograph of the cross section of the Airco mf Nb_3Sn conductor.

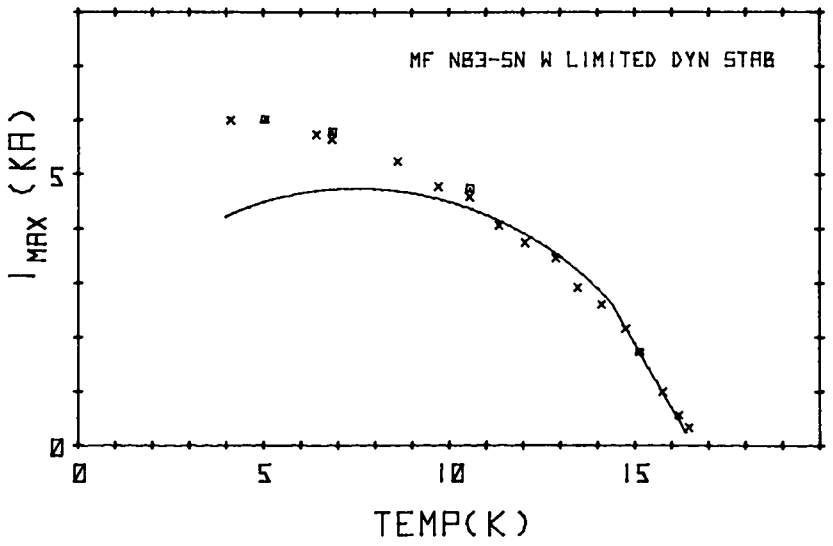

Fig. 5-18.
Comparison of current limits of Airco mf Nb_3Sn conductor (Fig. 5-17) predicted by limited dynamic stabilization (smooth line) with values that were experimentally observed in the test bed experiment (squares and crosses).

1. The conductor is <u>not</u> adiabatically stable under self-field conditions. Although the individual filaments are below the adiabatic limit, they are coupled by the self field. The bronze matrix is of such low thermal conductivity that it can be treated as the adiabatic region (with a smeared out, or averaged, critical current density). The size of this region then exceeds the corresponding stability limit of about 70 μm at 11 K and about 9 μm at 4 K.

2. Dynamic stabilization, i.e., eddy current damping of sudden flux motions, therefore, goes into effect once a conductor thickness greater than the adiabatic limit has been filled up to the critical current density.

3. The small copper veins within the material are probably of insufficient size and purity to be effective, and only the outer copper jacket provides dynamic stabilization.

4. At high temperatures (> 13 K) the entire conductor is dynamically stabilized, and thus can carry the full critical current. Here the measured limiting currents represent the true self-field critical current densities of the conductor and the transition to the normal state proceeds gradually, passing through the flux flow regime. The I_c vs temperature curve is essentially linear.

5. At lower temperatures, supercurrents are only carried in a surface shell whose maximum stable thickness is set by the theory of dynamic stability. Once that (temperature dependent) limit is reached, further current and flux penetration leads to a flux jump that drives the entire sample normal (cf. measurements on propagation velocity[17]). The current limits thus seen below 13 K are not characteristic of mf Nb_3Sn but only of the sample arrangement and geometry.

6. The agreement between calculated and measured current limits (Fig. 5-18) is reasonably satisfactory. The continued gradual rise of the limiting currents (against the drop predicted by the shell model) can probably be explained by an increase in the effective periphery of the shell as its thickness becomes thinner.

5.2.8.4. Cryostability Measurements on the Double Nb_3Sn Tape Sample. In this type of experiment electrical pulses of increasing energy are supplied to a heater in contact with the superconducting sample carrying a chosen steady current less than I_c for a selected T until a propagating normal zone is established. The heater was initially wound uniformly over a 45-cm length of the sample at the 15-m position (halfway down the return leg of the U-shaped sample), such that the resistance of the heater was approximately 1.0 Ω/cm. The heater was tapped 15 cm from one end so that heater resistances (and thus heated lengths) of 15, 30, or 45 Ω (cm) could be selected.

The results of such measurements on this sample at two different temperatures are given in Fig. 5-19 and show the applied steady current as a function of normalized (per unit heater length) pulse energy required to drive

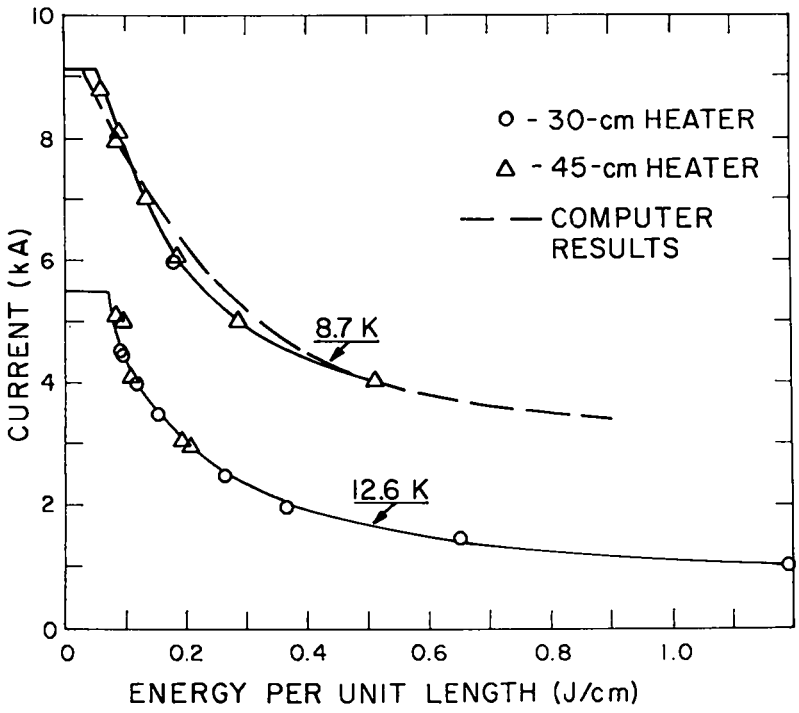

Fig. 5-19.
The energy pulses per unit length of heated section, ΔE, necessary to create propagating normal zones in the sample. The curved lines are drawn as an aid to the eye. The short horizontal lines represent the critical current at each temperature. The finite value of $\Delta E/\ell$ at the critical current is due in part because some energy is absorbed by the flowing helium coolant, and in part because the heater is not located at the warmest spot along the length of the sample. The dashed line is a computer simulation at 8.7 K.

the sample into its normal state. The data indicate that for these relatively long heated lengths the energy per unit length necessary to create propagating normal zones is independent of the heated length.

The finite value of $\Delta E/\ell$ at the critical current (at the top of the curves in Fig. 5-19) is due to two different effects. First, because the sample has a temperature gradient over its 20-m length, the temperature of the heater is not the warmest temperature along the entire conductor. Thus, if higher currents are introduced, the critical current is exceeded in warmer downstream sections and the resulting propagating normal zone eventually works its way back over the entire conductor. Put another way, at a current which is just stable for the entire conductor, a finite ΔE is needed to raise the temperature of the heated section to above that of the warmest section and thus cause a normal zone to develop. Secondly, even for an isothermal conductor at $I_c(T)$, the cryostabilizing effects of the flowing helium and current

sharing in the substrate allow the conductor to recover from a small but finite ΔE. This more complicated phenomenon has been subjected to a computer analysis, essentially using the method discussed in Sec. 4 (Eq. 4-11, 4-15, 4-16 and 4-17), but rewritten to include mass conservation, joule heating and current sharing, as described recently.[22] Using the measured critical current data for the double Nb_3Sn tape sample[12] and the appropriate geometry, the computer code simulates heating pulses and the ensuing recovery or propagation of the normal zone. The results at 8.7 K are shown as a dashed line in Fig. 5-19. The close agreements to the experimental measurements shows that the code can accurately simulate the cryostability of this sample.

5.2.8.5. Cryostability Measurements on mf Nb_3Sn Conductor. Thermal pulse measurements on this sample were made in the manner described in Sec. 5.2.8.4 for three isotherms at approximately 4.9, 10.5, and 15.1 K. The results are summarized in Fig. 5-20. Here dashed horizontal lines at the top of each curve indicate the values of $I_c(T)$ for each isotherm. This set of curves demonstrates a somewhat different type of behavior than that obtained from similar experiments on various tape samples. Again, a finite E is needed to initiate propagation at a given temperature at current levels equal to $I_c(T)$. As the current is lowered, the ΔE needed to initiate propagation

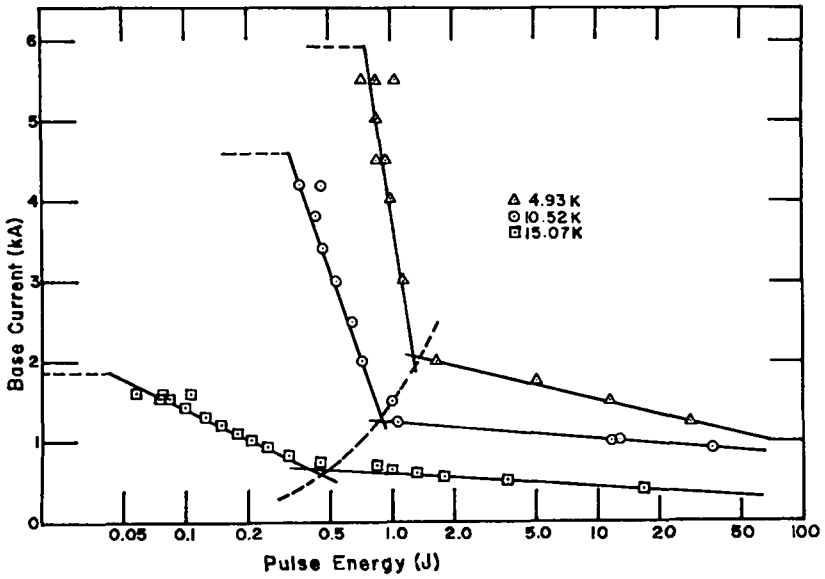

Fig. 5-20.
Effect of various sizes of heat pulses on the critical current of the Airco mf Nb_3Sn conductor at three temperatures.

increases at a rate roughly equal to that observed in the double Nb_3Sn tape sample, but at ΔE values which are approximately fifty times lower. This is due to the large difference in the amounts of cryostabilizing copper between the two samples. As the current is lowered still further, the ΔE values begin to increase substantially and, at the lowest currents, become nearly equal to the values of ΔE for the double tape sample. At such low currents, the effect of the cryostabilizer is clearly less important. What remains surprising is the abruptness with which this lack of cryostability manifests itself. It would appear that there are two different regimes of stability, bounded by the dashed line in Fig. 5-20. This may, however, be an artifact of the semilog display. No computer simulations of cryostability have been performed for this sample, but they might elucidate this atypical behavior.

5.2.9. Normal Zone Propagation Velocity. The observation of the growth or collapse of intentionally produced normal zones in a superconducting wire or cable provides an important experimental verification for some of our ideas on superconductor stability and stabilization. Additional insight can be obtained from measurements of the velocity of the normal-superconducting (N-S) interface.

We have reported measurements of the velocity of destruction of superconductivity in a copper-stabilized mf Nb_3Sn superconductor (67,500 filaments of 5.8-μm diam in a bronze matrix; dimensions 0.51 cm x 0.465 cm) at currents up to 1,100 A. This conductor, in a force-cooled cryogenic environment, exhibited an asymmetry of velocity with respect to cryogen flow direction (downstream to upstream) of 2-to-1 (midrange) at 14.2 K. The asymmetry increased to 7-to-1 (midrange) when the temperature was increased by only 1.6 K to 15.8 K. T_c of the conductor was 16.5 K. Earlier data and analysis[22] indicated that we could not explain this dramatic asymmetry solely in terms of warmer downstream cryogen gas, i.e., reduced heat transfer from superconductor to surrounding cryogen and reduced I_c as a function of increasing temperature. We therefore decided to look for a possible additional asymmetry of velocity with respect to electric current direction, such as we had observed previously in dirty Type II Ta wires.[23]

The new series of experiments with the sample in vacuum and exchange gas environment is our first such set in which there is negligible heat transfer from the moving N-S interface into the surroundings. The experimental arrangement is shown in Fig. 5-21. The only heat transfer involved now would

be from the filaments themselves into the bronze and copper mixed matrix and, of course, the longitudinal heat transfer along the conductor axis. Consequently, the instantaneous temperature is practically uniform over the cross-sectional area so that one-dimensional analysis of the propagation seems justified.

The experimental results at 15.75 K, shown in Fig. 5-22, are quite accurate and clearly show the asymmetry of thermal propagation velocity with respect to current direction. Similar results were obtained at 15.00 and 16.04 K. From these data we obtain the experimental dependence of velocity with respect to temperature for two currents, shown in Fig. 5-23. Once again we observe a significant asymmetry in the normal zone propagation velocity, the higher velocity always being associated with the parallel case where the interface velocity is in the same direction as the electron drift. We would expect that complications related to various flow conditions of the cryogen are absent in these experiments. For the limited data given, the ratio of the parallel to antiparallel propagation velocities at a constant temperature is

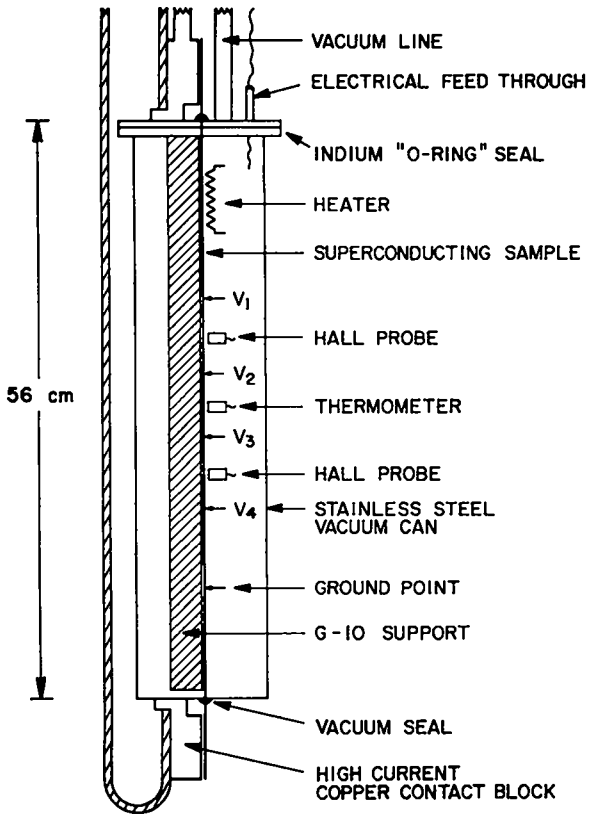

Fig. 5-21.
Schematic diagram of superconducting sample and sample holder showing vacuum enclosure and electrical, thermal, and magnetic probes. V_1 through V_4 indicate the voltage probes used to detect the N-S interface.

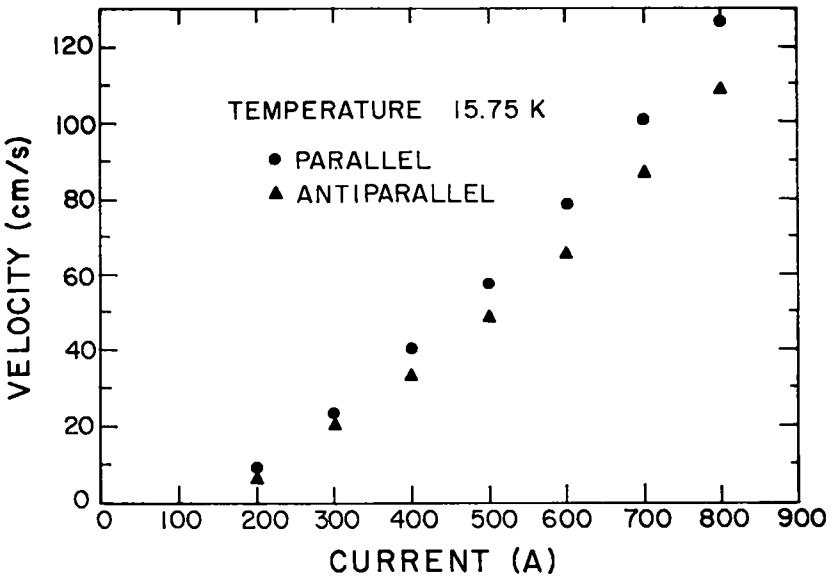

Fig. 5-22.
Velocity of N-S interface as a function of current through the sample. Initial temperature of the superconductor prior to the initiating heat pulse was 15.75 K. For all currents the parallel velocity (interface velocity same direction as electron drift velocity) was greater than the antiparallel velocity.

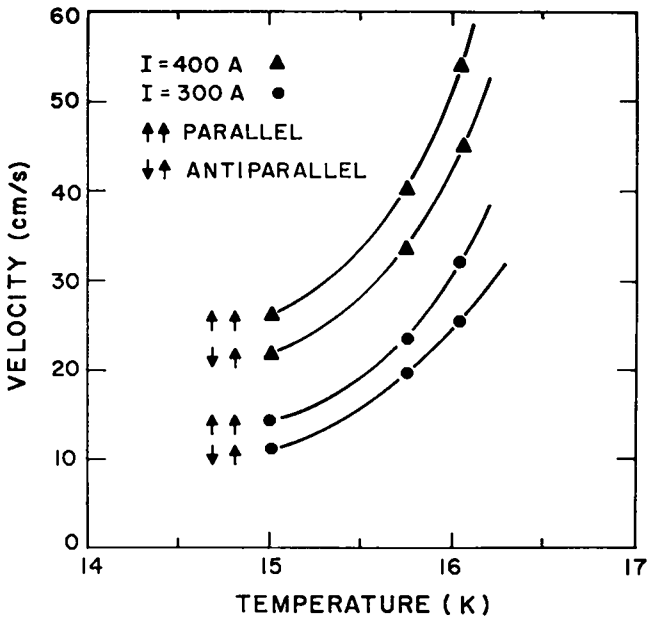

Fig. 5-23.
Velocity of N-S interface as a function of initial temperature of the sample for two applied currents.

roughly constant, independent of the operating current level. For a given current, the difference in the two velocities at various temperatures tends to be constant.

5.3. mf Nb_3Sn Wire Development for a dc SPTL

The work described in the previous cable development sections laid the ground work for selecting a conductor to be used in a dc SPTL. Although the previous work has shown that a number of conductor types could actually be used, a mf wire was chosen. In the mf wire the Nb_3Sn is distributed in fine filaments throughout a conducting matrix. The filaments are small enough so that they are adiabatically stable while the conducting matrix and/or added copper stabilizer provides dynamic and cryostatic stabilization. Because of the fine filaments and precompressive loading on the Nb_3Sn, the mf wire has reasonably good mechanical properties. Cables of mf wires also provide a measure of reliability by providing multiple parallel current paths. During our initial testing, commercial mf Nb_3Sn wire reached a high degree of perfection.

As mentioned earlier, two distinct line designs have evolved. The original design has a coaxial geometry with a low-temperature dielectric; it could be operated at high currents (50 kA) and relatively low voltage (100 kV), giving a power capacity of 5 GW per circuit, would have had an overall diameter of 40 cm, and originally was to have used thin Nb_3Sn films (tapes) for the conductor. In modifying this design we reduced the current, increased the operating voltage, reduced the overall size, changed the superconductor from tapes to mf Nb_3Sn wire and made the conductor flexible so that long lengths could be spooled and pulled into the cryogenic enclosure.

The second type of design consists of two independent conductor and cryogenic enclosure pairs to form one circuit; the dielectric is placed on the outside of the cryogenic envelope and thus operates near ambient temperature; the conductor is braided on cabled mf Nb_3Sn wire in or on the inner tube of the cryogenic enclosure; and the conductor, enclosure, and dielectric can be spooled in lengths up to 600 m. This type of design resembles the conventional self-contained oil-filled (SCOF) cables in many respects. Because the dielectric is outside the cryogenic enclosure, operating voltages up to $\pm$ 600 kV are feasible. Thus, depending on the magnitude of the current, this line can be either a high-capacity (12-GW for 10-kA) or a medium-capacity (3.6-GW for 3-kA) conductor pair.

Although the two types of lines are considerably different, the conductors in both designs could be quite similar. Even if the conductors are different in detail, most of the information needed for one design is applicable to the other.

To arrive at a satisfactory wire design optimized to dc service, we initiated a program to measure and improve the properties of Nb_3Sn tapes and mf wires. Test results obtained previously[17] were incorporated into our evaluation of mf Nb_3Sn wires. The wire properties important in the conductor design are:

1. the critical current and critical current density as a function of temperature;
2. the minimum bending radius that the wire can tolerate without degradation;
3. the compressive loading on the Nb_3Sn caused by differential thermal contraction of the materials in the wire;
4. the dependence of the critical current on magnetic field; and
5. the effect of heat pulses and electrical transients on the stability of the conductor.

Several mf wires were designed, fabricated, and tested to determine the value or range of the properties outlined above.

5.3.1. mf Nb_3Sn Conductor for dc SPTL. The desired properties and internal arrangement of the composite mf Nb_3Sn superconductor for use in a dc SPTL operating between 10 and 14 K are significantly different from those of the identically named materials planned for large, high-field magnets operating at 2 to 4 K or for rotating machinery. Most existing development programs for mf Nb_3Sn are sponsored by government organizations interested solely in the latter objectives. A specific dc SPTL wire manufacturing program was initiated in FY 1977 by LASL.

We have outlined the design and necessary steps in the fabrication of the composite mf wires or subcables that will serve as the building blocks for the complete high-current cable. We assume that "standard" alloy systems will be used so that published information can be applied on optimizing heat treatment times and temperatures for the formation of Nb_3Sn by the diffusion process.

5.3.1.1 General Requirements on Composite Superconducting Wires. Below are listed seven requirements to be met by dc SPTL conductors together with methods of attaining them.

1. Usable critical current densities at fields between 0.5 and 1 T and at temperatures of up to 14 K. Diffusion-reacted bronze assemblies (Nb-CuSn) with overall averaged critical current densities between 500 and 1000 A/mm^2 at 14 K will meet all foreseeable requirements of supercurrent density.

2. Sufficient fineness of superconductor filament to be adiabatically stable at the minimum operating temperature of 10 K. Nb_3Sn diffusion zones 15 μm or less in thickness will meet this criterion. Actually, 5 μm is a practical maximum for the thickness of the diffusion zones. However, if a tubular diffusion zone completely encloses the bronze, the diameter of that tube must be no larger than 55 μm.

3. Sufficient cryostabilizer of low resistivity and in close proximity to the superconductor to carry the full line current during accidental, locally limited normalcies while permitting the line to recover superconducting temperatures. Cryostabilizer incorporated into the wire with a matrix-to-superconductor ratio of 8, so that the OFHC copper cryostabilizer will be limited to a current density of 100 A/mm^2 and a corresponding power density of 1 mW/mm^3, is expected to serve satisfactorily. However, the effectiveness of the cryostabilization, which will vary with the extent of the fault or disturbance and with the heat transfer conditions, remains to be verified.

4. Proper arrangement of superconductor and cryostabilizer to minimize current transfer resistances and inductances. This is achieved by reducing the amount (distance) of high-resistivity material between the superconductor and the surface of each wire to less than about 100 μm.

5. Minimum permissible dimensions for cryostabilizer to avoid increase in low-temperature resistivity due to size effect and impurity diffusion. This requires minimum cryostabilizer dimensions of 2 to 5 mean free paths and effective, unbroken diffusion barriers. A cryostabilizer dimension of 10 μm should provide an adequate safety margin, but the minimum practical barrier thickness remains to be determined.

6. Optimal location of cryostabilizer to dynamically damp gross wire and cable motions or distortions. It is likely that requirements 3, 4, and 5 above will automatically help in meeting this goal.

7. Sufficient strength or intentional strengthening of the composite to avoid breakage of the brittle Nb_3Sn during cable manufacture and installation and consequent degradation of critical current.

5.3.1.2. Internal Layout of Composite Superconducting Wires. Composite mf Nb_3Sn superconducting wires containing protected (copper) cryostabilizer can in principle be designed with many different geometric arrangements of the bronze, niobium, and copper. We prefer those with essentially cylindrical, or finely grained hexagonal, symmetry to preserve electrical and mechanical isotropy and thereby minimize the possible effects of mechanical stresses. There are four basic arrangements or building blocks which can then be combined into more complex structures:

1. Niobium tubes containing bronze rods and embedded in a copper matrix. The Nb_3Sn layer is formed on the inside of the niobium tubes which also serve as diffusion barriers to protect the copper.

2. Niobium tubes containing copper rods and embedded in bronze matrix. The Nb_3Sn diffusion layer is now formed on the outside surface of the niobium tubes which protect the copper.

3. Surface-diffused niobium filaments in a bronze matrix surrounding a large copper core, which is protected by a separate diffusion barrier.

4. Surface-reacted niobium filaments in a bronze matrix which is, in turn, surrounded by a diffusion barrier and then by a high-purity copper shell.

The details of the various billet arrangements have been worked out analytically and graphically. However, of all the possible arrangements, only the first and the last (when multiply stacked to limit the size of the high-resistivity regions) meet the previously listed dc SPTL requirements. Figure 5-24 shows a sample layout of the wire (or of the extrusion billet). The small circles marked Nb can be either niobium tubes or tungsten diffusion barriers, containing pure bronze (BRZ) or bronze with many fine niobium filaments.

5.3.1.3. Conductor Design and Procurement. The wire differs from the more conventional mf Nb_3Sn in that it has a large ratio of high-conductivity-copper to superconductor-plus-bronze (8-to-1 and 5-to-1 for two different designs) and that the Nb_3Sn is in close proximity to the copper so that current sharing is enhanced in case of some kind of fault. A procurement request for the manufacture of three batches ($\sim$36 kg total) of such material in the form of 0.25-, 0.5- and 1-mm-diam wire was issued early in FY77. Bids were received from three vendors. Because of technical differences among the various bids and the desire to test several design concepts, a proposal from the Supercon, Inc. and a portion of a proposal from Airco, Inc. were accepted.

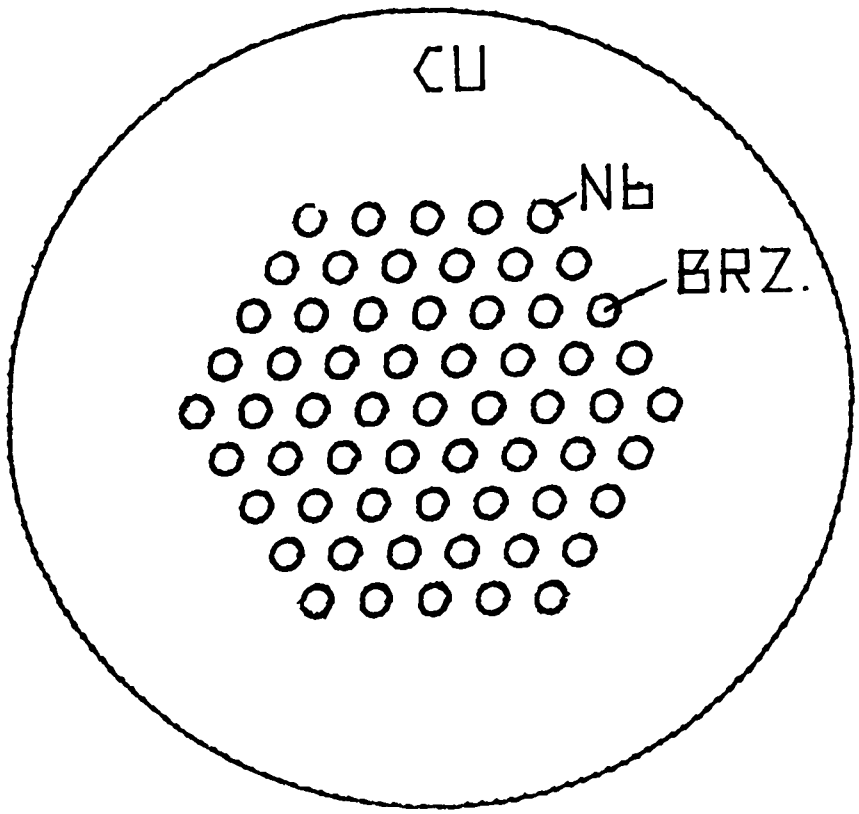

Fig. 5-24.
mf Nb_3Sn conductor proposed for dc SPTL. Large copper to superconductor ratio limits dissipation during faults to 1 mW/mm^3 at a current density of 100 A/mm^2. Nb_3Sn "filaments" have a current density at 14 K of 1000 A/mm^2 referred to the original Nb and bronze. For adiabatic stability, the regions of high electrical resistivity and of low thermal conductivity must have diameters of less than 55 m at 10 K or 35 m at 8 K.

The Supercon design uses single stacking of 37 bronze-filled Nb tubes arranged to form diffusion barriers preventing tin contamination of the high-purity copper matrix while keeping the stabilizing copper near the superconductor. Photomicrographs of the wire illustrating this design are shown in Figs. 5-25 and 5-26. Items (1) and (2) of the order have different copper-matrix-to-bronze-plus-niobium ratios R_M = 8 and 5, respectively, while item (3) has R_M = 8 but a different geometric layout, the filaments being uniformly distributed throughout the inner 80% of the cross section of the wire instead of occupying only the inner 35% of the area as in items (1) and (2). Item (3) also has 37 filaments per wire. The different geometric layouts have helped us to evaluate the bending performance of the three wires at several

fixed diameters. Originally the billet for item (3) was to have an aluminum bronze alloy shell which would later form an oxide surface layer on the wire during the heat treatment and would be evaluated as a means to insulate electrically adjacent wires in the cable to minimize transient and ac losses. Later it was decided to test this insulating scheme on less costly and more predictable mf Nb-Ti wire.

Wires drawn to several sizes by Supercon from items (1) and (2), as described in Table 5-III, were received and have undergone a series of heat treatments to determine the proper time-temperature schedules for obtaining a satisfactory combination of critical current, critical temperature, and mechanical properties.

Airco's proposal was divided into two phases. In phase (1) a bronze-niobium composite billet containing 109 niobium filaments distributed evenly in a copper-13 weight percent tin matrix was assembled and extruded. In phase (2) this "core material" was assembled with tantalum diffusion

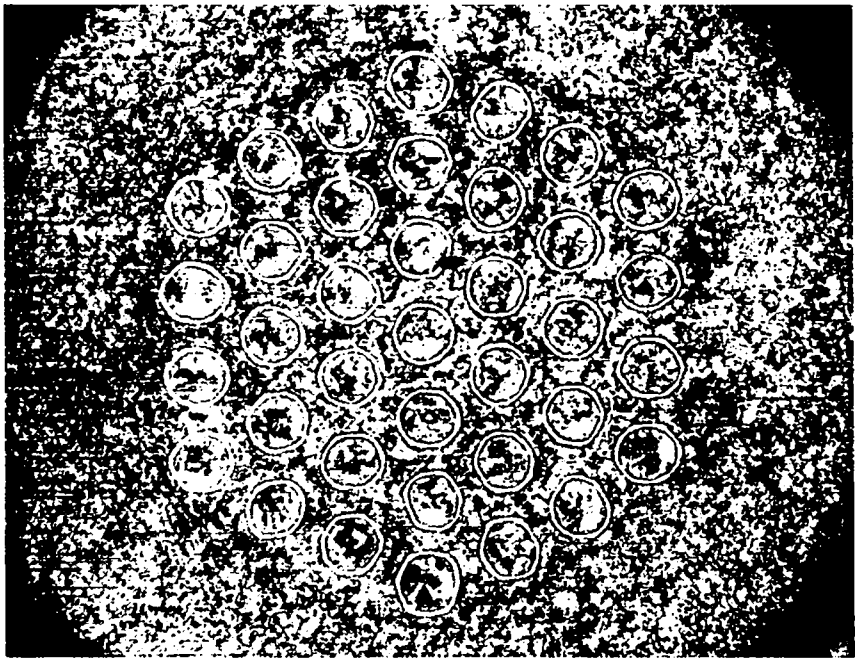

Fig. 5-25.
Transverse section of Supercon, Inc., mf Nb_3Sn wire 256XE-40-1A, 83% copper, 2.7-mm diam. Magnification is 50X.

Fig. 5-26
Transverse section of Supercon, Inc., 256X3-40-1A after reduction to 0.25-mm diam. Magnification is 1700X.

barriers and high-purity copper to produce five different wire configurations, three of which have an 8-to-1 Cu-to-(Nb + bronze) ratio and two of which have a 1-to-8 ratio.

5.3.2 Heat Treatment (HT) Optimization. For heat treating a procedure was selected in which 66-cm lengths of wire were heated in a 150-cm-long tube furnace with the temperature controlled to $\pm$ 2°C. Upon completion of the heat treatment the I_c of each sample was measured as a function of temperature between 13.8 K and T_c using a bath of pumped liquid hydrogen as the coolant. The results of the I_c measurements on four of the wires at 14 K for various HT's are shown in Fig. 5-27. These plots show the J_c (I_c divided by cross-sectional area of niobium + bronze) at 14 K for a given reaction temperature as a function of the square root of the reaction time. Because, at a given temperature, the diffusion distance of tin into the niobium is roughly proportional to the square root of the reaction time, the abscissa for each of these graphs is a relative measure of the Nb_3Sn thickness. Another way to consider the data is to plot J_c vs the HT temperature for a fixed reaction time; this is shown in Fig. 5-28. We concluded that the

TABLE 5-III
SUPERCON mf Nb_3Sn WIRE

	Designation	Wire Diam (cm)	No. of Filaments	Twist (turns/cm)	Filament Diam (μm)	Bronze-to-Niobium Ratio	Filament Distribution
1)	83% OFCH Cu Matrix						
	256XE-40A-1A	0.10	37	0	76	2.5:1	a
	256XE-40A-1B	0.10	37	1	76	2.5:1	a
	256XE-40A-2A	0.05	37	0	39	2.5:1	a
	256XE-40A-2B	0.05	37	2	39	2.5:1	a
	256XE-40A-3A	0.025	37	0	19	2.5:1	a
	256XE-40A-3B	0.05	37	4	19	2.5:1	a
2)	90% OFHC Cu Matrix						
	256XE-41A-1A	0.10	37	0	66	2.5:1	a
	256XE-41A-1B	0.10	37	1	66	2.5:1	a
	256XE-41A-2A	0.05	37	0	33	2.5:1	a
	256XE-41A-2B	0.05	37	2	33	2.5:1	a
	256XE-41A-3A	0.025	37	0	16	2.5:1	a
	256XE-41A-3B	0.025	37	4	16	2.5:1	a
	256XE-43A-1A	0.10	36	0	66	2.5:1	b
	256XE-43A-1B	0.10	36	1	66	2.5:1	b
	256XE-43A-2A	0.05	36	0	33	2.5:1	b
	256XE-40A-1B	0.05	36	2	33	2.5:1	b
	256XE-43A-3A	0.025	36	0	16	2.5:1	b
	256XE-40A-1B	0.025	36	4	16	2.5:1	b

[a]Filaments close packed over inner 35% of the cross section of the wire.
[b]Filaments spread out over inner 80% of the cross section.

highest J_c (at 14 K) is obtained with a HT schedule of 64 h at 750°C. A similar maximum was observed for all of the types of wire tested; however, at lower HT temperatures the peak was not determined because HT times in excess of 128 h were not considered useful. The slope and J_c values found in Fig. 5-27 do indicate that some further improvement in J_c is possible over that obtained at 750°C with even longer reaction times.

T_c^* is a measure of the highest temperature at which the wire starts to carry a practical amount of supercurrent. It is defined as the $I_c = 0$ intercept of the nearly linear portion of the I_c vs T curve. We had hoped that T_c^* could be increased by some combination of HT temperature and reaction time. Although we did observe small variations in T_c^* (higher T_c for longer reaction times at a given temperature), there was no really significant increase.

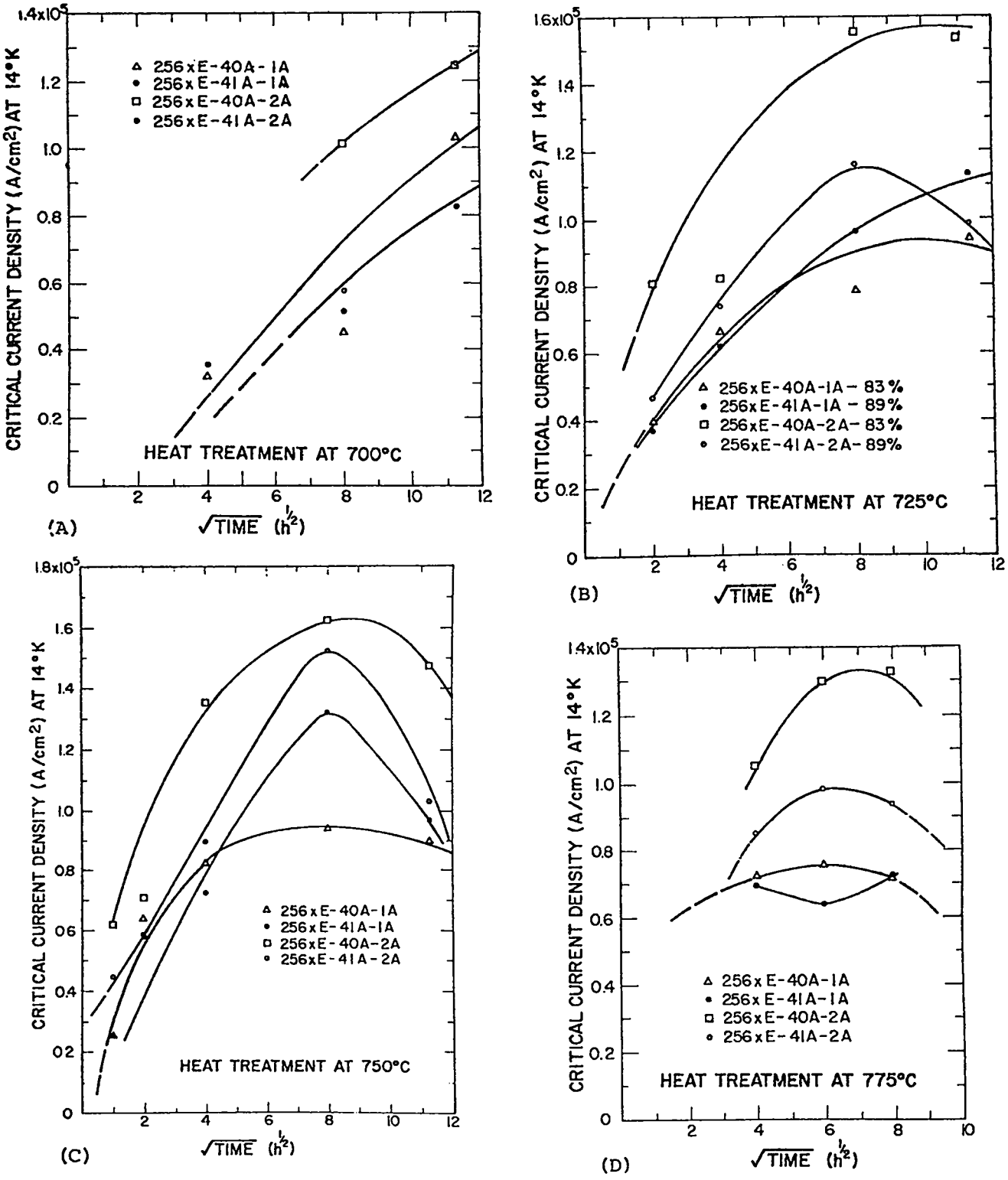

Fig. 5-27.
Graphs showing the effect of reaction time in hours for reaction temperatures of 700°C (A), 725°C (B), 750°C (C), and 775° (D) on critical current density at 14 K. The current density is plotted as a function of the square root of the reaction time because the Nb_3Sn thickness is proportional to this quantity. Sample characteristics are described in Table 5-III.

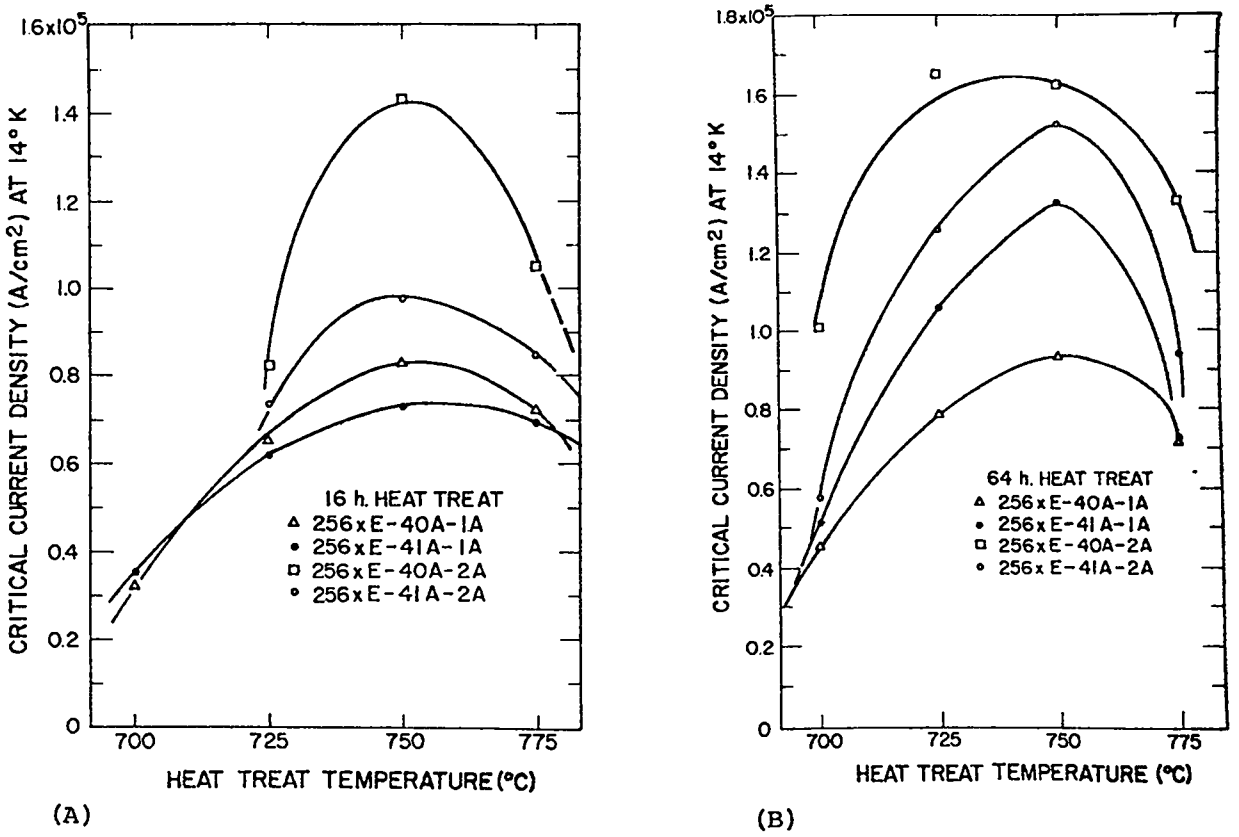

Fig. 5-28
Critical current density at 14 K as a function of reaction temperature for reaction times of 16 h (A) and 64 h (B). For all four samples and for both reaction times, the critical current density was a maximum for a reaction temperature of 750°C. Sample characteristics are described in Table 5-III.

In an earlier study[17] we had found that T_c was significantly reduced by strain in the Nb_3Sn caused by a mismatch between the coefficient of thermal expansion (CTE) of the Nb_3Sn and the substrate material. Thus we assumed that the relatively low T_c^*'s (15.0 to 15.5 K) measured in the present wires are also the result of compressive strain in the Nb_3Sn, induced by the difference in CTE between the Nb_3Sn and the bronze cores of the Nb_3Sn filaments. The combinations of reaction times and temperature that produced thicker layers of Nb_3Sn (and thus somewhat less strain) tended to have higher T_c^*.

We also produced a series of samples reacted at 750°C for 16 h then annealed at lower temperature. A typical sample reacted in this manner has a T_c^* of approximately 15 K. In Table 5-IV we list the T_c^*'s obtained for samples that received an additional anneal.

The anneals tended to increase T_c^*, but the changes are relatively small. Further discussion of the annealed samples is given in Sec. 5.3.3.

5.3.3. Mechanical Properties of Supercon Wire. As mentioned above, the mechanical properties of the superconductor play an important role in the design of the dc SPTL conductor. The amount of assembly that can be accomplished after the Nb_3Sn is formed in the conductor depends on the amount of strain and minimum bending radius that the wire can withstand without degrading the superconducting properties of the Nb_3Sn. In order to find these limits and to understand and, perhaps, modify them, we designed and performed a series of tests to determine the effect of bending on the critical current. These and tests on a related quantity, the effect of strain on the critical current, are described in Sec. 5.3.3.1. In order to understand the HT measurements, we made pinning force measurements on bent and as-reacted (not bent) samples.[24] These measurements are discussed in Sec. 5.3.3.2.

5.3.3.1. Results of Bend Tests. The samples subjected to bend tests were several types of wire, as well as similar wire with different HT's. First, a sample was mounted in the I_c holder-probe,[12] and the I_c of the as-reacted sample was measured. Each sample was then warmed to room temperature; one end of the sample was unsoldered from the current contact block and bent 180^o around a certain cylinder, straightened out, and resoldered to the contact block. We then remeasured I_c. This procedure was repeated 5 to 13 times on each wire. The results of these tests, showing the effect of bending on J_c at 14 K, are shown in Fig. 5-29, where J_c has been plotted against the number of bends and bend radius. On each graph the sample type and HT schedule are shown. Using the information in Table 5-III, the sample type can be inferred from the last five alphanumeric characters in the sample number.

TABLE 5-IV

T_c^* FOR SAMPLES (256XE-41A-1A) REACTED AT 750°C FOR 16 h FOLLOWED BY VARIOUS ANNEALING SCHEDULES

Anneal Time (h)	Anneal Temperature (°C)	T_c^* (K)
0	0	15.0
96	400	15.25
84	500	15.50
87	600	15.20

By comparing Fig. 5-29A with 5-29B and Fig. 5-29C with 5-29D we see that the effect of bending is independent of filament twisting. However, for smaller radii bends, a different amount of degradation might be expected for the twisted wires.

After the initial increase in the critical current, common to all wires, we observed degradation to be more severe in the 43-series wire than in the 40- or 41-series wire; that is, if the filaments are concentrated near the center of the wire, less damage occurs for a given bend number and radius. We expected this result because less strain is introduced for a given bend radius when the filaments are nearer the neutral axis; this is demonstrated by comparing Fig. 5-29A with 5-29C and Fig. 5-29B with 5-29D. It should also be noted that the increase in J_c for the first bend is greater in the 43-series wire.

In Figs. 5-29E and 5-29F the results for two similar samples are plotted; the difference is in the HT given each sample. The relative effect of bending is greater in the sample heat treated for 16 h at 775°C than in the one heat treated for 64 h at 750°C, indicating that the sample with the shorter HT (less Nb_3Sn) is affected more by the bending than the sample with the larger percentage of Nb_3Sn. Because the ratio of Nb_3Sn to bronze presumably determines the amount of initial strain in the Nb_3Sn, the sample having the shorter HT initially should have more strain.

A similar comparison can be made between two wires of different diameter. In Figs. 5-29E and 5-29G, the HT times are the same and the HT temperatures are similar, so the Nb_3Sn-layer thickness in each wire should be similar. However, the percentage of Nb_3Sn relative to the bronze is smaller in the larger diameter wire. We assumed that the larger wire had larger compressive strain on the Nb_3Sn, which should result in a greater initial rise in I_c with bending than that found for the smaller wire; such was the case.

In all wires and for all temperatures at which I_c was measured, I_c increased with the first few bends. At 14 K the relative increase ranged from 1.25 to 2 times the value for the as-reacted wire; at 15 K this increase was as high as seven times the as-reacted value. Of course, the increase is magnified both by the intrinsic increase in I_c and by the increase in I_c through an increase in T_c.

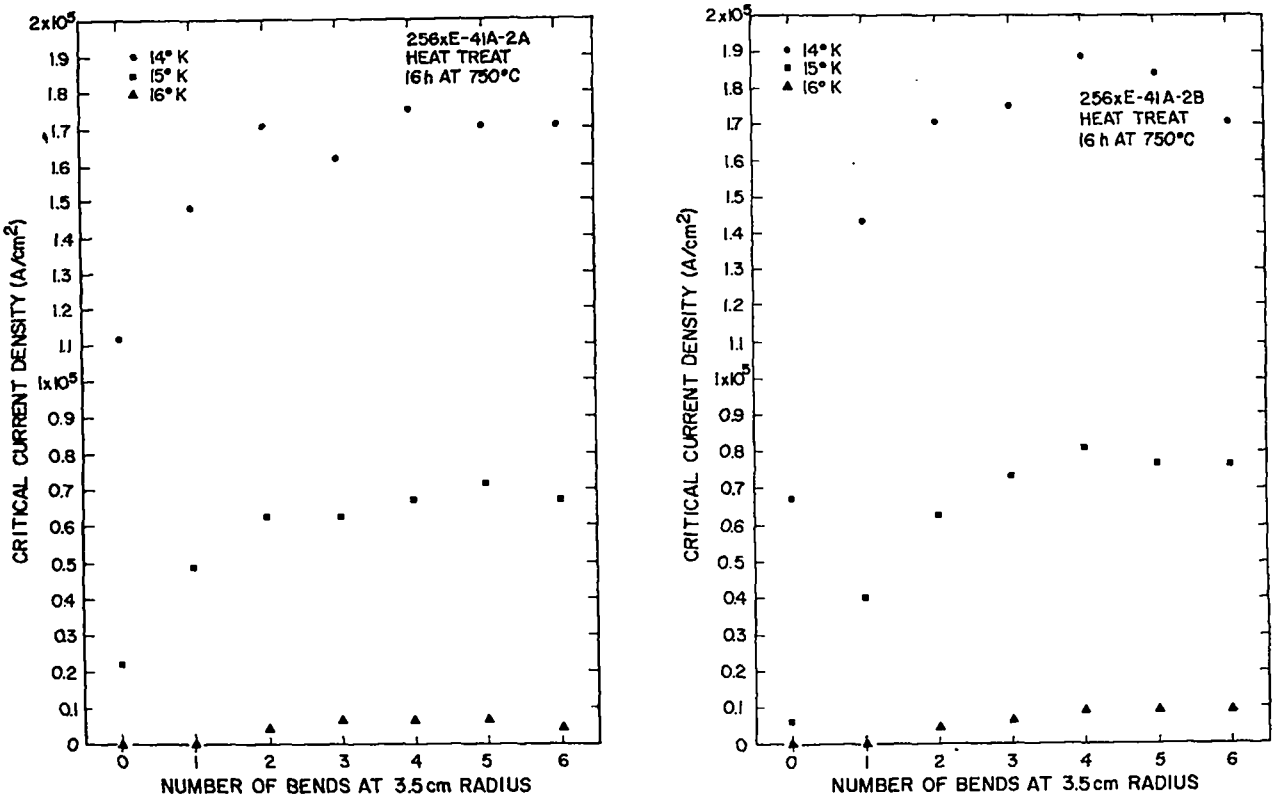

(A) (B)

Fig. 5-29.
This series of graphs displays the effect on J_c of bending the superconductor around various diameter cylinders at room temperature. J_c is plotted as a function of the number of times the sample was bent at a given radius. In all cases the initial bends caused an increase in J_c, indicating a relief of the compressive strain in the virgin wire. Note that only the most severe bends cause large degradation in J_c (see Fig. 5-29G).

For sample 256 XE-41A-1A, after an HT of 64 h at 775°C, we reduced the bending radii from 7.5 to 1.25 cm in several steps. These bends produced a maximum strain on the outside of the bend of 0.4 to 2.4%, respectively. Although the bending at the intermediate smaller radii caused reductions in I_c, only the bends at 1.25-cm radius caused large degradations.

We performed two more sets of bend tests consisting of a series of multiple bends at the same radius and a series of bends at decreasing radii. The first series of tests was performed to determine whether multiple bends in different directions would relieve more strain in the wire and thus increase I_c even more than single bends or multiple bends in the same direction. The tests were also designed to simulate the series of bends a wire might be

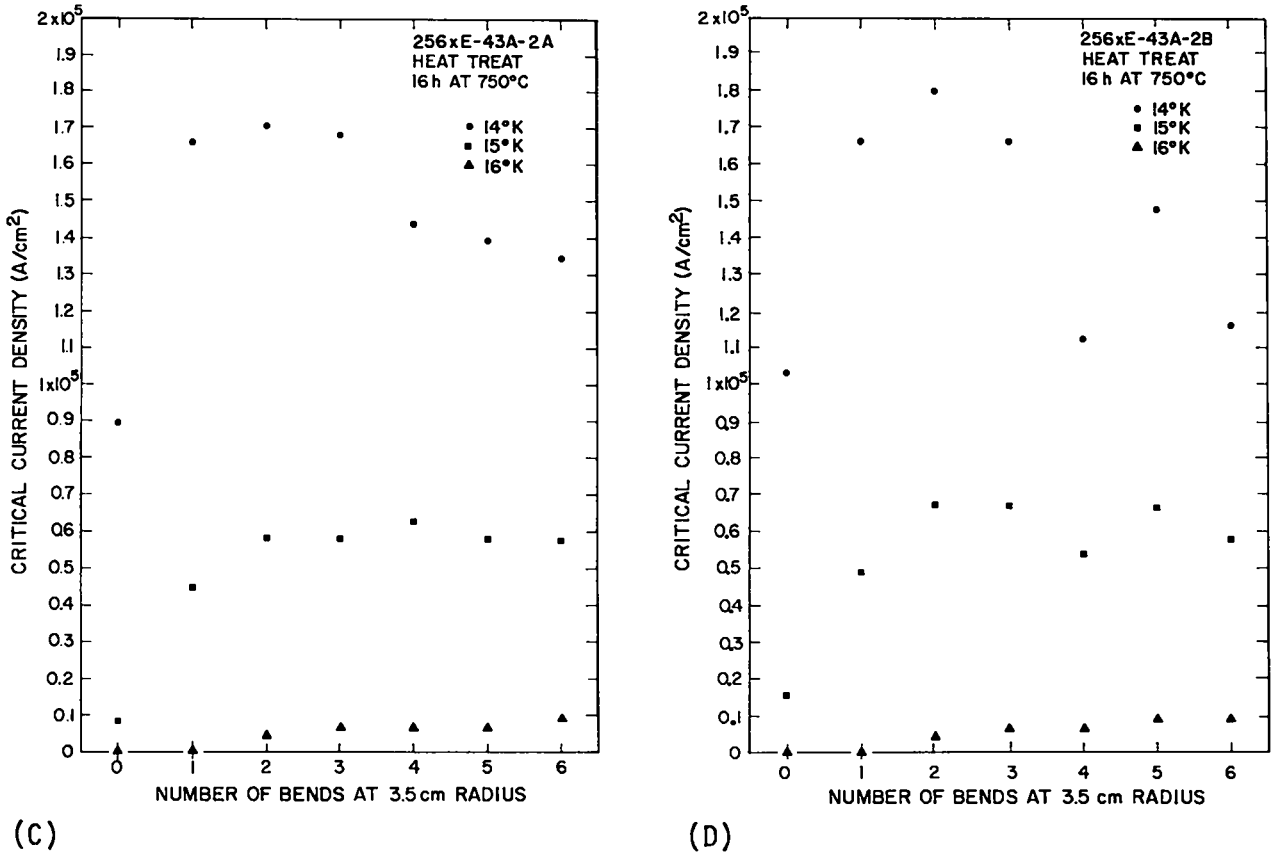

Fig. 5-29.
This series of graphs displays the effect on J_c of bending the superconductor around various diameter cylinders at room temperature. J_c is plotted as a function of the number of times the sample was bent at a given radius. In all cases the initial bends caused an increase in J_c, indicating a relief of the compressive strain in the virgin wire. Note that only the most severe bends cause large degradation in J_c (see Fig. 5-29-G).

subjected to as it passed through a cabling machine. The results show that I_c does not depend on the direction of the bends for a given radius but depends only on the number of bends. In all cases I_c increased for about the first 4 to 5 bends and then remained reasonably constant for at least another 7 to 10 bends. Reacted wire of this type has a good chance of surviving a cabling process.

The second series of tests involved bends where the radius was decreased after each bend. We performed critical current measurements to determine the degradation produced by a decreasing radius. Figure 5-30 shows the results of these tests on a 1-mm-diam wire with the filaments concentrated in the inner 35% of the cross-sectional area. Bends as small as approximately 1.9-cm

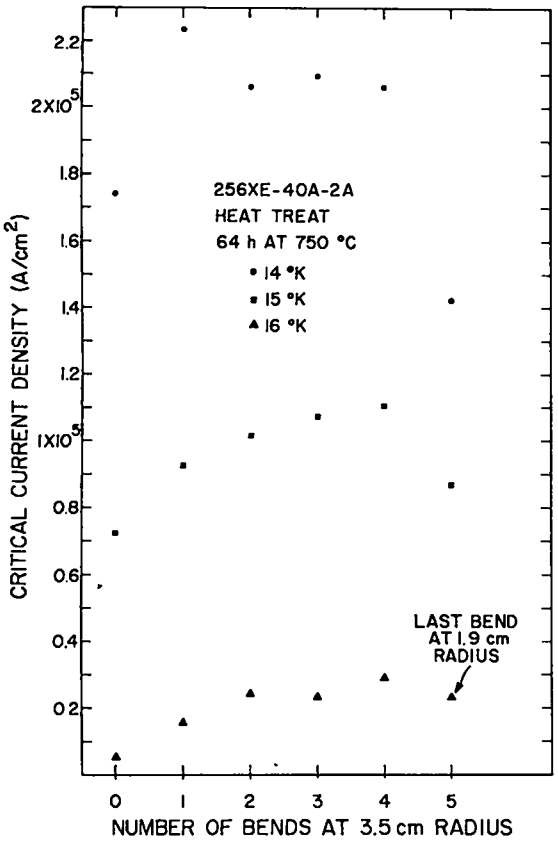

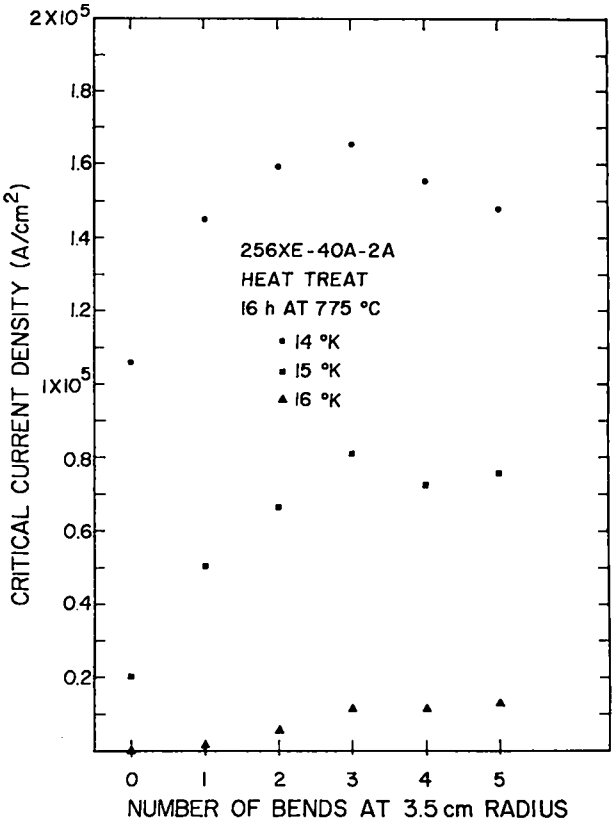

Fig. 5-29.
This series of graphs displays the effect on J_c of bending the superconductor around various diameter cylinders at room temperature. J_c is plotted as a function of the number of times the sample was bent at a given radius. In all cases the initial bends caused an increase in J_c, indicating a relief of the compressive strain in the virgin wire. Note that only the most severe bends cause large degradation in J_c (see Fig. 5-29 G).

radius reduced I_c only 15% from that of the as-reacted wire. For this wire the 1.9-cm bend produced a strain of $\sim$1.6% in the Nb_3Sn filaments near the outside of the bend. We therefore determined that a bend of approximately 2.5-cm radius does not reduce I_c.

In bend tests, the outside of the wire is placed in tension while the inside of the wire is under compression. This produces a complex strain configuration in the wire, which is difficult to analyze quantitatively. In order to get quantitative data on the strain effects, we initiated a testing program in collaboration with the National Bureau of Standards (NBS) at Boulder, Colorado. In these tests we applied a pure tensile stress to the samples and measured I_c under several strain conditions. Magnetic fields to

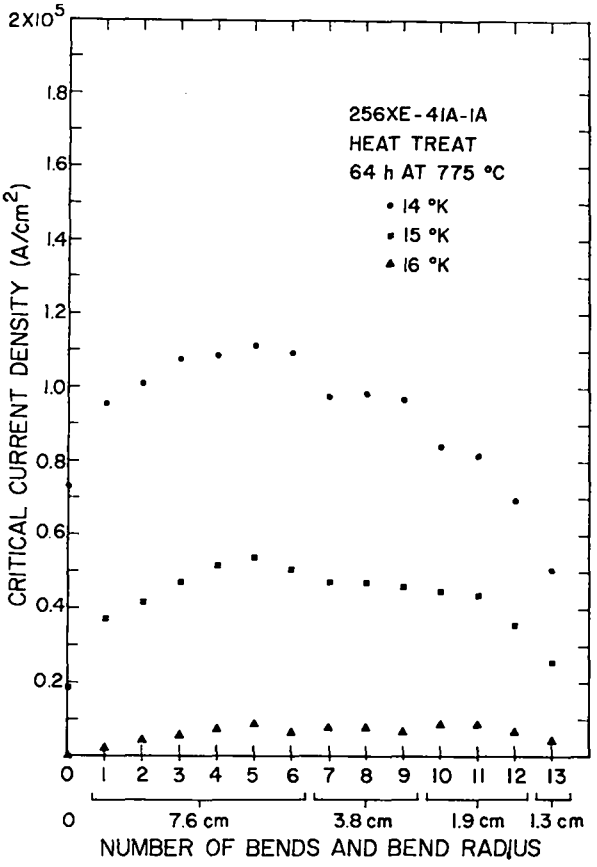

(G)

Fig. 5-29.
This series of graphs displays the effect on J_c of bending the superconductor around various diameter cylinders at room temperature. J_c is plotted as a function of the number of times the sample was bent at a given radius. In all cases the initial bends caused an increase in J_c, indicating a relief of the compressive strain in the virgin wire. Note that only the most severe bends cause large degradation in J_c (see Fig. 5-29 G).

7 T were applied. A plot of the results is shown in Fig. 5-31 for one sample. For zero applied field there is essentially no effect on I_c to approximately 0.7% strain. For the applied fields of 3 T and 7 T there is a slight increase in I_c with applied stress; the maximum occurs at about 0.35% strain. The critical current drops to a value equal to that of the as-reacted state at about 0.7% strain. These measurements strongly suggest that the Nb_3Sn is initially under approximately 0.35% compressive strain. This is in reasonable agreement with the results of the bend tests.

The compressive strain in the as-reacted wire reduces both T_c^* and I_c. However, this strain does allow the wire to be stressed somewhat more

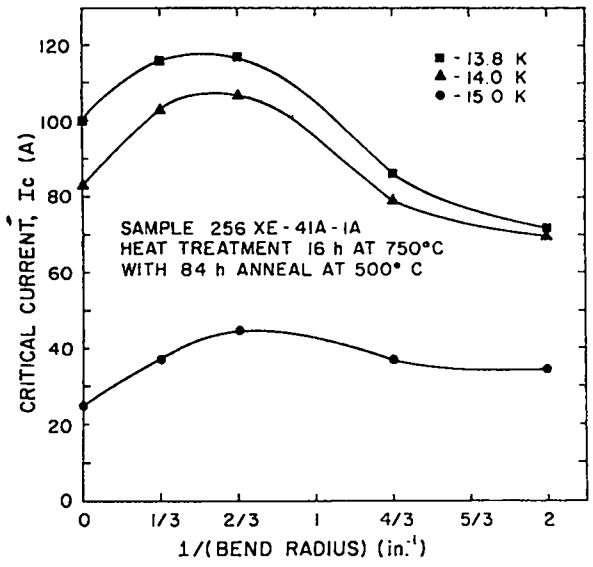

Fig. 5-30.
Critical current of a 1-mm-diam mf Nb_3Sn wire as a function of the bend radius. The Nb_3Sn filaments are located within the central 35% of the cross-sectional area.

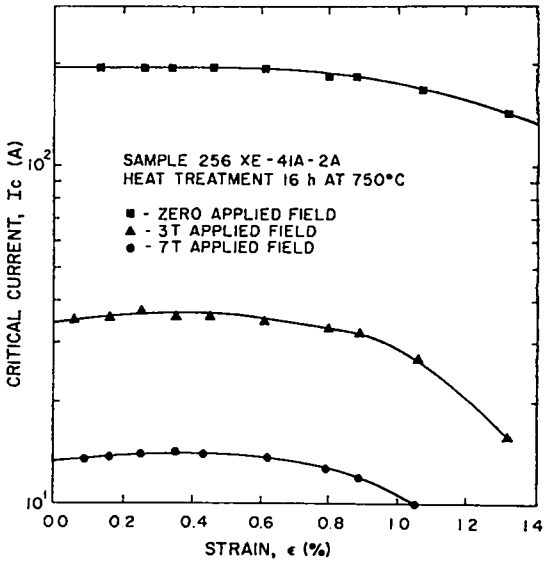

Fig. 5-31.
Critical current at 4 K as a function of strain for three magnetic fields of 0, 3 T, and 7 T. Data were taken at NBS, Boulder, Colorado.

during fabrication and under operating conditions without deleterious effects; in fact, one might expect some improvement of T_c^* and I_c. We now believe we can control the preloading in the wire to optimize its superconducting characteristics for the final working conditions.

5.3.3.2 Pinning Forces Measurements and Stress Effects. In order to add another dimension to the critical measurements and to further elucidate the stress effects in the Nb_3Sn I_c measurements as a function of applied magnetic field, tests were made on as-reacted and on stress-relieved bent samples. The measurements were performed at 4 K in fields to 10 T. In all cases the field was perpendicular to the direction of current through the samples. The sample holder provided mechanical support and prevented Lorentz forces from further straining the samples.

Past measurements of I_c in as-reacted and stress-relieved samples were used to determine the relative amount of strain-relief achieved by a sequence in which the wire was bent over various-sized mandrels and then straightened a number of times. We found for all the samples that a single bend over a 3.8-cm-radius mandrel was sufficient to increase the critical current in zero

magnetic field (I_{co}) at 14 K by $\sim$ 30% and to increase T_c^* by about 1 K. While the exact amount of enhancement of I_{co} and T_c depends to a limited extent on the HT of the wire (that is, on the thickness of Nb_3Sn), in no case was a decrease in I_{co} or T_c^* found using this bending procedure. Therefore, we concluded that this procedure did not break filaments nor place the filaments under tensile stress but did reduce the net compressive strain in the Nb_3Sn.

To determine the effect of this procedure on the flux-line pinning properties, curves of pinning force F_p were determined on some of these wires as a function of applied field at 4.0 K from the relationship $F_p = I_c \times H$. The bending procedure had an apparently unpredictable effect on the F_p vs H curves measured at 4.0 K. From the results for five different samples in the as-reacted and bent states given in Table 5-III, the effective upper critical field H_{c2} shows an increase after bending and straightening in all cases except for the sample that was given a low temperature anneal to relieve some of the initial compressive strain. Such increases in H_{c2} are expected because H_{c2} should be sensitive to strain relief, just as T_c should. However, changes in the maximum pinning force F_{pmax} and $h_p = H/H_{c_2}$ (the reduced field at which F_{pmax} occurs) do not correlate with changes in H_{c2}. Based on the Kramer[25] model of flux pinning, increases in H_{c2} should cause F_{pmax} to increase and h_p to shift to a lower reduced field if we assume that a single, uniquely valued flux pinner is acting in these samples. Therefore, it appears that bending the sample not only relieves strain but also alters some other parameters that affect the pinning of flux lines.

Because both grain boundaries and strain fields are known to pin flux lines, we considered a model with two pinners, each having its own distribution in effective pinning strength. Kramer[25] has calculated the pinning force in such a case, assuming a Poisson distribution for each of the pinners. The result is given by

$$F_p = \frac{h^{1/2}}{(1-h)^2}\left\{C_1\langle K_p\rangle_1^2\left[1-\left(\frac{K_{pm}}{\langle K_p\rangle_1}+1\right)\exp\left(-\frac{K_{pm}}{\langle K_p\rangle}\right)\right]\right. \quad (5\text{-}1)$$

$$\left. + C_2\langle K_p\rangle_2^2\left[1-\left(\frac{K_{pm}}{\langle K_p\rangle_2}+1\right)\exp\left(-\frac{K_{pm}}{\langle K_p\rangle_2}\right)\right]\right\}$$

$$+ K_c\, h^{1/2}(1-h)^2 \exp\left(-\frac{K_{pm}}{\langle K_p\rangle}\right),$$

where h is the reduced magnetic field H/H_{c2}, K_s is the flux line lattice (FLL) shearing parameter, and $K_{pm} \equiv K_s\,(1-h)^4$ represents a pinning strength below which flux motion occurs by a pin-breaking mechanism and above which the FLL will shear around the strongest pins. The mean pinning strength $\langle K_p\rangle$ in the sample is given by

$$\langle K_p\rangle = C_1\langle K_p\rangle^2 + C_2\langle K_p\rangle^2 \quad , \quad (5\text{-}2)$$

where C_1 and C_2 are normalizing factors such that

$$C_1\langle K_p\rangle_1 + C_2\langle K_p\rangle_2 = 1 \quad . \quad (5\text{-}3)$$

In the limit of $h \sim 1$, Eq. (5-1) reduces to a good approximation of the expression for a single-line pinning mechanism, namely

$$F_p = K_s\, h^{1/2}(1-h)^2 \quad . \quad (5\text{-}4)$$

We have used Eq. (5-4) to extract values of the effective upper critical field H^*_{c2} by fitting measured pinning force curves for $h \leq 0.5$ to Eq. (5-4) with the stipulation that $F_p = 0$ at $h^* = 1$, where $h^* = H/H^*_{c2}$. (H^*_{c2} will coincide with a resistively measured upper critical field only for a completely uniform, defect-free sample.[26]) Values of H^*_{c2} for the various samples are given in Table 5-V. We have used these values of H^*_{c2} and Eq. (5-1) to analyze the flux pinning curves in an attempt to describe the ob- served changes in $F_p(h)$ through changes in the distribution of the effective number and strength of active pinning sites.

Figure 5-32 shows an experimentally determined normalized flux pinning (F_p/F_{pmax}) curve as a function of reduced field for a sample reacted for

128 h at 700°C; this sample exhibited a 20% increase in H^*_{c2}, yet only an $\sim$ 3% decrease in F_{max} on bending. Also in Fig. 5-32, we show curves calculated using Eq. (5-1) for the two data sets. The calculated curves are in good qualitative agreement with the experimental data. The theoretical curves were obtained by varying only the effective number of active pinning sites of each species, that is, $C_1\langle K_p\rangle_1$ and $C_2\langle K_p\rangle_2$ such that Eq. (6-3) is satisfied, by varying the ratio $\langle K_p\rangle/K_s$, and by changing the effective strength of each pinning species ($C_1\langle K_p\rangle_1^2$ and $C_2\langle K_p\rangle_2^2$), such that Eq. (5-2) is satisfied. These parameters were adjusted to give the theoretical value of reduced field at maximum pinning force h_p that corresponded to the experimentally determined h_p and so that the relative increase or decrease in F_{pmax} corresponded to experimental observation. While the exact values of these parameters are important for obtaining quantitative comparisons between the two data sets (it should be emphasized that they are physically reasonable), trends in changes of the parameters can tell us what effect bending has on the distribution of number and strength of pinning sites.

TABLE 5-V

MEASURED PINNING FORCE DATA ON FIVE MF Nb_3Sn SAMPLES. SAMPLES ARE LISTED IN APPROXIMATE ORDER OF THE Nb_3Sn LAYER THICKNESS STARTING WITH THE THINNEST SAMPLES.

Heat treatment hours @ °C	H^*_{c2} (kG)	ΔH^*_{c2} (%)	Max. Pinning Force A·kG	ΔF_{pmax} %	h^*	Mechanical State
16 @ 700	143		3 337		0.23	as reacted
	157	9.8%	3 736	11.7%	0.24	after bending
16 @ 750	204		2 983		0.19	as reacted
	204	0%	3 983	33.5%	0.19	after bending
24 @ 750	183		1 778		0.16	as reacted
	202	7.4%	2 757	55.1%	0.15	after bending
128 @ 700	153		4 709		0.24	as reacted
	184	20.2%	4 570	-3%	0.21	after bending
64 @ 750	165		3 120		0.26	as reacted
	193	17%	2 764	-11.4%	0.19	after bending

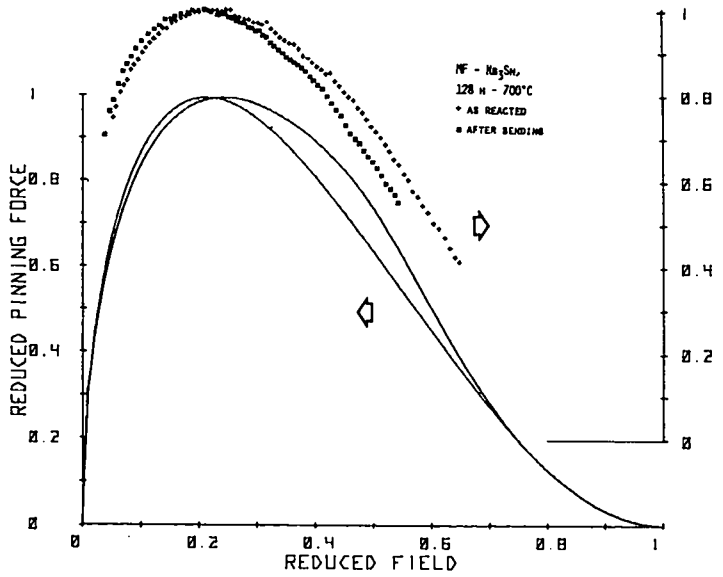

Fig. 5-32.
Reduced pinning force vs reduced field curves for a sample reacted 128 h at 700°C: + = as-reacted sample, ■ = after bending sample over a 3.8-cm-radius mandrel and straightening to original position. Also shown are calculated reduced pinning force curves based on Eq. (5-1) with parameters chosen so that the calculated curves are in good agreement with both sets of data. Note the vertical displacement of scales, done to show the data points more distinctly.

For this particular sample, we found that in the as-reacted state the mean pinning strength K_p was higher (that is, F_{pmax} is higher), because of a relatively large number of weak pins. After bending, the effective number of weak pins decreased dramatically, the number of efffective strong pins increased somewhat, and H^*_{c2} increased. The net result was a slight reduction in F_{pmax}, a slight narrowing of the normalized pinning force curve, and a shift in h_p to lower reduced fields. These results are consistent with what we would expect physically by noting that strain fields are much less effective flux pinners than grain boundaries.[27] (Typically we find the effective strength of the weak pinning species to be approximately 10^{-2} to 10^{-3} times less than the effective strength of the strong pinning species.) In the as-reacted state, strain fields act to pin flux lines and to decrease the number of effective grain boundary pins by smearing out the discontinuity of superconducting properties at the boundary. When some of the strain is removed by bending the wire, some of the strain-field pinning is lost and the number of grain boundaries that pin effectively have been enhanced.

In Fig. 5-33 we compare a sample heat treated for 128 h with a sample heat treated at the same temperature but for only 16 h. The Nb_3Sn layer in the second sample is only approximately 1/3 that of the former. Consequently, it should have smaller grains and be under greater compressive stress. As indicated in Table 5-V, strain relief resulted in an $\sim$10% increase in H^*_{c2}, an increase of F_{pmax} by $\sim$12%, and a slight shift in h_p toward higher reduced fields. Theoretical curves calculated in the manner described above also are displayed in Fig. 5-33. While it is not entirely evident in this reduced plot, the theoretical curves well describe the qualitative features observed experimentally.

By analyzing the trends we found that the strong pinning species (grain boundaries) are more effective pinners in the sample heat treated for 16 h than they were in the sample reacted for 128 h. This is expected because the shorter reaction time should produce smaller average grain sizes that, in turn, would increase the effectiveness of grain boundary pinning. After bending, the number of weak pinners (strain fields) decreased but not by as

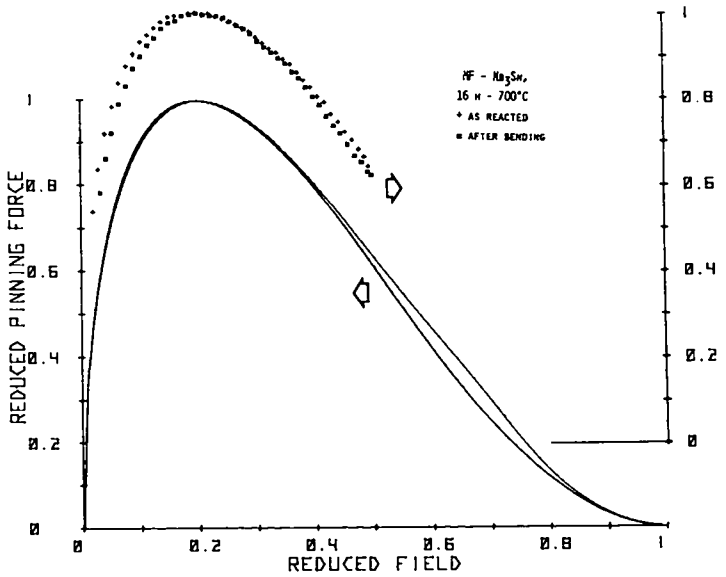

Fig. 5-33.
Reduced pinning force vs reduced field curves for a sample reacted 16 h at 700°C: + = as reacted sample, ■ = after bending sample over a 3.8-cm-radius mandrel and straightening to original position. Also shown are calculated reduced pinning force curves based on Eq. (5-1) with parameters chosen so that the calculated curves are in good agreement with the data. Note the vertical displacement of scales, done to show the data points more distinctly.

large a fraction as in the previous sample. Such a result is consistent with the smaller increase in H_{c2}^* for the 16-h sample if we assume strains are partially responsible for the depressed values of H_{c2}.[26] Also, the ratio of $\langle K_p \rangle / K_s$ was lower for the 16-h sample after bending, indicating that flux shearing is playing a more dominant role. This is in agreement with the Kramer model, because now the more effective grain boundaries suppress flux motion by pin breaking, enhancing flux flow by the shearing process.

Similar analyses have been performed on the other samples and results are tabulated in Table 5-V. In all cases qualitative changes in pinning characteristics, that is F_{pmax}, h_p, and H_{c2}^*, could be accounted for by using Eq. (5-1). The changes could not be explained on the basis of Kramer's model[25] for a single, uniquely valued flux pinning mechanism or modifications thereof.[28] While the concept of a distributed effective number and strength of flux pinning sites is very appealing intuitively and could be used qualitatively to explain trends in the data, it should be emphasized that we found an interdependence among the various parameters. Therefore it is difficult to determine unambiguously the real physical cause that produced the observed changes in the samples.

5.3.3.3 Discussion of Mechanical Tests. The Supercon wire is made of four component materials, the major one being the copper matrix, which constitutes between 83 and 90% of the total material. Niobium tubes filled with 13% bronze are embedded in the copper matrix, extruded, and drawn into wire. After heat treatment, a Nb_3Sn layer a few micrometers thick is present in the wire at the niobium-bronze interface, and the copper is fully annealed so that it has very little strength and exerts a minimal compressive stress on the Nb_3Sn. In their free states, there would be a change in length $\Delta\ell/\ell$ of approximately 0.75% for Nb_3Sn, 0.70% for Nb, and 1.80% for bronze on cooling from 1000 K to 15 K. The greater contraction of the bronze causes compressive loading of the Nb_3Sn that, for an infinitely small cross-sectional area, would produce a strain of 1.05% in the Nb_3Sn. For a finite cross-sectional area of Nb_3Sn, the strain would be reduced almost to zero as the Nb_3Sn content approaches unity. Thus the strain in the Nb_3Sn is not only a function of the difference in CTE's but also of the Nb_3Sn-to-bronze-area ratio and is determined by balancing the forces among the component materials. Approximately 75% of the material contraction takes place on cooling the samples from the reaction temperature (1000 K to 1050 K) to 300 K, so that even at

room temperature an infinitely thin Nb_3Sn sample would be under approximately 0.8% compressive strain. For the Supercon wire with a Nb_3Sn-to-bronze ratio α of about 0.4, this strain would be reduced to 0.5%, assuming a linear relation between strain and α. α is a function of the HT and the cross-sectional area of the filaments for a given HT, so the strain in the Nb_3Sn samples will have a range of values. The compressive strain in the Nb_3Sn will be relieved to some extent by bending the sample. The initial bends on each of the 40- and 41-series wires produced approximately 0.4% strain in the filaments on the outside of the bend. In the 43-series wire, where the filaments are dispersed over the central 80% of the cross section, the maximum strain was 0.6%. The larger radii bends probably relieve part of the strain induced by differential contraction but do not introduce any tensile strain, at least in the 40- and 41-series wires. Indeed, we always find I_c increases for the initial large radii bends. For the smaller radii bends the tensile strain in the Nb_3Sn will be several tenths of a per cent for portions of the wire near the outside of the bend and should cause some degradation of I_c.

When a sample is bent, both compressive and tensile stresses are involved. This complicates any quantitative analysis of the results. However, a qualitative picture of what takes place can be deduced from the measurements and from an understanding of the material properties of the wires. The Nb_3Sn is placed under compression by the bronze on cooling from the HT temperature because of the difference in CTE's of the materials. When the sample is bent, the compression is relieved in the Nb_3Sn on the outside of the bend, and the bronze plastically deforms so that when the sample is returned to its straight position the net compressive strain in the Nb_3Sn is partially relieved. On the inside of the bend, the Nb_3Sn is further compressed, and the bronze, which was under slight tension from the Nb_3Sn, is elastically compressed. On straightening, the Nb_3Sn on the inside of the bend is also strain relieved because the bronze was partially deformed on the outside of the bend and so does not return to its original length. Increases in I_c and T_c^* were observed for all samples that were strain-relieved. Such observations are consistent with results obtained by others on similar material. Furthermore, increases in H_{c2}^* were observed for all samples after bending, except one that was given a strain-relieving anneal before bending. This is consistent with the higher T_c^*'s of the annealed samples. However,

changes in the flux-pinning curves measured at 4.0 K could not be correlated directly with changes in I_c, T_c^*, or H_{c2}^*. We found that changes in $F_p(h)$ curves depend in a complex way on differences in the effective numbers and strengths of two separate pinning mechanisms identified as grain boundaries and strain fields. These changes in the flux-pinning curves because of strain relief are a result of competing mechanisms. Increases in H_{c2}^* act to increase F_{pmax}. However, bending also produced a redistribution of the relative number and strength of flux pinners, causing F_{pmax} and h_p to either increase or decrease depending on the distribution. To our knowledge, no previous measurements of the flux-pinning curves in strained and strain-relieved samples of mf Nb_3Sn have revealed such a complex interaction of competing mechanisms.

5.3.4. Conductor Stability

5.3.4.1. Theoretical Study of Conductor Stability. The theoretical study of the superconducting operating mode discussed in Sec. 5.2.8.1 conveys clearly the advantages of operating at currents corresponding to less than full stability. The study further shows that the conductor reliability can be expressed in terms of a stability margin and suggests a program of the experimental research to be implemented.

A superconductor is "fully stable" if it can carry all the current in the copper matrix without causing a thermal runaway. In its most economical form, the conductor, being a composite, contains only enough superconducting material to carry the fully stable current at or near its short sample critical current density. Typically, copper-to-superconductor ratios of approximately 10:1 are fully stable. This is somewhat dependent on the quality of the copper, but by using more superconductor and less copper the fully stable current limit can be exceeded. Thus it should be possible to carry considerable overcurrents without losing the superconducting mode. The reliability of such an operation is adequately described by a "stability margin," defined as the difference between the effect of real disturbances present during operation of the device and the effect needed to create minimum propagating zones (MPZ's). In order to determine the stability margin, we must study the likely disturbances. Some sources for such disturbances have been identified as plastic deformation, friction, and ac losses or flux jumps during current redistribution. The latter is likely during fast changes in overall transport current, such as might happen during any overcurrent condition. These

potential disturbances should be studied, preferably experimentally, to help us develop countermeasures. The energy needed to create MPZ's can be calculated; however, we are seeking techniques to produce a system that would tolerate larger disturbances. One such technique consists of subdividing the conductor along its length into modules separated from each other by high-stability barriers (similar to firebreaks) to stop the spread of a normal zone. Another technique would improve the heat transfer temporarily by changes in coolant operational parameters such as pressure, mass-flow rate, or temperature.

5.3.4.2. Wire Design and Stability. The Supercon wire design was described in Sec. 5.3.1.3. The two most important stability features of this design are the high copper-to-superconductor ratio and the geometric arrangement of the component materials. In this unique design, current can transfer from the superconducting material into the stabilizing copper without going through any high resistivity material; also, the separation distance of the stabilizing copper from the Nb_3Sn is quite short (on the order of 2 to 3 μm). For this type of conductor, the current transfer length is only 1 to 2 mm; in some of the other bronze-process Nb_3Sn conductors we have measured, the transfer lengths were as long as 10 to 15 cm. The short transfer length reduces the amount of I^2R heating that takes place when the current transfers into the stabilizer and thus reduces the likelihood of producing a MPZ. The high ratio of copper to superconductor also reduces the heating that takes place when the current is flowing outside the superconductor. The ratio of the resistance of the copper at 300 K to the resistance at 4 K (RRR) also affects the amount of I^2R heating produced. By increasing the RRR of the copper, the amount of heating can be reduced or, alternatively, the amount of copper can be reduced for a given heat level. One method of increasing the RRR is described in the next section.

5.3.4.3. Oxygen Anneal of Copper-Stabilized Multifilamentary Nb_3Sn Wire. Experiments by Steyert[20] and others have shown that the RRR of copper can be greatly increased by annealing the copper in oxygen at a reduced pressure. It would be most desirable if this procedure could be combined with the HT to form Nb_3Sn by the solid-state diffusion process without the oxygen degrading the superconducting properties of the materials. If so, a significant reduction could be made in the amount of copper needed to effect cryostatic stabilization in the material without increasing the complexity of the

HT process. We have performed a series of oxygen anneals combined with the HT of the highly copper-stabilized Supercon wire. Both the oxygen pressure and the reaction temperature were varied in order to study effect on the RRR of the copper and on the superconducting properties. The reaction temperature was varied between 750° and 780°C. The higher temperature was more suitable for the oxygen anneal because the oxygen diffused more rapidly into the copper; however, the higher temperature also caused degradation of I_c relative to samples reacted at lower temperatures. A temperature of 750°C gave high I_c and a reasonable RRR of $\sim$ 550. The partial pressure of the oxygen over the range tested (10^{-5} to 5 x 10^{-4} torr) did not have much effect on the critical current of the wire, but the improvements in RRR were quite sensitive to the pressure. All oxygen anneals were for 24 h at temperature. A partial pressure of 1 x 10^{-4} torr gave the best results, but we do not feel that we have optimized the conditions to give the highest RRR.

The RRR is affected by mechanical work hardening of the copper. In order to illustrate the degradation of the RRR from mechanical hardening, a 1-mm-diam sample of mf Nb_3Sn with an RRR of 490 was bent around a 7.5-cm-diam tube and then straightened four times. This caused the RRR to drop to 350 and caused I_c to increase, an increase observed in similar bend tests in the past.[3] The sample was then annealed at 400°C for 24 h in a chamber evacuated to a pressure of 10^{-5} torr. After this treatment the RRR increased to 400, but I_c was reduced to almost half its previous value. We believe, however, that most of this decrease was the result of sample handling damage because the I-V curves showed a slope even at low currents. This type of I-V curve is usually indicative of broken filaments in the wire.

Even though we do not believe we have maximized the RRR, we consider as significant the increase in RRR from approximately 80 for the non-oxygen annealed samples to about 500 for the oxygen-annealed samples, accomplished without a reduction in I_c. If an RRR of 500 or more can be consistently obtained, then the amount of stabilizing copper can be reduced by about a factor of five with no change in safety.

5.3.5. Wire Joints and Transfer Lengths. During cabling, the need will arise to join wires from different spools. Several methods of joining the wires are under consideration; some methods have been tried and the electrical characteristics have been measured, including electrically heated butt welds, cold-welded butt joints, and overlapped solder joints. So far, heated butt

welds have not been very successful. The resistance at 15 K of several such joints tested was approximately 5×10^{-6} Ω for 0.5-mm-diam mf Nb_3Sn wire. Spot-welded mf Nb_3Sn wires also produced joints with a resistance of about 5×10^{-6} Ω but seriously reduced I_c. Superconductors of 0.1-cm diam were cold butt-welded together to produce joints which are mechanically strong. The cold welds were tried on both reacted and unreacted mf wire.

Probably the easiest type of joint to make is the overlapped soft-solder joint. We have tested a series of these joints formed between 0.2-mm-diam mf Nb_3Sn wires having a R_M of approximately 1:1 joined together over a 5-cm length with 50/50 I_n-S_n solder. The average resistance was found to be $(8 \pm 1) \times 10^{-7}$ Ω. A similar type of joint connecting <u>four</u> wires from each direction, overlapped for 6.5 cm, gave a total joint resistance of 5.8×10^{-8} Ω, or 5.3×10^{-7} Ω per single joint overlapped 5 cm, a value in good agreement with the previous measurement. These measurements indicate that it will be possible to make solder joints over modest overlap lengths with a resistance sufficiently low for a dc SPTL.

At the electrical terminations of the dc SPTL, current must pass from a normal (resistive) metal to the superconductor. The transition is usually accomplished by soldering a length of the superconductor and its copper cladding to a terminal block of the pothead, the temperature gradient being taken over the normal metal only. The actual path of the current from the terminal block into the superconductor depends on many factors but for the steady-state condition is related to the relative resistance of the various alternative routes. The losses depend, of course, on the effective resistance of the junction. One readily sees that once the entire current is flowing in the superconductor, additional soldered contact length is of little value. The joint length necessary to introduce a fraction of the full current equal to (1-1/e) into the superconductor is called the "transfer length."

We have studied experimentally the current transfer into copper-clad Nb_3Sn tapes and into bronze-matrix multifilamentary Nb_3Sn wires. A short transfer length is associated with the former, while a greater transfer length is associated with the latter because of the high resistance bronze matrix in parallel-series with the high conductance copper terminal block. Calculations verify the qualitative behavior observed, namely, that the transfer length for copper-clad superconductors may be 0.1 to 1 mm, and for the bronze clad superconductors it may be 5 to 10 cm.

Joints within the dc SPTL will probably involve a normal metal; the current will pass from the superconductor through its normal metal cladding into a solder joint and back into the next conductor section. Thus the transfer length question applies to both in-line joints as well as the dc SPTL terminations.

Transfer lengths and the associated resistance are also important within conductors, where a broken filament or cracked tape will force the current to flow into the normal stabilizer, possibly through a high resistivity material, and then back into the superconductor. The losses associated with such a defect will be greatly influenced by the design of the conductor, i.e., whether the current must flow through a high resistivity material or not. Recently J. Clem, consultant from Iowa State University, has used a conformal mapping technique to address the question of a joint or a damaged conductor. His theoretical results of transfer length and power dissipation agree with our numerical results for these quantities.[29]

5.4. Conductor Development

After establishing the properties of mf Nb_3Sn wire, optimizing the heat treatment and measuring the mechanical properties the performance of the wire in cable configurations was tested. The following sections discuss the development of a cable that was ultimately tested in the cryoflow loop. The cable could be used in the small line design or the subcable components could be used in a coaxial design. Initially three- and seven-wire cables were tested, and finally 275 m of a 19-wire cable were made and used for a prototype cable.

5.4.1. Subcable Measurements. Three- and seven-wire cables were made from 1-mm-diam Supercon wire (256XE-41A-1A) and, after cabling, reacted at 750°C for 24 h. Single wires of the same type were also reacted at the same time for later comparison. After being heat treated, the cables were impregnated with 50/50 In-Sn solder. Current measurements and bend tests made on the cables are reported below.

5.4.1.1. Critical Current Measurements of Three- and Seven-Wire Cables. At 14 K we found the critical current I_c of the three-wire cable to be 184 A, that of the seven-wire 332 A, and that of a single wire 75 A. Based on the single-wire value, the three-wire cable carried 82% of three isolated wires and the seven-wire cable carried 63% of seven isolated wires. We assume that these reductions of I_c arise from the increased magnetic fields imposed on a given wire in the cable by current in the other wires.

To determine the plausibility of such an assumption, we calculated the current in the cable using an iterative process. We first calculated the magnetic field at each wire, assuming a value of current in all the wires. We then adjusted the current in each wire using the relation between the critical current density J_c and the local magnetic field B: $J_c = K/\sqrt{B}$, where K is a constant determined from self-field measurements of I_c on a single wire. The equation is a low-field approximation based on the Kramer pinning model.[25] This procedure was iterated until the current change was less than 0.5%. The results of the calculation are shown in Fig. 5-34, which shows the magnitude and direction of the field at each wire in the cable due to the current in the other wires. The current carried by each wire is indicated numerically. We assume the current in the center strand to be that of an isolated wire because the field is essentially zero at this location as a result of fields generated by the other six wires. The calculation does not take into account the fact that the cable is twisted. The twist adds an axial component to the field, which is relatively small in this case. The sum of the currents in the seven wires gives the total cable current and is 67% of what seven isolated wires would carry. This value is in agreement with the measured value of 63% and strengthens the assumption that the reduction in current in the cable from that of the same number of isolated wires is caused by the increased magnetic field experienced by the wires in the cable.

We note from our calculations that if the constant K is increased, that is, if an increase in the pinning force is effected, the cable reaches a higher percentage of the multiple of the single-wire values. This can be anticipated from the above relation between J_c, K, and B, where increases in K may influence J_c more strongly than increases in the field experienced by each wire, leading to an increase in J_c. Thus K should be as large as possible in order to minimize the current reduction in a cable.

The value of K depends on the heat treatment given the wire and is a function of the strain on the wire and its temperature. As we discussed in Section 5.3.3, the critical current of a wire increases with modest bending, an indication that K is being increased. The critical current capacity of the cable is also increased on bending and reaches a higher percentage of the multiple of single bent wire (Sec. 5.4.1.2).

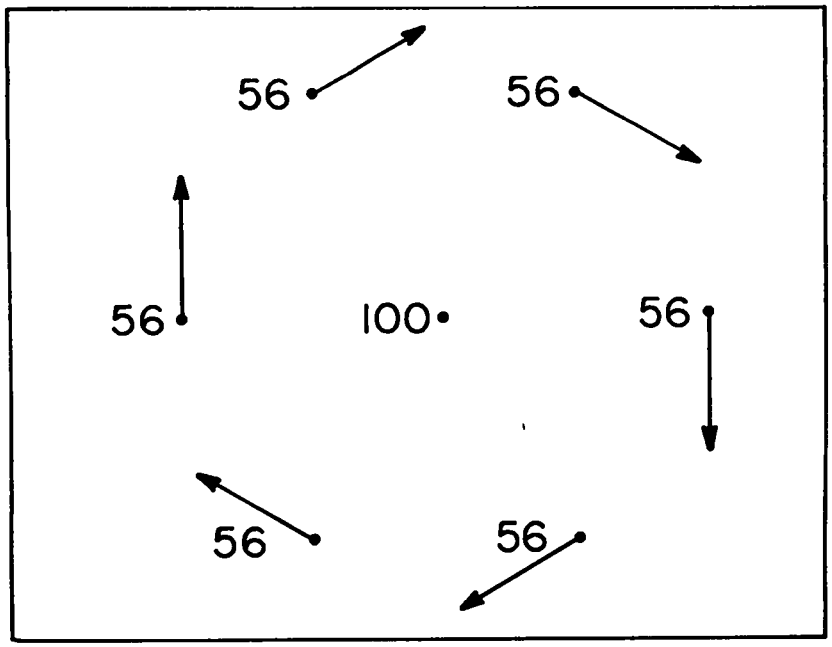

Fig. 5-34.
Schematic representation of seven-wire cable showing the magnitude and direction of the magnetic field at each strand and indicating the current in each strand.

In Table 5-VI the critical current of the seven-wire cable is listed for four temperatures. Also included are the average current per strand and the comparison with isolated wires. Table 5-III shows that as the temperature is decreased, the current is increased; and the current carrying capacity of a wire in a cluster approaches that of our isolated wire, in agreement with the above discussion.

5.4.1.2. Seven-Wire Cable Bend Tests. After measuring the critical current of the seven-wire cable, we removed it from the sample holder and bent it over a 7.5-cm-radius tube, straightened it out, remounted it in the sample holder, and remeasured the critical current.

Table 5-III compares the critical current of the as-reacted sample with that of the bent sample for several temperatures and shows that the critical current increased after the bend; this indicates that strain was relieved in the Nb_3Sn. The sample did not degrade on bending and the cable did not act as a monolithic conductor even though it was impregnated with solder. Had the cable behaved as a single wire, the portion on the outside of the bend would have been subjected to a 2% tensile strain, an amount far in excess of the 0.7% limit established earlier for the onset of damage to the wires.

TABLE 5-VI

CRITICAL CURRENT OF SEVEN-WIRE CABLE

Temperature (K)	I_c As-reacted state (A)	I_c Per Strand As-reacted state (A)	I_c Bent State (A)	Efficiency* (%)
15.0	56	8	132	42
14.5	173	24.7	280	59
14.0	330	41.7	460	63
13.8	410	58.6	540	71

*Comparison of I_c of seven-wire cable to seven isolated wires, all in the as-reacted state.

5.4.2. Nineteen-Wire Subcable. A prototype subcable was designed incorporating the information from the previous tests. The cable was a 19-strand concentric design with the 7 inner wires made of copper and the 12 outer wires made of 1-mm diam Supercon mf Nb_3Sn wire. The superconductors were placed in the outer shell in order to reduce the magnetic field affecting them. Also by keeping all the superconductors at the same radius in the cable, each strand had the same self inductance, thus assuring equal current sharing. The stability of the cable was guaranteed by the large copper-to-superconductor ratio provided by the inner seven copper wires and the copper incorporated in the Supercon wire. The overall ratio was approximately 13 to 1.

5.4.2.1. Cabling. The wire was cabled by New England Electric Wire Co. of Lisbon, New Hampshire before the Nb_3Sn-forming heat treatment was applied. A total of 275 m was cabled. In this length of cable, approximately 10 wire joints were necessary in the superconducting strands. These were made by butt welding the wires. The later heat treatment forming the Nb_3Sn caused the joints to have a negligibly small resistance. In fact no effect of the joints was seen in all of the critical current tests.

5.4.2.2. Heat Treatment of 19-Wire Cable. On the basis of our short sample heat treatments of individual wires and of short sections of the 19-wire cable, a heat treatment schedule of 64 h at 750°C was chosen for the

cable. In practice however the temperature was held to 740°C to reduce the chance of an "over temperature" during the run because it has been shown earlier that an over temperature for any great time was very detrimental to the I_c of the wire.

We first attempted to have the heat treatment done commercially, but we could not conveniently find a furnace that had the size, temperature range, and vacuum or inert atmosphere condition necessary for the heat treatment. For this reason and because we could have more control over the work, the heat treatment was performed at LASL, although this required several additional preliminary steps.

A large, steel vacuum-tight drum 1-m in diameter by 0.75-m high was constructed. A copper spool 1-m in diam with the cable on it was placed in the drum which was then sealed. The drum was then evacuated and flushed with argon gas, and placed in a large (1.1-m-diam by 1.5-m-long) furnace. The temperature was brought up to 740°C and held there for 64 h during which time argon gas was continually blown through the drum.

Two heat treatments were made, one first on a 20-m length of cable in order to check out the system and then a second to process the remainder of the 275 m of cable. In both cases the reactions were successful.

5.4.2.3. Critical Current Measurements of 19-Wire Cable. Short sample sections of the 19-wire cable were reacted for 64 h at 750°C in the small tube (1.5-m-long) furnace. The critical current of these samples averaged about 900 A at 14 K, or approximately 85 A per superconducting wire. A single isolated wire with a similar heat treatment carried about 90 A at 14 K, so the wires in the cable are carrying approximately 83% of their isolated value. This is consistent with our previous measurements on cables. Also short sections of the cable that were reacted in the large heat treatment furnace, described above, were tested. The I_c of these cables, approximately 1000 A, was slightly higher than the previous short sample results. This is probably due to variations in the reaction parameters; for example, the temperature is not known as well as in the big furnace.

5.4.2.4. Short Sample Mechanical Tests of the 19-Wire Cable. Bend tests were made on short samples of the 19-wire cable before heat treatment of the larger samples. The bend tests were necessary in order to insure that the diameter of the heat treatment spool was large enough to prevent damage to the Nb_3Sn when the cable was removed and straightened after the heat treatment.

Also it was important to know the bending limits for assembling the cable and pulling it into the cryogenic enclosure. Two different radii were tested, one of 7.5 cm and the other of 30 cm. For a bend of 30 cm, no degradation of the critical current was observed; however, for bends of 7.5 cm radius, the critical current was reduced by approximately 50%.

5.5. Cable Joints and Splices

Generally, joints or splices in composite superconducting materials involve normal metals (e.g., copper) and solder connections. Superconducting joints are possible in certain materials but probably will not be possible for mf Nb_3Sn wires and cables. Because the LASL coaxial cable design utilizes mf Nb_3Sn, we have initiated a program to study joints and splices. The program addresses not only the question of minimizing the resistive joint losses but also the constraints imposed by the wire and cable vendors, the mechanical, cryogenic, and high-voltage insulation aspects of proposed concepts, and the ease of field installation. We will employ the convention that a "joint" refers to the connection of a pair of superconducting wires and a splice refers to a connection of subcables composed of many wires or of the full cable composed of many subcables, dielectric insulation, armor, etc.

The practical maximum unit length of fabricated cable for the LASL design is about 600-900 m. Such lengths can be spooled and shipped and, furthermore, can probably be designed to sustain the forces of pulling the cable into the cryogenic envelope without damaging the superconductor.

5.5.1. Coaxial Cable Splices. Two cable splice concepts are shown in Figs. 5-35 and 5-36. Either splice could be accomplished in the field. It is necessary to prepare in the field the cable ends for the former design by carefully dissecting the end of the cable and peeling back the various layers. For the case shown in Fig. 5-35, a preformed copper collar is used to align and join the two sections of the inner former of the coaxial cable. The collar also serves to form a smooth tapered transition region from the inner conductor diameter up to the proper diameter for interlaying the subcables side by side. The overlap length, determined to be adequate for acceptable ohmic losses, will be specified later. By using a clam-shell heater jig and a low-melting ($150^{o}C$) solder one should be able to obtain a smooth, uniform splice ready for handwrapping the semiconducting layer and the dielectric tape. The splice in the outer conductor is similar, having a tapered copper sleeve to provide a uniform surface on which to lay out the subcables and a solderable

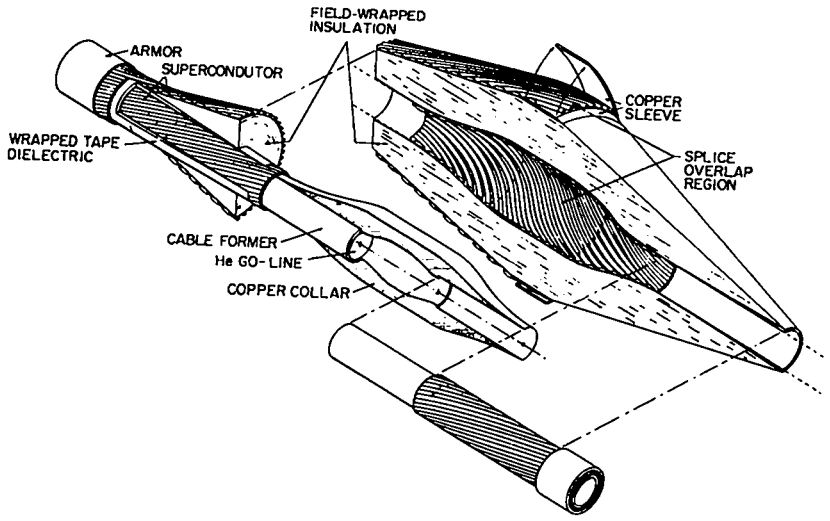

Fig. 5-35.
Cable splice design showing overlapped subcables. This design requires only one solder connection between each conductor.

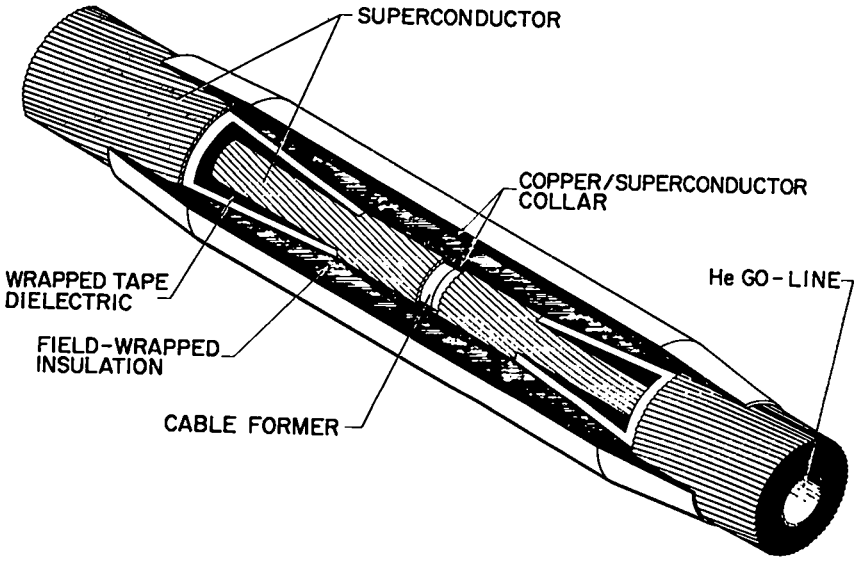

Fig. 5-36.
Cable splice design with copper/superconductor connecting collars. Two solder connections are required for each conductor.

solderable conductor to assist in the current transfer from subcable to subcable. We note that the splice areas provide a periodic radial short to all the subcable conductors. For the case of individual wires electrically insulated, this should allow some equalization of current should there be occasional defective wires or subcables. The alternative of not insulating the mf Nb_3Sn wires or subcables is also being investigated. Soldering the outer splice is somewhat complicated by the presence of the wrapped dielectric underneath but is not viewed as an insurmountable problem. Finally, the cable armor is joined to provide both a pressure-tight seal and good mechanical strength.

The scheme shown in Fig. 5-36 is similar except that the cable end is a series of stepped (or pencil-point) diameters which could be prepared by a special machine. The complication of handling individually large numbers of somewhat fragile subcables is avoided. In this case it is necessary for the current to pass wholely into and out of the splicing collar. Therefore, we propose the splicing collar itself be a composite of copper (to allow soldering) and superconductor (to reduce the effective resistance).

In either of these splices we believe the ohmic heating at the splices can easily be accommodated by the refrigeration system.

5.5.2. Subcable Splices. In the manufacture of the coaxial cable from subcables of finite length or for field installation it will be necessary to splice the subcable. An additional constraint is involved - the diameter of the subcable must be maintained through the splice region. Also the spliced subcable would have to match the lay of the cable if it were rigidly soldered together. An effective splice could be made by staggering the corresponding wire joints to distribute any ohmic losses over a long conductor length. A pair of wires butt welded end-to-end would depend on solder connections to neighboring wires and on the weld itself to provide the through current path; some reduction in I_c for the subcable is expected. This method was used without the solder in the 19-wire cables, described above, with very little or no degradation of I_c.

Joints between mf Nb_3Sn wires with different overlap lengths have been made and tested and support the view that adequate, low-resistance splices can be made using simple soldering techniques.

5.6. References

1. R. J. Bartlett, et al., "Progress Report USAEC-DAT DC Superconducting Power Transmission Line Project at LASL, November 1, 1972 to March 1, 1973," Los Alamos Scientific Laboratory report LA-5271-PR (May 1973).

2. W. E. Keller and R. D. Taylor, "Progress Report USAEC-DAT DC Superconducting Power Transmission Line Project at LASL, March 1 to June 30, 1973," Los Alamos Scientific Laboratory report LA-5361-PR (August 1973).

3. W. E. Keller and R. Dean Taylor, "Progress Report USAEC-DAT DC Superconducting Power Transmission Line Project at LASL, July 1 to September 30, 1973," Los Alamos Scientific Laboratory report LA-5468-PR (November 1973).

4. W. E. Keller and R. D. Taylor, "Progress Report USAEC-DAT DC Superconducting Power Transmission Line Project at LASL, October 1 to December 31, 1973," Los Alamos Scientific Laboratory report LA-5581-PR (April 1974).

5. W. E. Keller and R. Dean Taylor, "Progress Report USAEC-DAT DC Superconducting Power Transmission Line Project at LASL, January 1 to March 31, 1974," Los Alamos Scientific Laboratory report LA-5684-PR (July 1974).

6. W. E. Keller and R. D. Taylor, "Progress Report USAEC-DAT DC Superconducting Power Transmission Line Project at LASL, April 1 to June 30, 1974," Los Alamos Scientific Laboratory report LA-5787-PR (December 1974).

7. W. E. Keller and R. D. Taylor, "Progress Report USAEC-DAT DC Superconducting Power Transmission Line Project at LASL, July 1 to September 30, 1974," Los Alamos Scientific Laboratory report LA-5851-PR (January 1975).

8. W. E. Keller and R. D. Taylor, "DC Superconducting Power Transmission Line Project at LASL, USERDA, Division of Electric Power Transmission and Distribution Progress Report for October 1 to December 31, 1974," Los Alamos Scientific Laboratory report LA-5972-PR (May 1975).

9. W. E. Keller and R. D. Taylor, "DC Superconducting Power Transmission Line Project at LASL, USERDA, Division of Electric Energy Systems, Progress Report for January 1 to March 31, 1975," Los Alamos Scientific Laboratory report LA-6053-PR (September 1975).

10. W. E. Keller and R. D. Taylor, "DC Superconducting Power Transmission Line Project at LASL, USERDA, Division of Electric Energy Systems, Progress Report for April 1 to June 30, 1975," Los Alamos Scientific Laboratory report LA-6171-PR (December 1975).

11. W. E. Keller and R. D. Taylor, "DC Superconducting Power Transmission Line Project at LASL, USERDA, Division of Electric Energy Systems, Progress Report No. 11, July 1 - September 30, 1975," Los Alamos Scientific Laboratory report LA-6215-PR (February 1976).

12. F. J. Edeskuty and P. Chowdhuri, "DC Superconducting Power Transmission Line Project at LASL, USERDA, Division of Electric Energy Systems, Annual Progress Report No. 15, October 1, 1975 - September 30, 1976," Los Alamos Scientific Laboratory report LA-6699-PR (February 1977).

13. Y. B. Kim, C. F. Hempstead, and A. R. Strnad, "Magnetization and Critical Supercurrents," Phys. Rev. 129, 528-535 (1963).

14. A. Migliori, "The General Critical State Model in Two Dimensions and Zero Applied Field: A Uniqueness Theorem and Some Consequences," J. Appl. Phys. (submitted for publication).

15. A. Migliori, R. J. Bartlett, and R. D. Taylor, "Transport-Current-Induced Magnetic Field Profiles of Nb_3Sn Superconducting Tape," J. Appl. Phys. 47, 3266 (1976).

16. S. L. Wipf, "Stability and Degradation in Superconducting Current-Carrying Devices," Los Alamos Scientific Laboratory report LA-7275 (December 1978).

17. F. J. Edeskuty and P. Chowdhuri, "DC Superconducting Power Transmission Line Project at LASL, USDOE, Division of Electric Energy Systems, Annual Progress Report No. 19, October 1, 1976 - September 30, 1977," Los Alamos Scientific Laboratory report LA-7116-PR (January 1978).

18. H. London, "Alternating Current Losses in Superconductors of the Second Kind," Phys. Lett. 6, 162 (1963).

19. C. P. Bean, "Magnetization of High Field Superconductors," Rev. Mod. Phys. 36, 31 (1964).

20. S. L. Wipf, "Magnetic Instabilities in Type II Superconductors," Phys. Rev. 161, 404 (1967).

21. P. S. Swartz and C. P. Bean, "A Model for Magnetic Instabilities in Hard Superconductors: The Adiabatic Critical State," J. Appl. Phys. 39, 4991 (1968).

22. J. K. Hoffer, E. C. Kerr, and W. C. Overton, Jr., "Asymmetry of Thermal Propagation Velocity in a Long Force-Cooled Superconducting Test Line," IEEE Transactions on Magnetics MAG-13, 408-411 (1977).

23. W. C. Overton, Jr., and H. Weinstock, "Observations of Asymmetry in the Velocity of Destruction of Superconductivity by Current in Type II Ta Wires," Proceedings of the XIV International Conference on Low Temperature Physics, Krusius and Vuorio, Eds. (North Holland Publishing Co., Amsterdam, 1975) Vol. 2, pp. 149-152.

24. R. J. Bartlett, R. D. Taylor, and J. D. Thompson, "Stress Effects on Multifilamentary Nb_3Sn Wire," IEEE Transactions on Magnetics MAG-15, 193-196 (1979).

25. E. J. Kramer, "Scaling Laws for Flux Pinning in Hard Superconductors," J. Appl. Phys. 44, 1360-1370 (1963).

26. J. D. Thompson, M. P. Maley, L. R. Newkirk, and R. V. Carlson, "High Magnetic Field Properties of CVD-Prepared Nb_3Ge and $Nb_3(Ge,X)$," paper presented at Applied Superconductivity Conference, Pittsburgh, Pennsylvania, September 25-28, 1978.

27. A. M. Campbell and J. E. Evets, "Flux Vortices and Transport Currents in Type II Superconductors," Adv. Phys. 21, 199-428 (1972).

28. T. Luhman, C. S. Pande, and D. Dew-Hughes, "Flux Pinning in Bronze-Processes Nb_3Sn," J. Appl. Phys. 47, 1459 (1976).

29. R. J. Bartlett, R. V. Carlson, A. Migliori, and H. L. Laquer, "Considerations in Designing and Using Superconductors with High Resistivity Matrices," Proc. of Int. Conf. on Manufacture of Superconducting Materials, Port Chester, NY, November 8-10, 1976 (ASM, Metals Park, Ohio, 1977), pp. 184-194.

6. SYSTEM STUDIES

Even well-designed equipment may fail to function properly when installed in an electrical system because of incompatibility. Compatibility can best be insured if application studies on actual systems are performed. In addition, it is necessary to know the degree to which a new type of system is economically competitive. Although circumstances can arise which make the use of a new technology imperative, such occurrences are rare, and new developments should include efforts to determine system costs and to make the systems more economical where possible. Again, application studies on actual systems are the best solution.

General application studies were made to optimize the dc SPTL design. This study is described in Sec. 6.1.

In FY 1976, we participated in a DOE-sponsored study to transmit 10-GW of electric power for a distance of 106 km in the Philadelphia Electric Company (PECO) system. This study was completed during FY 1977 and is summarized in Sec. 6.2. We are also preparing for participation in a second study to be done by the PECO.

We found that the coaxial line design was not cost competitive for the required contingencies of the PECO study. Consequently, we have completed the conceptial design of a small line design that would be more competitive, as described in Sec. 6.3.

6.1. General Application Study.

We have made a generalized study of the design and cost for the LASL dc SPTL concept. The study incorporated the electrical, mechanical, cryogenic, and systems design considerations into a computer program to permit a rapid solution for many of the numerous design options. A wide range of parameters was considered: powers of 1 to 10 GW transmitted over 50 to 2000 km with line voltages of 100 to 600 kV and refrigerator spacings of 5 to 25 km. A sampling of results of the study are shown in Figs. 6-1 and 6-2; more details are presented in earlier reports.[1]

6.2. Study for the Philadelphia Electric Co. (PECO).

The PECO has completed a study (PECO-I) to compare the costs of various methods of transmitting, by the year 1990, 10 GW from a power park on the Susquehanna River into the center of the city of Philadelphia.[2] The line route traversed about 96 km of private right-of-way and 10 km of city streets. The normal system ratings, as well as first and second contigency specifications, are given in Table 6-I.

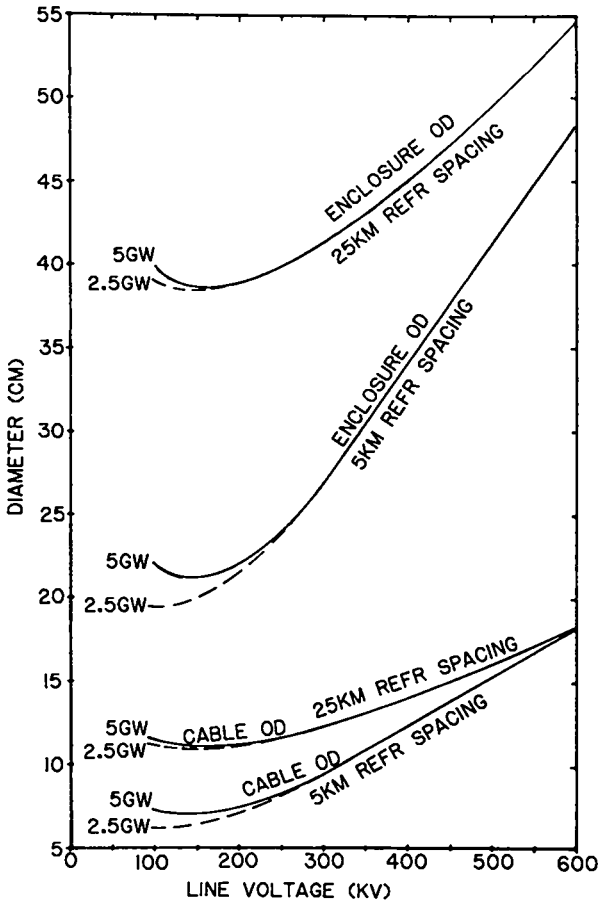

Fig. 6-1.
Diameter vs line voltage for 2.5- and 5-GW dc SPTL's.

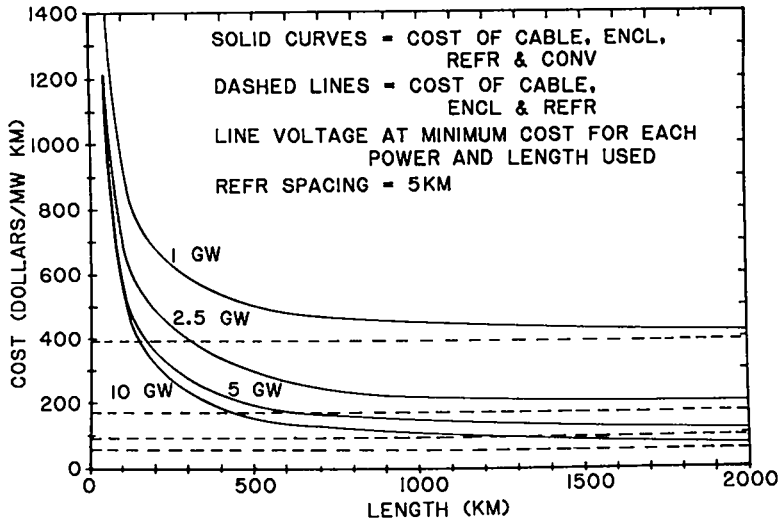

Fig. 6-2.
Cost vs length of dc SPTL's of 1- to 10-GW ratings.

The fundamental design assumptions for the proposed dc SPTL are shown in Table 6-II and the associated electrical ratings in Table 6-III.

It was clear that, with the relatively short (106 km) transmission distance considered in the PECO study, the converter terminal cost would be a significant part of the total cost. Therefore, the dc SPTL design was optimized with respect to the terminal converters. The data for the thyristor converter stations were obtained from a study under contract from LASL to the General Electric Co.[3]

6.2.1. Converter Design Study. The converter design study, performed by the General Electric Company, determined costs for converter stations in 1977 dollars for 2.5-, 5.0-, 7.5-, and 10-GW designs for dc voltages of 100 to

TABLE 6-I
TRANSMISSION REQUIREMENTS - PECO STUDY

Normal power rating	10 GW
Total distance	106 km
Private right-of-way	96.5 km
City streets	9.7 km
1st Contingency rating (continuous)	10 GW
2nd Contingency rating (4h)	7.5 GW

TABLE 6-II
FUNDAMENTAL DC SPTL DESIGN ASSUMPTIONS FOR PECO STUDY

Maximum dielectric stress (kV/mm)	20
Fanning friction factor inside cable	0.005
Fanning friction factor in annulus	0.010
Heat leak of cryogenic envelope (W/m)	0.20
Average energy losses in cable (W/m)	0.05
Current density in cryostabilizer (A/mm^2)	141

TABLE 6-III
DC SPTL RATINGS - LASL PROPOSAL FOR PECO STUDY

Number of parallel lines	3
Normal power loading, each line (GW)	3.33
1st contingency power loading, each of 2 lines (GW)	5.00
2nd contingency loading, one line (GW) (can continue for 24 h or more)	7.50
System voltage (kV)	300
Normal current, each line (kA)	11.1
1st contingency current (kA)	16.7
2nd contingency current (kA)	25.0

600 kV. Unit-diode, unit-thyristor, and ac bus (230 kV, 345 kV, 500 kV, and 765 kV) designs were considered.

The following conclusions were made:

1. For converter stations rated at 1.25 GW and higher, 1.25-GW modules would be constructed. Therefore, the price in $/kW would not vary with the power rating of the converter.
2. The losses in a thyristor converter of present design are 1.44% per terminal. We expected that by 1990 these losses can be reduced to 1.17%. For a diode-rectifier station, an overall loss of 1% per terminal may be expected.
3. For a conventional design with air-cooled, air-insulted valves, steel buildings, and transformers closely coupled to the valve hall, with bushings extending through the walls, the space requirements are estimated to be 5.3 m^2/MW/terminal. A compact design using gas-insulated valves, gas bus, and perhaps gas-insulated capacitors may require 1.8 m^2/MW/terminal.

Figure 6-3 summarizes the costs for various dc and ac voltages.[3]

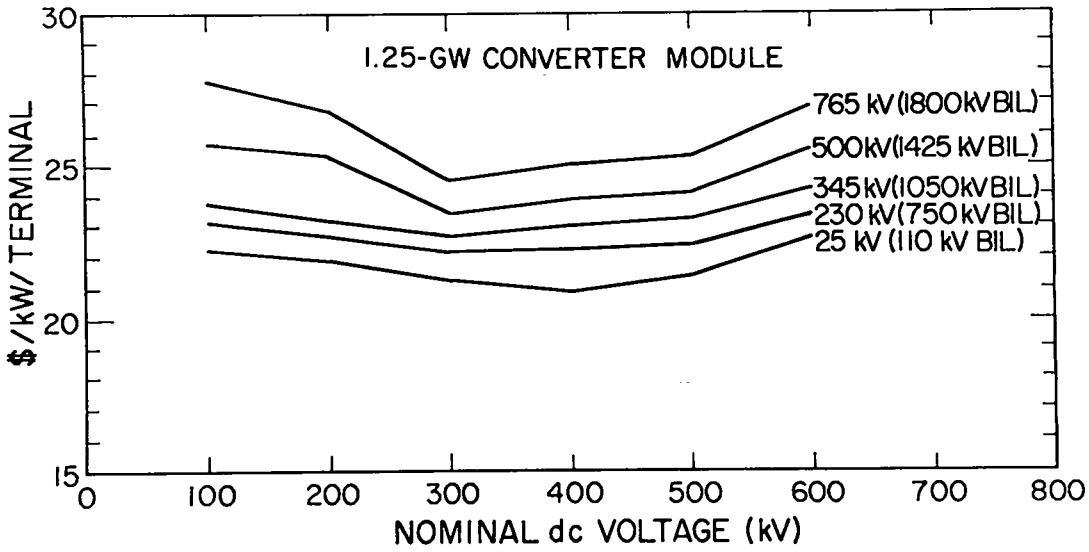

Fig. 6-3.
1.25-GW converter module cost per kW per terminal vs nominal dc voltage for different ac-side voltages.

6.2.2. Cable Design. A cable and refrigeration system similar to that shown in Fig. 1-1 was selected. Helium gas at 16 atm (1.6 MPa) and a temperature of 10 to 12 K flows through the central cooling channel defined by a thin spiral tape former. This former is covered by a layer of 40 to 50 closely adjacent spiraling subcables of copper-stabilized mf Nb_3Sn superconducting wires. The cable design current was chosen as 80% of the critical current of the superconductor at 14 K, which is the maximum operating temperature.

The inner conductors of the coaxial cable are enclosed by a 0.1-mm-thick layer of semiconducting tape and then by layers of Kraft paper dielectric tapes (permeated by helium gas). This is followed by another layer of semiconducting tape, and then by the subcables forming the outer conductor of the coaxial cable. These subcables are similar to, but of smaller diameter than, those used for the inner conductor. The pitch angle designed to minimize axial magnetic fields (and cable inductance). A gas-tight bronze armor shell 1 mm thick and with 3-mm-deep corrugations, completes the cable, which would be manufactured in 500- to 1000-m lengths. Table 6-IV shows the dimensions and weights of the dc SPTL cable design.

6.2.3. Cryogenic Enclosure and Refrigeration. The cryogenic envelope accommodates the cable and provides for the return flow of the helium gas refrigerant in a somewhat distorted annulus between its inner surface and the outer diameter of the cable armor corrugations. The size of the annulus is chosen to match the pressure drop in the cable bore, including the increased friction because of the corrugations. A total allowable pressure loss of 1 atm (0.1 MPa) has been chosen in order to avoid overly penalizing the refrigerator efficiency.

The compressor power expended at ambient temperature was taken as 150 times the sum of the heat leaks into the envelope, joint resistance I^2R losses, and ripple current losses. This value corresponds to a mean temperature of 12 K and a refrigeration efficiency of 16%.

Compressor stations and main heat exchangers are spaced at 10-km intervals and deliver refrigerant helium gas to the line in two streams flowing in opposite directions. Two turbine expanders are located at each halfway, or 5-km, point. Some of the cooling of the line is provided by the expansion of the 16-atm (1.6 MPa) go stream to the 8-atm (0.8 MPa) return stream. A

TABLE 6-IV
DC-SPTL DIMENSIONS AND WEIGHTS (PER LINE) - PECO STUDY

Central channel (mm)	34
i.d. of dielectric (mm)	39.2
o.d. of dielectric (mm)	84.3
o.d. of cable (mm)	96.9
Inner subcable diam (mm)	2.5
Number of inner subcables	43.
Outer subcable diam (mm)	2.2
Number of outer subcables	120
i.d. of enclosure (mm)	109.8
o.d. of enclosure (mm)	330
Mass of superconductor (kg/m)	4.0
Mass of dielectric (kg/m)	4.8
Mass of armor (kg/m)	2.5

redundancy in refrigerators (four refrigerators servicing three circuits) was assumed at each station. The refrigeration and hydraulic parameters for the final design are shown in Table 6-V.

6.2.4. Electrical Characteristics and Performance. The electrical characteristics of the dc SPTL are given in Table 6-VI. It is possible to increase the inductance and surge impedance by less effective compensation of the axial magnetic fields arising from the spiral pitch of the subcables. Although this may provide system benefits under certain circumstances, the present analysis omits consideration of this possibility.

TABLE 6-V
DC SPTL REFRIGERATION PARAMETERS FOR PECO STUDY
(FOR 10-km SPACING OF REFRIGERATORS)

Cryogenic heat load (W/m)	0.25
Thermal conductance of dielectric shell (W/m•K)	0.164
Helium mass flow rate in each line (g/s)	47
Helium mass flow rate in compressor (g/s)	94
Compressor power (kW)	375
Remote expander work (W)	250
Total power at each refrigeration station (kW) (Normal operation - 3 refrigerators)	1125
Total power at each refrigeration station (kW) (fault recovery and cooldown modes - 4 refrigerators)	1500

TABLE 6-VI
ELECTRICAL PARAMETERS OF 7.5-GW DC SPTL CABLE FOR PECO STUDY

Operating voltage (kV)	300
Maximum dielectric stress (kV/mm)	20
Minimum inductance (H/m)	1.5×10^{-7}
Capacitance (F/m)	1.8×10^{-10}
$Z_o(\Omega)$	29.0
Circumferential magnetic field	
at inner conductor (T)	0.26
at outer conductor (T)	0.12
Axial magnetic field (before compensation)	
at inner conductor (T)	0.093
at outer conductor (T)	0.043

The response of the cable to ripple and fault conditions depends on the overall system configuration and, specifically, on the type of converter (6- or 12-pulse) and the size of the smoothing reactors at each end of the dc line. In all cases, 12-pulse converters give the better performance; they will be used as there are no economic gains to be had from 6-pulse units.

Computations for the case of a 12-pulse converter and a 0.1-H reactor at each end of the dc SPTL showed that the ripple losses were 29 mW/m for the 300-kV system. This value is well below the thermal allowance given in the cryogenic design (Table 6-II).

Computations were also made for a ground fault of the line-end terminal of the smoothing reactor near the inverter. This was considered to be the most severe fault condition for the dc SPTL. As was discussed in Sec. 3.1.2, this fault current has two components: 1. a rectangular traveling-wave current caused by the discharge of the dc SPTL, and 2. a half-sine current wave caused by the voltage source behind the rectifier.

The temperature rise of the copper cryostabilizer caused by the rectangular traveling-wave fault current was found to be negligible--0.09 K for the 300-kV system.

For the half-sine fault current, the control system was simplified by assuming that it has a delay equal to the nth multiple of 1/720 s (for 12-pulse operation). Table 6-VII gives the maximum permissible delays, n_{max},

TABLE 6-VII
HALF-SINE WAVE COMPONENT OF FAULT CURRENT - PECO STUDY
(NORMAL LINE OPERATION)

L_T (H)	0.1
L_ℓ (H)	0.015
n_{max}	7
Peak current (kA)	35.3
Fault duration (ms)	29.2
ΔT_{cu} (K)	1.6
ΔT_{He} (K)	0.010

where the copper temperature is just below 14 K, for normal or noncontingency conditions. It is expected that the converter control will be faster than the values of n_{max} shown in Table 6-VII.

6.2.5. Results of the PECO Study. According to the estimates made by PECO, the dc SPTL system designed for this study will cost \$1.69 x 10^9. Of the 15 underground transmission systems studied by PECO, the highest and the lowest cost estimates were \$2.69 x 10^9 and \$1.31 x 10^9, respectively. While it is very difficult to estimate the cost of a developmental system that has never been manufactured on a large scale, several suggestions were made to PECO showing how their cost estimates of the dc SPTL system could be reduced considerably.

Most important of the suggestions was the elimination of the dc circuit breakers, which are not commercially available at the ratings needed for the dc SPTL. PECO used dc circuit breakers at the terminal converter stations for the dc SPTL application. Two schemes were proposed to PECO for eliminating the dc circuit breakers, thus taking full advantage of the blocking capability of the thyristor valves.

In Scheme 1 (Fig. 6-4), all the converters are blocked when a fault occurs in one of the three cables. The faulted cable is then isolated by opening the appropriate isolators of the ring bus. Once the faulted cable is isolated, the converters are deblocked and full power commences to flow through the remaining two cables.

In Scheme 2 (Figs. 6-5 and 6-6), each dc SPTL is connected to two converters through isolators. When one cable is faulted, the two converters

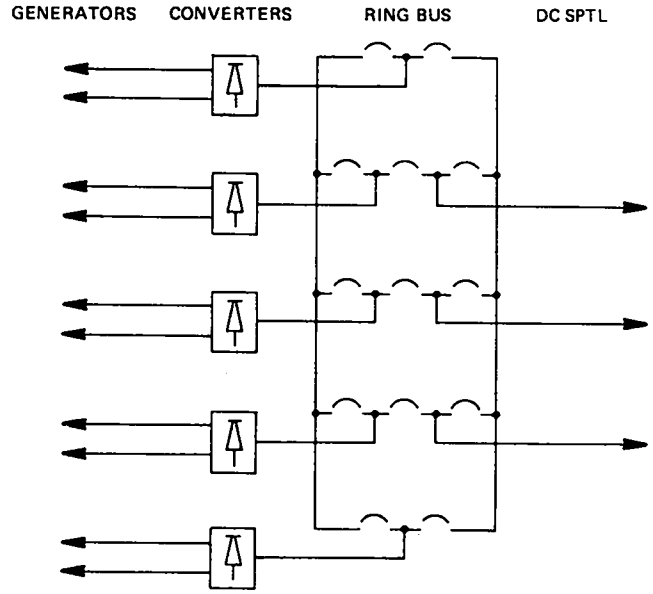

Fig. 6-4.
Schematic of proposed PECO 10-GW Energy-Park substation (Scheme 1).

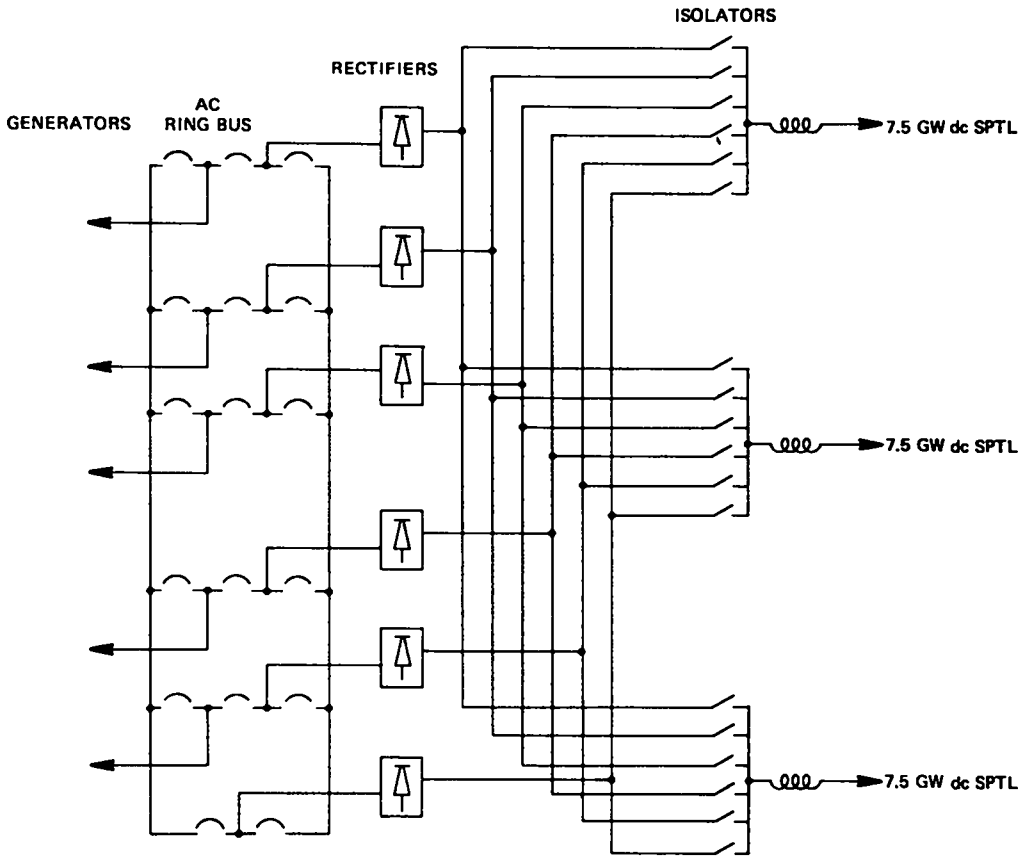

Fig. 6-5.
Schematic of proposd PECO 10-GW Energy-Park substation (Scheme 2).

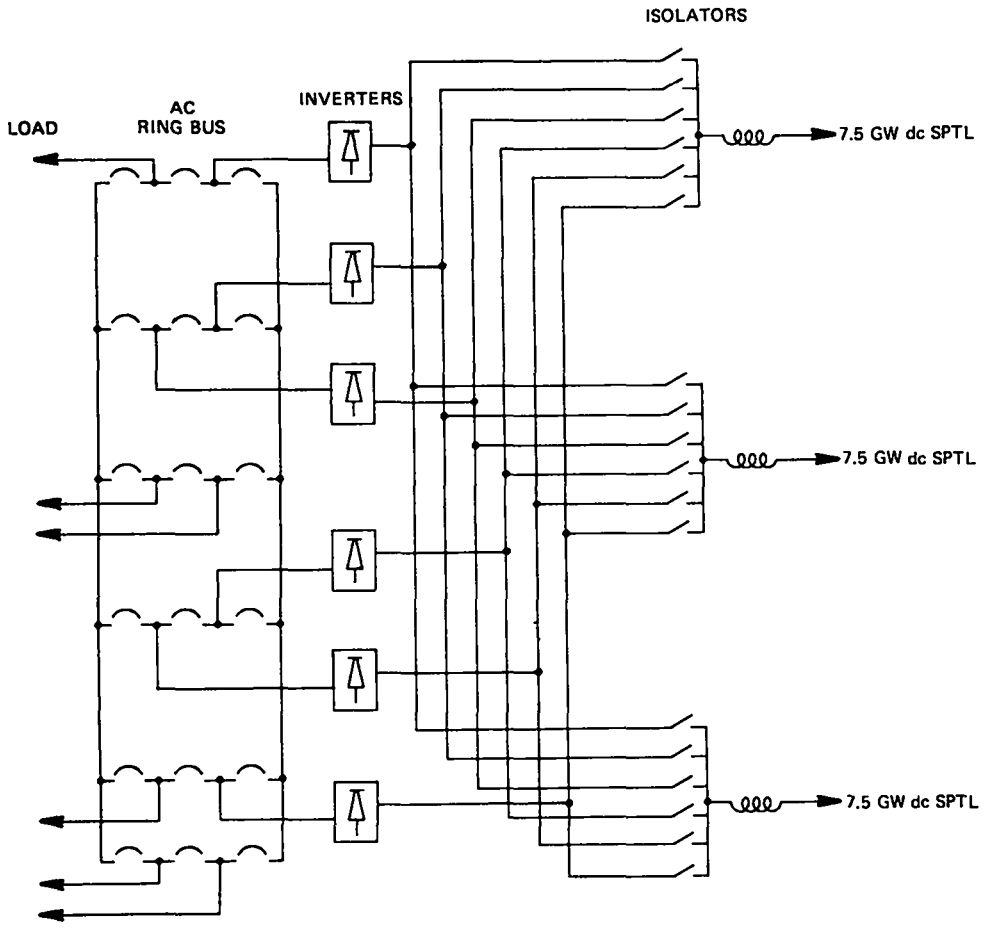

Fig. 6-6.
Schematic of proposd PECO 10-GW Mid-Site substation (Scheme 2).

connected to the faulted cable are blocked and the isolators connected to the faulted cable are opened. Subsequently, these two converters are connected to the remaining two cables, one converter to one cable.

In Scheme 1, all the power has to be interrupted during the process of isolating the faulted cable. In Scheme 2, full power can be maintained through the remaining two cables during this process. Another advantage of Scheme 2 is that the power flow through the three cables can be individually controlled. The best compromise can be obtained by applying Scheme 1 on the rectifier side and Scheme 2 on the inverter side.

Although the PECO study closure[2] does not agree, we believe that we can conservatively estimate the savings from the elimination of the dc circuit breakers to be at least $50M.

Another area where a significant cost saving appeared was in the cost of the cryogenic enclosure. We arranged for an independent study by a

manufacturer in this field, Minnesota Valley Engineering Co. (MVE).[4] Although we believe the results of this study still to be high, they nevertheless predict a lower cost than that used in the PECO at a saving of approximately $35M. This saving arises from a better knowledge of the reduced costs realized from large scale production of identical units.

A third area that seemed worth while to investigate was that of the cost of the superconductor in the cable. Another independent study was contracted to Airco Inc., a manufacturer of superconducting wire. The results of this study[5] showed a reduction in the cost of the superconducting wire, which when applied to the previously submitted cable design, produced a saving of an additional $25M.

The above savings, when totaled are not enough to change the relative ranking of the systems considered,[2] but they are significant. This should enable us to propose a better system in the next study, which will consider a longer distance transmission of electric power (Sec. 6.3).

6.3. Small-Line Concept

6.3.1. Introduction. The use of superconductors in electrical power systems is predicated on their ability to carry electrical currents with essentially zero power dissipation. Thus for power transmission applications the net effect is to replace ordinary copper or aluminum conductors, operating at current densities of 1 to 2 A/mm^2, with a material that is intrinsically capable of sustaining 1000 A/mm^2, but that actually operates at "only" 100 or possibly 200 A/mm^2 when the area of the stabilizer is included. From a cable designer's point of view, power levels of 5 to 20 GW per circuit become possible. The only significant additonal expense over ordinary transmission systems will be the cost of the refrigeration machinery and of the cryogenic envelope or Dewar system. Neither of these are a strong function of cable size or current so that the designer's tendency to suggest very high power levels is further reinforced.

Unfortunately, the near term needs and procedures of electric utility systems, even for a 10 GW power park, preclude individual circuits rated much above 5 GW. Moreover, the usual specifications on contingency performance favor a larger number of parallel (low power) circuits so that the maximum loss because of 2 nearly simultaneous failures is no more than 25% of the total capacity. The net effect then is to make the use of only 2 or even 3 parallel very high (5-10 GW) power circuits noncompetitive under the

transmission scenarios appropriate to the present century. Thus we will have to answer the question as to how dc superconducting transmission cables can be scaled down economically, so as to operate competitively with existing technology in the 1 to 5 GW range. Therefore, we wish to evaluate the concept of a "small" bipolar superconducting transmission line and compare it with conventional power transmission methods.

6.3.2. Characteristics of the Small-Line Concept. With the parallel pair of bipolar concept, Fig. 1-2, it becomes possible to place the dielectric insulation on the outside of the cryogenic envelope, thereby reducing the size of the envelope and making it independent of the transmission voltage. The smaller cryogenic envelope then makes it practical to consider a flexible and, therefore, coilable design that can be fully vacuum tested during manufacture and installed in relatively long lengths. This, then, is essentially a self-contained cable. Nevertheless, the conductor inside the cryogenic envelope is replaceable. Because heat leaks scale as the area of the cold surface, refrigeration requirements (per line) are lowered and the spacing between refrigeration stations may be increased. At the same time one avoids the uncertainties and costs associated with the development of a competitively priced high voltage insulation that operates at cryogenic temperatures. In effect, current, voltage, and the size of the cryogenic envelope being now "decoupled" are independent parameters. This concept had been considered earlier in the SPTL program, but was discarded because of mechanical and superconductor stability difficulties inherent in implementing it at the 50-kA level. Such difficulties, however, do not exist at currents of 2 to 10 kA.

Compared to ordinary resistive cables, the small-line superconducting cable places less severe demands on the dielectric. There is no resistive heating so that operating temperatures will be between 0^{o} and 25^{o}C rather than 0^{o} and 80^{o} or 90^{o}C. Nor will there be large cyclic temperature gradients and associated thermochemical stresses across the dielectric and, particularly, across joints in the dielectric caused by cyclic changes in the line current, including turn-on and turn-off. All of these facts should increase the life of the dielectric. As a further consequence of the lower and more stable temperatures, maintenance of the pressure of the oil impregnating the dielectric will not vary with the power carried by the line, as in conventional cables. As a result, smaller pumps and flow channels are required and, indeed, simple pressurized oil reservoirs may suffice. Nor need the oil be

selected on the basis of a low thermal resistivity; viscosity and dielectric properties can now be primary criteria. Lastly, it should be noted that joint failures from thermal stresses will be absent.

6.3.3. Application of the Small-Line Concept to the Original PECO Study. Although the primary purpose of examining a small-line concept is to prepare for the forthcoming Long Line Study (known as PECO II), it is instructive to see how the small line concept would alter the costs of PECO I.

The specific system carrying 10 GW over 106 km is implemented with three bipolar cables at ±300 kV and a single cryogenic neutral conductor insulated for 20 kV (seven cryogenic enclosures with superconducting cables). Normal operation would be at 1.667 GW per pole, i.e., at 5.56 kA. First contingency ratings would be at 2.0 GW or 6.67 kA and second contingency at 1.875 GW or 6.25 kA. The size or ampacity of the conductor is therefore determined by the first contingency requirement.

In the comparison of costs of the coaxial and small, bipolar line concepts it again became obvious that a considerable saving would be possible in the refrigeration system cost by using fewer, larger refrigeration stations. However, such savings are equally applicable to both systems and therefore we will not consider them further here. Similar conclusions apply to the superconducting wire. Hence, the major costs to be considered here are those of the cryogenic enclosure and of the cable.

6.3.3.1. Cryogenic Enclosure. In addition to the larger, rigid cryogenic enclosure needed for the coaxial system, the MVE study also considered a smaller, flexible cryogenic enclosure, and some cost breakdown data were made available. Although the MVE estimate was $170/m for this enclosure, using their data plus some material cost data obtained from the Vacuum Barrier Co. we estimate that the enclosure could be built for closer to $100/m (1977 dollars).[6] More recently acquired, actual cost data from Cablewave Systems leads us to believe that modification of the manufacturing process for air-dielectric coaxial cable (vacuum tight, concentric flexible tubing) could lead to even less expensive, but satisfactory cryogenic enclosures. We intend to investigate the possibility further. Pending results from this investigation, the $100/m figure given above would result in about a $35M saving in the PECO-I system. A similar saving is anticipated in the enclosure installation: however this needs further study.

6.3.3.2. Cable Fabrication. The simpler cable (possibly a single standard cable, or perhaps even superconductor simply plated on the inner wall of the cryogenic enclosure) will undoubtedly allow a saving in cable fabrication. The Phelps-Dodge Cable Co. is currently studying the cost of insulating the outside of the cryogenic enclosure, and the results of this study are needed before a meaningful cost comparison can be made for this item.

6.3.3.3. Cost Summary. The cost saving of the small line lie in the less expensive cryogenic enclosure and the simpler cable. The evaluation of these savings to date show that, while significant, they are not sufficient to change the ranking by cost in the PECO-I study. However, work is continuing and further savings are still possible.

6.4. References

1. F. J. Edeskuty and N. N. Sheheen, "Dc Superconducting Power Transmission Line Project at LASL, USDOE Division of Electric Energy Systems, Annual Progress Report No. 23, October 1, 1977 - September 30, 1978," Los Alamos Scientific Laboratory report LA-7707-PR (March 1979).

2. "Evaluation of the Economical and Technological Viability of Various Underground Transmission Systems for Long Feeds to Urban Load Areas," prepared by Philadelphia Electric Co. for USDOE Division of Electrical Energy Systems, HCP/T-2055/1 (December 1977).

3. C. B. Lindh and R. V. Pohl, "Design Study: Thyristor Converter Stations for Use with Superconducting Dc Power Transmission Lines," General Electric Co. report L67-71964-1 (June 24, 1977).

4. H. Michael Lutgen, "Engineering Price/Cost Analysis of Cryogenic Cable Enclosures," unpublished report by Minnesota Valley Engineering to the Los Alamos Scientific Laboratory on contract #L68-3031F1 (June 7, 1979).

5. E. Adam, P. Lum, and G. Rothschild, "Study to Determine the Cost of Large Quantities of Nb_3Sn Superconductor for a Superconducting Power Transmission Line," Central Research Laboratories, Airco, Inc. report RE-78-179 (September 1978).

6. H. L. Laquer, "Design of a Compact DC SPTL System," unpublished Los Alamos Scientific Laboratory Report (1979).

7. CONCLUSIONS

7.1. Summary of dc SPTL Program Results

During the course of the LASL dc SPTL development, the dominant modus operandi was: first, to formulate and define the problems that would be met in our pursuit of program objectives; second, to seek, where possible, both analytic and experimental solutions to those problems; and third, to direct and relate those solutions toward achieving optimal operation of dc SPTL components within the integrated dc SPTL system. In carrying out this program, clearly a number of new, unforeseen problems surfaced--some of these were significant, while others could be dismissed as trivial, but the program retained sufficient flexibility to allow pursuit of all relevant problems. As a result of this philosophy and the efforts to implement it, we believe that this program has identified and found solutions for the essential problems in the development leading to a practical dc SPTL system. That is to say, should it be desired to construct a dc SPTL now, we believe we would know how to do it successfully. To justify this statement, we recapitulate below the major technical accomplishments of the LASL dc SPTL Program.

7.1.1. Cable Design. Two conceptual cable designs have been completed:

- A coaxial cable, incorporating complete refrigeration and electrical circuits in a single envelope; most applicable where high-capacity (5 GW or more) single-circuit is required.
- A pair of monopolar cables with dielectric insulation at ambient temperature (i.e., outside the cryogenic envelope); single circuit capacity can be 10 GW, but this design is most useful when contingency requirements indicate multiple circuits.

7.1.2. Conductor Development.

- Superconducting material selection for cable operation at high temperature, high current density, and low magnetic fields (conditions not heretofore met in applications): studies on various high-T_c superconductors; studies on various superconductor configurations; discovery of current and field distribution within superconducting tape; selection of mf Nb_3Sn.
- Design of mf wire strand to optimize mechanical and electrical stability.

- Determination of optimum heat treatment for forming desired mf wire characteristics.
- Testing of strands and cables for $J_c(T)$, stability (normal zone propagation), effects on J_c of bending (as might occur in cable fabrication) and of cable configuration vs individual wires; discovery of asymmetric (with respect to current direction) normal zone propagation velocity.
- Design and construction of superconductor joints and testing of current transfer across joints.
- Production and heat treatment of 300 m of 17-strand mf Nb_3Sn in copper-bronze subcable and of cable composed of three such subcables.

7.1.3. Dielectric Development.

- Establishment of high-voltage testing laboratory: 300 kV dc supply; 600 kV impulse; screen room; clean room; two high-voltage cryostats (100 kV and 300 kV).
- Development of thickness monitor and pin-hole detector for dielectric tape samples.
- Dielectric material selection by screening tests and analyses of approximately 16 dielectric materials (sheet-form) at low temperature and under helium pressure; development of six-electrode testing apparatus for rapid data accumulation.
- Cable-sample tests of three most promising materials (tape-form); electric stress calculations and stress-cone development for rapid, reliable testing.
- Experimental determination of resistivities of dielectric materials.

7.1.4 Termination Development.

- Generalized electric and thermal analysis of high capacity current lead design and performance.
- Design, construction and testing of high capacity liquid-cooled and vapor-cooled current leads.
- Design, construction, and testing (temperature cycling and operation at voltages up to 300 kV) of epoxy and of novel composite (Mylar/epoxy) high-voltage bushings for cryogenic service.

- Design for high-voltage, high-current cryogenic cable termination, made on the basis of successful experimental testing of component parts.

7.1.5. Refrigeration System Development.

- Installation of a cryogenic refrigerator (100 W at 4 K), used in conjunction with either (1) a test bed incorporating 500 m of 0.25-in. o.d. copper tubing as a 1/10-scale simulation of a transmission line flow path, or (2) a 17-m length of 9-in. o.d. commercial cryogenic envelope (cryoflow loop).
- Determination, both analytical and experimental, of transmission-line cool-down methods and kinetics for unidirectional cryogen flow; thermal stresses in cable during the cool-down process have been studied analytically.
- Theoretical and experimental analysis of thermal wave propagation in cooled cable systems.
- Calculations and experimental verification of cable temperature and pressure profiles (i.e., as a function of distance along the cable) for a variety of coaxial cable cooling modes.
- Analytical and experimental determination of cryogenic refrigerator response to thermal upsets (faults).
- Measurement of thermal conductivity of oil-impregnated paper dielectric material.
- Development of flow meter technology.
- Analysis and experimental confirmation of operating characteristics of 100-W-at-4 K refrigerator when run at 10 to 14 K; provision of modifications to allow effective operation at the higher temperatures.
- Thermal and heat-leak measurements of a 17-m commercial cryogenic envelope.

7.1.6. Cryoflow Loop Test. A successful high-current (7 kA), zero-voltage test was made of dc SPTL components assembled in the cryoflow loop and operated in the temperature range from 8 to 14 K. These components included:

- The 100-W-at-4 K refrigerator.
- The 17-m cryogenic enclosure.

- A remote expander to return cryogen to refrigerator and produce additional refrigeration at the far end of the cable.
- A conventional, self-contained, oil-impregnated-paper insulated, copper cable (obtained from Phelps Dodge Co.) placed in the cryogenic envelope; helium cryogen was passed down the central bore of the cable and returned in the annulus between the cable o.d. and the envelope i.d., thereby simulating the cryogen flow in the LASL coaxial design. The thermal impedance of the Phelps-Dodge cable was measured.
- Three subcables of 17-strand mf Nb_3Sn superconductor, twisted to form a cable, passed down the center of the Phelps Dodge cable (higher-current-capacity superconductors provided the return current path to allow critical current tests of the three subcables).
- High capacity vapor-cooled current leads.

7.1.7. System Studies

- Analytical determination of the coaxial dc SPTL performance under: overcurrent fault conditions; transient overvoltage conditions; and superposition of harmonics on the dc.
- Analytic studies of load flow and stability for the dc SPTL in several transmission situations.
- Cost and system studies on dc transmission terminals, performed for the dc SPTL Program by General Electric Co.
- Cost study of mf and tape Nb_3Sn made with cooperation of superconducting wire manufacturers.
- Cost study of cryogenic enclosures performed for the dc SPTL program by Minnesota Valley Engineering Co., also with input from Kabelmetal and Vacuum Barrier Cos.
- Participation in a refrigerator reliability study made for DOE by AirResearch Corp. and Air Products and Chemicals, Inc.
- Analysis of refrigeration cycles, including spacing of refrigerators, heat inleak, refrigerator efficiency, operating temperatures, operating pressures, pressure drop, cryogenic envelope (flow channel) sizes, etc.
- Provision of dc SPTL specifications and cost estimates for reanalysis and inclusion in a comprehensive study of a

106-km, 10-GW transmission system, made by Philadelphia Electric Co. for DOE.

7.2. Future Program

When the dc SPTL Program began operation in late 1972, most predictions of electric power consumption growth in the U.S. indicated a need for doubling power plant capacity each decade. This, in turn, implied a commensurate growth of transmission systems and, in particular, a requirement for high-capacity underground cables of considerable length. The dc SPTL concept was geared to meet such requirements. Since late 1974, however, the growth in power demand has fallen far below earlier expectations, and the probable need for very high capacity underground transmission systems has been considerably deferred. Hence, the case for urgent development of the dc SPTL is rather weak, and this has been a primary cause of the cancellation of the dc SPTL demonstration at LASL. On the other hand, the case for development of the dc SPTL is not dead, but, rather, the time-table requires adjustment.

Under these circumstances, and given the successful initial results enumerated in Sec. 7.1, it is appropriate to ask, "What next?" Although a workable and respectable dc SPTL could be constructed now, it is clear that this is a young technology and that significant improvements in it can be expected from continued research. In effect, we don't know all the "answers" and we don't know how far the technology can be pushed to provide competitive alternatives to other underground transmission modes. Research directed toward those general areas is timely, insofar as the lead time is extremely long for incorporating the results of such work into practical systems.

Specific areas for research, which could promote application of the dc SPTL, and some other advanced transmission systems as well, include:

- Development of higher-temperature superconductors: the higher temperature buys more efficient refrigeration and greater thermal/electrical stability of the conductor. For ac systems, reduction of ac losses can be expected. One goal of this work should be to achieve systems that can be cooled by hydrogen rather than helium.
- Development of more efficient, less costly refrigeration and cryogenic envelope systems. These systems account for the major cost differential between conventional and superconducting cables; fortunately, considerable room exists for improvement and innovation

in the technology and economics of cryogenic systems. At the same time, cryogen flow phenomena require additional study to assure optimum effectiveness of cryogenic hardware use.

- Development of dc cryogenic dielectric systems. Polarization and space charge effects, in particular, are not well understood for conventional dc systems, so any work here would contribute immediately to useful applications. As aging problems are minimal in cryogenic environments, fundamental studies of dielectric breakdown at low temperatures permits the worker to isolate and focus attention on the basic electrical processes in breakdown. Recipes for reliable high voltage operation of cables and terminations should result from research in these areas.
- Development of dc switches and inverter/rectifier equipment. Impetus for this work has been provided by the emerging realization of the usefulness of HVDC transmission. Significant advances here appear achievable by the power industry.

The facilities and staff at LASL are well positioned to conduct productive research in important topics of the first three items above. Current plans call for a continuation of the dc SPTL program along those directions.

8. PRESENTATIONS AND PUBLICATIONS

During the course of the dc SPTL project over 250 presentations discussing the program were given at LASL. An almost equal number of presentations were given at places outside LASL.

Approximately 10 utility companies were briefed on the dc SPTL project. These included Arizona Public Service, American Electric Power, New Mexico Public Service, Consolidated Edison (NY), Commonwealth Edison (Chicago), and Philadelphia Electric Co.

Also about 15 congressmen were given tours of the dc SPTL project.

Thirty-eight papers dealing with different aspects of the project were published. Also quarterly and annual progress reports were written.

A list of the publications follows.

1. R. J. Bartlett, E. F. Hammel, J. K. Hoffer, W. E. Keller, E. C. Kerr, T. E. McDonald, R. D. Taylor, and W. J. Trela, "Conductor Tests for DC Superconducting Power Transmission," Proc. Fifth International Cryogenic Engineering Conference, Kyoto, Japan, May 7-10, 1974 (IPC Science and Technology Press, Whitstable, England, 1974) pp. 174-176.

2. T. E. McDonald, "Development Project for a DC Superconducting Transmission Line," Proc. 1974 IEEE Underground Transmission and Distribution, Dallas, Texas, April 1-3, 1974.

3. E. F. Hammel, "Energy and Cryoengineering," Proc. Fifth ICEC, Kyoto, Japan, May 7-10, 1974 (IPC Science and Technology Press, Whitstable, England, 1974) pp. 11-16.

4. H. L. Laquer, "Superconducting Magnetic Energy Storage," Proc. Fifth ICEC, Kyoto, Japan, May 7-10, 1974 (IPC Science and Technology Press, Whitstable, England, 1974) pp. 71-77.

5. J. K. Hoffer, "Investigations on Potential Conductors for a DC Superconducting Power Transmission Line in a 20-Meter Test Bed," Proc. 1974 Applied Superconductivity Conference, Oakbrook, Illinois, IEEE Trans. on Magnetics MAG-11, 385 (1975).

6. A. Migliori, R. J. Bartlett, and R. D. Taylor, "Magnetic Field Microprobe in Superconductors Carrying a Current," Proc. 1974 Applied Superconductivity Conference, Oakbrook, Illinois, IEEE Trans. on Magnetics MAG-11, 347-349 (1975).

7. T. E. McDonald, W. V. Hassenzahl, and W. E. Keller, "Economic and System Aspects of a Superconducting Magnetic Energy Storage Device and a DC Superconducting Transmission Line," Canadian Communications and Power Conference, Montreal, Nov. 6-8, 1974; IEEE 74 CHO 894-6REG7, p. 131b (1974).

8. E. F. Hammel, "Energy and Cryoengineering," Cryogenics 15, 57-63 (1975).

9. J. K. Hoffer, E. C. Kerr, and H. L. Laquer, "Stabilizing Superconductors for Power Engineering Applications," IEEE Trans. on Power Apparatus & Systems PAS-94, 2008-2014 (1975).

10. W. C. Overton, Jr., H. Weinstock, and A. F. Schuch, "Observation of Asymmetry Effects in the Velocity of Destruction of Superconductivity by Current," Proceedings XIV International Conf. Low Temperature Physics, Krusius and Vuoria, Eds. (North Holland Publishing Co., 1975), p. 149.

11. W. C. Overton, Jr., "Analysis of Asymmetry Effects in the Velocity of Destruction of Superconductivity by Current," Proceedings XIV International Conf. Low Temperature Physics, Krusius and Vuoria, Eds. (North Holland Publishing Co., 1975), p. 145.

12. W. C. Overton, Jr., and H. Weinstock, "Determination of Kapitza Conductance from the Velocity of Destruction of Superconductivity by Current," Proceedings 2nd International Conf. on Phonon Scattering in Solids, Challis, Rampton, and Wyatt, Eds. (Plenum Publishing Co., New York, 1976), p. 48.

13. J. W. Dean, "Calculating the Recovery Time of a Supercritical Helium Refrigerator After a Thermal Upset," Paper A-9, Proc. Sixth International Cryogenic Engineering Conference, Grenoble, France, May 11-14, 1976 (IPC Science and Technology Press, Guildford, England, 1976), pp. 80-81.

14. J. W. Dean and H. L. Laquer, "Conceptual Design of a dc Superconducting Power Transmission Line," Proc. 1976 Underground Transmission and Distribution Conference, IEEE Publication No. 76 CH 1119-7-PWR, (IEEE, NY, 1976) pp. 417-923.

15. J. D. Thompson, M. P. Maley, L. R. Newkirk, and F. A. Valencia, "Measurement of Low Hysteresis Losses in CVD Prepared Nb_3Ge," Phys. Lett. A, 57A, 351 (1976).

16. A. Migliori, R. J. Bartlett, and R. D. Taylor, "Transport-Current-Induced Magnetic Field Profiles of Nb_3Sn Superconducting Tape," J. App. Phys. 47, 3266-71 (1976).

17. J. W. Dean and H. L. Laquer, "Conceptual Design of a DC Superconducting Power Transmission Line," Conf. Record of IEEE Underground Transmission and Distribution Conference, Publication No. 76 CH1119-7-PWR, 1976, pp. 417-423.

18. W. E. Keller, "Applications of Superconductivity in Electric Power Systems," Proc. 1976 Frontiers of Power Technology Conference, Oklahoma State University, Stillwater, OK, October 28-28, 1976.

19. H. L. Laquer, "The Design of Multifilamentary Nb_3Sn Superconductor Tailored to the Requirements of a DC Superconducting Power Transmission Line," Proc. Int. Conf. on Manufacture of Superconducting Materials, Port Chester, NY, November 8-10, 1976 (ASM, Metals Park, Ohio, 1977), pp. 47-58.

20. R. J. Bartlett, R. V. Carlson, A. Migliori, and H. L. Laquer, "Considerations in Designing and Using Superconductors with High Resistivity Matrices," Proc. Int. Conf. on Manufacture of Superconducting Materials, Port Chester, NY, Nov. 8-10, 1976 (ASM, Metals Park, Ohio, 1977), pp. 184-194.

21. J. D. Thompson, M. P. Maley, and L. R. Newkirk, "Effect of Second-Phase Precipitates and Deposition Temperature on the Hysteretic Losses in CVD-Prepared Nb_3Ge," Appl. Phys. Lett. 30, 190-192 (1977).

22. J. D. Thompson and M. P. Maley, "Observation of a Minimum in the Hysteretic Power Loss of Type II Superconductors as a Function of DC Bias Field Applied Parallel to the AC Magnetic Field," Bul. Amer. Phys. Soc. 22, 425 (1977).

23. H. L. Laquer, J. W. Dean, and P. Chowdhuri, "Electrical, Cryogenic, and Systems Design of a DC Superconducting Power Transmission Line," IEEE Trans. on Magnetics MAG-13, 182-197 (1977).

24. A. Migliori, R. D. Taylor, and R. J. Bartlett, "Magnetic Field Profiles of NbTi Tapes," IEEE Trans. on Magnetics MAG-13, 198-200 (1977).

25. J. K. Hoffer, E. C. Kerr, and W. C. Overton, Jr., "Asymmetry of Thermal Propagation Velocity in a Long Forced-Cooled Superconducting Test Line," IEEE Trans. on Magnetics MAG-13, 408-411 (1977).

26. J. D. Thompson, M. P. Maley, and L. R. Newkirk, "Temperature Dependence of AC Losses in CVD-Prepared Nb_3Ge," IEEE Trans. on Magnetics MAG-13, 429-432 (1977).

27. R. V. Carlson, R. J. Bartlett, L. R. Newkirk, and F. A. Valencia, "Critical Current Measurements of CVD-Prepared Nb_3Ge Containing Various Amounts of Second Phase (Nb_5Ge_3) Material," IEEE Trans. on Magnetics MAG-13, 648-650 (1977).

28. J. K. Hoffer and J. W. Dean, "Propagation of Thermal Waves in Supercritical Helium," AIChE-ASME Heat Transfer Conference, Salt Lake City, Utah, 15-17 August 1977, Paper No. 77-HT-76.

29. W. E. Keller, "Applications of Superconductivity to Electric Power Equipment," Electric Power Systems Research (Lausanne, Switzerland), 1, 21-39 (1977).

30A. P. Chowdhuri and F. J. Edeskuty, "Bulk Power Transmission by Superconducting DC Cable," Electric Power Systems Research (Lausanne, Switzerland), 1, 41-49 (1977).

30B. P. Chowdhuri and F. J. Edeskuty, "Bulk Power Transmission DC Cable," Australian Electrical World 43, No. 3, 14-26 (March 1978).

31. W. E. Keller, "The Use of Superconductive Technology for Energy Storage and Power Transmission for Large Power Systems - Power Parks," International Scientific Forum on an Acceptable Nuclear Energy Future of the World, Nov. 7-11, 1977, O. K. Kadiroglu, A. Perlmutter, and L. Scott, Eds., (Ballinger Publishing Co., Cambridge, Massachusetts, 1978) pp. 661-673.

32. P. Chowdhuri and H. L. Laquer, "Some Electrical Characteristics of a DC Superconducting Cable," IEEE PAS 97, 399-408 (1978).

33. W. C. Overton, Jr., R. J. Bartlett, R. V. Carlson, and H. Weinstock, "Observations of Long N-S Interfaces During N-Zone Motion," Proc. Fifteenth International Conference, Grenoble, France, August 23-29, 1978 (Colloque 6, Supplement Au Journal de Physique, France, 1978) FASC-8, Vol. 1, pp. C-6-667-672.

34. J. W. Dean and W. F. Stewart, "Performance of a Liquid Helium Refrigerator Operated Above the Critical Temperature," Proc. Seventh International Cryogenic Engineering Conf., London, England, July 4-7, 1978 (IPC Science and Technology Press, Guildford, England 1979) Vol. 7, pp. 629-634.

35. W. E. Keller, "Dc Superconducting Cables," Proc. of 1979 Workshop on Public Policy Aspects of High Capacity Electric Power Transmission, Aspen Center for Physics, May 14-16, 1979, Aspen, Colorado; EPRI WS-79-164 (1979), p. 2-105.

36. P. Chowdhuri and M. Mahaffy, "Wave Propagation in a DC Superconducting Cable Part I: Analysis," presented at the 1979 IEEE Summer Power Meeting, Vancouver, July 1979, Paper No. A79 409-4.

37. P. Chowdhuri and M. Mahaffy, "Wave Propagation in a DC Superconducting cable, Part II: Parametric Effects," presented at the 1979 IEEE Summer Power Meeting, Vancouver, July 1979, Paper No. A79 410-2.

☆ U.S. Government Printing Office: 1980 — 677 — 115/66

Printed in the United States of America. Available from
National Technical Information Service
US Department of Commerce
5285 Port Royal Road
Springfield, VA 22161

Microfiche $3.00

001-025	4.00	126-150	7.25	251-275	10.75	376-400	13.00	501-525	15.25
026-050	4.50	151-175	8.00	276-300	11.00	401-425	13.25	526-550	15.50
051-075	5.25	176-200	9.00	301-325	11.75	426-450	14.00	551-575	16.25
076-100	6.00	201-225	9.25	326-350	12.00	451-475	14.50	576-600	16.50
101-125	6.50	226-250	9.50	351-375	12.50	476-500	15.00	601-up	

Note: Add $2.50 for each additional 100-page increment from 601 pages up.